Optimizing liquid Xenon TPCs

Inauguraldissertation
der Philosophisch-naturwissenschaftlichen Fakultät
der Universität Bern

vorgelegt von

Basho Kaminsky

von Leipzig (D)

Leiter der Arbeit:
Prof. Dr. M. Schumann

Albert Einstein Center for Fundamental Physics
Laboratory for High Energy Physics

source: https://doi.org/10.7892/boris.134683 | downloaded: 20.4.2024

Optimizing liquid Xenon TPCs

Inauguraldissertation
der Philosophisch-naturwissenschaftlichen Fakultät
der Universität Bern

vorgelegt von

Basho Kaminsky
von Leipzig (D)

Leiter der Arbeit:
Prof. Dr. M. Schumann

Albert Einstein Center for Fundamental Physics
Laboratory for High Energy Physics

Von der Philosophisch-naturwissenschaftlichen Fakultät angenommen.

Bern, 02. November 2017

Der Dekan:
Prof. Dr. G. Colangelo

Optimizing liquid Xenon TPCs

Detecting dark matter is one of the biggest challenges in modern physics. Many astrophysical observations indicate its existence, however a confirmed direct detection of dark matter is still missing. Weakly interacting massive particles (WIMPs) are possible candidates, which are predicted by extensions of the standard model of particle physics. The most sensitive WIMP searches employ dual-phase time projection chambers (TPC) filled with the liquefied noble gas Xenon to search for the expected extremely rare interactions of WIMPs with ordinary matter. These interactions yield to the emission of faint light at 178 nm. This demands for a huge number of possible scattering targets to increase the sensitivity, low backgrounds and a high efficiency to detect the scintillation light emitted by the Xenon-WIMP interaction. Current detectors, like XENON1T, reached ton-scale target masses. Their sensitivity can be optimized for example by reducing the loss of the few photons that emerge from the interaction of a WIMP with the target nuclei. That includes reducing the absorption of these photons on the detector walls by making them highly reflective. Since WIMPs were not detected yet, future detectors are required to have an even higher sensitivity compared to the current ones. It requires further optimization and novel technologies to reach this goal. This work presents contributions to the optimization of one of the currently most sensitive detectors, XENON1T, by optimizing the reflectivity of the inner TPC walls (chapter 2). The development of a cryogenic test platform for the development and research towards future detector is shown in chapter 3, including the first operation of a small TPC.

The optimization of the reflectivity of the PTFE reflectors of the XENON1T TPC (sec.2.1) is done by a surface treatment reducing the surface roughness to less than 0.1 μm (sec.2.3). The increased reflectivity was approved with a reflectivity measurement apparatus in the VUV range in LXe (sec.2) and the findings were confirmed in the optical wavelength range (sec.2.3.3). This effort results in a light yield of (8.02 ± 0.06) PE/keV at a drift field of 125 V/cm for the XENON1T TPC. Beyond the optimization of current detectors, the development of a cryogenic test platform is demonstrated, which will be used to develop future detector technologies. A small TPC (sec.3.5) was successfully installed and operated: first results of the characterization in terms of charge 10.8 PE/keV and light yield 3.7 PE/keV are presented in sec.3.10.

Contents

Abstract **v**

1 Introduction **1**
1.1 Dark matter . . . 2
1.1.1 Weakly interacting massive particle (WIMPs) . . . 4
1.1.2 Direct detection of WIMPs . . . 5
1.1.3 Other WIMP searches . . . 8
1.2 Liquid Xenon dual-phase TPCs . . . 9
1.2.1 Working Principle . . . 11
1.2.2 Performance Requirements of LXe TPCs . . . 13
1.2.3 XENON1T . . . 15
1.2.4 Challenges for future LXe TPC generations . . . 16

2 Light reflectors for XENON1T **19**
2.1 Reflectivity of PTFE at 178 nm . . . 20
2.2 The Münster reflectivity setup . . . 24
2.2.1 Hardware . . . 25
2.2.2 Data acquisition and analysis . . . 29
2.3 Design of the XENON1T reflectors . . . 37
2.3.1 Machining of reflectors . . . 37
2.3.2 Reflectivity outside the beam-PMT-plane . . . 44
2.3.3 Confirmation of the measurements in the optical range . . . 47
2.3.4 Performance of the XENON1T reflectors . . . 49
2.4 Summary and discussion . . . 55
2.4.1 Limitations of the measurements . . . 56
2.4.2 Possible improvements measuring the reflectivity of PTFE in LXe at VUV . . . 59
2.4.3 Improving the reflectivity further . . . 60

3 The Bern LXe test platform **61**
3.1 Cryostat and vacuum system . . . 62
3.2 Cryogenic System . . . 65
3.3 Gas handling and purification . . . 70
3.3.1 Gas panel . . . 70
3.3.2 Gas analysis . . . 73
3.4 Instrumentation and slow control system . . . 75
3.5 Time projection chamber . . . 82

3.5.1 High voltage system 84
3.5.2 Light sensors 87
3.6 Data acquisition 88
3.6.1 Selftrigger mode 91
3.6.2 External trigger mode 91
3.7 Data processing 92
3.7.1 Software trigger 93
3.7.2 Data processor 95
3.7.3 Peak finding and classification 97
3.8 Analysis of the TPC data 103
3.8.1 Gain determination 103
3.9 Co57, Cs137 and background data at lower gain 111
3.9.1 Drift time 116
3.9.2 Electron lifetime 119
3.9.3 S2 correction 122
3.9.4 Light yield 122
3.9.5 Charge yield 126
3.10 Summary and evaluation 127

4 Outlook **134**
4.1 Reflectivity measurements and reflector design 134
4.1.1 Reflectivity measurements 135
4.1.2 Reflector design 136
4.2 Future development of the Bern LXe test platform 136

Bibliography **138**

Chapter 1

Introduction

The standard models of cosmology and particle physics are well established, it seems that there is not much space for novel findings. But both show challenging problems that indicate the need for physics beyond these standard models. One of these problems can be found on the intersection of both theories: dark matter. It was postulated to explain the rotation velocities and velocity dispersions of stars in galaxies, which move faster than expected from the observed visible masses. One hypothesis explaining these observations is non-visible mass. Later more and more observation indicated that the observable mass is not accounting for the whole mass in the universe. While there is no alternative model yet, which can explain the observations that lead to the postulation of dark matter, its direct detection is still missing. Its existence seems currently doubtless in terms of astrophysical observations, as demonstrated in sec.1.1, but possible candidates within the standard model of particle physics are well excluded as dark matter candidates. Thus extensions of the standard model of particle physics might deliver new candidates. They might be found with currently or in close future deployed detectors with their increased sensitivity. A detection of such a dark matter candidate would thus confirm the postulation of it by the cosmological standard model and astrophysics, and open the gate towards physics beyond the standard model of particle physics.

An extension of the standard model of particle physics, supersymmetry, introduces for each particle in the standard model a supersymmetric partner, the superpartner [84]. This theory offers possible candidates, which can account for dark matter (sec.1.1, page 2). One likely candidate particle type is the Weakly interacting massive particle (WIMP) (sec.1.1.1, page 4). It is a generic particle that interacts mainly gravitationally and weak (considering the four forces in the standard model of particle physics: gravitation, weak interaction, electromagnetic interaction and strong interaction). The most sensitive detectors for the search for heavy WIMPs, $m_\chi \geq 10\,\mathrm{GeV}$, are time projection chambers

(TPCs), which aim for the direct detection with a liquefied noble gas as target medium (sec.1.1.2, page 5). This work presents some contribution to the design of one of the currently most sensitive dark matter detectors and towards the development of the next generation of dark matter detectors. In this first chapter at first the mandatory fundamentals of dark matter will be explained in sec.1.1 (page 2) and afterwards dual-phase time projection chambers (TPC) will be introduced in sec.1.2 (page 9). The detection efficiency for light defines among others the sensitivity of TPCs (sec.1.2.2, page 13). It is not only limited by the actual used light detectors and scattering in the target medium itself, but as well by the reflectivity of the detector walls. The optimization of the reflectivity of the TPC walls for one of the currently most sensitive dark matter detectors, XENON1T, is presented in chapter 2. The development of future detector generations aiming for the direct detection of dark matter demands for new technologies, as described in sec.1.2. The development of cryogenic test platform that will be used for the research and development for upcoming detectors, like the ultimate dark matter search DARWIN (sec.1.2.4, page 16), is presented in chapter 3.

1.1 Dark matter

The universe consists of visible matter and two invisible components that are yet only observed indirectly: dark energy and dark matter (DM). The visible matter (electromagnetic interacting) contributes only $\approx 5\%$ to the content of the universe: about 27% are dark matter and 68% is dark energy [186].

Dark matter was first suggest in order to explain the observed motion of stars in the galaxy 1922 [137] and 1932 [178, 144]. The application of the virial theorem[1] on the observed motion of the Coma cluster led to the first quantization of the dark matter content, comparing the expected mass and the observed mass [241]. Fig.1.1 illustrates the gravitational effect of dark matter on the rotation velocities in the M33 galaxy.

The cosmological standard model of the universe is the so-called ΛCDM model, which describes the universe according to general relativity with a Friedmann–Lemaître–Robertson–Walker metric including dark energy (cosmological constant $\Lambda < 0$) and cold dark matter (CDM) [230]. In the cosmological standard model, matter is defined generally as the content of the universe, which has an energy density of $\rho \propto a^{-3}$, where a is the scale factor that describes the expansion of the universe. It consists of baryonic matter, which is luminous and behaves non relativistic, and dark matter which is non luminous and non

[1] Virial theorem: $< T > = -\frac{1}{2} < U_G >$, with the total kinetic energy T and the total potential energy U_G (here gravitational energy).

baryonic but none relativistic too. Finally the universe contains radiation, which behaves relativistic. The radiative content of the universe shows a negligibly small mass contribution [186].

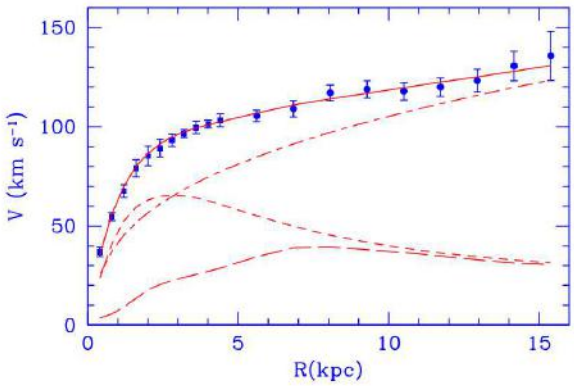

FIGURE 1.1: Rotation curves of M33. The measurement points were taken at the 21 cm H line and are shown with their best fit model (red line), which includes dark matter. The contributions from the visible matter (short dashed), interstellar gas (long dashed) and dark matter halo (dashed dotted) are shown. Taken from [75].

Dark matter is indicated by many direct observations:

- rotation curves of spiral galaxies: the observed rotation velocities are larger than expected for large radii according to the Kepler laws, this indicates a larger mass than the observed luminous matter [75]
- velocity dispersion of stars in galaxies (mentioned above): the observed velocity dispersions indicate missing mass according to the virial theorem [141]
- motion and dynamics of galaxies [241]
- gravitational lensing of background galaxies [220, 195]

and also by indirect observation, which require modelling and numerical analysis, but allow for the determination of cosmological parameters:

- cosmic microwave background (CMB) [115, 186]
- baryonic-acoustic oscillations (BAO) of matter on large scales in sky surveys [185]
- redshift surveys over large scales, which indicate that super clusters move faster than expected from their luminous matter [183]
- Supernova surveys measuring the cosmological expansion and thus allow the determination of cosmological parameters [142]

The list might not be complete but summarizes the most important indications for dark matter in observations. Furthermore, simulations of structure formation require dark matter [156]. The structure formation and distribution of matter in the universe also indicate that dark matter must be so-called cold dark matter with non-relativistic velocities. Otherwise dark matter would be homogeneously distributed in the current universe while its observed distribution is strongly localised [171, 163]. Furthermore, a composition of dark matter out of ordinary baryonic matter (massive astrophysical compact halo objects, MACHOs) is not likely because it would become directly observable, when being between some star or background galaxy and the earth, which is not observed [153]. MACHOs would furthermore be visible by micro lensing if they account for the majority of dark matter, what is not observable [103, 102, 96, 89]. A part of the cosmological standard model is the generation of nuclei in the early universe, the so-called nucleosynthesis [14]. This theory indicates also that dark matter could not consist out of MACHO because the abundance of the generated matter only accounts for the visible matter [192, 153, 77].

Other possible dark matter candidates come from extensions of the standard model of particle physics, like supersymmetry [84]. These theories introduce new particles that interact only gravitationally on large scales (e.g. axions; hypothetical, yet unobserved, very light particles [184], sterile neutrinos; only gravitational interacting neutrinos [167], and others). Following the analysis excluding baryonic matter as dark matter, one finds that dark matter has to consist out of particles, which do not interact electromagnetically or strong. Since possible candidates were not observed yet in accelerator experiments, it is very likely that dark matter consists out of very heavy particles ($\mathcal{O}100\,\mathrm{GeV}$). One candidate is introduced in the following section.

1.1.1 Weakly interacting massive particle (WIMPs)

One candidate for dark matter is the WIMP χ [102]. It can be understood as a generic new hypothetical particle that fulfills the requirements to be dark matter. WIMPs are supposed to have existed in the early universe in thermal equilibrium with the other matter via some light or even massless particle l [153]:

$$\chi + \bar{\chi} \leftrightarrow l + \bar{l} \tag{1.1}$$

When the universe expands, it cools down and at a certain point the leftwards proceeding process in eq.(1.1) becomes inefficient. That means the χ and $\bar{\chi}$ freeze out and behave non relativistic with annihilation of χ and $\bar{\chi}$ until only some remainders are left. Assuming now that l and $\bar{l}$ stay coupled to the other particles, one can constrain from

these assumptions the averaged thermal annihilation cross section of the process $\langle \sigma v \rangle$ in eq.(1.1) using the current dark matter abundance ($\Omega_{\mathrm{DM}} \approx 0.3$) [240, 212]:

$$\langle \sigma v \rangle \leq 10^{-28} m_{\chi}\, \mathrm{cm}^3 \mathrm{s}^{-1} \tag{1.2}$$

It indicates that the WIMP cross section is in the same order of magnitude than the weak interaction. However, the values found in literature fluctuate, e.g. [132, 155], depending on the initially used values and cosmological parameters. Nevertheless, this is of minor importance since the used assumptions are simplifying the problem anyhow and thus just giving a rough idea. Current detector generations that aim for a direct detection of WIMPs are able to find WIMPs or falsify the predictions leading to the hypotheses that WIMPs are the major contribution to dark matter [32]. A direct detection of WIMP dark matter would not only mean the detection of dark matter, it would even allow for the determination of cosmological parameters like the freeze out temperature of WIMPs and thus would allow a view in the universe shortly after the big bang [212]. The interaction channels of the WIMP, and their application in WIMP searches, is illustrated in fig.1.2. The different WIMP search channels and the experiments using these channels are explained in the following sections.

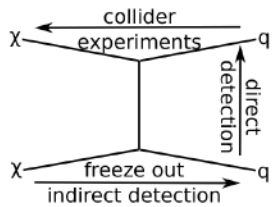

FIGURE 1.2: Feynmann diagramm illustrating the WIMP interactions with ordinary matter, showing the freeze out as it might have happened in the early universe, which is used for the indirect detection with WIMP annihilations (see sec.1.1.3), the production channel of WIMPs in collider experiments (see sec.1.1.3) and the direct detection channel (sec.1.1.2) as used by the experiments explained in this work (see sec.1.2). q is baryonic matter and can be the nucleus of an atom, fermions like neutrinos, electrons or muons or even bosons like gammas. The exchange process in the middle is unknown yet and there are various interaction theories predicting different cross sections.

1.1.2 Direct detection of WIMPs

As shown above, dark matter was observed on various channels via its gravitational interaction but it remained unclear out of what particles it is build. Several experiments aim for a direct detection of WIMPs as candidates for dark matter. The basic assumption is that the earth moves the dark matter halo[2] of the galaxy [172, 168]. If dark matter consists of WIMPs, they can scatter from time to time with ordinary matter atoms. For a

[2]The dark matter halo is a component of the galaxy, which is not rotating with the galaxy and even extends beyond the edge of the visible mass distribution [112, 95].

first approximation one can assume that the cross section is fixed to the above mentioned annihilation cross section and that the velocity is about the velocity of the sun moving around the galactic center: $v_\odot \approx 250\,\mathrm{km/s}$. Thus the interaction rate depends further only on the used target medium density and local dark matter matter density. The expected interaction rates per detector volume can be estimated from [56]:

$$R = n_\chi \cdot \sigma \cdot v_\odot \cdot N \tag{1.3}$$

with the WIMP number density n_χ and target number density N (with an expected WIMP flux of $j = \frac{\rho_\chi v_\odot}{m_\chi}$). Taking the standard literature value of $\rho_\chi = 0.3\,\mathrm{GeV/cm^3}$ [194] one gets a WIMP flux of $\mathcal{O}(10^5)\,\mathrm{cm^{-2}s^{-1}}$. But R depends furthermore on the spectral shape of the WIMP spectrum, the expected recoil energy and considered energy range of the detector. In the collision of a WIMP with a nucleus, the transfered energy can be simplified as elastic collision by:

$$E = \frac{\mu^2 v^2}{m_{\mathrm{nucleus}}} \cdot (1 - \cos\theta) \tag{1.4}$$

with the reduced mass μ, the scattering angle θ and the mass of the nucleus m_{nucleus}. The transfered energy, the recoil energy, has a characteristic spectrum, which depends as well on the incident WIMP velocity. The most likely energy is given as: $E = {}^1\!/\!_2 m_\chi v_\odot^2$. For the energy distribution of the WIMPs, a Maxwell-Boltzmann distribution can be considered [46].

From these points it follows that a dark matter detector should have a high target nuclei density N to increase the interaction probability. The sensitivity of a detector aiming for the direct detection of DM depends highly on the target mass: a high mass means many possible target nuclei. The expected rate gets smaller with an increased energy, which demands a low energy threshold. Since the expected rates for various considerable target media are all very low ($\mathcal{O}(10^{-6})\,\frac{\mathrm{events}}{\mathrm{kg\cdot d\cdot keV}}$ [45], the detector needs furthermore to have a very low intrinsic background to be able to separate the expected signal from the background. The signature of a WIMP interacting with a target nuclei is a low energetic nuclear recoil (NR) and depends on the target medium. The event rate underlays a potential annual modulation of the rotation of the earth around the sun that moves through the galactic DM halo, which can be used as a potential DM signature [97].

Backgrounds for DM detectors are usually radioactive contaminations, which yield to recoils on the electrons of the detector medium atoms (ER). Muons, as external background, generate ER as well but can be vetoed efficiently if their flux is already low enough. This is achieved by using underground laboratories [114, 29]. The lowered flux of cosmic radiation is also important due to the generation of cosmogenic neutrons in the

detector itself, as these show similar event signature like WIMPs: nuclear recoils (NR) [106, 1]. Other NR backgrounds are neutrons from external sources or from radioactive decays (especially alpha decays, which can emerge (α,n) reactions and free neutrons). Low energetic nuclear recoils due to neutrinos play a role as final irreducible background for future detectors since they cannot be shielded (ER can be rejected by ER/NR discrimination but NR from solar neutrinos [202] cannot be rejected or shielded).

The ER background from radioactive decays can be shielded with passive shields like lead, water or copper. Some DM detectors, like dual-phase TPCs, have the advantage to be able to discriminate these ER backgrounds from possible WIMP interactions (see above and explained in detail later). Cosmic rays in underground laboratories are mainly muons, which can be vetoed by an muon veto surrounding the DM detector and their flux can be reduced by some significant rock overburden [46, 165].

There are various dark matter detector types using various detection channels and technologies to reduce the background:

- solid state detectors at cryogenic temperatures: NR on solid state target: ionization+phonons(vibrations); high energy resolution, low energy threshold; CDMS [71], CRESST [16], CoGeNT [2]
- Scintillating crystals: scintillation light & annual modulation of the WIMP flux; low threshold, large mass; DAMA/LIBRA [52], ANAIS [15]
- superheated liquids: a small energy input yields to bubble creation and phase transitions; large mass, insensitive to ER; PICASSO [35], COUPP [49]
- liquefied noble gas: scintillation light & pulse shape discrimination or annual modulation; large mass; XMASS [162], DEAP-3600 [78]
- liquefied noble gas TPCs: scintillation and ionization of target nuclei; large mass, good ER/NR discrimination; LUX [6], PandaX [69], ArDM [196, 36], XENON100 [235], ZEPLIN [13]

None of the mentioned experiments showed any evidence for dark matter, apart from DAMA/LIBRA, who had reported a potential detection via annual modulation with a high significance of 8.9σ [54, 53] and CDMS-Si, who claim a potential discovery for a 8.6 GeV WIMP at $1.9 \cdot 10^{-41}\,\mathrm{cm}^2$ [70]. Nevertheless, these findings were not confirmed by any other dark matter search, e.g. [93], and disagree with each other. The second last mentioned liquefied noble gas detectors, like XMASS or DEAP-3600, use only the liquid phase as detector medium. The last mentioned TPCs utilize liquefied noble gasses

as target with dual-phase TPCs employing the gas phase as detector component. Dual-phase TPCs are explained in more detail in sec.1.2. Fig.1.3 gives an idea about the current status of the direct search for dark matter.

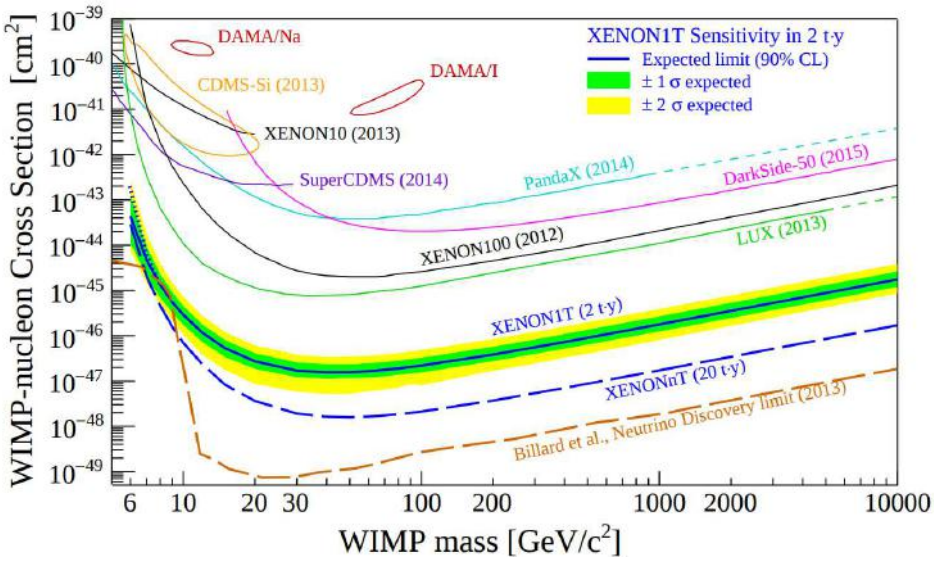

FIGURE 1.3: Limits from various direct WIMP searches and discoveries of DAMA-LIBRA [54, 53] and CDMS-Si [70]. Furthermore, the expected limitation of the direct dark matter searches due to coherent neutrino-nucleon-scattering is given as neutrino discovery limit [57]. The current limits from XENON1T [33], LUX [8] and PandaX [182] are missing in the plot. Taken from [32].

1.1.3 Other WIMP searches

Besides the direct detection, there are two more strategies to search for WIMPs, as illustrated in fig.1.2. The first one is the production channel, i.e. trying to produce WIMPs directly in collider experiments. The idea is that WIMPs might be created similar to the process in eq.(1.1) in collider experiments: $l + \bar{l} \rightarrow \chi + \bar{\chi}$. They would appear as missing transversal momentum [58]. The advantage of this channel is the ability to control the experimental conditions very well and a high sensitivity for WIMPs with low masses. They do not depend on cosmological or astrophysical parameters. Collider searches complete the search for WIMPs in the low mass region below 100 GeV. The generation of WIMPs in a collider does not necessarily mean that dark matter consists out of WIMPs but this could then be tested with a specified detector exploiting the then well-known WIMP properties. There are some searches on currently running experiments: [166, 118, 191, 92]. The sensitivity of collider searches depends strongly on the considered decay model and signal channel. For example with ATLAS one can place limits on WIMP-nucleon cross sections of $\mathcal{O}(10^{-44})\,\mathrm{cm}^2$ for WIMP masses below 200 GeV for various interaction models [166].

The second strategy is the indirect detection of WIMPs. The idea beyond this is the search for WIMP annihilation signals from places with higher WIMP densities, e.g. mono-energetic gamma ray lines in the cosmic radiation, which might be related to the WIMP annihilation. WIMPs are expected to aggregate, for example in the galactic center or dwarf galaxies, due to elastic collisions, which might cause their velocities to drop below the escape velocities. The results from indirect searches are again model dependent. They complete the search towards very heavy WIMPs in the TeV mass scale. Recent results exist for the space based Fermi-LAT experiment [73], the ground based gamma ray telescope HESS [4], MAGIC [85] and VERITAS [38]. Another indirect detection channel comes from neutrinos, which also might be emitted from WIMP annihilations. Signals would be expected from the WIMP annihilations in the sun and experiments like Super-Kamiokande [94], AMANDA [60] or IceCube [3] exploit this channel.

1.2 Liquid Xenon dual-phase TPCs

Time projection chambers (TPC) with liquefied noble gases as target medium are well suited for dark matter searches because they can be build with ton-scale target masses (e.g. XENON1T [23]), they offer a good 3D position reconstruction that allows to reduce the backgrounds with fiducialization of the sensitive detector volume (only inner detector volume get used exploiting self-shielding), a good signal to background discrimination using the independent ionization and scintillation signals and background reduction by filtering multiple scatter events [25]. Especially a high target mass and density are important to reach high sensitivities and thus low cross sections of the interaction of DM with the target nuclei. The target medium needs to have a low intrinsic background too, to be sensitive to the expected low interaction rates. These points are fulfilled for two liquid noble gases especially: Xenon and Argon. Considering now the expected interaction rate at a deposited recoil energy per WIMP interaction in the medium, Xenon is preferred at low recoil energies, as visible in fig.1.4 [200]. The further properties of Xenon make it a good dark matter target [46, 46, 233]:

- high number density of target nuclei [201]
- good scintillator and ionizer [218]
- low energy threshold [23]
- self shielding against external radiation [201]
- low intrinsic background considering instable isotopes, i.e. low abundance of ^{136}Xe (high purity) and no long-lived instable isotope [201]

- low intrinsic background considering other elements (high purity)
- ER-NR discrimination: exploiting their different energy loss using the combination of scintillation and ionization signal, which shows different responses for ER and NR (see below)
- high electron mobility [121]
- high purities can be achieved [233].

The interaction of a WIMP with a Xenon atom is sketched in fig.1.5. It yields to an excitation of the Xenon atom Xe^* [19], which can combine with another Xenon atom to Xe_2^*. This excited molecule (excimer) decays and de-excites under the release of VUV light with 178 nm and a FWHM width of 14 nm [173, 40]. If the initial Xenon atom gets even ionized, it forms with another Xe atom Xe_2^+. Xe_2^+ captures then an electron and decays afterwards into Xe and Xe^{**}, which again de-excites by the release of heat and combining with a neutral Xenon atom to Xe_2^*. This Xe_2^* decays again under the already mentioned release of VUV photons. The light and charge signals of this process are anti-correlated. The scintillation signal shows furthermore two different decay components in the time distribution of the observed prompt scintillation light, which differ between ER and NR [200, 116, 143]. The detection of the prompt scintillation light from interactions with the Xenon atoms (S1) and from the ionization signals (S2) allow for a good ER/NR discrimination > 99% [26].

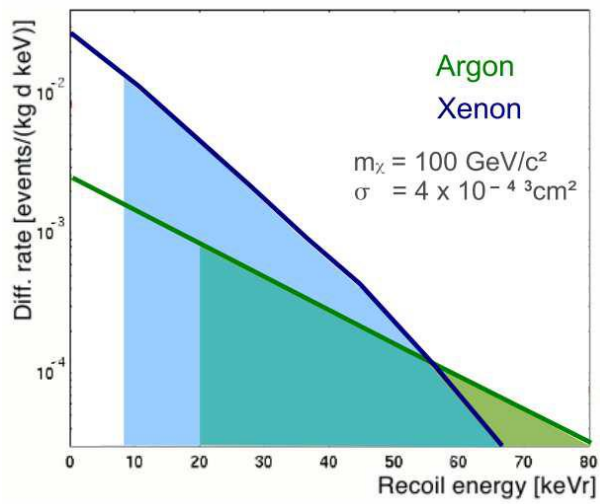

FIGURE 1.4: Nuclear recoil spectrum of a 100 GeV WIMP with $\sigma = 10^{-43}\,\mathrm{cm}^2$. The experimentally reached energy thresholds are indicated by the colored areas. Taken from [200].

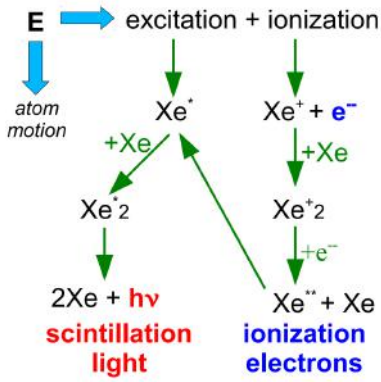

FIGURE 1.5: Sketch of the interaction process of a WIMP with a Xenon atom: yielding to motion of the Xe atom, excitation of the nuclei and ionization of the atom. The excitation and ionization are observable with LXe dual-phase TPCs. Taken from [200].

1.2.1 Working Principle

A liquid Xenon (LXe) dual-phase TPC uses Xenon in liquid form as DM target and detection medium. A gas phase above the liquid is used as detection medium for the ionization signal (see fig.1.5). A light detector array above the liquid level and a second light detector level on the bottom of the TPC volume are employed to detect the scintillation light emitted from the interaction of the WIMP with the Xenon atoms. They measure two signals: the prompt S1 scintillation light and the ionization signal in the gas phase. Photo multiplier tubes (PMT) are the standard detectors for the emitted faint light (single photons). The electrons from the ionized Xenon atoms are separated from the interacting atom with an electric drift field. It drifts the charge induced by a particle interaction towards the liquid gas interface from where it gets extracted into the gas phase by a second electric field, the so called extraction field. The drift field is applied between the cathode and gate, and the extraction field is generated between the anode and gate (see fig.1.6). The top screening mesh and bottom screening mesh shield the PMTs and the volume in front of them from the high fields in these regions. All electrodes are grids or meshes because a high optical transparency is required to minimize the absorption of the light signals. The drift field needs to be as homogeneous as possible to allow for a proper position reconstruction, which is done with the S2 signal, and to minimize charge loss. This is achieved with field shaping rings that are placed around the TPC volume and that are electrically biased such that the field becomes homogeneous. One field configuration example is shown in [237] for the TPC deployed in the Bern LXe test platform (chapter 3). The drifted and accelerated electrons collide then in the gas face with Xenon atoms, which get excited and de-excite under the emission of scintillation light. The thereby observed light signal S2 is proportional to the original charge signal (proportional scintillation) [147]. The number of generated photons per

electron and length can be described by [51]:

$$\frac{dN}{dx} = \alpha\,(E/p - \beta)\,p \tag{1.5}$$

with the electric field E, the pressure p and the constants $\alpha = 70\,\text{photons} \cdot \text{kV}^{-1}$ and $\beta = 1\,\text{kVcm}^{-1}\text{atm}^{-1}$. This makes even single electrons observable [83, 30]. The resulting scintillation light (S1 and S2) can be directly observed with PMTs since Xenon is transparent for its own scintillation light. The principle and possible signals from ER or NR are sketched in fig.1.6. Since neutrons and WIMPs interact only with the nuclei of the Xenon atom (NR), they generate a different S1 to S2 ratio than gamma rays or electrons, which are interacting predominantly with the atom shell (ER). The NR produce less ionization light (S2) compared to the prompt scintillation light (S1) while ER produce more charge signal compared to the prompt scintillation signal. The different observable energies of ER and NR are described by the so called quenching factor [210, 9].

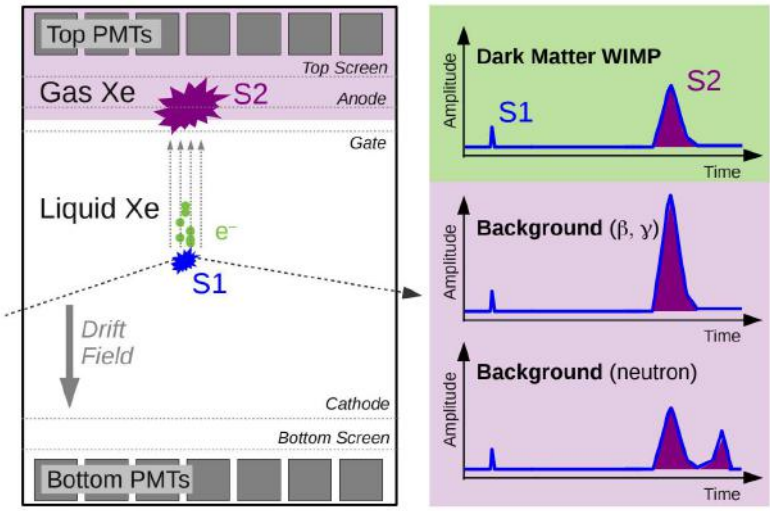

FIGURE 1.6: Sketch of an interaction process in a dual-phase TPC and the possible interaction signatures from ER and NR. The NR interactions from WIMPs and neutrons are shown: neutrons might scatter multiple times, which is very unlikely for WIMPs and can be used for neutron background rejection [202]. Taken from [233].

One can reconstruct the horizontal position of the interaction using the light detector array on the top of the TPC. The charge gets drifted straight (assuming a homogeneous drift field) upwards thus that the ionization signal determines the horizontal position of the interaction vertex. Furthermore, the time difference between the S1 and S2 signal can be used to reconstruct the vertical position of the event because the drift velocity of electrons in liquid Xenon is constant at a given drift field [86]. These information yield to the 3D event position. Knowing the event position allows for a fiducialization of the TPC: if one considers only events that happen in a certain volume in the TPC, one can reduce the background, which is mainly present at the detector edges because the

self-shielding of liquid Xenon suppresses it further in the detector volume. Background rejection with fiducialization allows to reject external gammas and neutrons.

1.2.2 Performance Requirements of LXe TPCs

A dual-phase TPC aiming for dark matter detection needs to be very sensitive for the direct scintillation light and for the detection of the ionization yield via the S2. This means it can be characterized mainly with two parameters: the light yield for S1s and the charge yield for S2s. They describe the sensitivities for the S1 and S2 signals and cover various effects that limit the sensitivity.

It is important for a efficient charge detection that the electrons from the ionization are not lost by recombination on electronegative impurities during the drift process towards the gas phase and to achieve a high amplification when extracting the electrons into the gas phase. Xenon itself is a good drift medium for electrons because it has a high average energy that is necessary to produce an electron-ion pair and a band gap between the valence and conduction band of 9.28 eV [219, 213]. The drift velocity v_d is constant at a given electric field [20, 12] and a higher drift velocity helps to reduce the charge loss (eq.(1.6)). The average time an electron can travel in Xenon is called "electron lifetime τ_e" and is characterized by the fraction f of the original electrons that are still there after a distance x:

$$f = \exp\left(-\frac{x}{v_d \tau_e}\right) \tag{1.6}$$

The electron lifetime is mainly limited by the Xenon purity [198, 74]. Electrons can get lost during the drift processes as well by colliding with the detector wall. Therefore it is crucial to achieve a linear field or a field that prevents the electrons from hitting the detector edges. Furthermore, the electric field should be homogeneous to avoid local inhomogeneities, which will make an event reconstruction more difficult. Especially the extraction field, which is needed to accelerate the electrons from of the liquid into the gas phase (potential barrier from a potential difference due to the different fields in gas and liquid due to the different dielectric constants $\epsilon_{LXe} = 1.88$ and $\epsilon_{GXe} = 1.0$ [104]), demands a high homogeneity to avoid a strong location dependence of the electron amplification.

The energy in a LXe dual phase TPC is often calibrated with sources which create ER while direct NR calibration gets used more and more [23, 159].

Light and charge yields The light yield of a TPC describes the amount of light observed by a recoil of a certain energy. The number of emitted photons depends linear

on the recoil energy [19]. It differs for ER and NR. The light yield ly is defined as number of photons seen per energy E:

$$ly = n_{\text{photons}}/E \tag{1.7}$$

It is often measured with gamma rays (ER) from a $E = 122\,\text{keV}$ Co57 source (standard candle, currently new standard candles get employed, e.g. Kr83m [138, 199, 158]). Since the actually measured light yield is reduced in presence of an electric field due to electric field quenching[3], one typically measures it at zero field or converts it back to a value at zero field [24, 218, 161]. The calibrated ER energy can be used to calculate the NR energy [188, 187]. The light yield for NR can also be measured directly [21, 120, 9].

The photon detectors sensitivity has a large influence on the light yield. In case of PMTs it is described by the gain[4] and quantum efficiency[5]. The geometrical acceptance characterize the sensitivity of a single PMT for the incident light and has an influence on the measurable light yield too. The measured light yield depends furthermore on the position of the PMTs, which are used to quantify the light yield: the PMT array on the bottom of the TPC will see the most light due to total reflection on the liquid surface. Beyond total reflection on the liquid surface, the required electrode meshes have a limited transparency and the absorption on them limits the light yield as well. The measurable number of photons depends also on the absorption of photons on the way to the PMT. They get absorbed on impurities in the Xenon and the process can be described by the absorption length of the scintillation light λ_{abs} and Rayleigh scattering length $\lambda_{\text{rayleigh}}$ [41, 208, 101]. The attenuation length $\lambda_{\text{att}} = (1/\lambda_{\text{abs}} + \lambda_{\text{rayleigh}})^{-1}$ combines both [19]: with a longer λ_{abs} more scattering processes can happen. Finally, the probability to loose a photon on its way to the PMT is increased by absorption on the detector walls. Therefore the light yield is also limited by the reflectivity of the detector walls (see chapter 2).

The charge yield of a dual-phase TPC is defined by the observed number of S2 photons per interaction energy:

$$cy = n_{\text{photons}}/E \tag{1.8}$$

It contains the charge losses during the drift process, the extraction efficiency into the gas phase and the proportional scintillation efficiency. The number of extracted electrons can be calculated from the observed S2s with eq.(1.5). While the charge yield is straight forward to measure for ER by integrating the number of photons seen from a

[3]Field quenching describes the decreased light yield under the presence of an electric field by suppressing the recombination of the electrons with the ionized Xenon (see fig.1.5) [27].

[4]The gain of a PMT characterizes the amplification of the PMT: how many electrons are generate by one photon.

[5]The quantum efficiency characterizes the fraction of incident photons, which yield to the release of measurable electrons.

mono energetic calibration source, it is more difficult for NR [187]. The ionization yield characterizes the response of the detector for nuclear recoils with an energy E_{NR} [46]:

$$Q_y = \frac{n_{\text{photons}}}{cy \cdot E_{NR}} \tag{1.9}$$

The light yield defines the energy threshold of the TPC for ER and NR by the S1 threshold: it is defined by the minimum S1 that is still separable from the electronic background. Typical thresholds for current detectors are in the order of a few keV [6, 33, 181], which is equivalent to S1s of $\mathcal{O}(2)$ PE. Typical S2 thresholds are in the order of $\mathcal{O}(200)$ PE, which is equivalent to a few electrons [170]. The energy resolution is straight forward defined as the width of the measured responses to mono energetic lines. For an improved energy resolution, the S1 and S2 response can be combined, exploiting an anti-correlation between S1 and S2 [154, 117, 202].

1.2.3 XENON1T

The XENON1T experiment is located in central Italy at the LNGS underground laboratory [233]. Fig.1.7 shows an image of the experiment. It aims for a direct detection of WIMPs with a 3.2 t LXe dual-phase TPC. The location provides a rock overburden of 3600 m water equivalent. The TPC is surrounded by a Cherenkov water muon veto detector as shielding and active muon veto [29]. The experiments top and bottom detector arrays utilizes 248 Hamamatsu R11410-21 PMTs [44] in a TPC with 96 cm diameter and a drift length of 97 cm. All materials and components of the TPC were screened for radio purity and carefully selected before the construction [234]. The TPC is contained by a double-wall stainless-steel cryostat and the LXe is cooled with pulse tube refrigerators (PTR) with ≈ 500 W cooling power to about $-96°$C [180, 233]. The Xenon is continuously purified with hot getters and can be distilled with a cryogenic distillation column to remove Krypton[6] [34]. The ReStoX system provides the storage for the Xenon inventory in warm or cold, gas or liquid phase [88]. The data acquisition system (DAQ) is shared between the TPC and the muon veto. It works triggerless and reaches a sub 1 PE digitization threshold (needs to be lower than the energy threshold to not limit it) while a software trigger reconstructs the structure of the recorded events. A drift field of 125 V/cm is applied and the extraction field is operated at 8.1 kV/cm. The inner TPC walls are completely covered with highly reflective PTFE panels (see chapter 2). The so achieved light yield is (8.02 ± 0.06) PE/keV and the charge yield is (198.3 ± 2.3) PE/keV for a Kr83m source (41.5 keV), which is even higher than expected [32]. First results were

[6] Some Krypton is contained in commercially available Xenon and Krypton contains again instable ^{85}Kr, which results in ER backgrounds.

published recently [33]: a limit of $7.7 \cdot 10^{-47}\,\mathrm{cm}^2$ for a 35 GeV WIMP at 90% confidence level was achieved.

(A) Image illustrating the XENON1T experiment with its TPC and cryostat in the Cherenkov water muon veto.

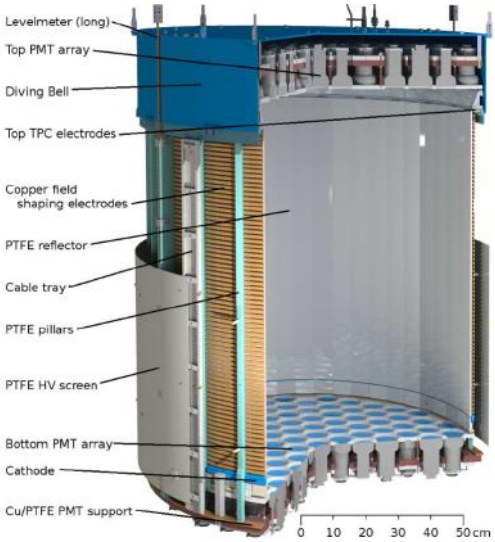

(B) Image illustrating the XENON1T TPC with the most important components. The diving bell gets externally pressurized with gaseous Xenon, such that there is even above the TPC some LXe. The levelmeter measure the liquid level in the detector and the PTFE HV screen shields the HV components from the stainless steel cryostat.

FIGURE 1.7: Illustrations of the XENON1T experiment. Taken from [233].

1.2.4 Challenges for future LXe TPC generations

Currently operated LXe dual-phase TPCs have ton-scale target masses and use a classical dual-phase TPC design. The coming detector generation will be slightly larger than their current predecessors, e.g. XENONnT or LUX-ZEPELIN [32, 223]. They share the general design with the current detectors. While these detectors improve the sensitivity, they are still not able to reach a fundamental background limitation. This limit is given by the coherent scattering of solar neutrinos off nuclei (CNNS) [57, 202], as shown in fig.1.8. The DARWIN project aims for reaching this limit [1] with a $\mathcal{O}(50)$ t TPC. The goal is to explore cross sections of $\mathcal{O}(10^{-49})\,\mathrm{cm}^2$ at 50 GeV and potential WIMP masses above 5 GeV. Before a detector of this size can be successfully operated, a few challenges have to be solved [1]:

- reduction of the NR background from (α, n)reactions and spontaneous fission of heavy elements in detector materials (especially PMTs and PTFE [202]) [114]

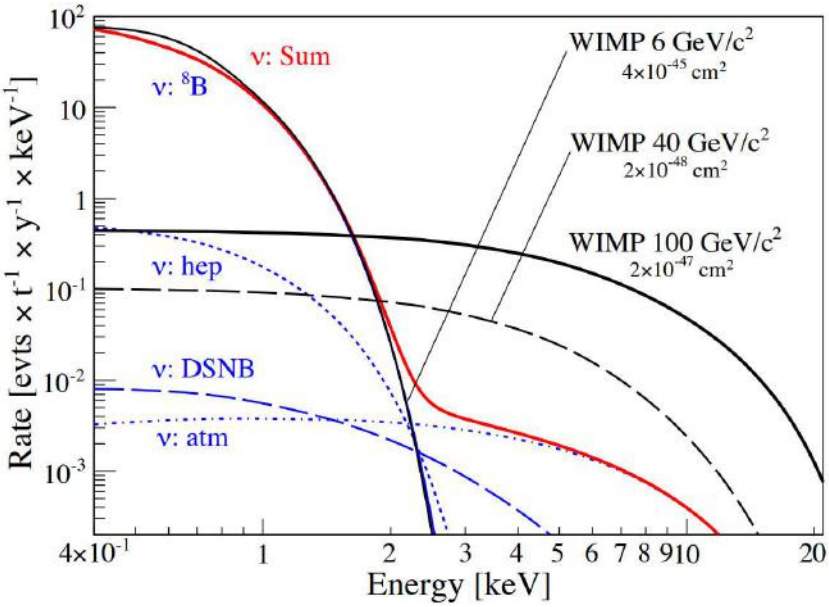

FIGURE 1.8: Differential NR spectra for various WIMP masses and interaction cross section (black, assuming a 50% NR acceptance), and the WIMP limiting backgrounds from CNNS neutrinos (red), which are composed out of solar neutrinos (^{8}Be and hep, blue short dashed), neutrinos from supernova (blue dashed) and atmospheric neutrinos (blue dashed dotted). Taken from [48].

- efficient removal of the ^{222}Rn background, which is emitted from detector surfaces [1, 193, 139]
- development of internal calibration sources for NR that do not contaminate the detector, since external calibration becomes difficult due to the self-shielding of Xenon
- achieve a lower radioactivity of the used light detectors (more light detectors lead to a higher total radioactivity in the TPC) and improved stability at cryogenic conditions and high pressures
- development of electric components allowing for a drift field of 500 V/cm need to be biased above 100 kV
- the grids used for the generation of the electric fields need to be highly transparent, being able to be biased at above 100 kV and mechanically stable (highly important for the anode: achieving a homogeneous field is critical for a homogeneous extraction efficiency)
- parallel gate, anode and liquid-gas interface to achieve a homogeneous S2 response, which becomes more and more difficult with larger radii
- development of simulation tools for the electric fields

- purification for the removal of electronegative impurities at very high flow, using low radioactive materials
- the demand for highly reflective inner TPC walls to ensure that the light collection efficiency is only limited by the scattering and absorption in LXe (assuming a dual-phase TPC design using PMTs; a further increased light collection efficiency requires different light detectors and higher coverage)
- a DAQ system that is able to read out $\mathcal{O}(1000)$ PMTs and events that span ms
- lowering the trigger threshold and electronic noise to achieve a lower energy threshold

Some of these problems are shown to be solvable with current technology (e.g. cryogenic distillation), other problems require even new technologies and some research and development, e.g. anode design, which is capable to be operated at the required high voltages and that has the required mechanical stability. Some effort towards the optimization of LXe dual-phase TPC is presented in this work, i.e., the optimization of the light yield by an increased reflectivity of the inner TPC walls and the design of a cryogenic test platform for the research and development towards novel detector technologies.

Chapter 2

Light reflectors for XENON1T

Dual-phase TPCs like XENON1T utilize the detection of the very low light level from rare particle interactions. Thus the sensitivity of such a detector is determined by its sensitivity to single photons. That is why these detectors are equipped with very sensitive PMTs, that are able to detect single photons. But not all the inner surface of a TPC is covered with PMTs, what means the isotropically emitted light needs to propagate to the PMTs. Therefore the light needs to be guided to the PMTs as efficiently as possible. This can be done by covering the non-sensitive inner surface of the TPC with a mirror. One needs special mirror materials for this purpose because the scintillation light of Xenon, which is emitted from particle interactions with Xenon atoms, is in the VUV range: 178 nm [173]. Furthermore the number of materials that can be used in a dark matter detector is limited due to outgassing, radioactive purity and resistance against liquid Xenon (LXe, which acts as solvent) and cryogenic temperatures. From the available materials (e.g. stainless steel, copper, PEEK, Torlon) one shows even a high reflectance for VUV light: PTFE [18].

The simulation of the light detection after an interaction in a dual-phase TPC depends highly on the light propagation processes in the TPC, as well as on the reflectivity on the TPC walls. Therefore a better characterization of the light reflection processes on the TPC walls would help to improve the Monte Carlo simulation of a TPC.

In this chapter the design and optimization of the inner TPC walls of the XENON1T TPC is described. Some general considerations about the reflectance at VUV wavelength are introduced in sec.2.1 (page 20), the experiment used for the measurements for the optimization of the reflector design is explained in sec.2.2 (page 24) and finally the design and performance of the reflectors is shown in sec.2.3 (page 37).

2.1 Reflectivity of PTFE at 178 nm

The choice of PTFE as reflector material for XENON1T was defined because it was from the available materials the one which showed even without any optimization already a high reflectance for VUV light: Xenon scintillation light has a wavelength of 178 nm [43, 39] (sec.1.2.1, page 11) for which sintered PTFE acts as a good reflector. Furthermore, PTFE resists LXe which acts as a solvent, does show the same mechanical properties over a broad temperature range (+20°C to −120°C and below), has reasonable outgassing rates (what is important for the required vacuum and for the minimization of impurities in the LXe, see sec.1.2.2, page 13) and is reasonably radio-pure [234]. Following this, it is clear that one wants to build the TPC reflectors out of PTFE.

PTFE (Polytetrafluoroethylene) is a polymer plastic that is used for many parts in the XENON1T TPC [234]. The used raw material is sintered from a fine powder under high pressure. Its mechanical strength and toughness stay constant until 5 K, thus it is well suited for cryogenic applications. Further properties of PTFE are given in [189].

The sensitivity of a classical dual-phase TPC for particle interactions is limited by (see also sec.1.2.2, page 13):

1. sensitivity of the light detectors (PMTs) to single photons: photon detection efficiency (PDE) [202]
2. attenuation length of the scintillation light in LXe [22, 40]
3. reflectivity of the TPC walls.

The number of scintillation photons generated by an interaction is about 63 photons/keV [218]. Thus the PDE depends only on the light yield ly, which is limited by the PMT sensitivity (gain; close to the threshold, angular acceptance and quantum efficiency: $> 28\%$ [44]) and absorption of photons on the way to the PMT. The number of absorbed photons depends on the Xenon purity (attenuation length) and reflectivity of the walls. Thus the light yield depends directly on the reflectivity of the TPC walls. That means the PDE can be increased by increasing the coverage of the detector walls with PMTs or minimizing the number of lost photons. Since the XENON1T TPC is employing a dual-phase TPC design, with a top and a bottom PMT array, there is only a limited coverage that is achievable. The purification of the Xenon [180] results in absorption lengths of the scintillation light in the meter-range [23, 40]. Thus the reflectivity of the TPC walls needs to be increased to further increase the light yield. Furthermore, a higher reflectivity minimizes the position dependence of the local light yield in the TPC because the photons can propagate longer without being absorbed on the walls.

Reflectivity The reflectivity of a surface describes the amount of light being scattered off the surface Φ_{out}, compared to the incoming light flux Φ_{in}:

$$R = \frac{\Phi_{out}}{\Phi_{in}}. \tag{2.1}$$

It depends on the wavelength, the incident angle, the surface material, propagation medium and the surface treatment. The fluxes can be transferred directly into the number of photons. Here the wavelength is fixed to 178 nm, the material determined to be PTFE and the propagation medium is LXe. At first order one can assume that the incident angles will be isotropically distributed, what means we consider the total incident flux integrated over 2π. Although single photons are detected in dark matter dual-phase TPCs, ray optics is used for the interpretation of the reflection processes. There are two types of reflections in ray optics:

1. specular reflection: R_S, light rays get reflected with their incident angle
2. diffuse reflection: R_D, light rays get reflected to many angles

The total reflectivity is defined as $R = R_S + R_D$ and the goal was to increase it for the XENON1T reflectors. For the PTFE reflectors a mixture of both reflection types is expected.

Specular reflection Specular reflection is described classically by *Snell's law*: the angle of the incident light rays to the surface normal agrees with the angle of the reflected light ray. It is illustrated in fig.2.1. But *Snell's law* makes no statement about the potential loss of radiance in case of a limited specular reflectance of the surface (which is described by eq.(2.1)). Pure specular reflection will happen on surfaces that show within the hit surface area much smaller surface irregularities than the incident lights wavelength.

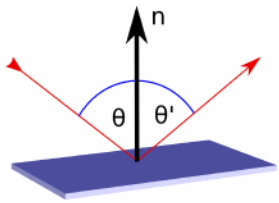

FIGURE 2.1: Sketch illustrating the specular reflection on a surface. n is the normal on the surface and the light rays are shown in red with the incident angle θ and the reflected angle θ'.

Diffuse reflection Diffuse reflection can be described with *Lambert's cosine law* [146] (see fig.2.2), which relates the total irradiated light (rate of photons) I_0 to the light seen

by an observer:

$$I_\theta = I_0 \cos(\theta) d\Omega \frac{dA}{dA_0} \tag{2.2}$$

in relation to the angle θ towards the surface normal $\overrightarrow{n}$, the covered solid angle element $d\Omega$ and the apertures dA and dA_0 of the illuminated surface and the observer respectively. Diffuse reflection will happen on rough surfaces, i.e. on surfaces that show different orientations of sub-surfaces (or micro-surfaces) with different surface normals within the spot size, so the initial aperture (assuming no scattering or refraction of the light from the emitter to the surface). Not all diffuse reflections on possible surface structures can be described with *Lambert's cosine law*: even absorption can appear on strongly tilted micro-surfaces because a part of the light will never leave the surface again. PTFE is used as nearly perfect diffuse Lambertian emitter in optics, e.g. [82]. It is used for this purpose over a broad wavelength range with reflectivities over 99%. Nevertheless a decrease for VUV wavelengths below 220 nm was found [133].

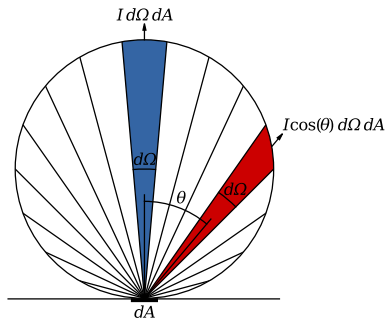

FIGURE 2.2: Sketch illustrating the diffuse reflection according to *Lambert's cosine law*. Taken from [231].

Combined specular and diffuse reflection At room temperature and in vacuum or normal atmosphere it was found that PTFE surfaces show not only a strong diffuse reflection but also a specular component [61, 130, 128]. Following *Snell's law*, which describes the refraction when light sees a boarder from one medium with the refractive index n_i to another medium with the refractive index n_j,

$$\frac{\sin(\theta)}{\theta'} = \frac{n_i}{n_j}, \tag{2.3}$$

total reflection must happen as well when PTFE is immersed in LXe, since the refractive indices are $n_{\mathrm{PTFE}} = 1.35$ [98] and $n_{\mathrm{LXe}} = 1.69 \pm 0.02$ [209]. Thus one expects total internal reflection above 53°. However, this is only true for perfectly flat surfaces.

There are extensive and detailed models of the reflection processed of VUV light in LXe on PTFE, e.g. [204], which often use Bidirectional Reflected Intensity Distribution Functions for the modelling of the reflection profiles (BRDF) [176, 119]. The quoted

numbers of the total reflectivity for PTFE in LXe and Xenon scintillation light differ between 60% [42] and 97.8% [175]. The exact surface treatment and bulk material is unknown for the many PTFE samples in the literature. Also Monte Carlo simulations are often used to calculate a total reflectivity [174, 59, 236, 205, 129, 233]. It is expected that the surface treatment and bulk material have the greatest influence on the results. The transmittance of the PTFE increases for porous bulk materials, which yields to a lower reflectivity because more photons penetrate deeper into the bulk material without getting scattered back to the surface, where they would contribute to the observed reflection.

The surface structure should have the highest influence on the reflectivity. If the micro-surfaces of the surface are strongly tilted against the surface plane, it is more likely that photons get trapped and thus absorbed or scattered into the bulk where they get absorbed afterwards as well. Following this, a surface as flat as possible against the surface plane tilted micro-surfaces would yield to a high reflectance (see sketch in fig.2.3).

(A) Micro-surface which yield to a flat surface and high reflectance.

(B) Micro-surface which are strongly tilted to the surface and low reflectance.

FIGURE 2.3: Sketch of different surface models with their different micro-surface structures: a rough and a flat surface. The absorption and reflection depend on the surface roughness. The surface normals are illustrated in red and the light rays in yellow.

Optimization of the reflectivity The light yield of a TPC can be increased by increasing the reflectivity of the inner TPC walls. Since the material was already fixed for the XENON1T PTFE due to outgassing and radio-pureness, the reflectivity of the inner TPC walls could only be increased by surface machining of the reflector panels. Other materials or even compound-materials were tested before, e.g. a composite foil of Kapton on PTFE, which delaminated and broke in LXe. In addition the reflectivity was measured at varying PTFE panel thicknesses [150, 226]: a reduced reflectivity due to an increased transparency when reducing the wall thickness was observed. This is relevant for the XENON1T reflectors because they are recently thin on their edges due to the interlocking functionality.

A raw PTFE surface after molding shows a high diffuse reflectivity $> 40\%$ but a low specular reflectivity $< 12\%$ [204]. Furthermore, it was found that the XENON100 panels already show an increased total reflectivity compared to a simple steel-tool-milling [150]. It was found as well that the reflectivity is highly angular dependent, especially when the PTFE gets machined towards a finer surface. The study in [150] suggests that an

increased specular reflectivity yields to a reduced diffuse reflectivity for some incident angles but increases the total reflectivity.

Following these arguments, we searched for a surface machining procedure that generates the smoothest possible surface. The surface smoothness can be characterized by its surface roughness R_a, which describes the mean deviation of a surface from its mean. The following surface treatment methods were considered during the design process because they lead to a flatter surface:

1. steel-tool-cutting of the surface (so called HM blade)
2. polishing of the PTFE with several grit papers, down to sub μm grit lapping sheets (fibre optics polishing)
3. polishing with polish milk as used for fibre optics as well
4. rolling of the surface
5. diamond tool-cutting

Sec.2.3 (page 37) shows a detailed description and summary of the results of the different machining techniques. The evaluation of the different machining options demanded for the measurement of the reflectivity of the different achieved surfaces in LXe with 178 nm light, which is described in the following section.

2.2 The Münster reflectivity setup

The "Münster reflectivity setup" (from now on called the reflectivity setup) was created to measure the reflectance of the XENON100 reflector panels and to explore possible improvements for the XENON1T reflectors. It was set up by the Columbia group (Prof. Aprile) and the WWU Münster group (Prof. Weinheimer). The original setup was dedicated to measure not only the reflectance of PTFE but also the quantum efficiency of the PMTs used in XENON100 [28]. The setup then was modified and improved 2011 by K. Bokeloh to measure an angular dependent reflection profile of a PTFE sample in vacuum [59]. After various measurements of the reflectance of PTFE in vacuum, the setup was upgraded by C. Levy enabling measurements of samples emerged in liquid Xenon [150]. Apart from some minor modifications of the setup, all measurements shown in this work were performed with the setup as described in [150]. Only a brief overview will be given since the experimental setup is described extensively there.

2.2.1 Hardware

The system consists of a cryostat with a rotatable inner glass vessel, a rotatable PMT and a monochromatic VUV light source emitting at 178 nm. The photo in fig. 2.4 shows the most important components that are visible from the outside. Fig. 2.5 gives an impression about the components in the cryostat vessel.

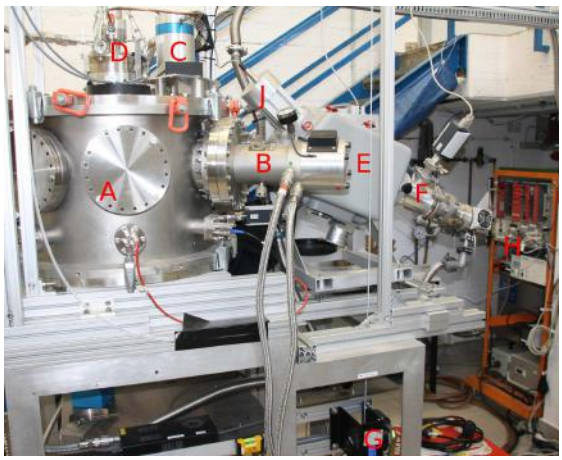

FIGURE 2.4: Photo of the Münster reflectivity setup from the outside. Visible components are: A: outer cryostat, B: PTR for cold shield and PMT, C: PTR/ valve for cold finger LXe, D: rotatable feedthrough of inner vessel, E: monochromator, F: vacuum pump for the monochromator and the deuterium lamp, G: pulley for the inner vessel, H: DAQ, HV supply and control for the PMT rotating motor, J: deuterium lamp.

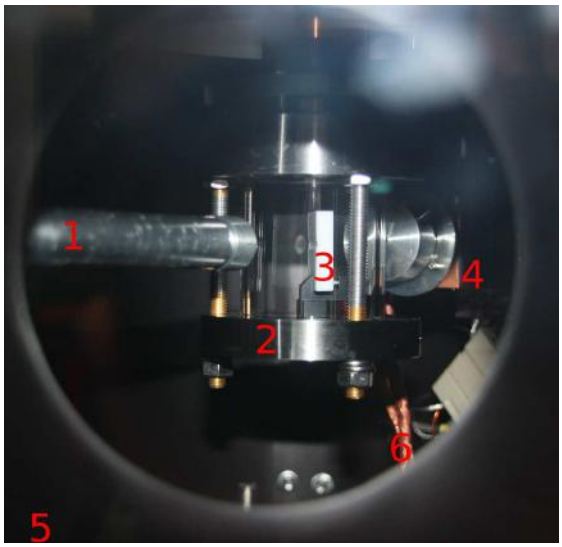

FIGURE 2.5: Photo of the Münster reflectivity setup looking inside the outer vessel through the view port. Visible components are: 1: collimator, 2: bottom of the inner vessel with glass tube, 3: PTFE sample with sample holder, 4: PMT with aperture and copper housing, 5: black cold shield, 6: copper cold lines for the PMT. A photo of the inside of the cryostat from on top is shown in [150].

Cryogenics The outer cryostat is a 65 cm stainless steel vessel, sealed with Viton O-rings. It has several ports for various applications:

- view port on the side with glass window (closed light-tight if PMT is operated)
- pump port on the side
- vacuum gauge port
- cold head and cold lines towards the cold shield and the PMT (on the side)
- entrance window for the beam from the light source (on the side)
- rotation feedthrough for the PMT with 3D manipulation (on the bottom)
- rotation feedthrough for the inner glass vessel, height adjustable (on the top)

The outer vessel is kept under vacuum with a turbo pump. A scroll pump provides the necessary fore-vacuum via a buffer tank. It serves as well for the separate turbo vacuum pump evacuating the light source and monochromator. The vacuum pressure is monitored with a gauge in the outer cryostat and a separate gauge in the monochromator. Additional insulation from radiative heat transfer is provided by a black cold shield, which is directly cooled with a pulse tube refrigerator (PTR). The PTR is as well the heat sink for the copper housing of the PMT (thus cooling the PMT), which is connected via cold lines.

The Xenon is provided by a gas system [198], which also allowed to purify the gas. However, the purification was never used, apart from filling, since the LXe volume is small and has thus short path lengths, and therefore does not require a high purity. A second PTR, which is directly coupled to the inner vessel (see fig.2.6), provides the cooling power for liquefying the Xenon. The cooling power is regulated by a 25 W heater.

The inner cryostat (shown in fig.2.6) consists of a top copper part, attached to a quartz glass cylinder, which is closed on the bottom with a stainless steel bottom flange. A sample holder is mounted on this flange. The glass cylinder consists of a quartz glass being $\mathcal{O}(80\%)$ transmissive for $\sim$ 180 nm light [100]. The sealing is done with Viton O-rings. The complete structure is mounted inside an open CF100 stainless steel piston. This piston is inserted in a rotational feedthrough that allows for vertical motion through moving the piston against the sealing O-rings. The length of that piston limits the range to about 10 cm. The sample is mounted on the bottom flange of the sample chamber. The normal sample holder centers $(5 \times 25 \times 25)$ mm samples in the middle of the flange (see fig.2.6). Three rods are holding the bottom flange, two on the backside of the sample

FIGURE 2.6: Photo of inner vessel with the quartz glass tube (I), the Xenon supply lines (II), the copper part which is used for the Xenon liquefaction (III) and the PTR itself (IV). Furthermore visible are the chains that are used to lift the tube with the pulley system, a PTFE sample in the sample holder and the top flange of the inner vessel.

and one on the front, that is used for calibrations due to its well known position of 10° against the surface normal of the sample.

The rotational feedthrough, as shown on fig.2.7, allows for 360° rotations. However, the actual available freedom of motion for the rotation is much smaller due to the Xenon gas lines, which are connected to that structure. They limit the rotation to about 100°. The rotational feedthrough is used to read the rotation with respect to the outer cryostat from a scale. Rotating this feedthrough sets basically the incident angle of the light ray on the sample.

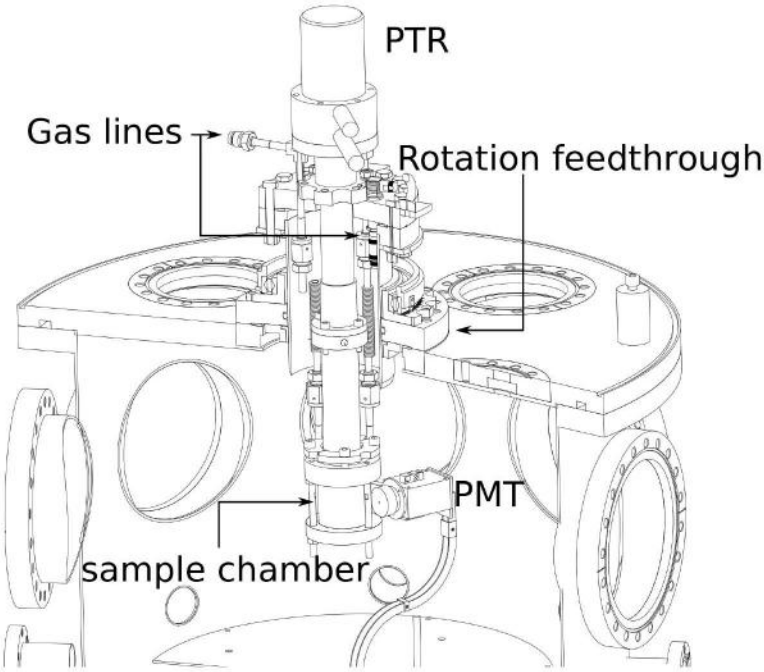

FIGURE 2.7: CAD image of the rotational feedthrough, which holds the sample chamber. With this, the sample can be rotated and set at a certain height. Furthermore shown are the gas lines, sample chamber and PMT.

The second rotational feedthrough (see fig.6.10 and 7.2 in [150]) allows for the rotation of the PMT. It is located directly under the top rotational feedthrough of the inner vessel. Besides a possible 360° rotation, it allows for translation on 3 axes with micrometer precision via a vacuum manipulation table. The alignment of the center of rotation of the PMT with the center of rotation of the top rotational feedthrough is done with this 3D manipulation table. The rotation of this feedthrough is performed with a step motor on, which the PMT is coupled with a long lever arm. The available angular range is limited by the collimator tube and the lever arm to about 320°.

The monitoring and control of the experiment is done with a custom made slow control system. It is designed in Lab View and uses a NI USB6008 interface [125] that is employed as well for the DAQ. It monitors the temperature of the PMT housing, the temperature of the cold shield and the vacuum pressure in the outer cryostat vessel. The step motor, which rotates the PMT, is controlled by this slow control software as well. The temperature of the Xenon liquefaction copper part of the inner vessel is controlled with a Lakeshore 336 temperature controller [145] and its PID loop coupled to a heater. It is not readout or monitored by the slow control system but it is integrated in the local gas system [198].

Light source The light source is a McPherson Model 632 Deuterium lamp [164] with a continuous emission between 170 nm and 400 nm. The light passes through a McPherson Model 218 vacuum monochromator. The wavelength was selected as 178 nm with a resolution of 5.3 nm [59, 150]. The calibration is shown elsewhere [211, 59] and was not verified during this work. The lamp and monochromator are installed inside a dedicated vacuum system, separated from the rest of the experiment, to minimize the absorption of VUV light on residual gas. The light beam leaves the monochromator through a MgF_2 window that separates both vacua. It transmits light at 178 nm with about 80% [113].

Inside the outer cryostat the light is first focused by a quartz lens (focal length 80 mm) and then guided by a collimator with a length of about 30 cm. Its aperture is about 1 mm. The distance between lens and sample is about 400 mm. More details are given in [211, 59, 150]. For this work we assume to have a collimated beam spot of 1 mm diameter in front of the sample glass vessel.

Light detector The light sensor is a 1” Hamamatsu R8520-406 PMT, as used in XENON100 [235, 107]. It is mounted on a lever arm on the height of the collimator. The lever arm is fixed on the lower rotational feedthrough (described above), such that it can be moved manually with the feedthrough manipulation in x-y-z direction (see fig.2.8) to align of its center of rotation with the center of rotation of the sample chamber and with

the height of the beam from the collimator. The spatial alignment was performed within [150] and repeated within this work as shown in sec.2.2.2.

The PMT can be rotated around the sample chamber with a step motor (see fig.2.8). The measurements were taken with 0.9° steps (minimal step width 0.45°). After each step there was a 5 s delay before starting actual data taking, to make sure the PMT does not vibrate because the step motion lets the PMT vibrate.

The PMT is installed in a cooled copper housing to lower the thermal noise. Its temperature was monitored. It should be mentioned that during the measurements shown here, the PMT temperature was higher than originally observed in [59]. The high voltage for the PMT was provided with a CAEN N470 power supply. The PMT was operated at its nominal voltage of +800 V (positive HV in contrast to XENON100). An aperture with a diameter of 2 mm was placed in front of the PMT, which is equivalent to 2.9° on the actual scale of the PMT rotation (see sec.2.2.2). It was installed to minimize the impact of scattered light.

2.2.2 Data acquisition and analysis

Data acquisition The signal from the PMT is fed into a 10× amplifier (CAEN N979) and triggered by a CAEN N840 leading edge discriminator. The trigger signal of the discriminator is directly acquired with a NI-USB6008 DAQ system, operating as a scaler. The discriminator threshold was set to about 100 mV. The DAQ is connected to a readout PC. The readout is done with a custom-made Lab View DAQ software, which also controlled the step motor of the PMT. The step width (multiples of 0.45°) $\Delta\theta_{\mathrm{PMT}}$, initial angle setting θ_{PMTref}, start angle $\theta^{i}_{\mathrm{PMT}}$ and stop angle $\theta^{s}_{\mathrm{PMT}}$, as well as the pause time t_{delay} before each acquisition window and the length of the acquisition time window t_{acq} are configurable. A correct setting is crucial to prevent the system from mechanical damage and to acquire correct data. It starts with moving the PMT from the initial PMT angle θ_{PMTref} to the start angle $\theta^{i}_{\mathrm{PMT}}$, from where the measurement starts. The system moves the PMT by $\Delta\theta_{\mathrm{PMT}}$ and pauses then for t_{delay} to let the PMT come to rest, as it appeared to vibrate due the motion from the step motor. Afterwards the acquisition of the scaler data is running for t_{acq}. The rotation and acquisition steps are repeated until the stop angle $\theta^{s}_{\mathrm{PMT}}$ is reached. The software writes the measured data into ascii files, which contain the total step time $t_{\mathrm{acq}} + t_{\mathrm{delay}}$, the angle θ_{PMT} and the counts observed during t_{acq}. The latter gets calculated from a continuously running scaler. The cumulative number of counts of the scaler was recorded as well and is used by the analysis software to calculate the number of counts per t_{acq}.

Coordinate systems The system has two rotation axes that need to be aligned (purpose of the x-y-z coordinate system, see fig.2.8), corrected and transferred to one final coordinate system with respect to the surface normal of the sample. The following angles can be read directly from the two scales:

- θ'_{PTFE}: angle on the PTFE angle scale in degrees with an arbitrary reference point
- θ'_{PMT}: angle on the PMT angle scale in degree with an arbitrary reference point, 0° close to the beam start point and 180° on the opposite site where the beam would be visible without anything between beam and PMT, measured in degrees

These angles are directly corrected within the DAQ software to θ_{PMT}, θ_{PTFE} with respect to a manually set reference angle θ_{PMTref}. θ_{PMTref} is callibrated such that the beam maximum appears at $\theta_{\mathrm{PMT}} = 180°$. Fig.2.20 (page 43) shows some example raw measurements.

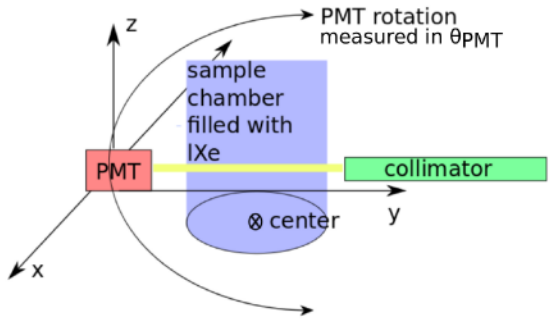

FIGURE 2.8: Sketch of the setup with the axis of the manipulator for the PMT position and PMT rotation around the sample chamber. The rotation axis of the PMT should be aligned with the center of the sample chamber.

Other angles or reference points that have to be determined with respect to the PTFE normal (green, fig.2.9b) or reference points are:

- the PTFE normal: vertical to the PTFE surface
- the incident angle θ_i
- the angle of the reflected light with respect to the PTFE normal θ_r
- the position the rod in front of the sample (holding the sample chambers bottom flange) with respect to the PTFE normal, that should appear by design at $\theta_r = 10°$

The angles, as used here, are illustrated in fig.2.9. $\theta_r(\theta_i)$ can be reconstructed from the measured curves. One method is demonstrated in [150]. It uses the position of the shadow of one of the rods, which hold the sample chamber bottom flange, in the

reflection profile and a PTFE alignment angle $\theta_{\text{PTFE_aligned}}$ that needs to be measured independently. One found in later measurements that the shadow is not always visible if the diffuse contribution get shallower. Thus this method is not usable in these cases. In addition, this method results in reflection profiles that extend beyond 180°, what would mean shining light through the PTFE sample.

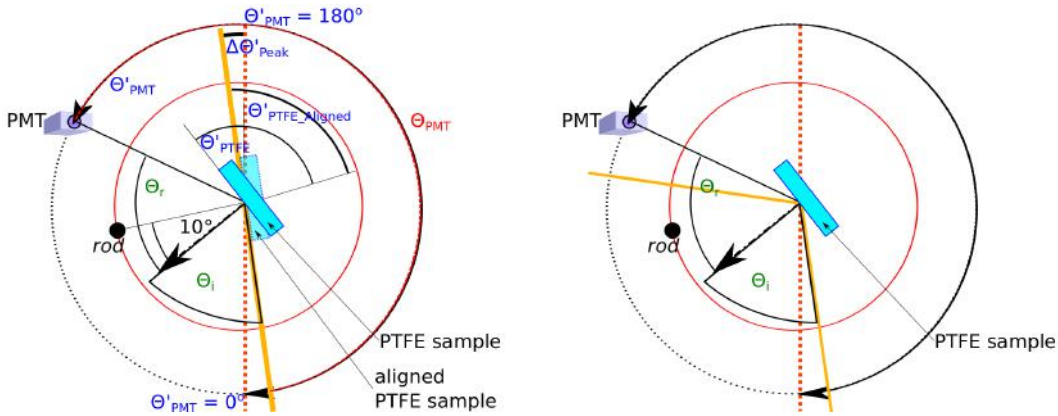

(A) Used coordinate systems and angles. (B) Derived angles (green).

FIGURE 2.9: Top view of the setup, with measured and calculated angle coordinates. The sample chamber and the PTFE rotation are illustrated by the red circle. The black (solid and dotted) circle illustrates the path described by the PMT rotation. The yellow line represents the beam and the vertical red dotted line represents the axis through 0° and 180° on the PMT angle scale θ'_{PTFE}. The angles to be read off the slow control system or experiments scales are written in blue, derived angles in green. The second, vertical PTFE sample (light blue) represents the situation when the PTFE surface is aligned with the beam.

An alternative method to reconstruct the real profiles was developed assuming that the specular reflection happens according to *Snell's law*: incident angle = reflection angle. This yields to:

$$\theta_r = 180° - \theta_{\text{PMT}} - \theta_i + \theta_{\text{PMTref}} \tag{2.4}$$

Resulting in an aligned angle of the PTFE sample of:

$$\theta_{\text{PTFE_aligned}} = \theta_{\text{PTFE}} - \frac{\theta_{\text{PMTref}} + \theta_{\text{specular_peak}}}{2} \tag{2.5}$$

with the position of the specular peak $\theta_{\text{specular_peak}}$. This method assumes that the maximum of the reflectivity profiles marks the specular reflection angle. The differences between both methods are demonstrated in fig.2.10. One can see that for the new, so called "$\theta_i = \theta_r$" method, the profiles stop at about 90° as expected, but the position of the shadow of the rod is not at its expected position on the θ_r scale as shown in fig.2.10b. Besides this drawback, it was decided to use the new method for the analysis shown here because the appearance of light beyond the sample was not explainable otherwise while the shift of the shadow might be an artefact of an imperfect alignment. The new

method is also in good agreement with measurements done at optical wavelengths, which confirmed the "incident angle = reflection angle" assumption [135].

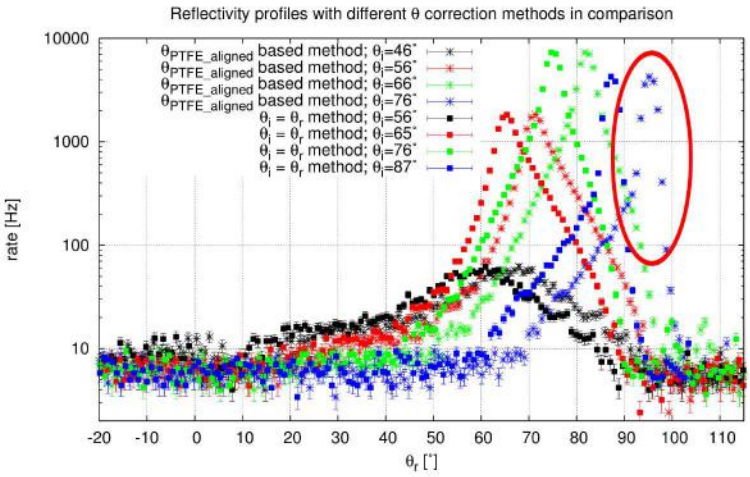

(A) The red circle marks the strange reflection profile at flat incident and reflection angles. It might be caused by light passing by the sample.

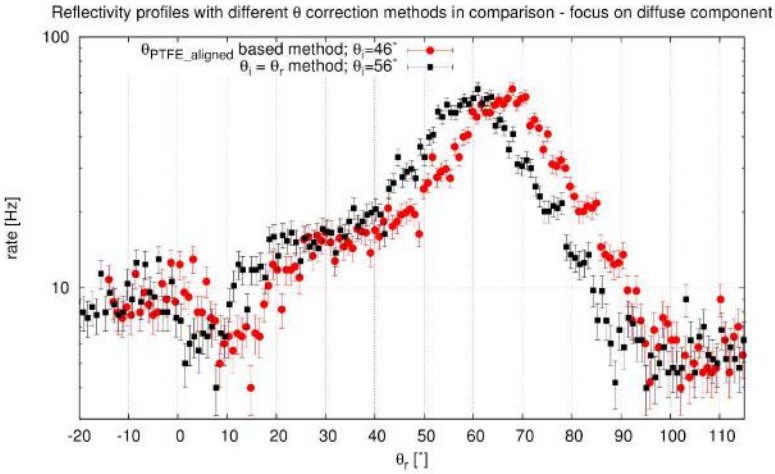

(B) Shown is a profile with a significant diffuse component. The shadow of the rod of the sample chamber should appear by design at $\theta_r = 10°$.

FIGURE 2.10: Resulting corrected reflection profiles of the original method from [150] in comparison with the new $\theta_i = \theta_r$ method. The reflection profile does not extend beyond 90° for the new method but the shadow of the does not appear at its expected position.

x-y-z alignment The rotation axes were aligned in x-y-z direction (see fig.2.8) the first time as demonstrated in [150]. The alignment is done by modifying the PMT position in one direction over several millimeters in steps of 1 mm, iterating through all three axes. For each step the light beam profile is measured by rotating the PMT around the new

rotation axis. The intensity profile of the beam at each new position was finally fitted with a Gaussian to approximate the beam profile.

The error on the counts n was assumed to be given by $\sqrt{n}$. The error on the rotation positioning was assumed to be in total 0.45°, which is the minimum step width of the step motor and appeared from observations to be a reasonable error. The manipulator can be tuned with a precision of 0.05 mm. Therefore the error on the adjustment of the manipulator axis is neglected.

The alignment in x direction was done first, ranging from 17 mm to 23 mm. The result is shown in fig.2.11. The x-value with the best alignment in x direction was derived from the fit of the maxima positions as (19.3 ± 0.05) mm.

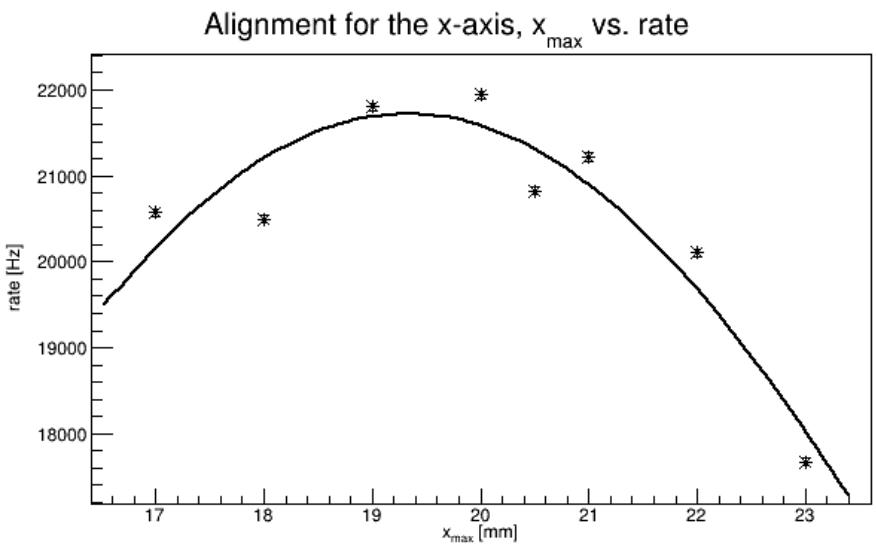

FIGURE 2.11: Resulting distribution of the maxima of the fitted Gaussians for the x alignment. The error bars represent the fit error. The setup appears to be aligned at $x = (19.3 \pm 0.05)$ mm.

Afterwards the z direction was aligned, scanning from $z = 34$ mm to $z = 39$ mm. Fig.2.12 shows the results from this alignment procedure. The fit of the maxima shows an maximum at (36.2 ± 0.2) mm, which is selected as z-value with the best alignment.

Finally, the y alignment was done with aligned x- and z-axis. It employes the shadowing effect of the rods, which hold the sample tube. For this alignment measurements were performed at each y value for two different PTFE angles θ_{PTFE}: $-8°$ and $-18°$, with a well visible diffuse component. A cross correlation analysis with an enlarged integration time of 20 s was applied here. The angular shift $\Delta\theta_{\mathrm{PMT}}$ between the two profiles for each y setting is used to measure their correlation [239], thus their overlap. A suitable y axis setting should show the same measured shift $\Delta\theta_{\mathrm{PMT}}$ as set on the PTFE angular scale θ_{PTFE}, so 10° here. Figure 2.13 summarize the results of the cross correlation analysis for the various steps on the y axis. The data show the expected shift between

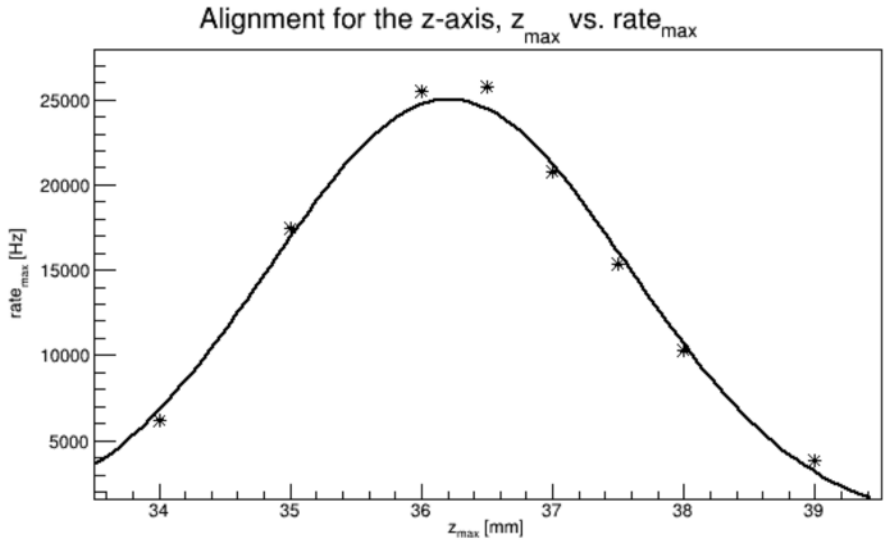

FIGURE 2.12: Resulting distribution of the maxima of the fitted Gaussians for the z alignment. The error bars represent the fit error. The system was set to $z = (36.2 \pm 0.2)\,\mathrm{mm}$.

the curves of $\Delta\theta_{\mathrm{PMT}} = 10°$ for $y = 6.0\,\mathrm{mm}$. The error was estimated from the error on the shift of the cross correlation of 0.2° and the error on the angles on the PTFE scale $\sigma\theta_{\mathrm{PTFE}} = 0.5°$. Thus the error on the y value with the best alignment can be estimated from simple trigonometry as: $\pm 0.5\,\mathrm{mm}$ at a distance PMT-PTFE of $\approx 40\,\mathrm{mm}$. The best alignment setting is found at $y = 6.0 \pm 0.4\,\mathrm{mm}$.

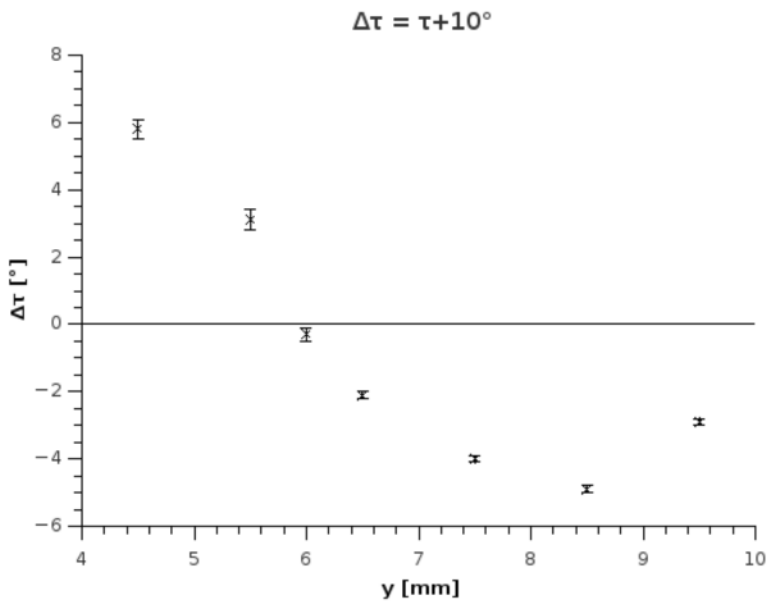

FIGURE 2.13: Result of the cross correlation analysis for all steps on the y axis. The plot shows the difference to the expected shift of 10°. The black line illustrates the "ideal" case of a shift $\Delta\tau = 0°$. The best alignment is found at $y = 6.0 \pm 0.4\,\mathrm{mm}$.

Analysis The recorded number of counts should be linear to the photon flux as long as the initial intensity of the beam is low enough, such that neither the DAQ saturates nor the trigger signals from single photons merge or overlap. The discriminator can resolve double pulses down to 12 ns [63] corresponding to a theoretical maximum rate of about 80 MHz, which is far from the observed rates during the beam calibration of $\mathcal{O}(20\,\mathrm{kHz})$. The system measures a trigger rate as function of the PMT angle positions θ_{PMT}. The rate is integrated over the aperture in front of the PMT and the acquisition time t_{acq}, such that it creates integration bins over an angular range (see fig.2.14).

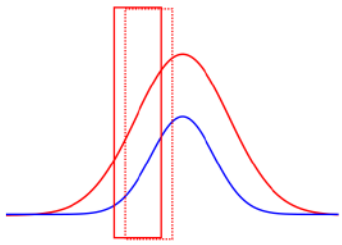

FIGURE 2.14: Sketch illustrating the integration of the true beam profile (blue) through the aperture at step 1 (red solid box) and through the aperture at step 2 (red dotted box), which yield to the fitted profile (red Gaussian).

Each measurement starts with a normalization measurement of the light source, during which the beam profile (see fig.2.15) is measured directly by scanning some angular range around the expected beam position. The normalization measurement is done above the sample in the gap between sample and upper glass cylinder edge through LXe (see fig.2.5). No distortions are expected due to the transmission of the beam through the glass - LXe interfaces if the x-y alignment is good enough (coordinate system shown in fig.2.8, more about possible distortions in sec.2.4.1, page 56). The purpose of this normalization is to determine the beam spot position. Furthermore, it allows to measure the beam width. The initial intensity can only be measured with some limitations because the integration bins overlap and the exact point spread function (PSF) of the aperture is unknown. Nevertheless, the comparison between the single runs is possible assuming a constant trigger efficiency. It is done with the integrated Gaussian fit of the measured beam profile. It could have been done also with its linear interpolation or integrating it bin wise, whereas the results differ significantly in shape and integrated area.

The reflectivity measurements are performed for the chosen incident angles θ_{PTFE} and incident heights z_h. They are set by rotating and moving the sample chamber manually and thus the sample itself. For each incident angle, the PMT is configured to scan a certain angular range. This range is limited by stopper rods, which prevent the PMT from hitting the collimator tube.

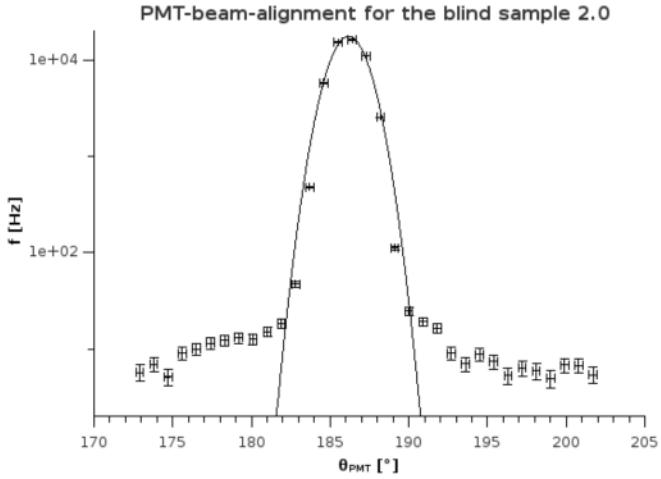

FIGURE 2.15: Example for a beam normalization measurement. The black line shows the resulting Gaussian fit that is used to determine the beam position angle θ_{PMTref}.

The sensitivity of the measurements is limited by the trigger threshold, which limits the sensitivity to above 1 PE, the electronic and thermal noise. Fig.2.16 shows a characteristic baseline, which was taken without any light source (dark count rate) in comparison to a background measurement with light source switched on but scanning some angular range $> 45°$ away from the beam. The comparison shows some contribution from scattered light to the background and the dark noise measurement should show only electronic noise.

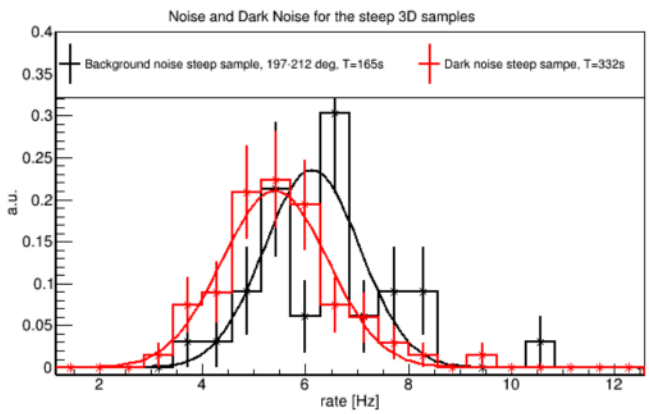

FIGURE 2.16: Baselines (dark noise in red; 34 entries, background with beam on but away from the beam in black; 37 entries) measured with the reflectivity setup, which show typical background rates. Shown are the distributions of the frequencies of the noise measurements. The curves show the resulting Gaussian fits of the noise profiles. The means of the fits are at $(6.57 \pm 3 \cdot 10^{-2})$ Hz for the background noise and at (5.4 ± 0.1) Hz for the dark noise profile. Both distributions are normalized. The dark noise distribution (red) is due to electronic noise.

2.3 Design of the XENON1T reflectors

The goal of this work was the optimization of the reflectivity of the reflector panels of the XENON1T TPC. This should be achieved by preparing the PTFE panels in a way that the surface roughness, thus the reflectivity, improves. Eq.(2.1) defines the reflectivity and sec.2.1 (page 20) introduces the other used variables, like the surface roughness R_a. All measurements that were performed with the reflectivity setup in the beam-PMT-plane are called furthermore "2D measurements" ($\varphi = 0$) while the measurements, which achieve a full 2π coverage by extending the measurements outside this plane are called "3D measurements" (see sec.2.3.2).

2.3.1 Machining of reflectors

In sec.2.1 we presented various machining techniques, which can be used to optimize the surface roughness. It needs to be considered that the machining techniques need to be applied on the roughly 1 m long, 5 mm thick and 50 cm wide PTFE panels, which will be used in interlocking mode (panels are coupled mechanically without a gap inbetween them, and this results in thinner edges than the over all panel thickness) for the TPC walls. Thus it needs to be doable in an industry workshop on the available machines and show an as small as possible material removal in order to keep the interlocking functional. Furthermore it needs to be robust against cryogenic temperatures and a cleaning procedure that will be applied to all PTFE parts of the TPC: immersed in 5% HNO3 solution, rinsed with ethanol and water [23].

The last two points were straight forward to fulfill because PTFE works generally well at cryogenic temperatures and surface machining does not change the mechanical properties of the bulk material. Furthermore, PTFE is nonreactive to nearly all aggressive chemicals, thus allows as well for cleaning with acids and solvents. The final panel machining was tested against the finally to be applied cleaning technique to make sure that the reflectivity does not suffer from the cleaning with HNO3, ethanol and water [23].

Machining techniques The surface roughness was measured for each machining technique with a roughness tester and the ability to apply this technique on the big reflector panels was considered and tested as well. The polishing with various grit sand paper was discarded because the surface roughness did not improve compared to the bulk material. Also polishing the PTFE with 6 μm, 1 μm and 0.01 μm grit polish sheets from a fibre optics polishing tool set was tested. It yielded a very good surface roughness, but occasional little graters appeared in the surface (even when cooling with water or ethanol),

which might be caused by heat from the polishing process together with some impurities. Thus this method was discarded as well. Rolling of the surface led to a inhomogeneous surface smoothness. Thus it was discarded as well. Table 2.1 summarizes the measured surfaces roughness of the remaining machining techniques for various samples. The "HM plate" and "1st diamond" sample were produced at the University of Zürich by the particle astrophysics group. All other samples were produced by the LHEP workshop at the university of Bern.

no.	sample	machining technique	$\bar{R}_a$ [valley to peak μm]
1	blind sample bad surface	HM blade milling	2.3 ± 0.2
2	blind sample good surface	diamond tool milling	0.7 ± 0.1
3	1st diamond	diamond tool milling	0.1 ± 0.1
4	HM plate	HM blade milling	$1.5^{+0.4}_{-0.3}$
5	3D sample vertical part	diamond tool milling	0.3 ± 0.1
6	diamond RnHNO3 samples	diamond tool milling	0.1 ± 0.1

Table 2.1: Surface roughnesses of the measured PTFE samples. The $\bar{R}_a$ value was always calculated as mean from three single values measured at different spots and sample orientations and the uncertainty illustrates the maximum difference to the mean. The achievable sensitivity is $0.1\,\mu$m. The different samples were prepared with various machines, tools and machinist, the details are described in the text.

It turned out that the smoothest samples showed the best reflectivity in the measurements in the optical range (see sec.2.3.3) as well with the reflectivity setup in LXe. From the resulting surface roughnesses it is thus pretty clear that a diamond tool-based milling improves the surface roughness and thus it is expected to improve the reflectivity as well. The used diamond-tool was also optimized. The finally used tool was not yielding an optimal surface smootheness (see sec.2.3.4) but it worked with the machines in the workshop of the company (Amsler & Frey) who applied the machining to the PTFE reflector panels. The last entry in table 2.1 "diamond RnHNO3 sample" (6 in table 2.1), showed the smoothest surface of all. For this sample the tool itself, the machining direction, frequency of rotation of the mill, cooling and lubricant, infeed and feeding were improved towards the smoothest possible surface. With this machining, even the mechanist who produced the sample had a significant influence to the surface roughness: $\leq 0.05\mu$m. The cleaning with HNO3 solution, ethanol and water was tested with this sample because it is expected to have the highest possible sensitivity to changes of the reflectivity. The surface roughness was at this stage only observable by visual inspection looking for surface patterns, and reflection pattern from various light sources, e.g. sun, light bulbs, green laser, red laser, since the roughness was below the measurable $0.1\,\mu$m. The diamond milling has furthermore the advantage to reduce the panel thickness only by about 0.1 mm. The milling process also removes a possibly ^{222}Rn contaminated surface of the bulk material [32].

The reflectivity setup was used before to measure XENON100 reflector samples [150]. Fig.2.17 shows the results of these measurements in comparison with two samples that were produced during the XENON1T reflector design study: the "1st diamond"(3 in table 2.1) and the "HM plate"(4 in table 2.1). The specular regime is defined by the appearance of a distinct and significant peak, which is assumed to be the specular peak. It covers the angular range above $\theta_{\mathrm{PMT}} = 50°$ while all other angles are dominated by diffuse emission. The diffuse emission is characterized by a broad angular range and shows a low, featureless (no peak) amplitude. It is well visible how the reflectivity in the specular regime increases with decreasing surface roughness. For large incident angles the reflectivity increases by about an order of magnitude peak-to-peak value of the specular peak. This first measurement, that was done within this work, demonstrates as well that the specular component is able to contribute a major distribution to the total reflectivity (see also [204, 150]). Nevertheless, the shown comparison does indicate some problems, for example a changing specular peak position or a changing normalization. Both are discussed in detail in sec.2.4.1 (page 56).

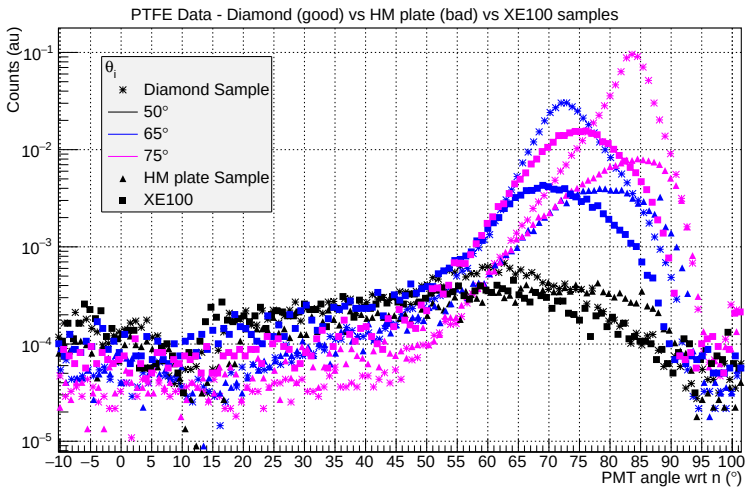

FIGURE 2.17: Resulting profiles of the measurements of the XENON100 sample [150] in comparison with the new steel tool milled "HM plate sample"(4 in table 2.1) and the "1st diamond"(3 in table 2.1). The rates are normalized with their beam normalization measurements (Gaussian fit). The positions of the specular peaks appear for the same incident angle at different angles. The diffuse component shows the same amplitude for all 3 samples.

The systematic uncertainty of comparing various samples at different normalizations (beam intensity and detection efficiency) was assessed with a "blind sample"(1 & 2 in table 2.1), which was also used to test the reproducibility of the measured reflection profiles. This sample, called "blind sample"(1 & 2 in table 2.1), was on one half of the surface machined with a diamond tool and on the other half with a steel tool. Which part was machined how, was not known before, such that the measurement was blind. The results from the two different surfaces are directly comparable because the normalization,

which is a source of uncertainty (see below), does not change between the two surfaces since the sample chamber was not opened between the measurements. Fig.2.18 shows the resulting measurement curves, as well as new samples, which are described later, in comparison. It is interesting to note that the diffuse component does not show a difference between the two parts of the blind sample(1 & 2 in table 2.1) and thus seems to be independent of the surface machining technique. The large increase of the specular component is visible in the peak height of the specular peaks. Furthermore, the shape of the peaks changes towards a sharper peak with decreasing surface roughness. Since both samples were measured in one run, an improper alignment of the rotation axes of the sample chamber and the PMT cannot explain this effect.

With the results from the blind sample measurements as shown in fig.2.18 and the results of the tests with the other machining techniques we decided for a diamond-tool-machining of the PTFE reflector panels for XENON1T. Follow up measurements with the reflectivity setup should clarify possible systematic effects as well as possible improvements of the machining process. A measurement was performed, which covered a reflection profile out off the beam-PMT-plane ("3D sample", sec.2.3.2). Last but not least a sample(6 in table 2.1) that was cleaned according to the XENON1T cleaning recipe for the PTFE panels was measured.

Evaluation of systematic effects The results of the vertical section of the 3D samples (5 in table 2.1) are shown in fig.2.18. A new spacer was invented that allows for a stable fine adjustable height setting of the sample chamber such that the beam would hit the sample at different z positions (see fig.2.19). Furthermore, two 3D samples(5 in table 2.1) were measured, the so called steep and the flat sample, both with vertical sections. Such also a statement about the systematics uncertainties of the measurement and of the machining was possible. The sample exchange required a complete recuperation and refill of the setup, such that the normalization might have changed. Although the two normalizations only varied within their normal fluctuation appearing within one run, it appeared to be a major source of uncertainty. Nevertheless, one can say that both samples show the same qualitative behaviour and that, compared to the blind sample(1 & 2 in table 2.1), the brilliance (the sharpness of the specular peaks) increased further. The specular components also became way brighter than in the previous samples. The difference in terms of surface roughness was not measurable anymore but visible by eye (visual inspection with various light sources, e.g. sun light, light bulbs, green and red laser): the 3D samples showed one the most shiny surfaces so far.

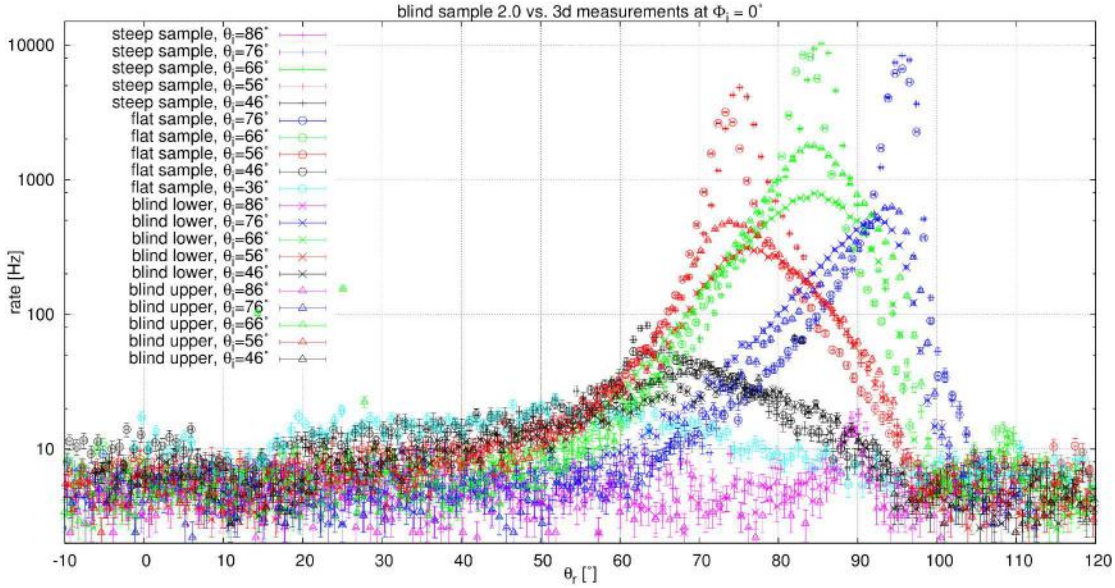

FIGURE 2.18: Reflection profiles of the blind sample(1 &2 in table 2.1) parts together with the vertical parts of the 3D samples (steep and flat sample, 5 in table 2.1). The different normalization for the 3D samples was not corrected here since the beam normalization showed no difference in the beam normalization beyond the systematic fluctuation which appears during one measurement. The normalization of the blind samples is the same for both.

FIGURE 2.19: Photo of the new height adjustable spacer which allows for a precise z setting of the sample chamber.

With the fixed surface machining parameters, the reproducibility of the machining was tested. The previous diamond-machined samples showed always a problem in the comparability due to possible variations in the normalization. Furthermore, it was observed that the normalization (combining effects of detection efficiency, readout noise and light intensity fluctuations) was changing between the runs, which might yield to problems in the comparability of the measurements. Therefore, one sample was measured, which consisted of three different, identical machined subsamples, thus that the sample chamber had not to be recuperated, opened and refilled between the measurements. Only the beam intensity and detection efficiency could fluctuate between the measurements of the subsamples (see table 2.2).

The three surfaces were machined identically (same day, same tool, same machinist, same machining parameters), however sample C(6 in table 2.1) was optically the most shiny

one of the three (visual inspection with various light sources, e.g. sun light, light bulbs, green and red laser):

- sample A: middle sample
- sample B: lowest sample
- sample C: top sample, special cleaning treatment, 6 in table 2.1

Before the measurements of the samples, the height was calibrated by looking for the shadowing of the beam vs. the sample height. A hole in sample A was used to calibrate the height of the sample chamber for sample A and B. The measurements were then done by setting the height thus that the samples were hit in their center.

date	measurement mean [°]	max. intensity [kHz]	σ [°]
2014-12-09	188.12 ± 0.02	27.21 ± 0.37	1.15 ± 0.02
2014-12-09 2nd	188.13 ± 0.03	26.90 ± 0.52	1.14 ± 0.03
2014-12-10	188.32 ± 0.03	30.11 ± 0.59	1.13 ± 0.03
2014-12-11	188.62 ± 0.02	30.54 ± 0.45	1.15 ± 0.02
2014-12-11 2nd	188.81 ± 0.03	29.80 ± 0.55	1.14 ± 0.03
2014-12-15	187.03 ± 0.03	28.39 ± 0.69	1.14 ± 0.03
2014-12-15 2nd	187.02 ± 0.03	28.69 ± 0.71	1.14 ± 0.03
2014-12-16	186.99 ± 0.02	30.12 ± 0.49	1.16 ± 0.02

Table 2.2: Comparison between the normalization measurements taken during the systematics run. σ is the FWHM beam width. The beam and PMT were switched off between the certain days.

Fig.2.20 shows the measured raw reflection profiles of the "three sample" measurement. The change of the specular peak positions (assuming that there is no physical reason that the peak positions changes so much between the samples) shows nicely the systematic uncertainty of setting the incident angle with the PTFE sample angle. It indicates furthermore that the difference seen by eye between the sample surfaces is visible as well in the reflection profiles in LXe with 178 nm light. The difference between sample A and B is in the order of the beam intensity and detection efficiency fluctuations. Thus it is assumed that they have the same reflectivity. The difference to sample C(6 in table 2.1) exceeds the fluctuations caused by these effects. Fig.2.21 shows a comparison of the three samples considering their integrated reflection profiles, which were normalized with the beam normalization measurements. The differences between the samples are in the order of 10% until $\theta_i = 66°$ but much larger for $\theta_i = 76°$, because the increased amplitude of the specular component at large incident angles is more sensitive to the incident angle setting. Nevertheless, the plot also confirms, within these systematics, that sample C (6 in table 2.1) is the brightest reflecting one. From the differences between the other two samples one can assume a typical systematic uncertainty of 10% up to 50%. The

cleaning with HNO3 solution, ethanol and water was not affecting the reflectivity of sample C (6 in table 2.1) beyond the systematic uncertainties, as expected as well from visual inspection and the fact that PTFE is stable against the used chemicals. More systematic measurements related to the calibrations (sec.2.2.2, page 29) and testing the background, noise and normalization stability are shown elsewhere [136] and confirm the demonstrated fluctuations and uncertainties.

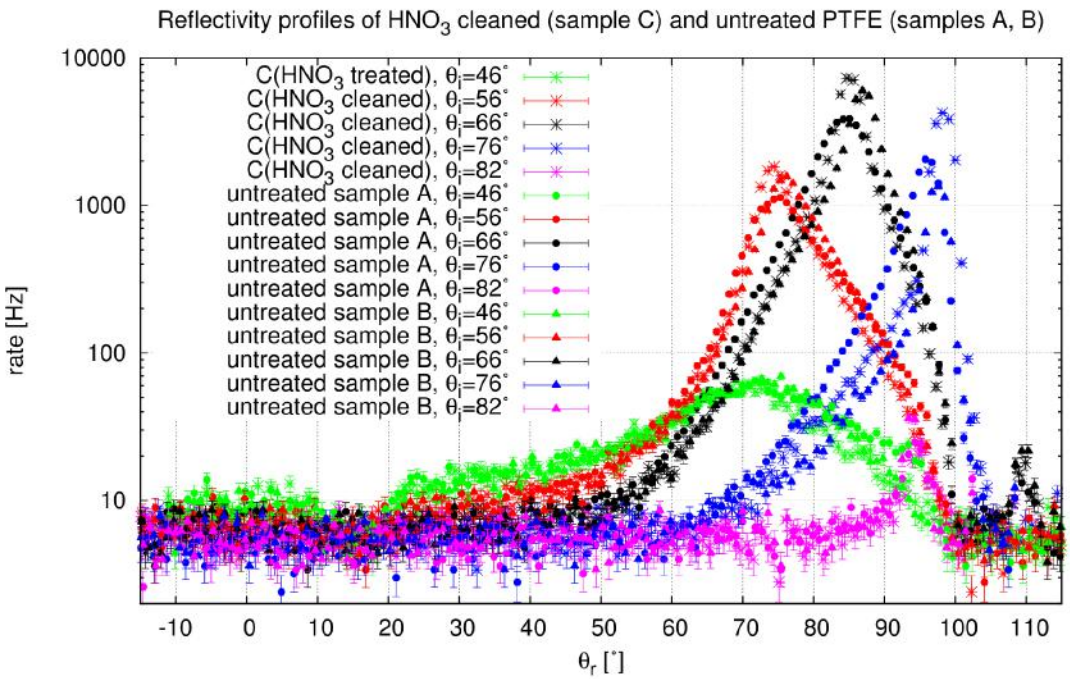

FIGURE 2.20: Raw reflection profiles of the 3 sampled systematic measurement. The untreated samples A&B were simply not cleaned with HNO3, ethanol and water according to [23] while sample C was cleaned so.

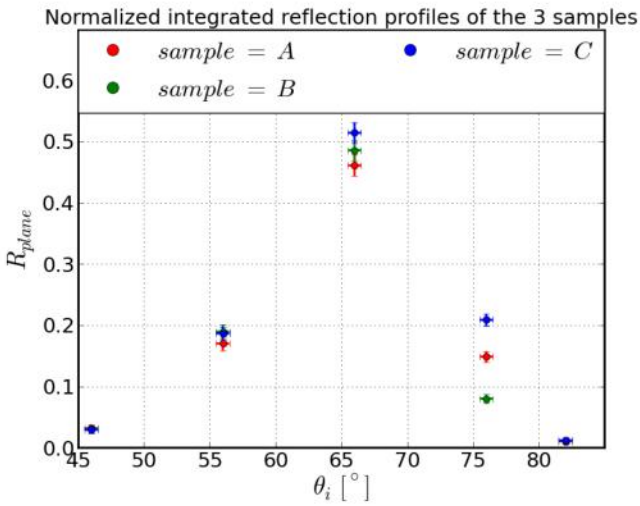

FIGURE 2.21: Comparison of the integrated reflection profiles R_{plane} for the various incident angles, normalized with the integrated beam normalization.

2.3.2 Reflectivity outside the beam-PMT-plane

It was assumed that most of the light reflected from the PTFE surface will be reflected back in the plane defined by the beam and the PMT. This is very likely true for the majority of the total specular reflection. But there are some diffuse and specular reflexes, which are reflected off this plane, as visual checks with lasers showed. The diffuse contribution is also included in the simulation shown in [59]. Machining structures (grooves) might yield to inhomogeneous specular reflection off the PMT-beam plane. Therefore a measurement was performed to extend the reflectivity measurement outside the beam-PMT-plane. This is done with a PTFE sample with several tilted surfaces, as shown in fig.2.22.

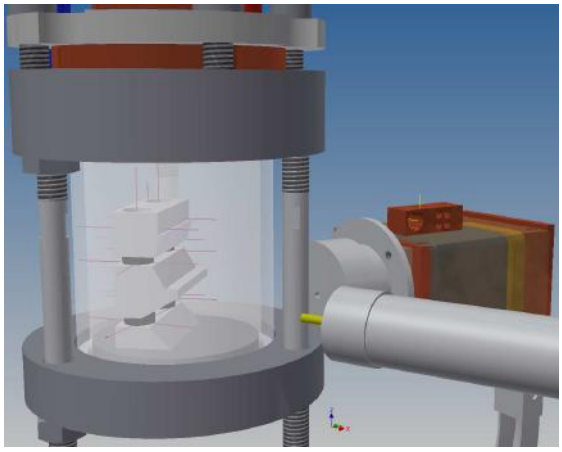

FIGURE 2.22: CAD image of the 3D sample in the sample chamber with PMT, collimator and beam. The sample is shaped such that the beam will hit the sample surfaces always in the center and thus at the intersection of the sample chamber rotation axis with the surfaces.

Two of these samples were measured, covering different incident tilt angles: the "steep sample"(5 in table 2.1) covering $\varphi = \{0°, 10°, 20°, 30°, 45°\}$ and the "flat sample"(5 in table 2.1) with $\varphi = \{0°, 15°, 30°, 60°, 40°, 60°\}$. The tilt angles appearing twice, allow for a direct comparison and some statement about systematics. Fig.2.23 shows the measured reflection profiles of the two samples. Interesting is a decrease of the diffuse component that indicates that reflections beyond 40° are completely negligible. Once more it is worth to point out the differences observed between both samples at the same incident angles, eg. fig.2.23d and 2.23e, which indicate strong systematic effects from the varying beam intensity, detection efficiency and angular setting of θ_{PTFE}. The differences of the shapes of the peaks in the specular regime are most likely due to machining artefacts, i.e. little grooves. They indicate that the specular reflectivity depends also on the sample orientation. The integrated and normalized profiles, as shown in fig.2.24 and 2.25, confirm this fact. The normalization in both plots is based on an integrated Gaussian fit of the beam normalization measurements. The derived absolute reflectivity

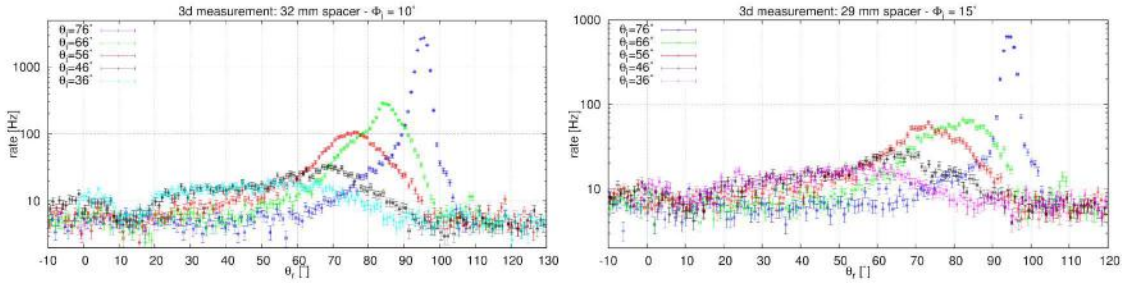

(A) Steep sample at $\varphi = 10°$.

(B) Flat sample at $\varphi = 15°$.

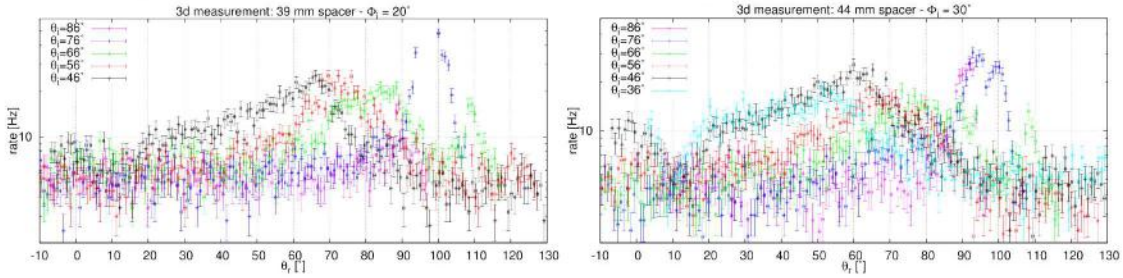

(C) Steep sample at $\varphi = 20°$.

(D) Steep sample at $\varphi = 30°$.

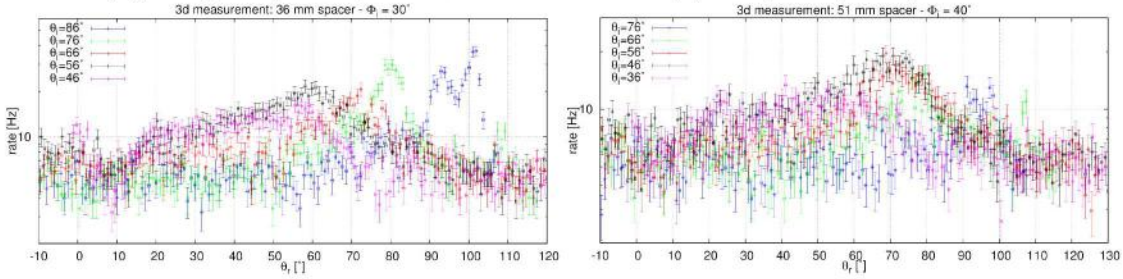

(E) Flat sample at $\varphi = 30°$.

(F) Flat sample at $\varphi = 40°$.

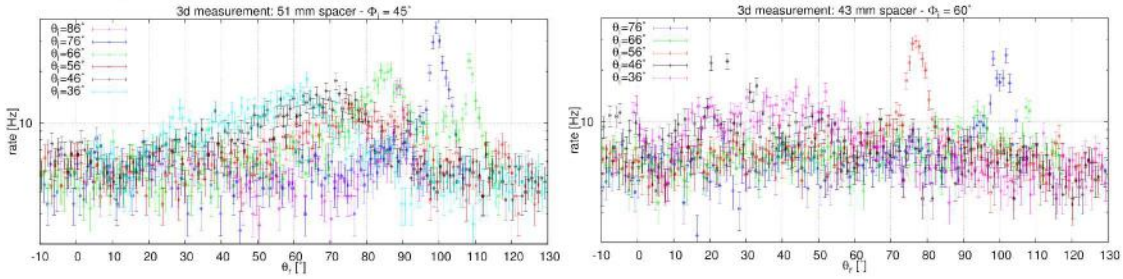

(G) Steep sample at $\varphi = 45°$.

(H) Flat sample at $\varphi = 60°$.

FIGURE 2.23: Raw reflection profiles of the 3D samples. Fig.2.23b, 2.23c, 2.23d, 2.23e, 2.23g and 2.23h indicate with the excesses appearing at large reflection angles $> 90°$ some systematic effects due to scattering. The observed intensities above $\varphi \leq 15°$ are completely negligible. Even $\varphi = 10°$ is only showing negligible contributions compared to $\varphi \leq 0°$, as shown in fig.2.24.

proxy R_{plane} depends highly on this normalization method while the relative differences between the samples and different incident angles stay the same within the measurement uncertainties. Thus R_{plane} has not to be understood as a reflectivity as defined in sec.2.1.

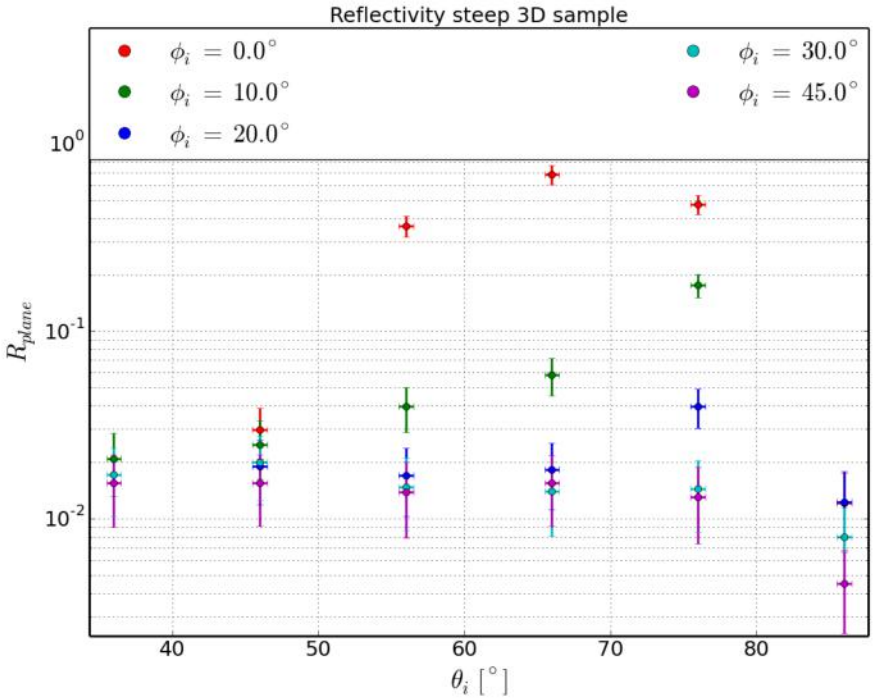

FIGURE 2.24: Results of the integrated beam profiles of the steep 3D sample. The low reflection intensities at $\varphi \leq 10°$ are well visible.

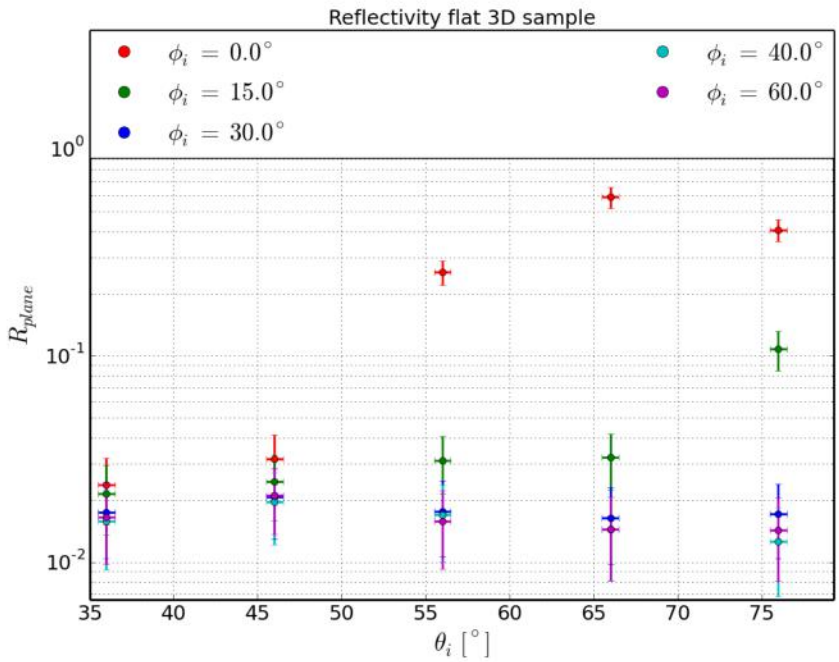

FIGURE 2.25: Results of the integrated beam profiles of the flat 3D sample. The spacer height defines the hit surface, so the tilt angle. It required a careful height calibration beforehand.The low reflection intensities at $\varphi \leq 15°$ are well visible.

2.3.3 Confirmation of the measurements in the optical range

Since the measurements with the reflectivity setup showed some systematic effects (see sec.2.3, page 37), the reflectivity was measured additionally in the optical range for several wavelengths (450 nm to 1064 nm). An extension of the previously shown findings to other wavelengths would be of interest, especially when comparing the VUV results to optical ranges, because a decreased reflectivity was found towards shorter wavelengths in the publications, which consider the optical range while the measurements in the VUV range often suggest a higher reflectivity ($R = 0.99$ at 440 nm and ≈ 0.9 at 260 nm vs ≈ 0.98 at 178 nm) [174, 134, 128, 130]. First tests were performed with green lasers already on the reflectivity setup samples. A more sophisticated approach is presented here, using the PHIRE setup [105, 131], which is a gonio-radiometer. The measurements from the here used "PHIRE-2" setup were performed by the Planetary Imaging Group of the university Bern. PHIRE-2 allows for reflection measurements at various optical wavelengths over a large reflection and incident angle range. The measurements were performed at room temperature and in air. It measures the reflectivity REFF normalized to a photometric standard such that the results are directly comparable to each other. The measured sample was especially produced for the shown measurements because the reflectivity setup samples would not fit for the PHIRE-2 setup. It was produced out of the XENON1T reflector panel bulk material but with another diamond tool than the finally used tool. Thus it showed a slightly different surface structure (only visible by eye) with visible curved (round) grooves from the machining. The final XENON1T reflectors were measured with this setup as well (second sample), see sec.2.3.4.

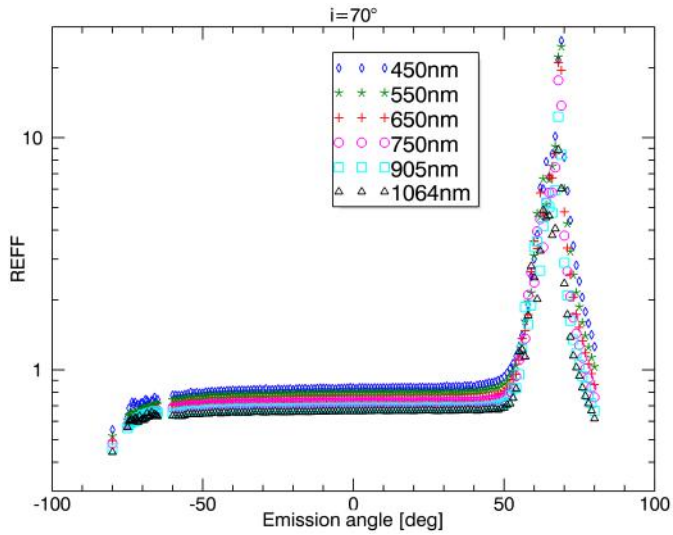

FIGURE 2.26: Reflection profiles from the PHIRE-2 setup at 70° incident angle. The missing part in the profile around 70° is due to the incident beam. The reflectivity increases towards shorter wavelengths.

The measurements confirmed that the incident angle for the specular component is equal to the reflected angle, which confirms the assumption for the angle corrections of the reflectivity setup (see sec.2.2.2). Fig.2.26 shows this finding for a steep incident angle of 70° over a broad wavelength range. The reflectivity increases in the diffuse and also specular part of the profile towards shorter wavelengths. Furthermore, the peak is asymmetric, as already observed in the reflectivity setup measurements for VUV light in LXe. This is also visible in all optical wavelengths and shows that this is not an artefact of a misalignment or caused by LXe. The refraction index of LXe enhanced the asymmetry only. It is very likely that the asymmetry is caused by the machining, since it appears to be wavelength dependent. The width of the specular peak changes also with the wavelength. These effects are reasonable since the machining structures are sized in the order of the wavelength what means each wavelength "sees" different surface structures.

The effect of the structures from machining that were visible, was investigated as well by measuring the sample a second time, rotated by 90°. The result is shown in fig.2.27 for two wavelengths. In the diffuse reflection range the difference between the two orientations is about 5% and reaches up to a factor ≈ 4 for the specular peak between the profiles at identical wavelengths but with the sample rotated by 90°. A third measurement rotating the sample by 180° reproduces the first found profiles.

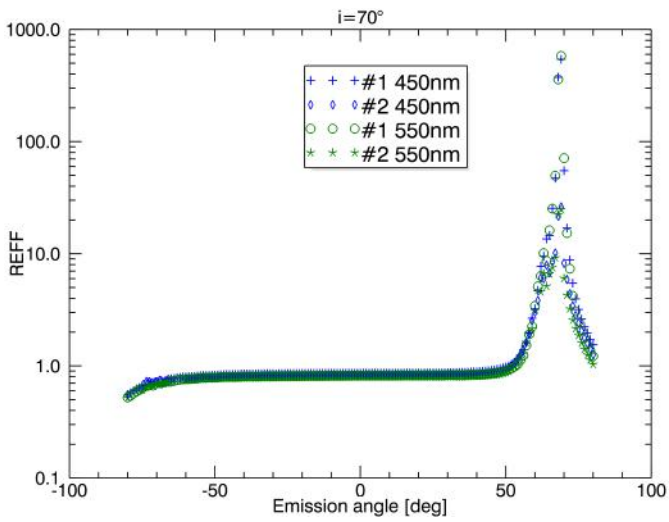

FIGURE 2.27: Optical reflectivity measured for two different orientations (#1 and #2), with the sample rotated by 90° at two wavelengths. The specular reflectivity is highly dependent on the sample orientation, indicating surface structures from the machining with sizes in the order of the used wavelengths or below.

2.3.4 Performance of the XENON1T reflectors

Basing on the previous findings it was decided to machine the XENON1T reflector panels, which form the TPC walls, with a diamond tool aiming for an as small as possible surface roughness R_a. Various tests were performed together with the company who produced the panels, aiming for a homogeneous surface machining according to the specifications. The achieved surface roughness ($\mathcal{O} \leq 1\,\mu$m) was worse than for the previous samples due to machine restrictions and missing tools for the machines of the company. Fig.2.28 shows the surfaces of various samples in comparison with the actual XENON1T reflector panel prototype that was machined identically with the actual panels. Furthermore, some samples were cut off the real reflector panels, what allows to measure the final reflectivity of the XENON1T reflector panels.

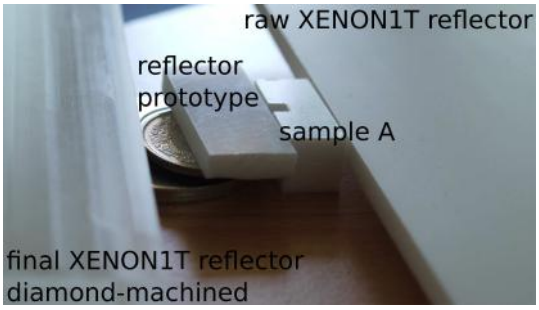

(A) Comparison of the final diamond machined XENON1T reflector with the raw steel-tool-milled PTFE panel, a "XENON1T reflector prototype" and sample A from "Evaluation of systematic effects" (sec.2.3).

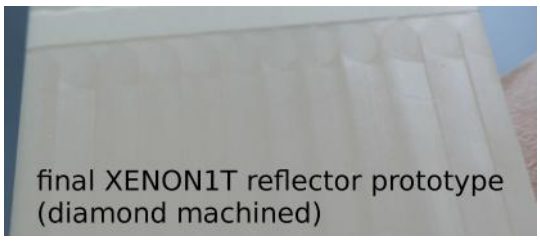

(B) Detail photo of the final diamond machined XENON1T reflector prototype with the grooves and inhomogeneities due to the machining tracks.

FIGURE 2.28: Photos showing the final machining of the XENON1T reflector panels. The XENON1T reflector prototype demonstrated the application of the diamond-machining using a better suited tool on a part of the XENON1T panel bulk material. It was a demonstrator for the company who applied the machining, that was used for machine adjustments. The surface structure of the XENON1T reflectors caused by the used tool is well visible.

Reflectivity of the XENON1T reflectors in the optical range One reflector sample was measured again with the PHIRE-2 setup (sec.2.3.3). The results (fig.2.29a, 2.29b and 2.29c) show an increased reflectivity towards shorter wavelengths in the specular peak for steeper incident angles. This would indicate a Rayleigh scatterer with structures smaller than the tested wavelengths. For smaller incident angles, it shows a higher reflectivity for blue light in the diffuse regime and a lower reflectivity in the specular regime. Also the width of the peak changes again with the wavelength. Fig.2.30 summarises this behaviour in terms of the so called Albedo[1] value of the sample.

[1]Albedo: reflectivity $REFF$, relative to an optical standard, averaged over the hemisphere.

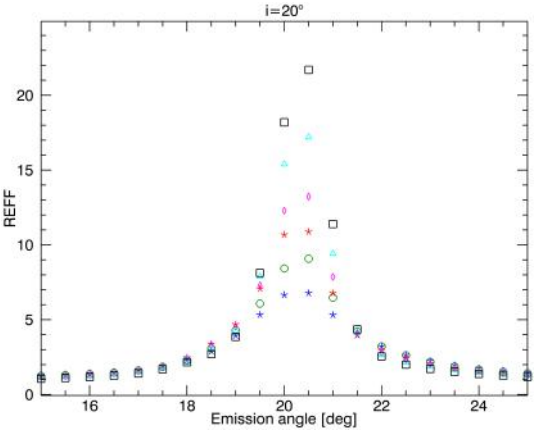

(A) Incident angle: 20° towards the surface normal.

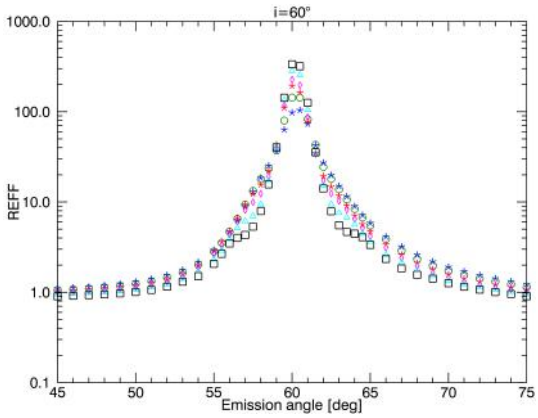

(B) Incident angle: 60° towards the surface normal.

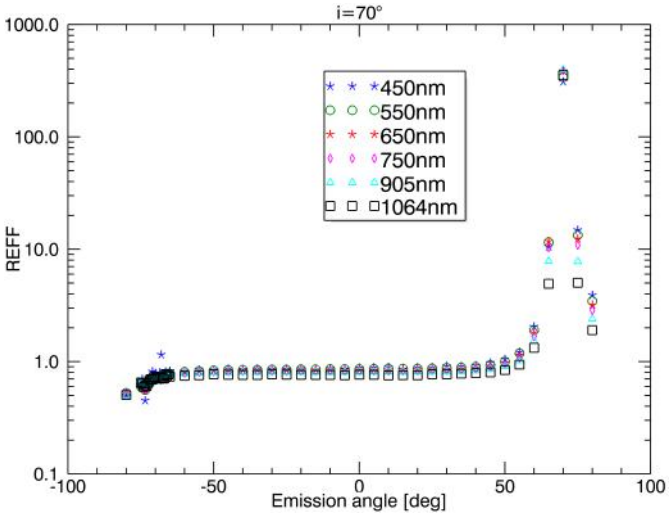

(C) Incident angle: 70° towards the surface normal.

FIGURE 2.29: Reflectivity profiles of the XENON1T reflectors for the various wavelengths for various incident angles. The reflectivity increases with the wavelength at low incident angles, what changes towards steeper incident angles.

The surface structures from the machining of the sample lead to a strong asymmetry depending on the sample orientation, as shown in fig.2.27. The results of the optical measurements are summarized in fig.2.31. The reflectivity of the XENON1T sample is in the optical range about a factor 3 lower for the specular peak height than of the previous prototypes for one sample orientation but slightly higher for the 90° rotated sample orientation.

Reflectivity of the XENON1T reflectors in LXe at 178 nm Finally, the XENON1T reflector panels (forming the TPC walls) were measured with the reflectivity setup in LXe at 178 nm. Based on the findings of the orientation asymmetry of the reflectivity at optical wavelengths, the samples always measured for two orientations, rotated by 90°. The measurements were performed with parts that were cut off a real, but spare, XENON1T

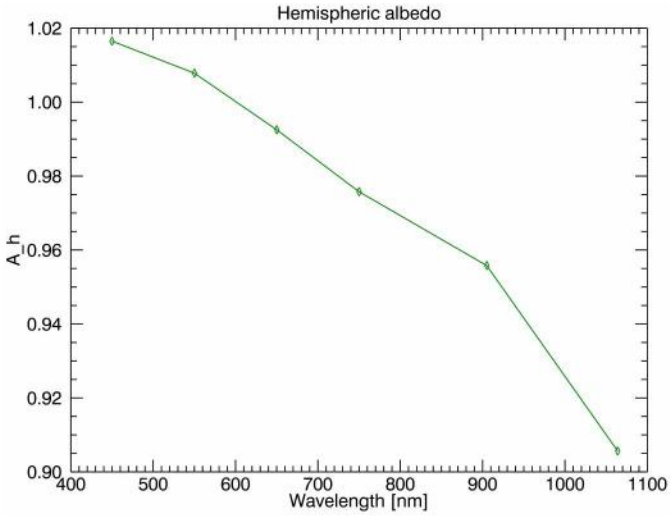

FIGURE 2.30: Albedo spectrum for the measured wavelengths. The albedo value is given by the reflectivity $REFF$ ($REFF$ is the measured emission normalized to a photometric standard) averaged over the hemisphere. The increase of the reflectivity with decreased wavelength indicates that a possible decrease of the reflectivity with decreased wavelength, as discussed in sec.2.3.3, cannot be confirmed and does not apply for the diamond-machined PTFE samples here. Furthermore, it does indicate that the found high reflectivities are qualitative reasonable.

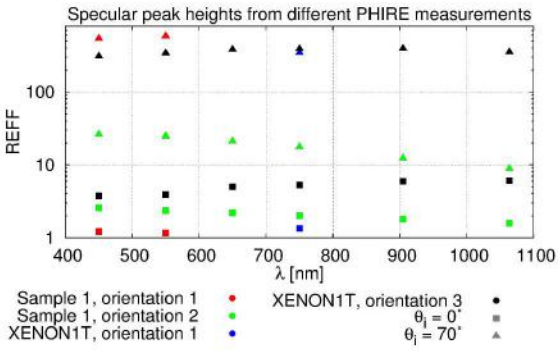

FIGURE 2.31: Comparison of the height of the optical specular peaks for the measured incident angles and wavelengths. The diamond-machined reflector sample, which is presented in sec.2.3.3 is shown as Sample 1. The sample was rotated by 180° for "orientation 3". The strong orientation dependence is well visible over the entire wavelength range.

reflector panel. Furthermore, two more XENON1T samples were measured: grooved reflectors that installed between cathode and bottom screening mesh in the TPC. The grooves ((1×0.5) mm) decrease possible surface currents by increasing the path free electrons have to travel. The surface was machined by the Uni Bern LHEP workshop according to the specifications that yield the smoothest possible surface, such that there should not be an orientation dependency as observed from the big XENON1T panels. The grooves were cut in the surface afterwards, so that they lack a special surface treatment. Even though, the above described orientation dependency should not appear, the sample was also measured in two directions because of an orientation dependency is

expected due to the deep grooves itself. Fig.2.32 shows a photo of the grooved reflector sample in the sample holder. Two measurement runs were done, one with the grooved sample and one with the big reflector panel samples (TPC wall segments). Each run includes measurements of two differently oriented samples and a reference sample that should allow a direct comparison to previous measurements. The reference sample is sample B from the systematics measurements (see sec.2.3, and fig.2.20).

FIGURE 2.32: Photo of the grooved XENON1T reflector sub samples mounted in the sample holder. The samples will be measured in one measurement run. The right, thus lowest sample was replaced later with the reference sample B.

Fig.2.33 shows the results of the comparison of the normalized and corrected reflection profiles of the reference sample (sample B, sec.2.3). The sample showed a decreased reflectivity compared to the previous measurements. Uncertainties due to the fluctuating light intensity, detection efficiency and determination of the incident angles (as visible in the shifted specular peaks for same incident angles) play a role for the observable differences. Beyond these effects, the reflectivity is still lower than expected from the previous measurement, which is especially visible at $\theta_i = 66°$ and $\theta_i = 70°$. That would mean a real decrease in the reflectivity of the sample and thus a higher surface roughness. It can be caused by getting the sample in touch with dust and dirt, which act as an abrasive. Therefore, sample B is not used as a normalization standard.

The incident orientation-asymmetry, which was found with the PHIRE-2 measurements of the XENON1T reflector samples was expected to be also seen at VUV in LXe. As shown in fig.2.34, this effect was indeed found: differences in the measured fluxes of more than 35% appeared. Surprisingly, the sample was reflecting brighter than expected from the "by eye" visible machining grooves. The XENON1T sample showed a similar reflectivity than the reference sample that was only much brighter at $\theta_i = 83°$. The varying positions of the specular peaks for same incident angles indicate again the big systematic uncertainties of these measurements, although the presented measurements were taken within one single run.

It is expected that the grooved reflector has a lower reflectivity than the big reflectors, especially in the specular regime because the surfaces of the grooves are not diamond machined. Fig.2.35 shows the results from the measurements of the grooved sample,

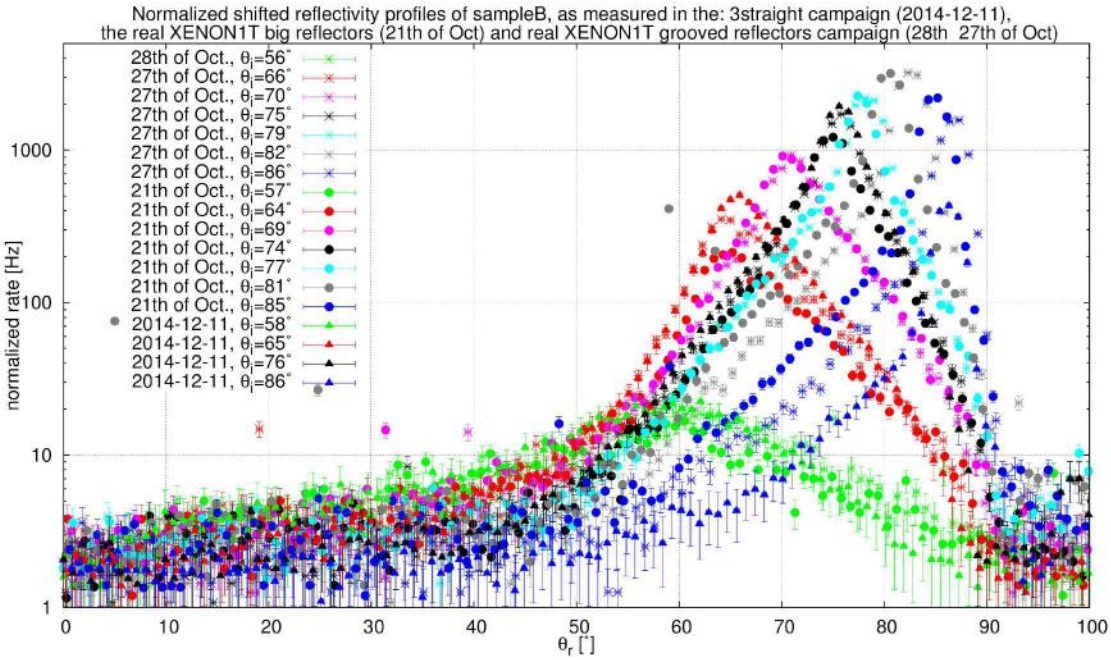

FIGURE 2.33: Reflection profiles of sample B. The profiles are normalized and corrected to the coordinate system with respect to the normal on the Teflon surface. The sample shows a decreased specular reflectivity compared to the previous measurements.

which confirm this expectation: the heights of the specular peaks are about 50% to 80% lower, depending on the incident angle and sample orientation.

One would expect that hitting an edge has a bigger effect for the vertically grooved sample (same as horizontally grooved but rotated by 90°). But the reflectivity profile of the horizontal sample is more irregular than the vertical grooved sample (fig.2.35): it shows more random fluctuations in the reflectivity profile. The irregularities in the reflection profiles increase towards steeper incident angles. This explains the found effect (sketch in fig.2.36): the steeper the incident angle is, the more does a surface machining matter due to being in the specular regime. Therefore, two components appear: a specular component from the diamond machined surface and one from the normally milled part down in the groove: Up to about $\theta_i = 70°$, vertical and horizontally grooved sample are comparable. Above that a significant differences of about 40% up to 80% appear because mainly the diamond milled top surface is visible from the vertically grooved sample. In contrast to that the visible surface layers (top and bottom in the grooves) of the horizontal sample are for all incident angles the same.

The grooves of the grooved reflectors have the size of the beam spot of the reflectivity setup. While the incident point should not matter for the vertically oriented grooved sample, the height and thus the incident point would matter for the horizontally grooved sample. Therefore, it was measured for two different heights (fig.2.37), which are about 2 mm apart. The measured reflectivity profiles show no significant difference above $\theta_i =$

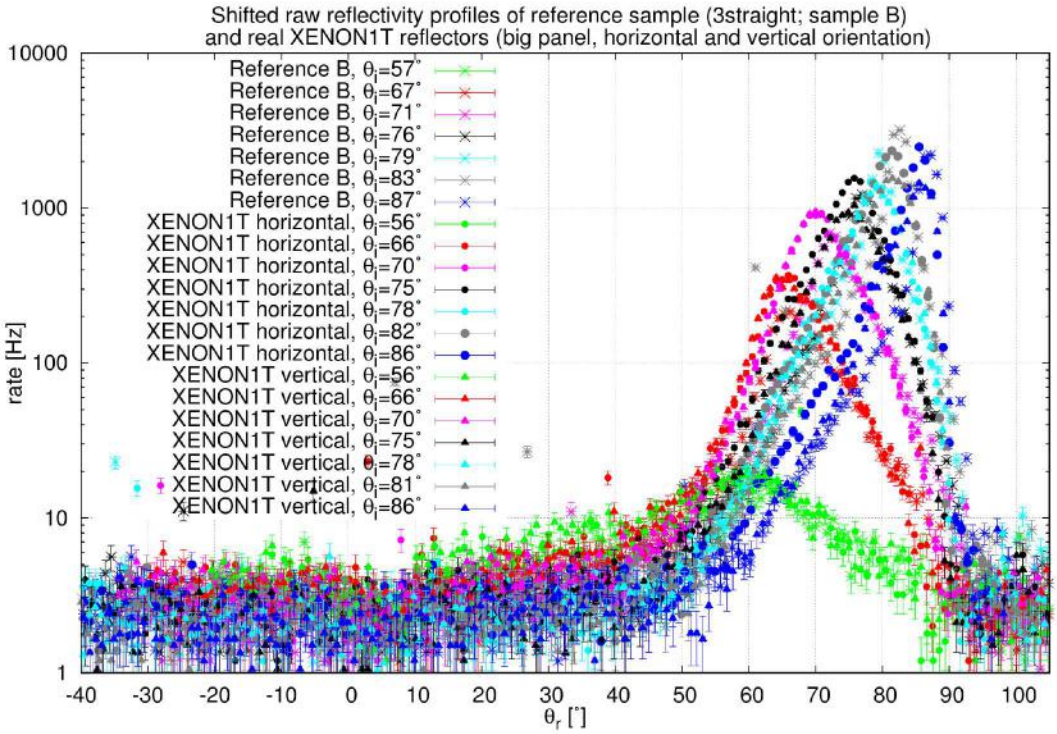

FIGURE 2.34: Corrected reflection profiles of the big XENON1T reflector panels. Two samples with different sample orientations rotated by 90° were measured. The reference sample was measured before during another measurement campaign. The reflectivity of the XENON1T sample is comparable with the reflectivity of the reference sample. The orientation dependence yields to differences of more than 35% in the peak height.

82°, but significant differences appear in the specular peak maxima below that. It is caused mainly by the different surfaces hit, but with some contribution from the slightly shifted incident angles (systematic effect of setting θ_{PTFE}) as well.

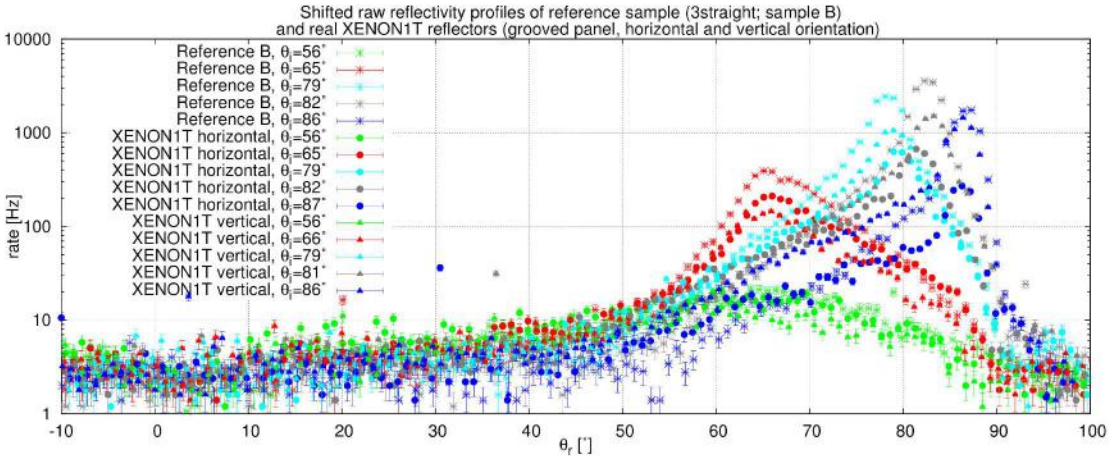

FIGURE 2.35: Corrected and shifted reflection profiles of the grooved XENON1T reflector panels. Two samples with different sample orientations, so different orientations of the machining directions of the sample, were measured. The reference sample was also measured during an other measurement campaign before.

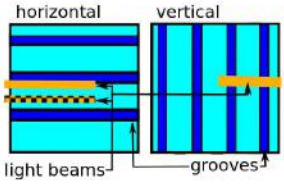

FIGURE 2.36: Sketch of the grooved samples in the two sample orientations. The incident light beam is shown in yellow or dashed yellow and the grooves in dark blue. For the horizontal sample are the two different incident beam height settings illustrated that either mean the beam hits a groove or not.

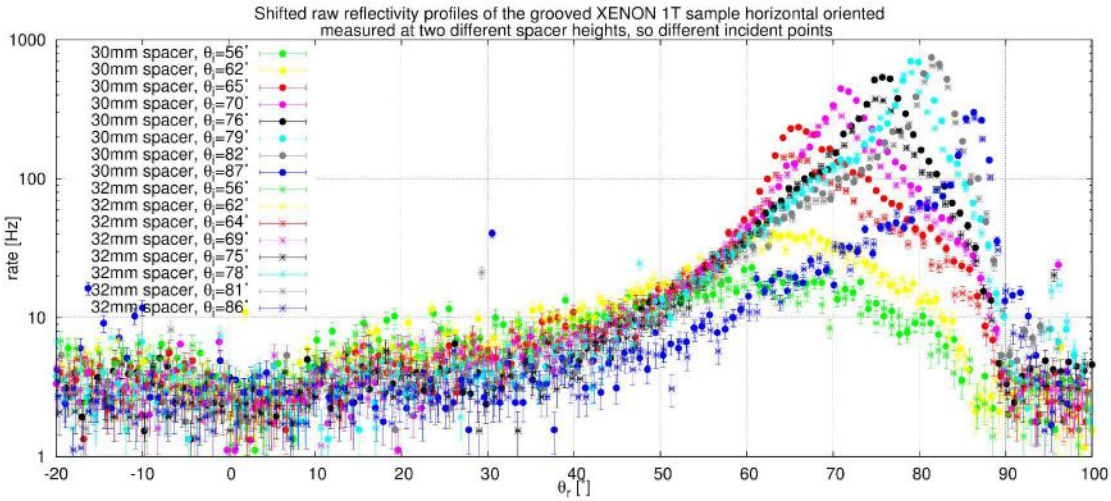

FIGURE 2.37: Reflection profiles measured at two different heights (different beam incident points) of the grooved sample in horizontal orientation. The profiles are scaled with respect to the beam normalization to be directly comparable. Shown are the raw but shifted and angular-corrected profiles. The differences might be due to the uncertainty in setting the incident angle (the measurement is for the specular regime very sensitive on this).

2.4 Summary and discussion

The goals of the PTFE reflectivity studies were to define a suitable machining technique for the PTFE reflector panels of XENON1T, and to measure the reflectivity of the machined panels. An improved knowledge about the reflection processes of 178 nm light in LXe would allow to improve the simulation of the light propagation in the TPC. Various machining techniques were studied and evaluated considering their applicability and stability against cleaning procedures. Based on the findings, a machining was chosen and optimized, leading to an optimal reflectivity. The design goal for XENON1T was a light yield of 7.7 PE/keV for a 122 keV Co57 source at zero field assuming a PTFE reflectivity of 99% [32]. It was even outperformed by the measured light yield of (8.02 ± 0.06) PE/keV at 41.5 keV from a ^{83m}Kr source [233]. A high reflectivity, as assumed there, is in good agreement with the findings by the LUX collaboration of $\geq 97\%$ [174]. Due to machining restrictions, the final machining of the XENON1T reflectors suffered in

quality compared to the optimal machining (40% to 80% specular peak height difference). The reflectivity measurements were done with the Münster reflectivity setup in LXe with 178 nm light (sec.2.2, page 24) and supported by measurements in the optical range (sec.2.3.3, page 47). Furthermore, some systematic measurements were done with the reflectivity setup to study the impact of the systematic effects of the apparatus on the findings.

The found orientation dependency and locally varying reflectivities (sec.2.3.3, page 47 and 2.3.4, page 49) make it impossible to quote a single value for the reflectivity because the variations are too large. Thus a reflectivity map would be necessary for the actual XENON1T reflectors. The reflectivity depends highly on the incident angle: its amplitude and composition between diffuse or specular reflection varies. This might yield to an incident angle bias: for certain interaction positions, and thus incident angles, more light might be reflected than for others. It might result in a local depending light yield as already observed in XENON1T [233]. This will be clarified with the help of the XENON1T Monte Carlo simulation.

2.4.1 Limitations of the measurements

It turned out already during the first measurements that some points of the results from the reflectivity setup were not completely understood:

1. normalization
2. impact of the aperture in combination with the step width: resolution and point spread function
3. emission and detection efficiency
4. alignment of the rotation axes of the PMT and sample chamber
5. sample orientation dependency and capture of reflexes at $\varphi \neq 0$.

1., 2.: The normalization is done by scanning the beam in one plane, fitting the measured profile with a Gaussian and integrating the result. Since the scanning step-width is smaller than the aperture of the PMT, the single bins are overlapping, what means double-counting occurs and gets integrated as well. Thus the resulting beam profile fit is a convolution of the aperture with the true beam profile. The unknown point spread function of the aperture might affect the results with captured scattered light in an unpredictable way. This is also true for the measured reflectivity profiles but the impact on the results is not yet fully understood. Furthermore, the used aperture might be too

large to resolve the true shape of the specular peak. This is indicated by the width-decrease of the specular shape towards shorter wavelengths, as seen in the PHIRE-2 measurements (sec.2.3.3, page 47).

3.: The LXe reflectivity setup measures a count rate from discriminator trigger signals. Normally, the maximum trigger rate of the discriminator is far higher than the encountered count rates, but no dead time handling is existing for the measurements. This yields to an unknown trigger efficiency (lifetime corrected by deadtime), affecting especially high rates. Although the system setting using a PMT as sensor generally features single photon sensitivity, a precise sensitivity calibration was never done. Thus the interpretation of the measured count rates is not clarified so far. Nevertheless, it does not play a role as long as the measured curves are normalized properly with the same method. Within this work it is interpreted as a "flux or flux proxy", ignoring the unknown detection efficiency (sensitivity of the PMT with aperture, trigger rate of the discriminator and scaler behaviour).

These uncertainties should be of minor importance because the normalization of the measured profiles with the integrated beam profile removes these effects. But this applies only in the case of a negligible bin width, i.e. a fine enough resolution of the measured profiles, because otherwise it does matter whether the profiles are integrated bin-by-bin, or via integrating a fitted model or smoothed profiles. Regarding this, the large aperture of 2 mm, which is good for a fast sampling, smears out the shape of the measured reflectivity profiles. Additionally, fluctuations of about 10% in the measured beam intensity were observed during one day. During one measurement run, that might span several days, more than 10% were observed (see table 2.2, page 42). The beam spot position also varied by nearly 2° what leads to shifts in the measured incident and reflected angles. Combined with the poor precision of the θ_{PTFE} scale, this results in irreproducible reflectivity profiles for one sample (e.g. specular peak positions in fig.2.20, page 43), as visible by the non-stable specular peak positions. Also the consistency within one single measurement run suffers from that because it requires setting θ_{PTFE} for each incident angle.

4.: Another weak point is the alignment of the two rotation axes of the PMT lever arm and of the sample chamber. A misalignment would violate the assumptions that are used for the angle corrections as shown in sec.2.2.2 for eq.(2.4 (page 31). Light rays that hit the quartz glass tube not rectangular to its surface tangent would lead to scattering on the two glass surfaces, away from the original direction of the reflected light ray. These effects would generate random results depending on how off-axis the two rotation centres are. While the z alignment showed good results, the x alignment was already less straight-forward to interpret but still good enough within its uncertainties. The y

axis alignment required a not straight-forward-to-interpret method that relies fully on a precise position of a rod towards the sample chamber center and beam. Beyond the stated uncertainties of the alignment results, the size of the effects due to misalignments within this uncertainties is not quantifiable (although it might be possible with a ray tracing simulation, see sec.2.4.2 on page 59). Furthermore, the alignment of the beam direction versus the center of rotation of the sample chamber is absent. It is assumed to be correct but it was not provable with the necessary high precision. On top of that, the beam is not really focused in the center of rotation of the sample, the distance between the lens and the sample is far more than the 80 mm focal length. This also explains the disagreement between the aperture of the collimator (1 mm) and the observed beam widths. Thus the true shape of the specular peak gets smeared out as well, what gets then enhanced, as mentioned above, by the 2 mm PMT aperture. Therefore, the scanned beam profile is actually a convolution of the two apertures with the true beam spot, which gets smeared out by them.

5.: The 3D measurements, extending the measured angular range out of the beam-PMT-plane (see sec.2.3.2, page 44), showed that the diffuse and specular component decays fast towards bigger φ. Measured angles beyond $\varphi = 10°$ showed some contribution, which is not covered by the PMT aperture and thus missed in all 2D measurements. Nevertheless, this contributions are negligibly small. This is important since the optical measurements (see sec.2.3.3, page 47) showed a strong orientation dependence of the samples what means one might have measured only a part of the full reflectance profile during the normal measurements. It appears that there is a gap between $\varphi = 2.9°$ (defined by the aperture) and $\varphi = 10°$ (first step of the 3D sample, precision limited), which could not be covered with the precision of the reflectivity setup. Thus a prediction of the expected reflectance of the XENON1T reflectors for light propagation simulations is not possible.

One can conclude that the measured profiles and their interpretations are not good quantitative measures, but give a reasonable qualitative impression. The results were cross-checked with a well calibrated apparatus at optical wavelengths in air because there is no reasonable argument why the reflectivity should differ in LXe with VUV light, apart from the different refraction indices. So it is pretty likely, that the machining artefacts that were found on the final XENON1T reflector panels, have a bigger impact than the measurement uncertainties (orientation dependence, see sec.2.3.4, page 49).

2.4.2 Possible improvements measuring the reflectivity of PTFE in LXe at VUV

The optimization of the reflectivity of PTFE and characterizing the reflection processes, to improve the knowledge of the light propagation processes within the TPC will be crucial for future detectors [1, 238]. From this work some lessons emerge that might be useful for future reflectivity measurements. First, after finding the orientation dependence of the real XENON1T reflectors it would make sense to separate the measurement of the total reflectivity and of an angular reflectance profile. The total reflectivity should be measured with full 2π coverage avoiding sampling, because a sampling method leads to possible difficulties with the light source stability and varying detection efficiency. Instead of measuring a total reflectivity as R (e.q.(2.1), page 21), one can simplify the principle drastically by aiming for a relative reflectivity, which depends on some reference. This simplified approach can help for a fast and reliable measurement of different surface machining techniques or even searching for new reflector materials. It can be performed in vacuum or LXe using something similar to an integrating sphere apparatus. The inside design would not matter if the Xenon purity and light source are reproducible stable, or one can imagine a kind of "two sub chambers" design, which allows to measure both surfaces at once.

When a surface machining procedure or reflector material is chosen, one needs to quantify a reflectivity profile as precise as possible because the simulation of a dark matter search TPC employs "single photon ray tracing". That means the measurement of the reflectance profiles requires a directed light source with a precisely as possible known intensity, which has a stable performance, e.g. a laser. This would allow for a disentanglement of the diffuse and specular components. It should allow for a 2π coverage to identify possible orientation dependencies. The detection efficiency needs to be stable if a scanning detector gets, used or well calibrated for the single pixels if a detector array gets used (e.g. with an internal calibration source in the LXe). A detector array, for example made of PMTs, would limit the resolution but accelerate the measurement time and avoid problems with scanning detectors. Furthermore, surfaces between media of different refractive indices should be avoided because they introduce a big systematic uncertainty depending on the incident angles on the surfaces.

Since setting up two complete new devices for these measurements will be very time intensive and expensive, one can also imagine improving the understanding of the systematic effects of the reflectivity setup. This should include the precise alignment of the optical components using lasers: collimator, beam, sample chamber and PMT. The use of different wavelengths in the optical range would allow for a extrapolation towards VUV using

easily available lasers. A wavelength scanning device like the already installed monochromator (currently fixed to one wavelength) would allow for a wavelength-dependent reflectance measurement, which would allow for a better understanding of the reflectivity processes, i.e. the role of specular reflectance and its dependence on the incident angle. Thus, it would be possible to clarify whether the observed specular reflectance is due to the dependence of the reflectivity on the surface roughness, as suggested within this work. Furthermore, a ray tracing simulation would allow to efficiently evaluate systematic effects due to misalignments, double counting etc. On the hardware side it would make sense to deploy the light source, detector and DAQ components in a temperature stabilized environment and to carefully measure their stability and efficiency. Beyond that, a deadtime monitoring and DAQ that directly measures the PMT response would make sense. Also the aperture in front of the PMT should be minimized while enlarging the integration time. The used aperture should be large enough to cover possible uncertainties of the alignment thus making them negligible (if the aperture is bigger than the uncertainties they are not dominant for the measured profile and would not be resolved while being completely covered within one angular step). A minor improvement would be the measurement of the point spread function of the aperture and possible scattering artefacts on its edges. This can also be captured within a more detailed ray tracing simulation.

2.4.3 Improving the reflectivity further

The reflectivity measurements presented here do not allow for a quantitative statement about the total reflectivity. But Monte Carlo simulations [32], measurements of others [206, 204, 205, 61, 130] and this work indicate a reflectivity close to 100%. Thus a large further improvement of the total reflectivity is not very likely. But avoiding effects like the orientation dependence due to machining artefacts by using sufficiently large tools (customized larger cutting edge diamond tools, which also would allow for an even smoother surface) would be an improvement that yields to a more isotropic light yield. The impact of the strong specular component at steep incident angles, which is correlated with a lower diffuse component, should be studied with the XENON1T Monte Carlo simulation, to get a hint whether in future the "simple" surface machining is sufficient or whether one should enlarge the diffuse component with the surface machining again. The second point might mean the need to improve the total reflectivity using for example composite materials. Furthermore, some possible improvement is expected for medium incident angles due to the expected total reflection above 53° (see sec.2.1, eq.(2.3), page 22).

Chapter 3

The Bern LXe test platform

The Bern LXe test platform was build to host experiments for the research and development for future Xenon dark matter experiments. The cryogenic environment of the platform offers fast Xenon liquefaction in a double wall cryostat. Currently a 6.5 liter inner cryostat with a classical dual phase time projection chamber (TPC) is installed. With a diameter of 48 cm and a usable height of roughly 1 m the outer cryostat offers enough space for even quite big installations. The Xenon gas handling and cryogenic system is completely modular and scalable designed and offers therefore the ability to be used for bigger installations as well (range of 50 kg Xenon). Up to 24 signal channels (eg. PMTs) can be read out and powered in the current status. The platform was developed and build at LHEP Uni Bern. Furthermore a fast and modular data processor and an analysis software were developed.

The currently installed dual-phase TPC aims for the development of a single-phase TPC[1]. This concept might be able to challenge the issue of generating an anode field for the ultimate dark matter detector DARWIN, as explained in sec.1.2.4 (page 16) [1], because the need of parallel arrangement of gate, anode and liquid-gas interface is avoided. Its design allows for a direct transformation into a single-phase TPC thus allowing for direct comparison of the performances [237]. In this work the development of the infrastructure is shown, as well as a first characterization of the TPC in the dual phase mode.

The system was operated with several smaller experiments before: PMT characterization, LXe levelmeter calibration and development of the cryogenic system. These use cases are not shown here explicitly but the current use case as TPC development platform. In this stage there are two run modes:

[1] A single-phase TPC is completely filled with LXe and uses proportional scintillation in LXe in the presence of a strong electric field to acquire the ionization signal[31].

- TPC mode: TPC is operated with applied drift field and extraction field, scintillation and ionization light signal are acquired from the PMTs
- LED mode: TPC can be operated with any field, light signals in coincidence with a LED light pulse get acquired to calibrate the PMT gains.

The cryogenic system is the basic infrastructure of the Bern LXe test platform. It is required for the liquefaction of the Xenon gas (GXe), cooling of the liquefied Xenon (LXe) and keeping it stable at a given temperature. It employs a double wall cryostat and cold head that is cooled with liquid nitrogen (LN2). Sec.3.1 (page 62) introduces the cryostat and the vacuum system while sec.3.2 (page 65) is explaining the cryogenic system itself. In sec.3.3 (page 70) the gas handling and gas analysis features are described. The sensor environment of the setup, their units and variables are explained in full detail in sec.3.4 (page 75). The currently installed TPC is described in sec.3.5 (page 82) and the data acquisition system capabilities are demonstrated in sec.3.6 (page 88). The first results from the TPC being operated as dual-phase TPC were processed with the data processor described in sec.3.7 (page 92) and their analysis is shown in sec.3.8 (page 103). The last section of this chapter (sec.3.10 (page 127) summarizes the measured performance of the TPC in dual-phase mode and the performance of the platform.

3.1 Cryostat and vacuum system

The cryostat contains the liquefied Xenon and accommodates the installed experiment. It is a double wall cryostat with a vacuum insulation and a radiation shielding made of Mylar foil.

The outer cryostat is a 130 cm high Aluminium cylinder with a diameter of about 48 cm, which was build by Oxford Instruments [126]; it offers about 0.93 m^3 inner volume that is used for the cooling system and the inner cryostat. The inner walls of the outer cryostat were carefully prepared by cleaning with soap, ethanol and water to reduce outgassing from the walls. It is closed with a custom made stainless steel (SS) flange (as shown in fig.3.2) that has 5 KF-40 ports towards the insulation vacuum and 4 ports going directly to the top flange of the inner cryostat. The outer cryostat rests on three points on its outer circumference of the top flange on adjustable pins, which are the levelling mechanism (described in detail in sec.3.4, page 75). A sketch of the system from the outside is shown in fig.3.2.

The top flange of the outer cryostat is directly connected with the top flange of the inner cryostat with 3 CF-40 pipes and 1 CF-16 pipe, which end directly in the inner cryostat

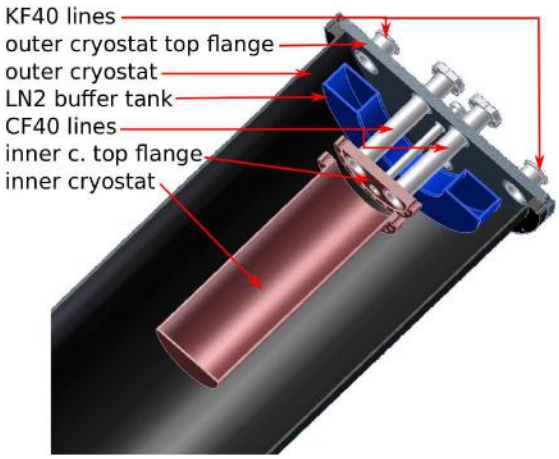

FIGURE 3.1: CAD image with an overview over the main components of the Bern LXe test platform. The outer cryostat is shown in black, the inner cryostat in brown and the LN2 tank in blue. The top flange of the outer cryostat with 2 of the 5 KF-40 flanges is shown in grey and the top flange of the inner cryostat is shown in brown with 2 of 3 CF-40 and the one CF-16 flange going through the top flange.

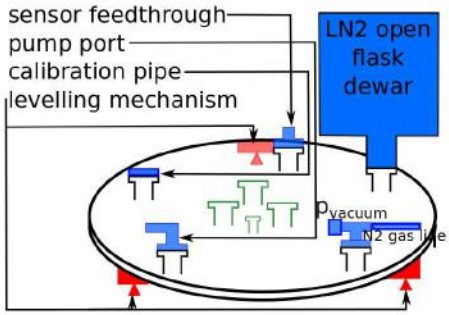

FIGURE 3.2: Sketch of the top flange of the outer cryostat with the KF-40 feedthroughs (black&blue) and the 3 CF-40 and the CF-16 flanges (green), which lead to the inner cryostat. The 3 suspension points of the levelling mechanism are shown in red (see sec.3.4).

(see fig.3.1). The top flange of the inner cryostat is a CF-150 flange. A future extension is foreseen by installing an intermediate CF-250 sized cylinder in between the both CF-150 flanges, offering space for cables, patch panels and further installations in the inner cryostat volume. The inner cryostat is an about 37 cm long SS CF-150 cylinder that is closed on the lower end by a welded plate. It was carefully cleaned on its inner- and outer side to reduce outgassing, whereas especially the inner walls were cleaned more careful. The cryostat walls were not machined specially. In the top flange of the inner cryostat are blind threads for mounting the TPC and other installations: 3×3 threaded holes M5 at radii of: 30 mm, 52 mm and 72 mm.

On the outer top flange are furthermore installed (see fig.3.2): an open flask dewar for the LN2 filling (sec.3.2, page 65), a calibration source pipe, a feedthrough for the sensors needed for the operation of the cryogenic system and the LED calibration (sec.3.4, page 75) and a gas port for a controlled vacuum shutdown with a dry and clean gas (technical

N2). The open flask dewar for the LN2 filling is mounted on a KF-40 flange on top of the outer top flange. It is directly connected with the main insulation vacuum. The calibration source pipe that is used for external calibration sources, follows the shape of the inner cryostat, which yields to a better source response because the calibration sources are less than 5 cm away from the inner cryostat volume (depending on the exact position in the pipe). Between the outer and the inner top flange, a ring shaped LN2 buffer tank with rectangular cross-section is located (see sec.3.2, page 65).

The space between the two cryostats is hermetically sealed by an O-ring between the outer cryostat and the outer top flange and by KF gaskets for all vacuum installations. The vacuum installations aim for a fast applicable and robust vacuum volume, which is easy to open and close to achieve short service times. The insulation vacuum was tested to be leak tight to below 10^{-9} mbar $\cdot$ l/s. The vacuum gets pumped with a roughing pump (Trivac D8B [151]) and a turbo pump (Turbovac 450i [152]). It is operational after 30 min to 1 h depending on the cleanliness of the system and the desired final pressure (regularly below $5 \cdot 10^{-4}$ mbar). A TPR 280 Pirani gauge monitors the vacuum pressure [227]. The inner cryostat, the open flask dewar for the LN2 refilling and the LN2 buffer tank are shielded on their vacuum sides with Mylar foil (10 layers) to improve the insulation against heat radiation. Typical achieved vacuum pressures are in the range of below 10^{-4} mbar, which tend to be much lower when the cooling is running due to cryogenic pumping by freezing out residual gases ($\mathcal{O}(10^{-6})$ mbar). Cryogenic pumping has some impact on the vacuum itself, because it yields to pressure instabilities and makes switching the vacuum system off more difficult due to melting substances that cause a fast rising vacuum pressure. The major contribution is suspected to be water. Therefore a dry purge gas inlet (eg. technical N2) is installed to avoid problems with water in the insulation vacuum when doing a fast recuperation or shutting down the vacuum while parts of the system are still cold. Also the vacuum pump system is designed with the capacity to be able to handle this.

The inner cryostat and all parts belonging to it are sealed with metal seals: CF Copper seals or VCR copper seals. This ensures a higher leak tightness, the ability to be backed at high temperatures and chemical tolerance. It was leak tested before being filled with Xenon to leak rates of about $\mathcal{O}(10^{-10})$ mbar $\cdot$ l/s. Before being filled with Xenon, the inner cryostat was cleaned (Acetone, ethanol and water) and baked (heated to about 150°C pumped to below $1 \cdot 10^{-5}$ mbar). Only the cable feedthroughs are not all metal parts: they are floating RHseals feedthroughs (ground or shield are not connected to the vacuum part of the feedthrough but use dedicated cables). The inner cryostat can be pumped through an all metal CF-40 angle valve [190]. Furthermore, on the inner cryostat are installed:

1. a coax cable feedthrough (24× RG196)
2. a high voltage feedthroughs (a): 26 × 30AWG Kapton insulated
3. a high voltage feedthroughs (b): 8× Kapton insulated for the field HV supply, sec.3.5 on page 82)
4. a coax cable feedthrough for the levelmeter (8×RG196, see sec.3.4 on page 75)
5. a dual $^1/_4''$ VCR port feedthrough for the Xenon supply
6. a multi pin feedthrough for the instrumentation of the TPC (see sec.3.4 on page 75 and sec.3.5 on page 82)
7. pressure sensor (PX302-100AV) for the gas pressure in the inner cryostat.

3.2 Cryogenic System

The cryogenic system of the Bern LXe test platform liquefies the Xenon in the inner cryostat and keeps it liquid, thus also cooling the whole inner cryostat with the contained detector (here the TPC, see sec.3.5). It uses a cold finger in the inner cryostat that is coupled with a liquid Nitrogen (LN2) cold bath in the outer cryostat.

The cooling medium (LN2) gets heated up and evaporated by the heat flux from the cold finger to the LN2 bath. The LN2 is lost during that process and needs to be refilled. It is supplied from the nitrogen liquefaction plant of the ExWi[2] from where it gets to the laboratory through vacuum insulated supply lines. A Teragon LC2 liquid nitrogen filling controller [222] controls a solenoid LN2 valve, which is placed on the lab LN2 supply lines. From there a LN2 line ends in a open flask dewar that is installed on top of the outer cryostat. The insulation vacuum of the open flask dewar is directly connected with the insulation vacuum of the outer cryostat and thus gets pumped through it. Two switching semiconductor sensors are placed in the open flask dewar and are readout by the LC2 controller. If both are warm (set point at $\approx 78\,\mathrm{K}$) the solenoid valve is opened and refills LN2 until both are cold (77 K) again. The placement of the sensors is very critical for a successful LN2 refilling because the response of the sensors is very sensitive against getting hit by LN2 drops. The sensors were placed in a pipe protecting them from splashing LN2 to minimize the effect of unwanted switching of the solenoid valve caused by boiling LN2 and turbulent filling (wall supply line runs at about 3 bar).

The open flask dewar is connected via a CF-16 flexible line with the ring shaped LN2 buffer tank, which goes around the CF-40 and CF-16 lines coming from the inner cryostat

[2]Exakte Wissenschaften building of the university of Bern.

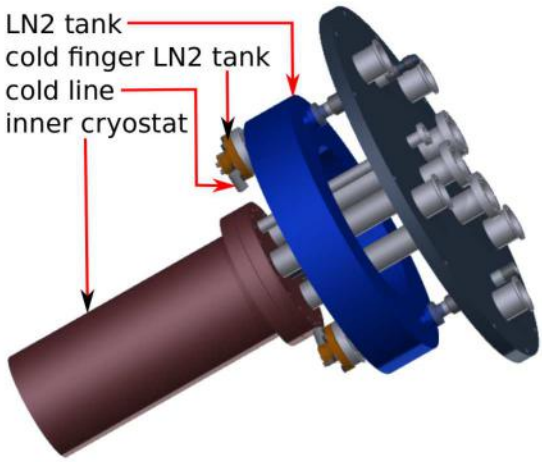

FIGURE 3.3: The inner cryostat with the cryogenic components that are located in the outer cryostat. The inner cryostat is shown in brown, the LN2 tank in blue and the copper CF-40 cold fingers in the LN2 tank in orange. Also shown in grey is the first part of the cold lines, which are hooked into the cold fingers that conduct the heat through the cold finger into the LN2 reservoir.

(shown in blue in fig.3.3). The refilled LN2 and the gaseous nitrogen boil off go both through the CF-16 line. The tank has a rectangular shape and a volume of 5.8 l. Thus the buffered LN2 volume is sufficient for about 3 hours without external LN2 supply when the system is kept with 4 kg Xenon at $-100°$C. Nevertheless, the refilling set point is set such that about every 1.5 h LN2 gets refilled. The LN2 sensors and filling cycles are monitored with the slow control system (see sec.3.4, page 75).

In the bottom of the LN2 buffer tank are three CF-40 flanges, on which copper cold fingers are installed (fig.3.4). Each offers plugs for two 1 cm diameter copper cold lines. The cold lines are custom-made high density braided copper cables with a cross section of 0.8 cm^2 and a length of 20 cm. Both values are optimized for high thermal throughput by minimizing the length and maximizing the cross section. The cross section is chosen higher at the connection points to balance the efficiency of the coupling and thus guaranties the design heat conductivity. In the current status, only three of the cold lines are used because they offer enough cooling power. The cold lines on the inner cryostat side are connected to a cold finger again.

The cold finger in the inner cryostat (see fig.3.5) consists of two copper parts. An outer CF-40 flange with a thread on the inside. Three cold lines can be connected directly through the recesses in it (see fig.3.6) while more cold lines require simple stacking. The second part is the slitted cold finger itself that is screwed into the upper flange on the cryostat side. Both parts are shown in fig.3.5 and the finally installed components are shown on the photo in fig.3.6. On top of the Cu flange, in the insulation vacuum, a top cap gets mounted with two 25 W heaters. They are installed in series and regulate the cooling power.

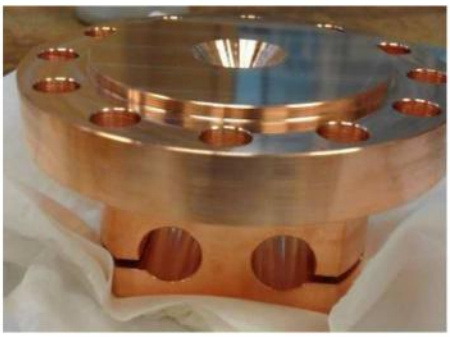

FIGURE 3.4: Photo of the cold finger flange, which sits in the bottom of the LN2 tank.

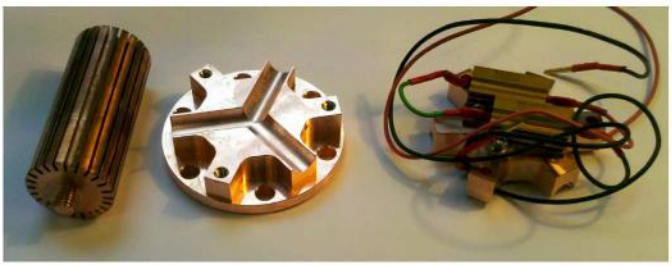

FIGURE 3.5: Photo of the cold finger, which sits in the inner cryostat. Left to right: slitted cold finger, cold finger top flange, top cap of the flange.

FIGURE 3.6: Photo of the cold lines (copper cable) connecting the cold finger in the inner cryostat (right) with the cold finger (left) on the lN2 tank (top).

The cooling power is controlled with the heaters that are powered by a CryoCon 22C cryogenic controller [76]. The cryogenic controller regulates the heater power depending on a set temperature with a PID loop. The PID loop was tuned carefully [232] to optimize the system for a stable operation, minimizing thermal fluctuations (constant temperature) while still being robust against smaller fluctuations in the heat influx due to, for example, changing recirculation conditions (the recirculation circuit is used to pump Xenon gas with a gas pump through the gas panel, including a getter for gas purification, see sec.3.3, page 70). Fluctuations of below $\pm 0.02\,\mathrm{K}$ absolute over several hours were achieved while in normal operation typical fluctuations are in the range of $\pm 0.03\,\mathrm{K}$, when operating the recirculation as well (see fig.3.7). Two temperature sensors

(PT100) are installed on or in the cold finger. The first one, $T_{\text{coldfingerLXe}}$, is installed on the bottom of the slitted cold finger and is in direct thermal contact to it. The second sensor $T_{\text{coldfingerLN2}}$ is placed in a little hole on the vacuum side in the CF-40 copper flange (see sec.3.4; table 3.2, page 81). By default the temperature is controlled basing on $T_{\text{coldfingerLXe}}$, which offers a higher stability during normal operation and a lower probability for temperature oscillations. Controlling the temperature with the $T_{\text{coldfingerLN2}}$ sensor allows for fast reactions and steeper power gradients but it tends to oscillate earlier. Fig.3.7 and fig.3.16 (page 78) show examples of typical temperature trends during stable operation.

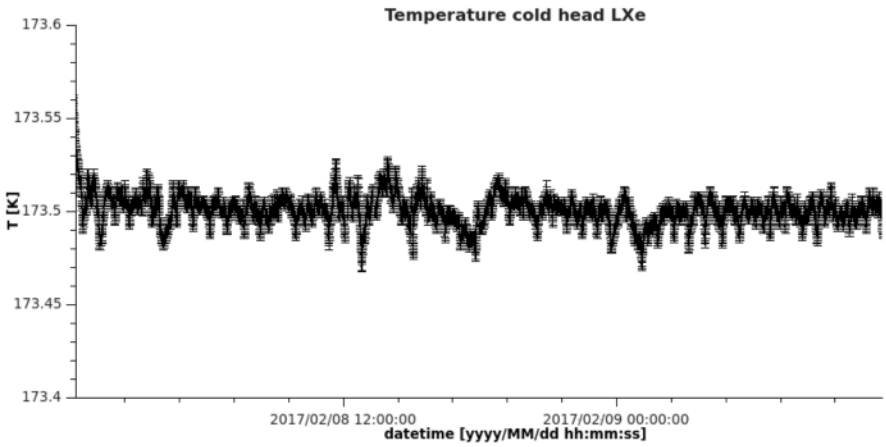

FIGURE 3.7: Temperature measured on the bottom of the cold finger in the inner cryostat over 4 days. During that run about 4 kg of LXe were contained in the inner cryostat. The recirculation pump was not running.

The cryogenic system was optimized for a high cooling power for the liquefaction of up to 10 kg Xenon over about half day. The system was designed basing on the *Fourier law* [68]:

$$q_x = -k\frac{dT}{dx}, \tag{3.1}$$

which describes a heat flux q_x through a unit surface depending on a temperature gradient $\frac{dT}{dx}$. k is a material constant that describes the one-dimensional heat flux in the material, the so called thermal conductivity. From eq.(3.1) it follows for the complete surface:

$$\frac{dQ}{dt} = -kA\frac{dT}{dx} \tag{3.2}$$

with the heat flux $\frac{dQ}{dt}$ through a surface A. The heat conductance describes how heat is conducted through a material between two points, which are Δx apart:

$$U = \frac{k}{\Delta x} \tag{3.3}$$

Since copper is the material with the highest thermal conductivity, that is available ($k \approx 400\text{Wm}^{-1}\text{K}^{-1}$ [225]), it was chosen for the cold lines, cold flanges and cold fingers.

With a given distance of 20 cm between the LN2 buffer and the cold finger in the inner cryostat, the given cooling medium LN2 and a target temperature of about −100°C, one can calculate the cooling power that is needed to fully use the dynamic range of the CryoCon 22C heater output of 50 W. The resulting cooling power, depending on the number of cold lines, is shown in fig.3.8. At about −95°C a bit less than 50 W are available, using 3 cold lines. The set temperature has a minor influence on the cooling power. In contrast to that, the largest influence comes from the target mass (calculated here from 0.1 kg to 10 kg).

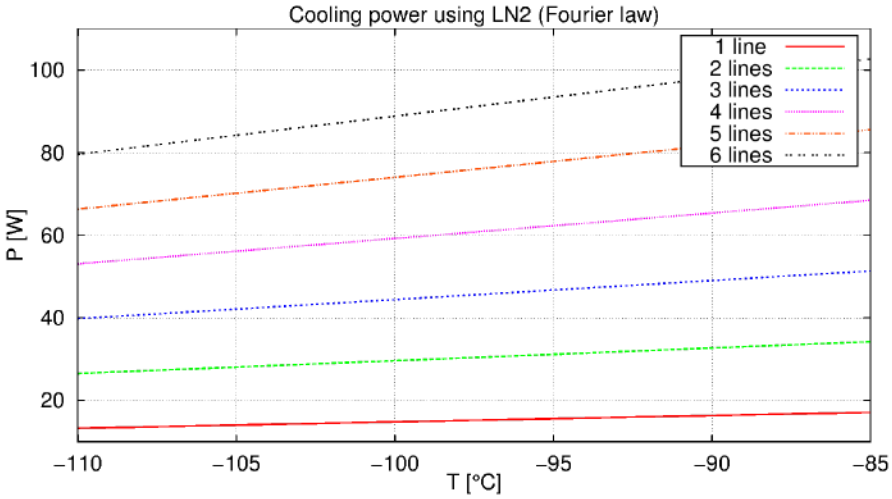

FIGURE 3.8: Theoretical cooling power P basing on Fouriers law. The available cooling power is shown as function of the temperature for various cold lines (currently installed: 3). The efficiency of the couplings was assumed to be 100%.

Following this calculations, the cool down time is of interest. It is shown in fig.3.9 for various target masses including liquefaction and cool down of the Xenon to −100°C. The additional mass that has to be cooled down, in form of the TPC, the cryostat itself, etc., was ignored because its effect is negligible since most power is needed for the liquefaction process. The interesting mass range for the current detector is 3–5 kg, resulting in 5 to 8 hours cool down time. Three measured cool downs are shown in the figure as well, the first one for a run with reduced cooling power (2 cold lines only) and the other two (red) from runs with 3 cold lines. The first 3-cold-lines run was taken without recirculation, thus a higher heater power was required while the second point is from the low gain run cool down (sec.3.9, page 111), where the recirculation was operated. From these measurements one can conclude that the cooling system works according to its design parameters. The neglected coupling efficiency has obviously a minor impact, since the mechanical coupling is good (according to the design). The lower measured cooling power of the third data point at 9 h from the low gain run can be explained by the heat influx from the running recirculation that is not included in the calculations. The experience tells that a higher cooling power would be nice, when filling or operating the recirculation

at high flow, but it might required a larger contact surface to transfer the heat efficiently between Xenon and the copper cold finger.

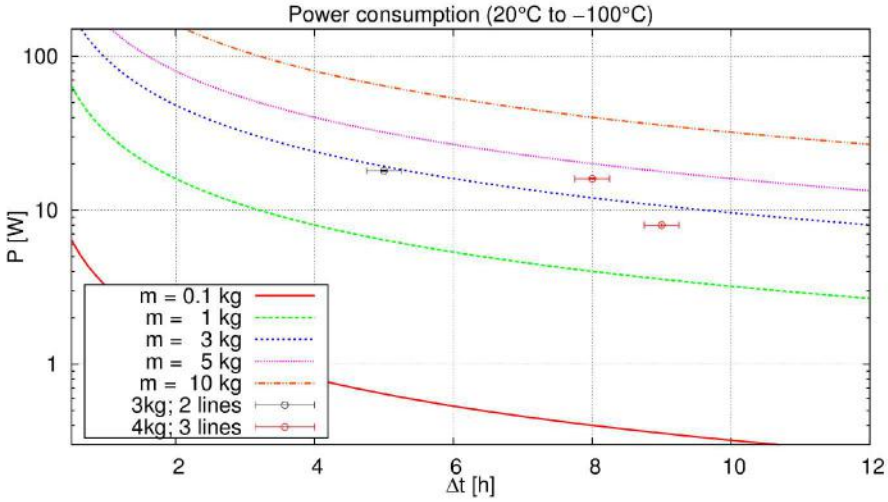

FIGURE 3.9: Theoretically necessary cooling power to cool various masses of pure LXe down to −100°C as function of cool down time. The power necessary for the phase transition from gas to liquid was taken into account. Three measured cool downs are shown: 1st) for a run with reduced cooling power and 3 kg LXe (2 cold lines only) in black, 2nd) source run in April 2017 with 4 kg LXe and 3rd) from the low gain run cool down with 4 kg LXe in red lower point. The measurements match the expectations from the design.

3.3 Gas handling and purification

The gas system of the Bern LXe test platform is a closed system because Xenon is one of the most expensive noble gases. The gas system consists of a gas storage, supply lines and purification system on a gas panel and a separate part for gas analysis (residual gas analyzer; RGA). The gas panel can be decoupled from the detector itself and from the gas analysis station. The gas system can be split into two parts: a high pressure side including the storage that can hold up to 200 bar and a low pressure side, including the RGA, purification system and inner cryostat itself that is designed to work up to 3.5 bar (beyond this the system can be damaged).

3.3.1 Gas panel

The gas system is a moveable custom-made rack. Fig.3.11 shows a photo of it. All gas lines are $^1/_4''$ VCR pipes with Copper gaskets. The connections to the inner cryostat and to the gas analysis station are done with flexible $^1/_4''$ lines. The valves installed in the gas panel are Swagelok diaphragm valves [214] and Swagelok diaphragm high pressure

valves [215] on the high pressure side. Both valve types are not fully leak tight what has no major practical impact. Between the inner cryostat and the gas panel Swagelok bellow valves [216] are installed, which are also not fully leak tight, what appeared to be a problem when opening the inner cryostat or pumping it. Furthermore two pump ports are installed, one KF-40 port on the high pressure part of the gas panel and one CF-40 port on the low pressure part. The gas panel was completely pumped and baked to about 10^{-6} mbar at 150°C. The residual outgassing gas was checked with the RGA. As shown in fig.3.13, the major contributions are from hydrogen ($m = 2$ amu), oxygen ($m = 16$ amu), water ($m = 17, 18$ amu), nitrogen ($m = 28$ amu) and CO_2 ($m = 44$ amu).

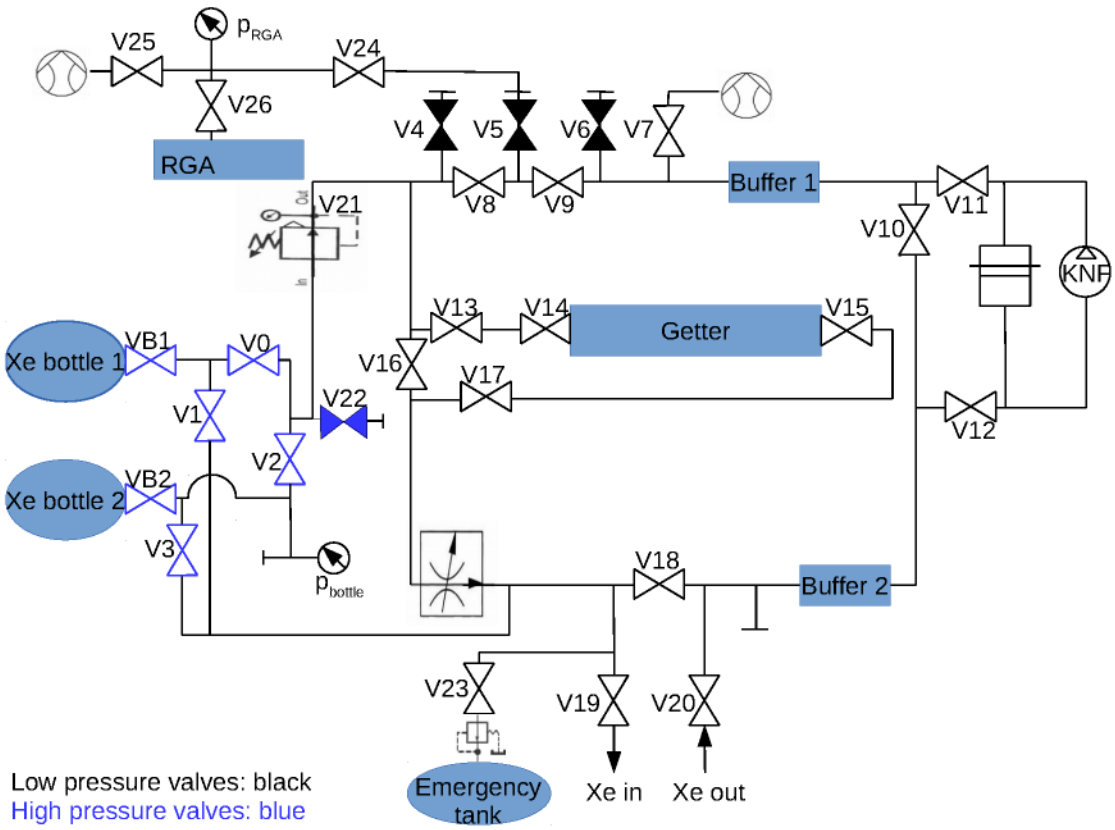

FIGURE 3.10: Flow chart of the gas panel.

The panel accommodates two gas bottles for storage, with a maximum capacity of 2×51 kg (currently ≈ 11.5 kg). The storage bottles are Al-bottles with CGA-580 valves [37]. Both are suited for cryogenic applications, what is important because the Xenon gets recuperated from the cryostats by cryogenic pumping by cooling the storage gas bottles with LN2 until the Xenon freezes out. The maximum pressure in the high pressure part is 200 bar. The gas bottles are freely suspended on weight bridges to monitor the gas inventory. A pressure sensor is installed in the high pressure part of the panel, which is used for monitoring and control of the filling and recuperation processes. A pressure

FIGURE 3.11: Photo of the gas panel. 1: gas bottle 2, 2: pressure gauge for p_{cryostat}, p_{hp}, 3: pressure reducer, 4: vacuum pump port KF-40, 5: flow controller, 6: getter, 7: recirculation pump (behind the panel), 8: gas lines to the experiment, 9: displays (l. to r.: scale bottle 1, flow, scale bottle 2, p_{cryostat}, p_{hp}), 10: RGA.

reducer connects the high pressure part with the low pressure part of the gas panel (see fig.3.10).

Besides gas storage, the gas system is used to purify the Xenon. Due to outgassing and residual gas the Xenon would be contaminated with impurities that than reduce the electron lifetime (sec.3.9.2, page 119), the attenuation length of the scintillation light and the dielectric strength. The purification is done with a hot getter [99], which filters the impurities (non noble gases) down to a sub-ppb level by bonding them on a hot metal (Zr) surface. The gas is circulated through the getter with a KNF neoprene diaphragm pump (PM28544-022). Since the maximum flow through the getter is limited to 3 SLM and the recirculation yields to a heat influx into the detector, a flow controller and monitor

is installed as well (Teledyne Hastings HFC-302 [111]). The Xenon is taken from the cryostat in liquid form (sec.3.5, page 82), which evaporates in the line to the pump and gets then pumped through the getter, after that it will condense and liquefy on the cold finger again. A valve (V18, see 3.10) allows for a bypass mode reducing the flow through the inner cryostat itself while keeping the recirculation flow through the getter constant.

Fig.3.10 shows a flow chart of the gas panel. Standard scenarios were developed for the purification mode, recuperation mode, filling, emergency recuperation and pumping and baking of the gas panel. During normal filling and recuperation the gas is always passed through the getter but this is bypassed during emergency mode to allow for a fast as possible recirculation.

The standard operation pressure of the system is between 1 bar and 2.5 bar. In case of cooling failures the pressure in the inner cryostat rises fast. A too high pressure would damage at first the KNF pump (4 bar) and then the PMTs (5 bar–6 bar [157, 160]). To prevent the system from damage, an emergency catch system was installed. It is sketched in fig.3.12. It consists out of two big stainless steel gas tanks ($0.33 \pm 0.01\,\mathrm{m}^3$) that are connected with the gas panel via a back pressure regulator, used as blow off valve (Swagelok KBP1F0A4A5A20000, [217]), behind a normal diaphragm valve. The back pressure regulator opens at a set pressure and closes again when the pressure on the inlet side drops below this pressure. It was calibrated (with N_2 against the high pressure gauge) and set to open at (3.7 ± 0.1) bar. The system was tested to be stable for various pressures on the outlet side (catch tank side) and at various temperatures.

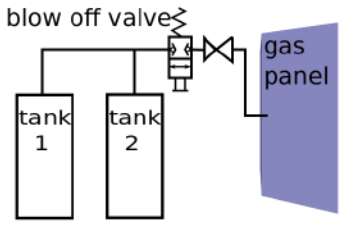

FIGURE 3.12: Sketch of the emergency system with its two tanks, the back pressure regulator used as blow off valve and the normal diaphragm valve.

3.3.2 Gas analysis

The gas analysis station (see fig.3.11 and 3.10) consists of a RGA, which can be used for leak tests and residual gas analysis. It is attached on the valve V5 port on the gas panel and consists of a regulation valve, a sample chamber, a pressure sensor (Pfeiffer PKR251 [228]), a dedicated pump station (Pfeiffer Hicube 80 Eco [229]) and the RGA[3]

[3] A RGA is a quadropol mass filter with a detector, which is here a Faraday cup or a electron multiplier.

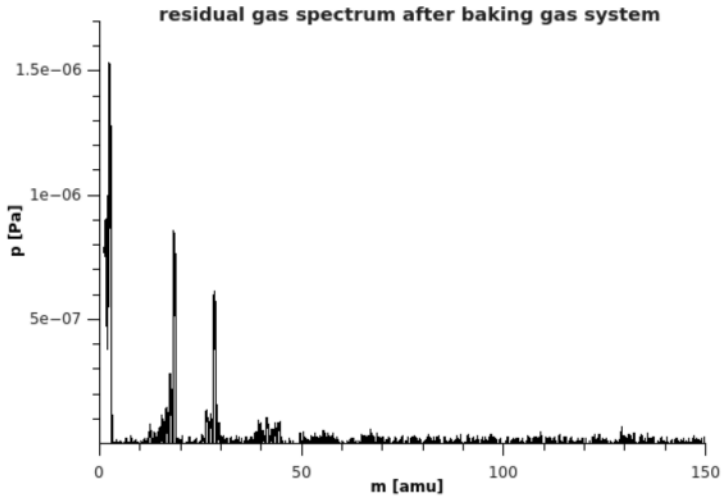

FIGURE 3.13: Mass spectrum of the residual gas in the gas panel after backing. The residual gas comes mainly from outgassing and shows major contributions from hydrogen ($m = 2$ amu), oxygen ($m = 16$ amu), water ($m = 17, 18$ amu), nitrogen ($m = 28$ amu) and CO_2 ($m = 44$ amu).

itself (Extorr X200M [124]). The gas analysis station was carefully cleaned with acetone, ethanol and water, pumped and baked before the initial use ($\mathcal{O} \leq 10^{-7}$ mbar and 200°C) and baked and pumped before every use. The sample chamber itself has a volume of ≈ 0.35 l and is separated by an all metal angle valve from the RGA chamber, which has a volume of again ≈ 0.3 l. This allows to be used as a pipette by repeatedly pumping the sample chamber and flooding it again with the sample gas in the volume between V5 and the regulation valve. The so found gas concentrations are more a qualitative measure because the exact volumina coefficients are not well enough known. The resolution of the RGA is better than 0.5 amu and the minimal detectable partial pressures are $4 \cdot 10^{-12}$ mbar with the Faraday cup detector[4] and $4 \cdot 10^{-14}$ mbar with the electron multiplier[5] as detector. The RGA is controlled and readout by a proprietary software. Fig.3.14 shows an example mass spectrum of contaminated Xenon. The peaks at 2 amu are mainly from H_2, 16 amu from water, at 28 amu from N_2 and CO, at 45 amu from CO_2 and the peaks around 130 amu are from the Xenon itself.

[4]An Faraday cup is metal cup with charge detector.
[5]An electron multiplier is a vacuum tube that uses multiple electrodes to amplify the initial charge.

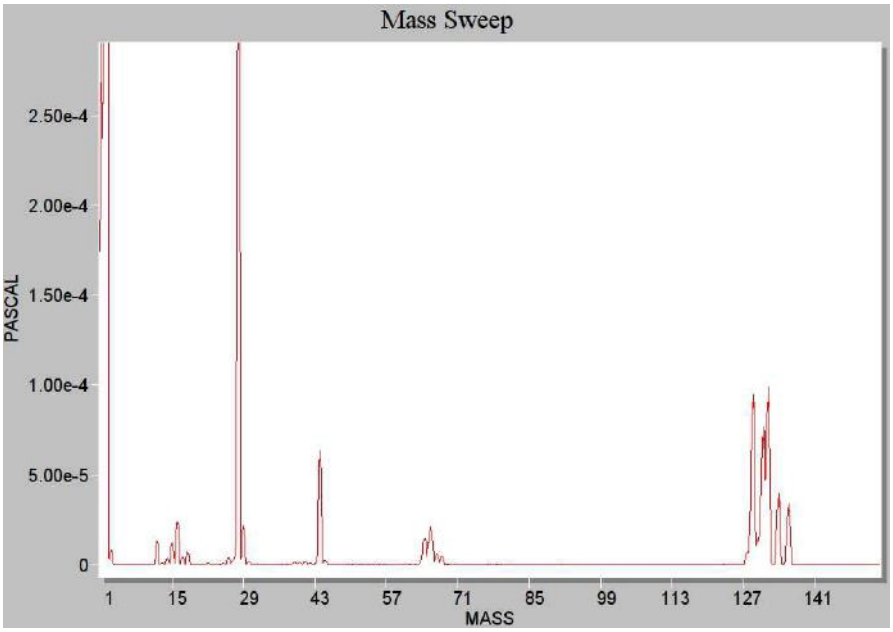

FIGURE 3.14: Mass spectrum of the Xenon after washing the anode with LXe. The Xenon was not circulated through the hot getter at this point. The mass is given in amu. The major contributions come from hydrogen (m = 2amu), oxygen (m = 16amu), water (m = 17, 18amu), nitrogen (m = 28amu), CO_2 (m = 44amu), Hydrocarbons (together with $m = \{27, 28, 28, 41, 43\}$amu around m = 60amu) and Xenon (around m = 130amu).

3.4 Instrumentation and slow control system

Various sensors and devices are necessary for the controlling, monitoring and operation of the TPC, cryogenic system and gas handling. The sensors and devices regulating the operation of the cryogenic system and the gas handling are described in sec.3.2 (page 65), sec.3.3 (page 70) and table 3.1 in more detail. The monitoring of the system is done with a slow control system[6] that is described in [238] and its development by P. Zappa is shown in [237].

The cryogenic system is operated mainly manually with the help of a set of sensors being installed inside the inner cryostat or in the TPC itself. The only automated procedures are the temperature control of the cold finger and the flow regulation of the recirculation flow. They also regulate the pressure in the inner cryostat. The operation of the TPC (and other installable detectors) can be divided into three major phases:

1. Filling the TPC: starting with the warm system until having filled the TPC with LXe.

[6] A slow control system monitors and controls all variables being relevant for the detector operation and that are readout slowly compared to the data taking process of the physical variables of the experiment itself.

2. Operating the TPC: keeping the cryogenic conditions in the inner cryostat as stable as possible during running the TPC (data acquisition, physics measurements).

3. Recuperation: recuperating the LXe and warming the TPC up again.

Fig.3.15 shows one example of a complete measurement cycle containing all three phases, starting with the cooldown of the cryostat, filling LXe, keeping the system stable for physics measurements, recuperating the Xenon over the weekend and refilling, another physics measurement and final recuperation of the LXe.

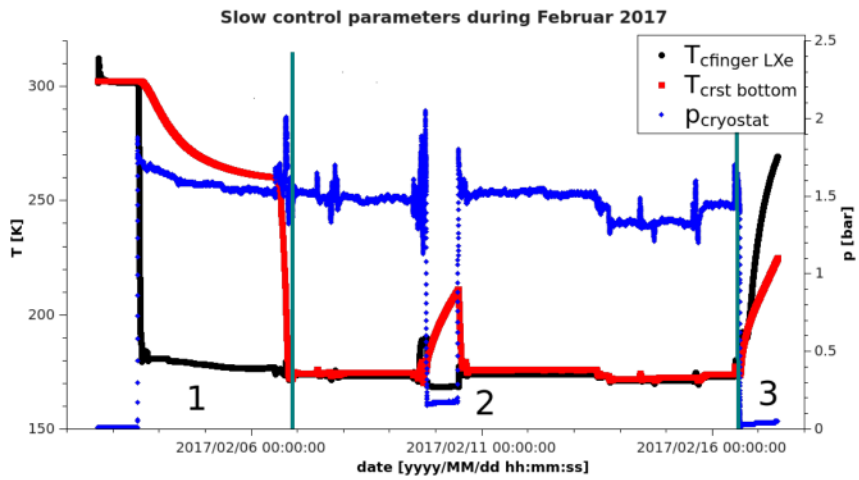

FIGURE 3.15: Most important slow control parameter (see tab.3.1): $T_{\text{cfinger LXe}}$, $T_{\text{crst bottom}}$ and p_{cryostat}. The different phases are tagged. The pressure changes are caused by manipulations of the recirculation flow, filling more Xenon or recuperating it. The system was recuperated over the weekend, 2nd February to 18th February. The plot covers a period of $\approx$ 16 days.

Filling and recuperation of LXe Phase 1 and 3 are most critical since the system is operated out of thermal equilibrium. Normally one starts the filling process with a warm system. Nevertheless, it turned out that pre-cooling (cooling the system before with gaseous Xenon or already a small amount of liquid) yields to a faster filling and a more stable operation depending on the time the system is kept cold (more parts get closer to thermal equilibrium). The best results were achieved by filling the system in three stages. The first stage is the pre-cooling stage when the system gets cooled down to a bottom temperature of the inner cryostat of around 260 K with about 1.5 bar Xenon gas ballast. This takes around 2 to 6 hours, depending on the gas pressure, LN2 filling efficiency and thermal coupling of the cold lines. Afterwards one keeps the system cold at these thermal conditions over night. Followed by filling a few hundreds grams Xenon, thus filling some LXe. Normally this takes about 1 to 3 hours depending on the temperature and amount of filled Xenon. The system is then kept either for at least one day in this stage containing the LXe or it gets recuperated (e.g. case of necessary interruptions) but keeping the

system cold. When starting the complete filling, most components are then already cold, thus less heat needs to be transported out of the system and the components are less stressed due to thermal contraction (especially PMTs). During the filling (phase 2), the system is operated at a higher pressure than during normal running operation (phase 2) and thus at a higher pressure than in thermal equilibrium because the boiling point rises with the pressure. This is necessary to achieve an efficient liquefaction, increasing the amount of LXe in the cryostat. After starting filling, a quasi thermal equilibrium will establish, allowing to fill nearly without any manual intervention at around 1.5 to 2 SLM. The last critical part of the filling operation is closing the gas supply because the system has to establish a new thermal equilibrium without the heat influx from the in-flowing gas. Sometimes some manual intervention becomes necessary at this point (heat influx via recirculation, starting heating before the PID loop would kick in, etc.) because the PID loop would not regulate the temperature fast enough or lacks dynamic range for a proper regulation.

The recuperation (phase 3) works straight forward: additional heat influx is necessary to evaporate the LXe. Since the regulation heater on the cold head is not sufficient for this task (see sec.3.2, apge 65), two additional heaters are installed: on the CF-40 flange, in which the cold finger is installed, with 25 W and on the bottom of the inner cryostat with 100 W heater power. Beyond that, operating all three heater yields to a more homogeneous heating, which lowers temperature differences inside the TPC, thus minimizing thermal stress, which then allows for a faster recuperation. The two extra heaters are manually driven and run at constant power. The recuperation gas flow scheme is described in sec.3.3 (page 70). The recuperation is normally done through the getter. It needs to be taken into account that the gas flow is limited by the gas lines cross section and corners to below 3 SLM at a pressure gradient of 1.8 bar. Higher flow rates can be achieved using the recirculation pump or further increasing the pressure gradient. The Xenon gas is pumped into the storage gas bottles that are cooled with LN2, such that the Xenon freezes out.

The filling and recuperation phases are monitored with a long levelmeter (LLM) that measures the liquid Xenon level in the inner cryostat with a sensitive range of 138 mm [55], starting around 108 mm above the bottom of the cryostat. It has a total uncertainty of 0.3 mm while its statistical fluctuation is much smaller thus allowing for an even more precise relative measurement of the filling level. The TPC is filled completely in dual-phase mode when reaching ≈ 83 mm on the LLM. The readout of the levelmeters (short and long) is done with two UTI development boards [207] and reference capacitors that are specially selected for a low temperature dependence (for a detailed description see [55]). The readout was fully embedded in the slow control system. The temperature in the box housing the UTI chips and reference capacitors is monitored as well, allowing

for a temperature dependent correction of the measured capacitances and thus liquid levels as described in [55]. The levelmeters were designed and calibrated by R. Berner as described in [55].

Operating the TPC In phase 2, the system is controlled by the PID loop of the heater and the recirculation flow. The system is requested to run stable within tight boundaries that depend on the physics measurement that is performed, e.g. within $\Delta T_{\text{coldfingerLXe}} \leq \pm 0.1\,\text{K}$ to keep the gas pressure p_{cryostat} stable with fluctuations below 0.01 bar for TPC performance measurements, as shown in sec.3.8 (page 103). The recirculation flow is controlled with a Teledyne Hastings HFC-302 flow controller that also measures the gas flow. Intervention is only necessary when changing the heat load, so changing the liquid level or the recirculation flow drastically. Fig.3.16 (page 78) shows one example of the fluctuation of the most important detector operation parameters. Typical fluctuations, when not intervening manually, are in the range of $\pm 0.02\,\text{K}$ for the temperature on the cryostat bottom, $\pm 0.08\,\text{K}$ for the temperature in the weir (sets the liquid level in the TPC, see sec.3.5; page 82), $\pm 0.02\,\text{K}$ for the cold head LXe side temperature, $\pm 0.25\%$ for the heater power, $\pm 0.01\,\text{K}$ for the upper cold head temperature, $\pm 0.15\,\text{SLM}$ for the recirculation flux, $\pm 0.05\,\text{mm}$ for the liquid level (LLM) and $\pm 0.01\,\text{bar}$ for the cryostat pressure.

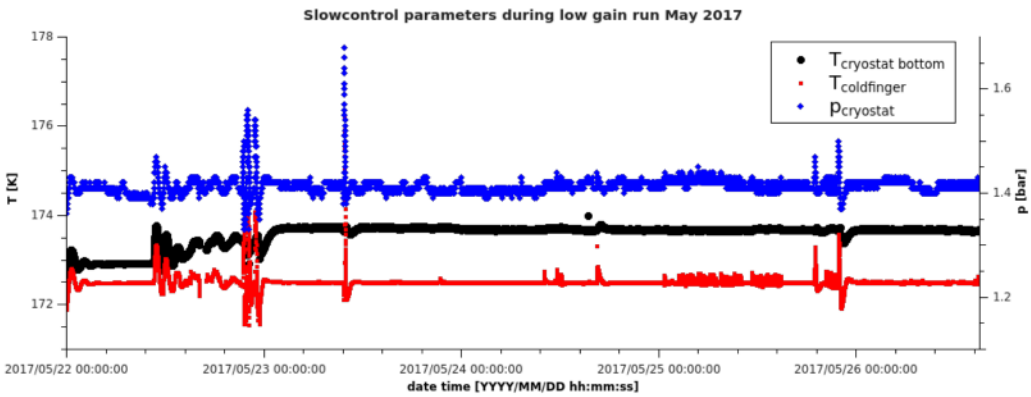

FIGURE 3.16: Most important slow control parameters (Temperatures in the cryostat and pressure) representing the measurement stability during the data taking for a measurement run ("low gain run", described in detail in sec.3.9, page 111). The measurement errors on the values are not shown since they would be too small to be seen anyhow (see sec. 3.4). The plot covers a period of ≈ 5 days.

Instrumentation To collect all the necessary operation parameters, the TPC and cryostat (sec.3.5; page 82) were equipped with various sensors. Their signals are guided through PTFE insulated cables (non coaxial and RG196 coaxial cables), which are coupled with MMCX plugs to a FEP insulated ribbon cable and guided through a multipin 10pin feedthrough [148]. The temperature sensors $T_{\text{cfinger LXe}}$, $T_{\text{cfinger LN2}}$ and the heater

on the cold finger are described in sec.3.2 (page 65). The TPC itself is equipped with two PT100 sensors: $T_{\text{cryostat bottom}}$ on the bottom of the filler, measuring the temperature of the medium on the bottom of the cryostat and the T_{weir} sensor that sits on the bottom of the weir giving an idea about the temperature gradient over the TPC and whether some LXe is in the weir. Furthermore, the TPC has two LEDs installed, which are used for the PMT gain calibration as described in sec.3.5.2 (page 87).

The TPC $x-y$ (horizontal) plane is not precisely aligned with the top flange of the inner cryostat (about ± 0.5 mm). To achieve a homogeneous S2 amplification (see sec.1.2.2, page 13) and response over the whole TPC $x-y$ area, it is necessary to align the anode electrode with the liquid level. This is done by tilting the TPC over a tilt adjustment system, which holds the outer cryostat on three points where each point is individually height adjustable. The tilt adjustment system allows for adjustments down to about 0.04°, corresponding to about 7 μm height difference across the TPC. This is limited by the used normal M6 screws. The tilt of the TPC against the liquid level is measured with three short levelmeter (SLM) that are installed on the axis of the tilt adjustment system points to the center [55]. The SLM have a sensitive range of 11 mm at an absolute precision of 0.1 mm while again the relative uncertainty is much smaller. The levelling process during one measurement run (described in sec.3.9, page 111) is shown in fig.3.17. The TPC tilt was adjusted successfully during that run to about $\leq$ 0.4 mm at the SLM positions (below 0.5°, depending on the tilt axis). A more precise tilt adjustment is possible letting the liquid surface calming down (waves).

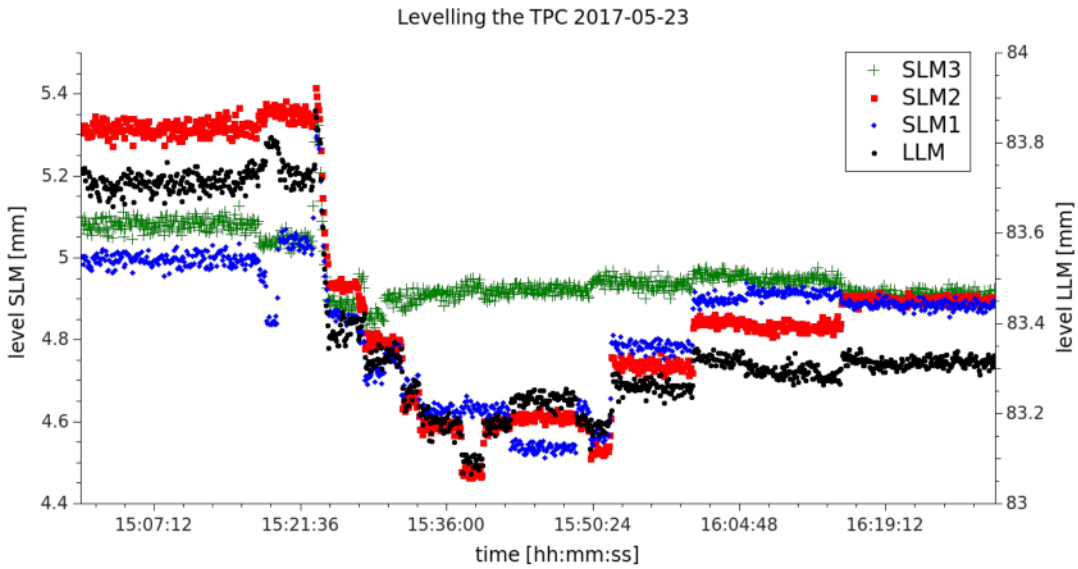

FIGURE 3.17: Levelling process as performed with the level adjustment system during the low gain run (see sec.3.9, page 111). The three short levelmeter SLM1, SLM2 and SLM3 and the long levelmeter LLM are shown. The step structure is originated by adjusting the mechanical tilt adjustment system.

All the before mentioned sensors were implemented in the Doberman slow control system [238] that was developed by P. Zappa and L. Bütikofer. Several plugins were developed for the devices reading the detector operation variables or doing the detector control (e.g. the CryoCon 22C, see sec.3.2 (page 65) and 3.3 (page 70) for more details). Table 3.2 lists the devices registered in Doberman for monitoring and control of the detector operation.

variable	description	unit	sensor	device (table 3.2)
$T_{\text{cfinger LXe}}$	cold finger temperature LXe side	K	PT100	2
$T_{\text{crst bottom}}$	cryostat bottom temperature	K	PT100	2
$T_{\text{cfingerLN2}}$	cold finger temperature LN2 side	K	PT100	1
P_{heater}	power of the heater	%	CryoCon 22C	2
p_{cryostat}	pressure in the inner cryostat	bar	PX302 100AV)	8
p_{HP}	pressure in the high pressure line	bar	PAA23-C-400	9
p_{vacuum}	isolation vacuum pressure	mbar	Pfeiffer TPR 280	10
T_{weir}	temperature in the weir	K	PT100	1
T_{lab}	lab temperature	K	NTC	6
T_{UTI}	temperature in the UTI box	K	PT100	1
l_{LLM}	liquid level in the LLM	mm	LLM	4
C_{LLM}	capacitance of the LLM	pF	LLM	4
l^1_{SLM}	liquid level in the SLM 1	mm	SLM 1	5
l^2_{SLM}	liquid level in the SLM 2	mm	SLM 2	5
l^3_{SLM}	liquid level in the SLM 3	mm	SLM 3	5
C^1_{SLM}	capacitance of the SLM 1	pF	SLM 1	5
C^2_{SLM}	capacitance of the SLM 2	pF	SLM 2	5
C^3_{SLM}	capacitance of the SLM 3	pF	SLM 3	5
U^{set}_{cathode}	set voltage of the cathode	V	CAEN N1470	11
U^{set}_{anode}	set voltage of the anode	V	CAEN N1470	11
U_{cathode}	voltage applied to the cathode	V	CAEN N1470	11
U_{anode}	voltage applied to the anode	V	CAEN N1470	11
I_{cathode}	current drawn by the cathode	μA	CAEN N1470	11
I_{anode}	current drawn by the anode	μA	CAEN N1470	11
F	Xe gas flow (eg. recirculation)	SLM	Hastings HFC-302	3

Table 3.1: Slow control variables with their sensors (sensor placement), unit, reading device (see table 3.2) and meaning.

Table 3.1 summarizes the accumulated and measured variables with their meaning, sensor placement and measurement unit. For each variable a value range was defined in Doberman and in case of critical parameters, like the cryostat pressure, a two stage alarm system was activated (1st level: warning via email, 2nd level alarm via SMS). The alarm and warning settings were adjusted depending on the set points, the 3 operation phases and on the detector conditions. In principle also the PMT high voltage could be monitored but the LAN and the RS232 port of the used CAEN main frame were broken, thus a readout of the CAEN A1535 was not possible.

no	device	description	readout variable
1	Oxford temperature monitor	monitors 3 temperatures from PT100 or PT1000 sensors	T_{weir}, T_{UTI}, $T_{\text{coldfingerLN2}}$
2	CryoCon 22C cryogenic controller	monitors and controls the most important cryogenic detector variables	$T_{\text{coldfingerLXe}}$, $T_{\text{cryostat bottom}}$, $T^{set}_{\text{coldfingerLXe}}$, P_{heater}
3	Flow controller Teledyne Hastings HFC-302	monitors and controls the gas flow (recirculation but also filling and recuperation gas flow)	F
4	long levelmeter LLM	monitors the LLM	C, l
5	short levelmeters SLM	monitors the 3 SLM	C_1, l_1, C_2, l_2, C_3, l_3
6	lab temperature sensor TemperNTC	T_{lab}	
7	LN2 cooling Labjack	monitors the Teragon LN2 controller; LN2 sensor status and LN2 refill valve	$LN2_{\text{valve}}$, $LN2_{\text{sensor}}$
8	pressure iseries omega PX302 100AV	monitors the pressure in the inner cryostat	p_{cryostat}
9	high pressure iseries omega PAA23-C-400	monitors the pressure in the high pressure line of the gas panel	p_{HP}
10	insulation vacuum pressure Pfeiffer PTR 280	monitors the insulation vacuum pressure in the outer cryostat	p_{vacuum}
11	high voltage power supply CAEN N1470	monitors the HV bias for the TPC electrodes; setting, voltages and currents of the unit	U^{set}_{cathode}, U^{set}_{anode}, U_{cathode}, U_{anode}, I_{cathode}, I_{anode}
12	Live remote monitoring supervision	monitors the status of the Doberman system from a remote side	

Table 3.2: Devices used to readout the instrumentation of the test platform.

3.5 Time projection chamber

The here presented time projection chamber (TPC) is currently installed in the Bern LXe test platform, although the cryostat can also be used with different detectors (done before, e.g. 3"PMT test platform, levelmeter calibration [55]). It was designed by M. Schumann and build by the LHEP workshop. It is a classical dual-phase TPC, which will be modified later to be operated as a single-phase TPC. Fig.3.18 shows a CAD illustration of the TPC with its most important components. The TPC is deployed from the top flange of the inner cryostat. The horizontal plane goes in $x - y$ direction (with the 0 origin in the middle of the center PMT) while the vertical axis is the z axis of the TPC (origin for TPC signals at the LXe surface). The dimensions of the TPC are shown in fig.3.19.

The TPC has an active volume of $\approx 1.5\,\mathrm{l}$ ($(\oslash 7.6 \times 6.8)\,\mathrm{cm}$) that starts above the cathode and ends on the liquid surface, respectively the anode in the single-phase mode with about 2.1 l. That means 5 kg or 6 kg Xenon are needed to fill the TPC, respectively. A cut through the CAD model of the TPC is shown in fig.3.18c. The inner wall is a PTFE tube, covering the entire side wall to increase the light yield (PTFE as VUV reflector, see as well chapter 2, page 19). The bottom opening is almost completely covered by the active area of the bottom Hamamatsu R11410-21 PMT while the base plate of the top PMT array is build of PTFE again, to furthermore increase the reflective surface inside the TPC. The only none reflective parts are the rings holding the cathode, gate and anode and their meshes, which are made of stainless steel (SS). Other materials used for parts, which are not in contact with the active TPC volume, are copper, PEEK(screws) and Torlon (screws, mount plates for the levelmeter). In the inner cryostat all cables are either Kapton-, PTFE- or FEP-shielded (or as dielectric): various RG HF cables [122], various AWG Accu-Glass single core or multicore cables for HV applications [5], PTFE-insulated cables, FEP-insulated ribbon cables and blank copper wires. All cables and materials were chosen to show a low outgassing, resistance against LXe as solvent and ability to work between $-200°$C and $+20°$C (for tests with LN2). The instrumentation and cabling is described in sec.3.4 (page 75). The TPC was assembled and cleaned (water and ultrapure ethanol) in the clean room to avoid a contamination with dust and dirt as far as possible. A photo of the TPC after assembly is shown in fig.3.20a.

There are two supply lines for the handling of the LXe ending in the inner cryostat (see sec.3.2, page 65): one guiding the in-flowing Xenon gas above the cold finger and a second one, the outlet, ends in a weir (described below). The Xenon will then condensate on the cold finger and drop down, what would result in a inhomogeneous cooling of the TPC. Therefore a SS funnel was installed above the TPC (see fig.3.20b). The liquid is guided via a PTFE pipe to the bottom of the inner cryostat. The liquid height in

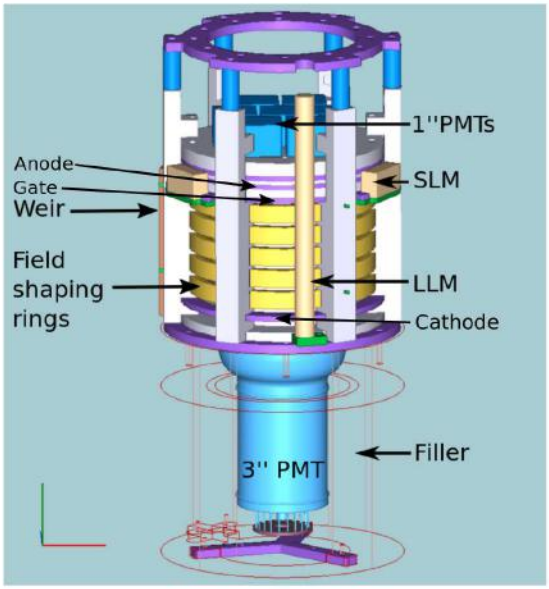

(A) Side view of the TPC (CAD).

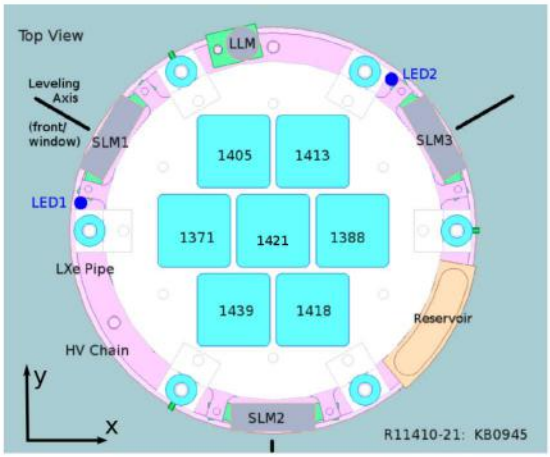

(B) Top view of the top of the TPC. Shown is the top 1"PMT array with their serial no.(blue squares with number) and the calibration LED positions.

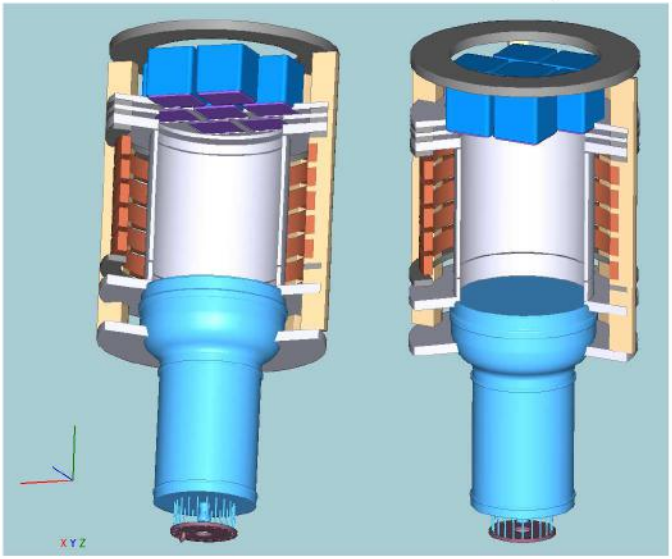

(C) CAD cut through the TPC.

FIGURE 3.18: The TPC CAD model. Shown are: bottom PMT (light blue), bottom filler around the bottom PMT (opaque), top PMTs (light blue), long levelmeter (LLM, dark yellow), field shaping rings (light yellow), short levelmeter (SLM, greyish-yellow), PTFE parts of the TPC body (white), cathode (2nd lower violet ring), gate (3rd violet ring), anode (4th violet ring), the weir (reservoir) and the top PMT array mount structure (top violet ring on blue spacers).

the TPC is regulated with the help of a weir (Torlon), which means the liquid height is fixed during operation and can only be changed opening the cryostat. It keeps the liquid surface height constant between the gate and anode. The recirculation (see sec.3.3, page 70) sucks the Xenon out of that reservoir that thus reduces the mechanical impact on the liquid in the active volume.

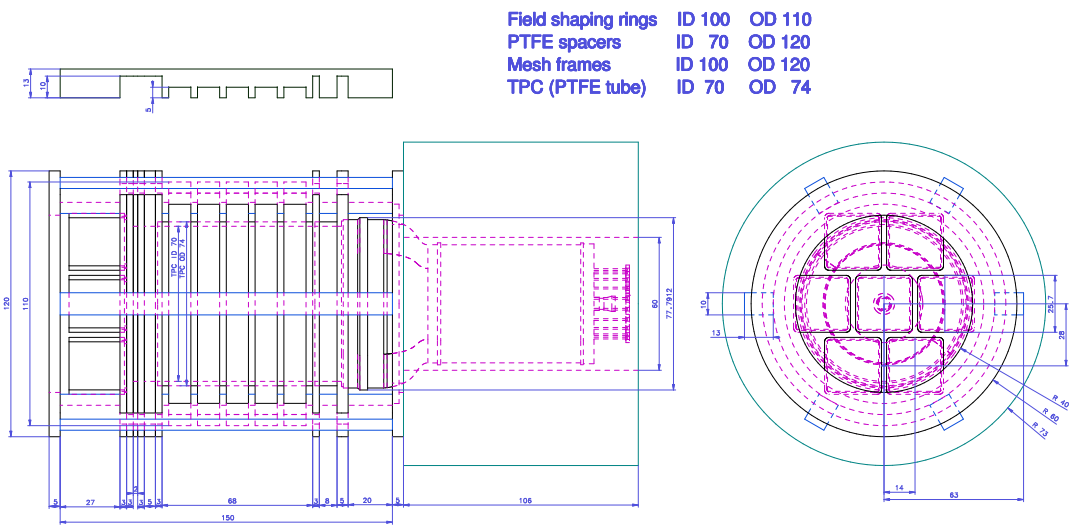

FIGURE 3.19: Drawing of the TPC with the most important dimensions.

3.5.1 High voltage system

Two electric fields are necessary for a dual-phase TPC. The first one is the drift field, creating the time resolution between S1 and S2 by separating the electrons from their Xenon atoms after the ionization. The second field is the extraction field, which extracts the drifted electrons out of the liquid detector medium into the gas phase. After the charge extraction, the spatial projection of the event can be reconstructed from the S2 position. A full 3D position reconstruction of the event is possible with the drift time between S1 and S2 (see sec.1.2.1, page 11). The two fields: cathode - gate, gate - anode are generate between meshes. The hexagonal shaped meshes are etched from SS and spot welded on SS rings [87]. They are 0.006" thick and have an opening of 0.1182". The high voltages for both fields are provided with a CAEN N1470 HV supply [64] over a multipin HV feedthrough [149].

The drift field is generated between cathode and gate. The gate is on ground and the cathode gets biased by a negative high voltage. The drift field needs to be as uniform as possible to avoid charge losses by moving charges into the TPC walls. Furthermore it needs to be homogeneous to generate a constant force, guaranteeing a constant drift velocity. Therefore, field shaping electrodes are installed round the TPC volume that deform the original field, making it homogeneous and linear. They are made of copper and hold in place by the TPC's outer pillars. The field shaping rings get biased via a voltage divider chain from the cathode HV. The electrical configuration was simulated and optimized for high linearity and a homogeneous field by P. Zappa [237]. The realized

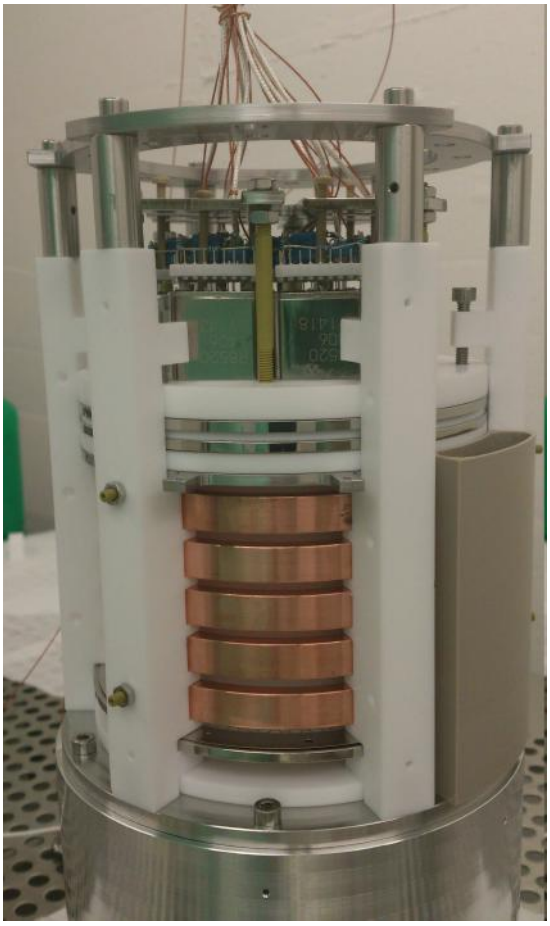

(A) Assembled TPC in the clean room. The Copper field shaping rings and the weir on the right are visible.

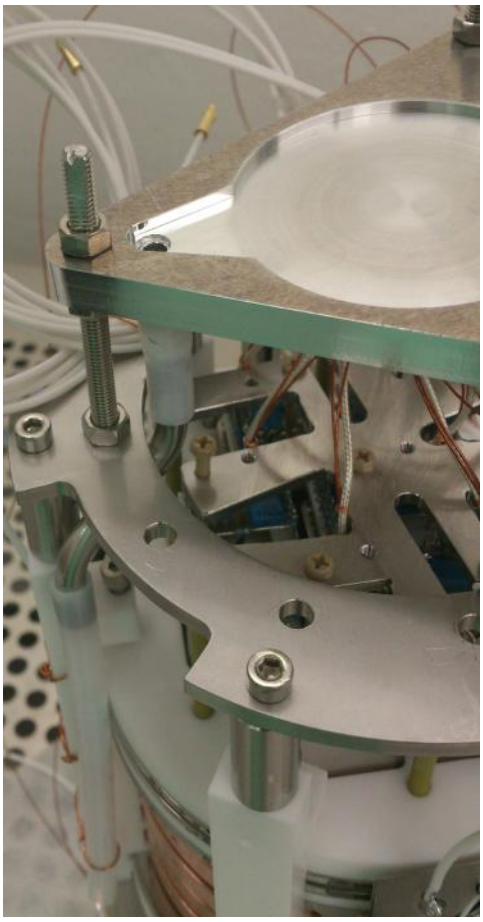

(B) Funnel above the TPC, which collects the LXe and the PTFE pipe that guides the LXe to the bottom of the inner cryostat.

FIGURE 3.20: Photos of the TPC in the clean room during assembly.

HV configuration is shown in fig.3.21. The used SMD chip resistors are soldered between short Cu-wires and cable shoes and placed directly between the rings.

The extraction field HV is applied directly to the anode. The anode is positively biased against the gate and it does not need a dedicated high voltage return channel because no current is allowed to be drawn by the anode. Since the highest bias voltage differences appear from the anode to the gate, the highest field is there. This requires a careful handling of the high voltage parts. Special connectors were developed to supply the anode with HV (see fig.3.23) that aim for maximizing the distance to the gate and avoid sharp edges (reduces the field there and thus reduces the risk of field trips) to reduce the risk of high voltage trips. This is less urgent for the cathode because the fields to surrounding metal parts are lower due to bigger distances to other metal parts.

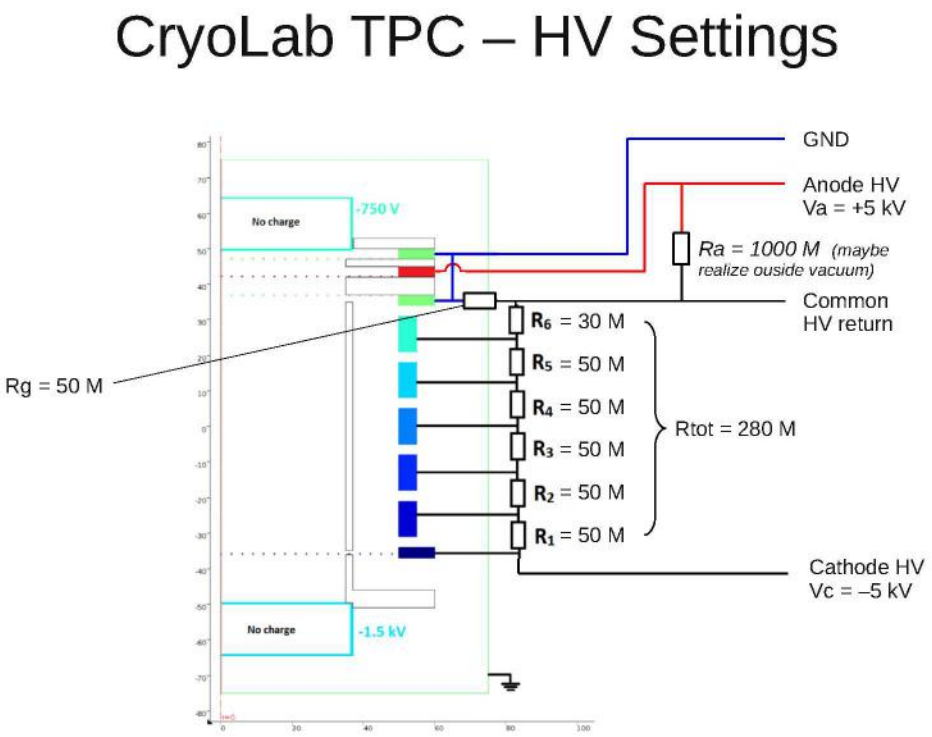

FIGURE 3.21: High voltage configuration of the Bern test platform TPC. The resistor Ra = 1000 M was not realized.

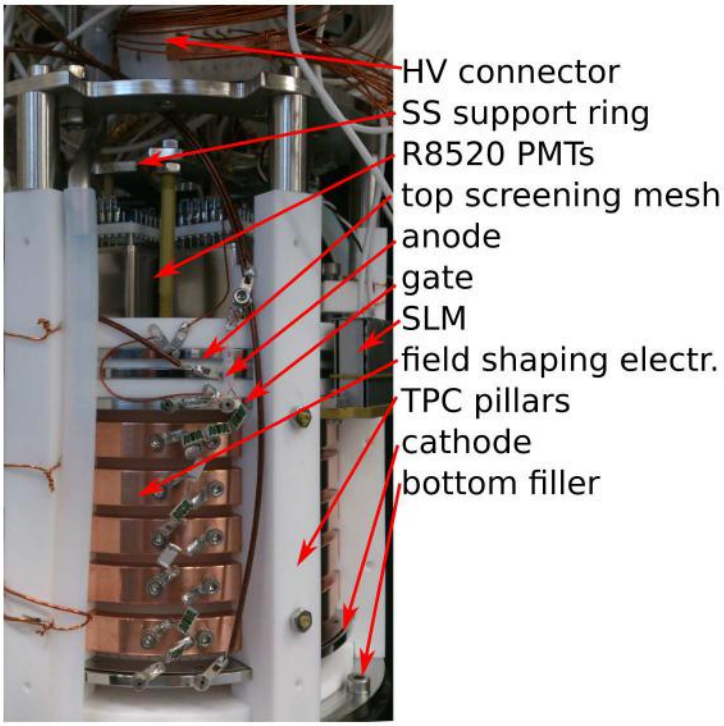

FIGURE 3.22: Photo of the TPC from the side. Visible are the HV installations, anode, gate and cathode rings and the field shaping rings. The photo was taken before the special HV connectors were installed (shown in fig.3.23).

FIGURE 3.23: High voltage connectors (copper parts), specially developed for the anode HV supply. The field shaping ring is about 3 mm thick.

3.5.2 Light sensors

The TPC uses two types of light sensors, a single one on the bottom and 7 smaller PMTs on the top in an array. The bottom sensor is a 3" Hamamatsu R11410-21 PMT, as used in XENON1T [108]. The performance of this type of PMTs was examined before [44]. It has a nominal gain of $5 \cdot 10^6$ at $-1500\,\mathrm{V}$, a quantum efficiency of 26% at 175 nm and was designed to be operated in LXe. The second sensor type in the PMT array is the square 1" Hamamatsu R8520-410 PMT [109]. They were used in XENON100 as well [28] and have a nominal gain of $1 \cdot 10^6$ at $-800\,\mathrm{V}$. Their time response is significantly faster than the R11410. Fig.3.18b shows the top PMT array and surrounding TPC parts. The gain of all the PMTs, used in the current version of the TPC, are characterized in sec.3.8.1 (page 103). While the bottom PMT, with its much higher gain, offers the major sensitivity to S1 and S2 signals and trigger performance, it can not be used for any $x-y$ position reconstruction. The position reconstruction is done with the top PMT array (see fig.3.24). Since the top PMTs are less sensitive (lower gain and looking basically through 3 meshes; top screening mesh, anode and gate, and the LXe surface), they might offer the possibility to enlarge the dynamic range towards bigger signals without lowering the sensitivity of the bottom PMT artificially. A Aluminium filler was placed around the bottom PMT to reduce the amount of Xenon needed to fill the TPC. The top support structure above the top PMT array (SS ring on the TPC pillars in fig.3.22) keeps the PMTs in place. All PMTs are operated with negative high voltage.

The signal cables are RG196 RF cables [122] with MMCX plugs, which connect them with a coax RG196 cabled RHseal feedthrough. The HV supply cables are 30 AWG single core cables with Kapton insulation [5]. Two HV returns are shared between all PMTs, as common PMT HV ground. The high voltage lines are connected via a HV connector (as it is used in XENON1T) to a floating (ground or shield are not connected to the vacuum part of the feedthrough but use dedicated cables) RHseal HV feedthrough. The high voltage divider circuit is of the top PMT array are custom made of PTFE with SS

pins but normal resistors and its design is shown in [237]. For the 3"PMT a XENON1T Cirlex high voltage divider circuit [50] was used.

The PMTs can be calibrated with two blue LEDs (470 nm). LED 1 is mounted above the first field shaping ring and the cathode (as much as possible in the gap to the next ring) and LED 2 is mounted above the second field shaping ring (again as much as possible in the gap to the next ring). Both LEDs are identical (nominal 3 V, 20 mA) and share a common return. They can be operated individually, offering some sort of redundancy and different enlightening of the TPC volume.

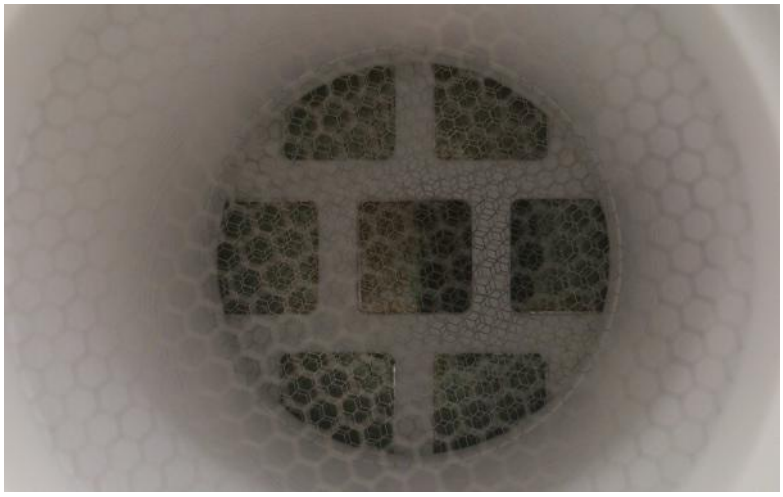

FIGURE 3.24: Photo showing the inner volume of the TPC looking from the bottom up, visible are the meshes of cathode, gate and anode and the top PMT array.

3.6 Data acquisition

The PMTs in the TPC generate signals that need to be amplified, digitized, triggered and recorded. This is done with the so called data acquisition system (DAQ). The PMTs generate a voltage signal depending on the high voltage, gain and photons hitting the PMTs. Table 3.3 shows the gains of the PMTs in the TPC and the applied high voltage and fig.3.25 illustrates the PMT positions within the top array. At the given voltage the PMTs run stable and the gain within the top array should be as homogeneous as possible while being as high as possible. PMT 2 could not be operated stable and PMT 7 showed no signal any more after opening the cryostat. Since the small PMTs should be exchanged anyhow, they were just switched off and not fixed. The goal of the deployment of the cryogenic test platform and first characterization of the TPC is not affected. The high voltage and thus the gain of the R11410 PMT was set such that it shows a maximum gain without saturating the PMT itself and the following DAQ chain. The DAQ handles all PMTs equally.

PMT no	PMT type	serial no.	HV [V]	gain (warm) [10^5]	gain (cold) [10^5]
0	R11410-21	KB0945	1300	20.75 ± 1.41	18.91 ± 0.31
1	R8520-406	LV1405	850	5.88 ± 0.09	6.28 ± 0.99
2	R8520-406	LV1413	850	7.28 ± 19.62	–
3	R8520-406	LV1371	900	3.92 ± 0.22	5.08 ± 0.01
4	R8520-406	LV1421	900	4.24 ± 0.17	5.93 ± 0.02
5	R8520-406	LV1388	900	5.22 ± 0.19	6.87 ± 0.03
6	R8520-406	LV1439	850	6.41 ± 0.16	8.26 ± 0.05
7	R8520-406	LV1418	900	4.88 ± 4.48	–

TABLE 3.3: PMTs as installed May 2017 in the TPC. The PMT number identifies as well the cabling channel on the ADC. The gain in warm was determined at room temperature while the gain in cold was measured with PMT 0 immersed in LXe and the other PMTs in cold GXe. For the PMTs LV1413 and LV1418 no gain is given in cold because they were switched off. The gain is given without an amplifier. The positions of the R8520 PMTs within the top array are illustrated in fig.3.25.

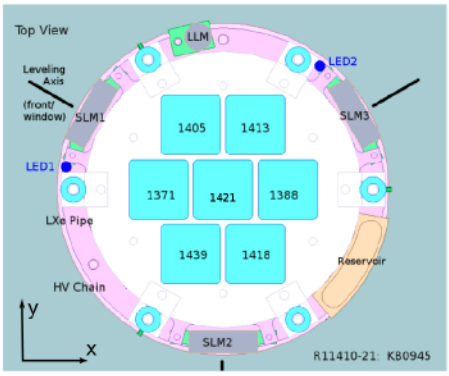

FIGURE 3.25: Sketch of the top view on the TPC with the top PMT array.

The signals from the PMTs get amplified with a NIM 10×gain Phillips 776 16-channel amplifier [203]. Afterwards it gets digitized by a V1724 ADC [65] if a trigger condition is fulfilled. The condition triggering the ADC should allow it to acquire signals ("waveform") at high efficiency but also prevent the system from recording noise. All PMTs share two common floating ground return lines. Due to this setting the large PMT on the bottom picked up noise from the small PMTs because its impedance on the signal way was with $51\,\Omega$ much smaller than the impedance on the signal way of the small PMTs ($12\,k\Omega$). Some electronic noise was picked up radiatively and some noise in the power network was picked up by the PMTs and their HV and signal cables or the HV power supplies. The PMT HV power supply itself contributed to the observed noise as well. The electronic noise conditions varied strongly irregular in time and amplitude. The noise conditions were improved by carefully selecting cables, minimizing cable length, positioning of power supplies, cable placements and the use of ferrites. This yields to low data acquisition thresholds of about 7 mV. Nevertheless, higher thresholds between 13 mV and 55 mV were chosen for stability reasons and to further reduce the amount of digitized data. Since only relatively large signals are expected from the used calibration

sources (Co57 source with 37 kBq and Cs137 source with 185 MBq), this has no large impact on the result.

The ADC can be triggered in two different ways: by a selftrigger or externally (see more details below). This results in each mode in digitizing the signals from all channels set in the channel mask of the DAQ configuration. The signal is continuously digitized and read into an internal ring buffer by the ADC. Due to that a predefined window before and after the trigger can be recorded. The digitized signal is sent via a fibre link to a computer, which reads the signal out. The readout and control is done with a modified version of kodiaq [72] that is was designed for the XENON1T DAQ by D. Coderre (see sec.1.2.3, page 15), where it is used with 32 V1724 ADCs [23]. Kodiaq was modified by D. Coderre to work with a single readout computer and one digitizer only. The signals acquired by the digitizer are written to a database (DB), containing the raw data (mongo DB [169]). Kodiaq creates a new collection for each run. Each document in the collection contains one digitized waveform in a binary raw data format, the start time with respect to the run start time (timestamp of the computer) and the end time with respect to the run start, digitizer channel. The physics conditions and run parameters are stored in a second database, the runs database. It contains informations like the run start, run end, ADC settings, HV settings, detector conditions, source conditions, electric field settings and further comments.

The V1724 ADC is characterized by (giving only the most important properties):

- channels: 8
- dynamic range: 2.25 Vpp
- resolution: 2^{14}bit
- bandwidth: DC to 40 MHz
- sampling rate: 100 MS/s.

Any signal that gets recorded by the ADC and written to the database is called a waveform. It can contains everything from noise, to complete events, single S1 or S2s or baseline only. The document in the database contains the waveform itself with the overhead (start time, end time, channel, ADC identifier).

There are two two different ADC trigger scenarios. The first one is used to acquire TPC data and sets a threshold to start the readout: selftrigger mode, sec.3.6.1. The second one requires an external trigger to start the readout: External trigger mode, sec. 3.6.2. It is used to take LED calibration data or TPC data in a simplified readout scheme. They are discussed in the following.

3.6.1 Selftrigger mode

A signal from one channel is digitized in the selftrigger mode when it exceeds a threshold. The digitized window gets extended until the signal drops below the threshold again. This allows to record very long signals as well. It also reduces the data rate by not digitizing for example empty baselines between an S1 and S2, if the signal dropped again below the threshold. The disadvantage is that a software trigger is necessary later to correlate the signals from the different channels in time to reconstruct the physical event. The advantage is that even very long events from very long drift times can be acquired without exceeding the size of the ring buffer and without digitizing empty parts of the event between an S1 and S2. The selftrigger thresholds were adopted individually per run depending on the used source and electronic noise conditions. They range from as low as 5.4 mV to typically 13.7 mV and up to 55 mV. This mode is the standard mode when not running in LED mode (see explanation of run modes on page 61).

3.6.2 External trigger mode

The external trigger mode is used for the LED calibration and to acquire TPC data (see explanation of run modes on 61). In the external trigger mode all channels set in the channel mask of the DAQ software get readout when the trigger is fired. This ensures that the channels get acquired regardless the signal amplitude. In LED mode the ADC gets triggered by the LED pulse generator and in TPC mode the trigger signal comes from a discriminator. Since the discriminator did not allow for very low threshold settings, the discriminator was fed with a signal being amplified with the 10x amplifier before. The discriminator threshold was set to 400 mV, which means $\approx$ 40 mV for the unamplified signal that was directly fed into the digitizer. Fig.3.26 illustrates the used setting for acquiring TPC data with a discriminator. A pretrigger window and a acquisition window itself can be configured. The acquisition window for LED data was set to 10μs while the LED signal typically occurred after $\approx 1\,\mu$s. For TPC data taking (see explanation of run modes on 61) this would be configured in a way that the full possible drift time is covered. This mode was used for the low gain run presented in sec.3.9 (page 111). For this run 50 μs were acquired covering the full possible drift distance of the Bern test platform TPC (sec.3.5, page 82) and the maximum event length that can be digitized by the V1724 ADC.

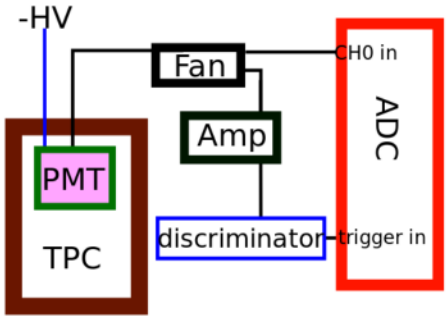

FIGURE 3.26: DAQ scheme using the external trigger mode of the ADC for TPC data taking.

3.7 Data processing

The data in the raw data database (DB) is in a raw data format and handles each PMT equally. Therefore it needs to be processed to be used in a physics analysis: reconstructing the S1,S2 event structure with their characteristic properties. The expected event structure of a physical TPC event is sketched in fig.3.27: an event contains a S1 followed by one S2 or multiple S2s. While this is the normal event structure, an event can also contain S1s without S2s if the charge is lost or if the S2 amplitude is below the threshold. Also lonely S2 events exist due to electrons, which are emitted by ionization of metal parts, impurities or delayed electron extraction [30]. Also the S1 can be too small to trigger the DAQ.

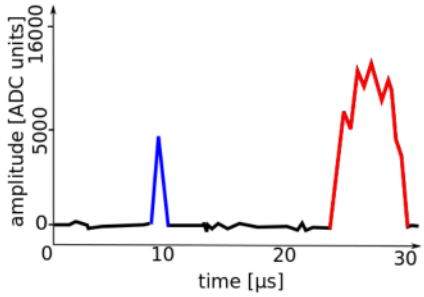

FIGURE 3.27: Sketch of a physical event in TPC mode. The S1 is shown in blue and the S2 in red. Multiple S2 can occur due to scattering of the initial interacting particle (double scatter).

When an event gets recorded in selftrigger mode (sec.3.6.1, page 91), the S1 and S2 can be split into different waveforms (from one channel) and the S1 and S2 can also be observed by different channels since the channels trigger the DAQ individually in selftrigger mode. Thus the S1s and S2s belonging to one event need to be identified by their time correlation. Both problems are solved by a software trigger. The readout scheme is illustrated in fig.3.28

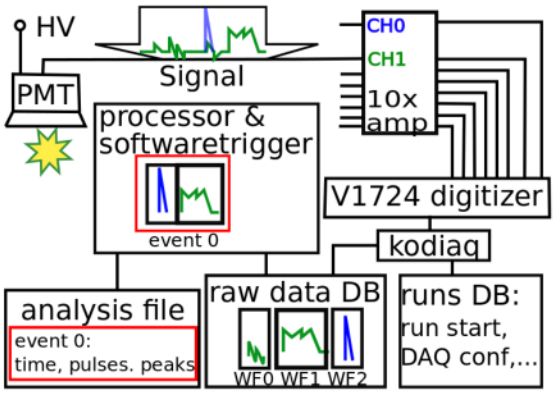

FIGURE 3.28: Sketch of the digitization, trigger and readout scheme and following data storage, software trigger and event builder process acquiring in selftrigger mode TPC data. It shows signals from two different PMTs in blue and green, which appear in the raw data DB in an arbitrary order, get time correlated by the software trigger and their properties get written to the file by the processor.

3.7.1 Software trigger

The trigger reconstructs the events. This is essential for a data processing. In the following "trigger" refers to the software event trigger that reconstructs the event structure and not the selftrigger or external trigger of the ADC. The software trigger is not needed in LED data mode.

It is a multiplicity trigger that looks for waveforms being in time coincidence. It does not consider the information in the waveforms itself (waveform gets not analysed). The event structure with its S1s and S2s can be identified by its time coincidence. It means that a single S1 or S2 being visible in multiple channels can be identified in the different channels because it happens at the same time (± one ADC bin dither). The S1s and S2s of one physical event can be identified by their order, the first signal needs to be a S1, followed by more S1s or none, followed by S2s. This can only be done after peak finding and classification, as described in sec.3.7.3 and it is done by the data processor (sec.3.7.2). Due to delayed charge extraction or double scattering a second S2 (or multiple) can appear as well. Nevertheless, the event is identified as the first S1 and any signal following within the drift time. The following settings configure the trigger:

1. drift time t_D [10 ns]: coincidence time window for the event defined by the maximum drift time, eg. 5000
2. trigger channel list: ADC channels that can trigger an event, eg. [0,1,7]
3. multiplicity m: requires at least a waveform in m channels plus the triggering channels, eg. 2

The used trigger logic depends on the trigger mode of the ADC, so whether the ADC was triggered externally or by its selftrigger threshold:

ADC selftrigger mode The trigger loops in this mode in time order over all waveforms in the raw database, where the channel appears in the trigger channel list (see point 2 in the list on page 93). The default setting is channel 0 because the large PMT is most sensitive for prompt scintillation signals. Starting from this waveform, the trigger selects all waveforms that happened within $\pm t_D$ around the initial waveform. It looks forward and backward in time because the S1 could be missed if the initial trigger came from the S2. If these waveforms are less than required by the multiplicity m (all channels excluding the triggering channel) the event gets discarded. The multiplicity is a strong noise filter because thermal or electronic noise will only seen by the individual PMT. Nevertheless, it turned out that this requirement is rather critical due to the low sensitivity of the small PMTs (low gain and they "look" through three meshes, top screening mesh, anode and gate, plus the LXe surface in dual phase mode). Therefore, the sensitivity can be increased by lowering the multiplicity and accepting more noise as well.

At this point a "potential event" is formed. It contains the initial waveform plus at least m additional waveforms. The time window of the "potential event" gets set by the start time and end time of the first, and the last waveform respectively. Then the trigger checks for further waveforms appearing within $\pm t_D$ around the "potential event". Thus the event can be extended until all waveforms in time coincidence with the event are reached.

Due to the trigger channel list, the same physical event can be reconstructed with this logic by several trigger channels (see point 2 in list on page 93). They get identified by their time structure (overlap) and get merged. Thus the final event contains all waveforms being in time coincidence and fulfilling the multiplicity condition. This logic allows for events larger than the internal buffer of the ADC (see sec.3.6, page 88). The trigger does not consider the content of the waveform itself for performance reasons, thus the drawback is a missing check whether the event structure contains at least one S1 and one S2. Thus an event can lack a proper event structure. When the complete event reconstruction is done, a filter can be applied to the results to get only proper S1 and S2 containing events (see sec.3.8, page 103).

External triggered mode When being triggered externally, the previously explained trigger logic does not work anymore. In this trigger mode a "potential event" in the raw data data base contains already all signals from all channels. They are already in time coincidence with the ADC triggering signal. A multiplicity logic (see point 3 in list on

page 93) is still applied on these "potential events". The DAQ took over the task of acquiring events that span the whole potential event length.

This logic simplifies the timing logic and event reconstruction. It is able to catch small S2s below the selftrigger threshold when having a sufficiently large S1 (can be used to increase the threshold when larger S1 signals are expected). A too small S1 in front of a sufficiently large S2 might still be missed due to the limited pretrigger window. So this logic might introduce as well a potential bias towards bigger S1s when running with a higher discriminator threshold.

3.7.2 Data processor

After the trigger identified an event from the raw data stream, the data processor calculates the parameters of it. One event can contain several waveforms that are in the raw data format in the database when the processor is started. The processor does the waveform analysis: calculation of waveform properties, filtering waveforms, peak finding and classification, measurement of the peak properties and calculation of the event properties. A position reconstruction was implemented in the data processor but it was not used in the analysis so far because the top PMT array showed not a sufficiently good performance for a useful x–y position reconstruction.

Waveform: Any signal in a single ADC channel that gets recorded by the ADC and written to the database with the course of the amplitude over time. It can be anything and does not need to contain any TPC event with S1s and S2s.

Pulse: A waveform gets transferred after the processing into a so-called pulse. It contains the derived properties of the waveform but not the raw electrical signal information, so the course of the amplitude over time. A pulse can contain peaks: a peak is the occurrence of the part of the waveform that fulfills certain conditions (described in sec.3.7.3). The physical pulse properties are described in table 3.4.

Event: An event is defined as set of pulses that are in time coincidence. The properties of an event are summarized in table 3.4. It contains at least m pulses plus the amount of triggering channels.

The processor calculates first the properties of the pulses, starting with a baseline calculation. The baseline can be determined in various ways. All methods described in the following but the *const method* and the *mean method* use a window with fixed length,

the "baseline determination window" at the start of the waveform to determine the baseline. For the LED data, the baseline is recalculated on the waveform section around the expected LED pulse, which is used for the gain calculation to ensure a good baseline quality (integral of the waveform without peaks is about 0, oscillates around zero, as flat as possible) and high efficiency. 4 methods for baseline determination are implemented:

- *const method*: a user configurable constant is taken as baseline.
- *sampling method*: the waveform average of the "baseline determination window" is taken as baseline.
- *mean method*: the mean of the entire waveform is used as baseline.
- *RMS method*: the RMS of the waveform in the "baseline determination window" is calculated first. Then all samples in the baseline window that are more than 0.5% away from the RMS are excluded. The baseline is recalculated as mean of the remaining samples. In very noisy waveforms nothing might remain. In that case the baseline is the RMS of the original baseline window.

Depending on the waveform quality and pretrigger window, one of the methods can be chosen. For waveforms being affected by high frequency electronic (HF) noise over the entire waveform, but with a stable electrical ground, the *const method* is well suited because it is fast and reliable. For low frequency (LF) oscillation on the waveform, deforming the whole waveform rather linearly (e.g. 50 Hz noise from the power network), the *sampling method* would work better. Another way for determining a baseline for HF noise-affected waveforms with a stable baseline is the *mean method* if the ground fluctuates from baseline to baseline. If both HF and LF noise occur within the baseline calculation window, the *RMS method* works reasonably well. It is the standard method for the TPC data analysis presented here because it is pretty robust against noise and works as well for good noise conditions.

Afterwards, filters can be applied on the pulses, filtering them according to conditions on their properties. The currently defined filter conditions are a RMS filter or a bipolar noise filter. The RMS filter passes only pulses, which have a smaller (or equal) RMS than required. The bipolar noise filter works on the waveform itself and filters out bipolar oscillating waveforms. The multiplicity condition is not approved after applying the filter. The bipolar filter was switched off in the analysis shown in sec.3.8 (page 103), since noise reduction methods were applied specifically for each analysis. The RMS filter was applied by default but can be switched off. For the LED calibrations both filters were activated.

The peak finding and integration is performed on the filtered set of waveforms after baseline calculation. It is followed by the peak classification based on the derived peak properties (see sec.3.7.3). The peaks are than added to their pulses. Finally, the event properties are calculated and the event gets written to a serialized pickle file [90].

3.7.3 Peak finding and classification

A peak is a part of the waveform that rises significantly above the neighbouring parts of the waveform. Significantly means a certain height above the surrounding waveform (needs to be determined and configured within the peak finder algorithms) and a steep rising and falling edge. Although there is a common understanding what a peak is, its mathematical description is not straight forward. Two peak types with quite different characteristics appear in a dual-phase TPC: S1 and S2 peaks. Both are sketched in fig.3.27. The S1 originates from the prompt scintillation light, thus a fast signal with short rise and decay time. That means it has a low width compared to its area (integral of the waveform section containing the peak). The S2 peaks are the light signals that are emitted by excited Xenon atoms that were excited by the collisions with the drifted and extracted electrons in the gas phase. They are much broader, have a longer rise and decay time compared to S1s and have often a larger area. The properties of peaks in the data processor are summarized in table 3.5. The peak finder algorithm has to deal with saturation as well: a signal fills the complete dynamic range of the ADC of 2.25 V. The further course of the signal is thus unknown, what impacts the seen shape of the peak and thus its classification into S1 and S2.

The here used peak finder algorithm is called *FastPeakFinder*. It works with a sliding window that scans the waveform and within which the algorithm is looking for significant excesses (defined below) over the surrounding waveform. The thresholds are configurable. The size of the sliding window can be adjusted and determines basically the resolution of the peak finder. The algorithm searches for parts of the waveform exceeding a fixed threshold (typically about 7 mV) within the sliding window. The sliding window gets extended around its local maximum for the length of the height excess of the local maximum (plateau, e.g. in case of saturated peaks). If the previously found local maximum is not the highest one in the new window, the new highest local maximum gets selected by enlarging the sliding window around its position. This local maximum is now called a "potential peak". The potential peak gets checked whether it is saturated, what basically means it covers the whole dynamic range of the ADC. If the peak is saturated, it gets tagged as such and the peak finding is continued at the end of the extended sliding window. The "potential peak" becomes a peak when it exceeds the mean amplitude within the extended sliding window by a user definable significance called relative threshold r,

such that it excesses the mean amplitude by $100\% + r$, or if it exceeds the mean of the complete waveform by $300\% + r$. The significance levels are tuned empirically on a set of a few thousand training peaks.

When a peak is found, its properties get calculated and then it can be classified. In addition to S1s and S2 peaks, another peak-type was introduced in cases where the peak classification was not clear or misleading: so-called "S3 peaks". The used classification algorithm (*BERN3* algorithm) is based on the original XENON1T algorithm [11]. The decision parameters are peak width and area. If a peak has a large area ($\geq$ 10000 ADCunits $\cdot$ 10 ns) at a low width of less than 100 ns it is assumed to be a S1 peak, and if the width is larger than 200 ns it is assumed to be an S2. All other cases with a large area are classified as S3s because the shape with its width to area ratio does not allow a clear identification. They are often S1 clusters that were not resolved. For smaller areas, all narrow peaks below 80 ns are expected to be S1 peaks while all peaks broader than 250 ns are S2s. In case of really small peak areas the S1 width has to be smaller than 50 ns while for S2s it has to be larger than 100 ns. All other cases including peak areas below $\approx$ 1PE are classified as unknown peak type, so as S3.

Fig.3.29 shows examples of different waveforms with the found peaks and the variables calculated by the peak finder and fig.3.30 shows an complete event display. Although the responses of the 3"PMT and the small 1"PMTs are significantly different (the 1" PMTs show a nearly 3 times faster response time [109, 108] while their gain is only about half of the large PMT; sec.3.5), the peak finder and also the peak classifier *BERN3* work for both PMT types.

Peak clusters get identified and merged when the peak finding and calculation of the peak properties including classification is done. The merging is based on a minimum distance between neighbouring peaks (configurable, typically 50 ns). After the merging, the highest peak position becomes the new peak position. The new properties and peak type are recalculated. A second cluster algorithm is applied afterwards. It is only applied for S2 and S3 peaks with a minimal width of 100 ns. It clusters peaks around these peaks and merges them if they are close enough (configurable distance, typically 50 ns). This S2 cluster algorithm catches cases where a S2 is followed by afterpulses or smaller peaks at its tail. It improves the peak classification and recognition of S2 peaks significantly.

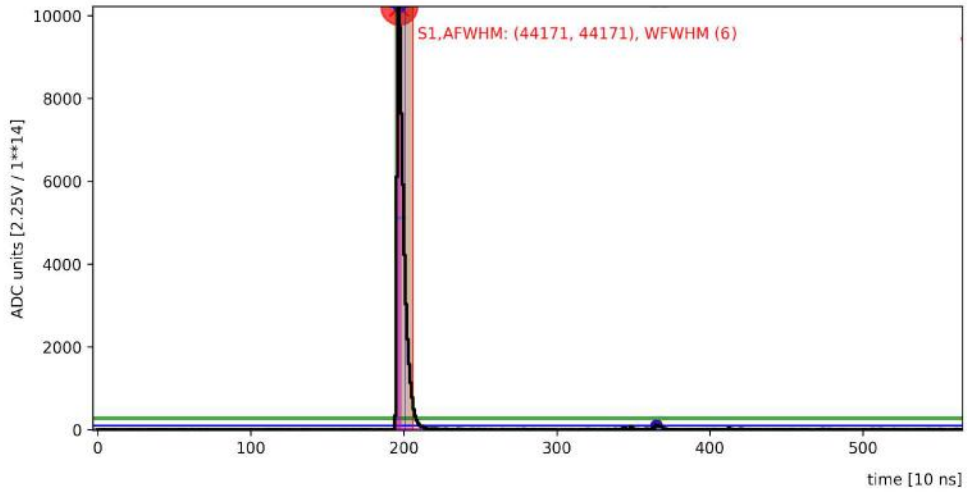

(A) Example of an S1 peak as observed by the large 3" PMT operated at −1300 V in LXe.

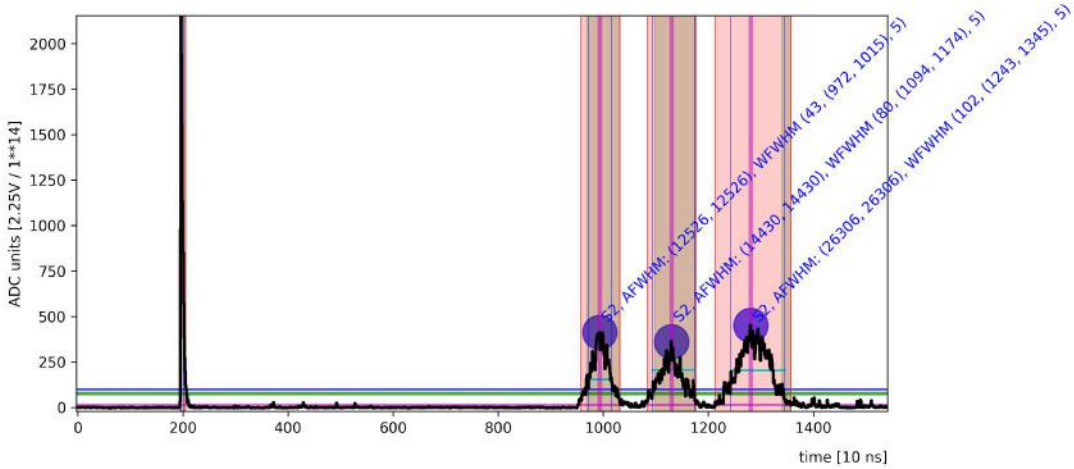

(B) Example of an event with 3 S2 peaks (multiple scatter) as observed by the large 3" PMT operated at −1300 V in LXe.

FIGURE 3.29: Example waveforms after peak finding and processing with tagged peaks, peak width and area as seen by the peak finder and peak width after peak merging. The absolute threshold of the peak finder is shown as blue horizontal line and the RMS of the waveform is shown as horizontal green line.

property	default	definition	unit
event properties			
start time	x	start time stamp of the first pulse of the event, relative to the run time stamp	10 ns
end time	x	end time stamp of the last pulse of the event, relative to the run time stamp	10 ns
raw position		spatial position of the event, weighted with the uncorrected charge	mm
weighted position		spatial position of the event, weighted with the corrected charge	mm
mean position	x	mean spatial position of the event	mm
drift time	x	time between last S1 before the first S2 peak	10 ns
pulse properties			
start time	x	start time stamp of the pulse, relative to the run time stamp	10 ns
end time	x	end time stamp of the pulse, relative to the run time stamp	10 ns
channel	x	ADC channel of the waveform	
area	x	integral of the waveform	10 ns · ADC counts / PE
RMS	x	RMS of the waveform	ADC counts

TABLE 3.4: Most important event and pulse properties defined by the processor framework without extra plugins. If a property is marked as default (def.), eg. FWHM width, all the time the name is not specified more precise this property is meant, as for the width: *width* refers always to *FWHM width*. The unit applies if no other unit is specified. Some properties are available in their raw unit or corrected (eg. gain corrected).

property	def.	definition	set by	unit
peak properties				
position	x	peak position as returned from the used peak finder algorithm within the waveform	peak finder	10 ns
height	x	peak height, baseline to height at found position	peak finder	ADC counts/ $2.25\,\mathrm{V}/2^{14}$ / $137\,\mu\mathrm{V}$
type	x	peak type	peak classifier	
pulse time	x	pulse time of the related pulse	processor	10 ns
FWHM width	x	width defined by the left and right peak edge at half of the peak height	peak finder	10 ns
10% width		width defined by the left and right peak edge at 10% peak height	peak finder	10 ns
90% width		width defined by the left and right peak edge at 10% peak height	peak finder	10 ns
THR width		width defined by the left and right peak edge where the peak rises above a defined threshold	peak finder	10 ns
THR area		area defined by the left and right peak edge where the peak rises above a defined threshold	peak integrator	10 ns · ADC counts / PE
FW area		area within a fixed window around the peak	peak integrator	10 ns · ADC counts / PE
FWHM area	x	area defined by the left and right peak edge at half of the peak height	peak integrator	10 ns · ADC counts / PE
10% width area		width defined by the left and right peak edge at 10% peak height	peak integrator	10 ns · ADC counts / PE
90% width area		width defined by the left and right peak edge at 10% peak height	peak integrator	10 ns · ADC counts / PE

TABLE 3.5: Peak properties defined by the data processor. The properties marked as default (def.), e.g. FWHM width, are always meant if it is not specified differenly, as for the width: *width* refers always to *FWHM width*. Some properties are available in their raw unit or corrected (e.g. gain corrected).

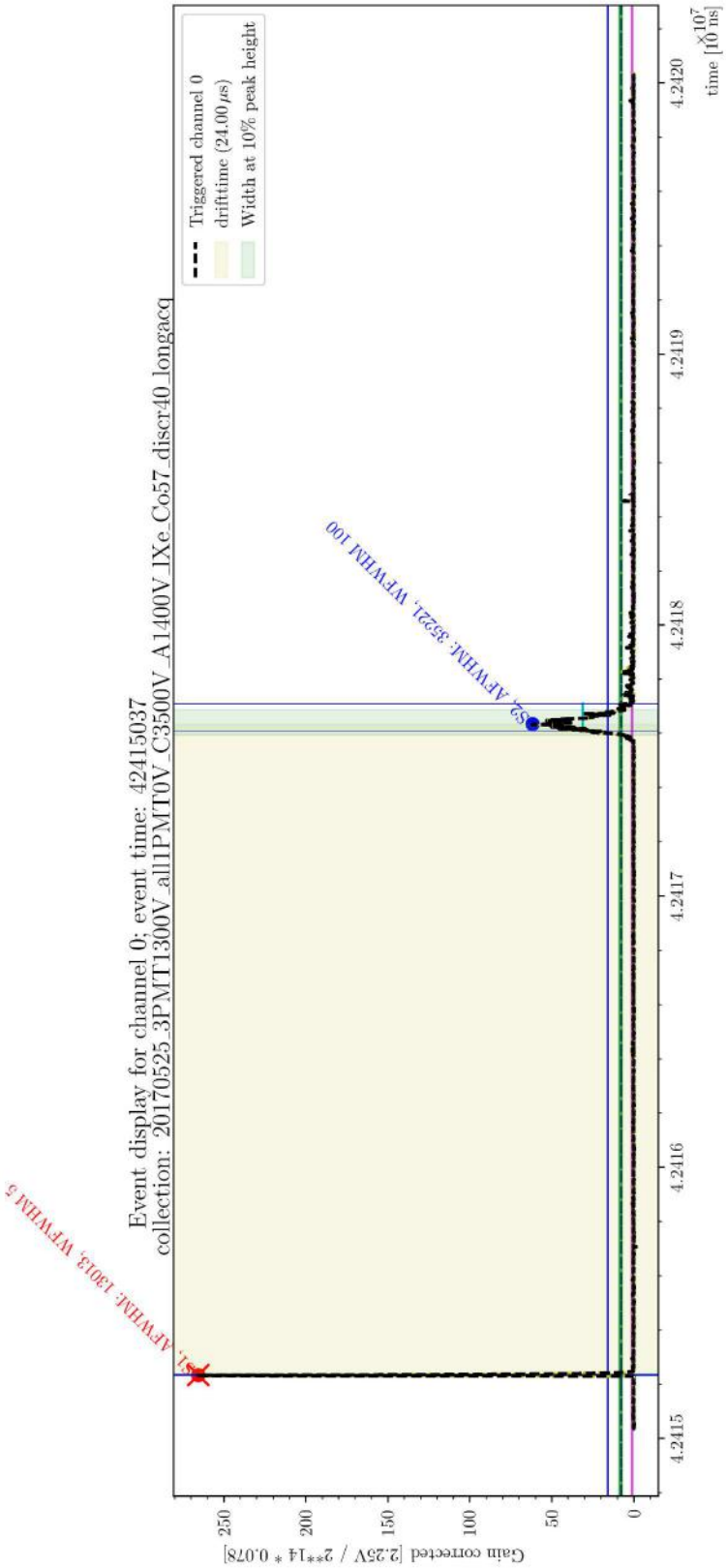

FIGURE 3.30: Example event from the waveform display as observed during a measurement run with running TPC fields and having the TPC filled with LXe. The RMS of the event amplitude is shown as green horizontal line, the mean of the event amplitude is shown as pink horizontal line, the absolute peak finder threshold in blue (solid: S1, dotted: S2 and dashed: S3).

3.8 Analysis of the TPC data

The analysis of the TPC data, presented here, aims for a first characterization of the implemented dual-phase TPC. This means a LED calibration of the used PMTs and an evaluation of the response towards calibration sources. Here a Co57 source is used to test the performance of the TPC in terms of light yield and charge yield. First the software used for the data analysis and the PMT gain measurements are introduced, followed by the presentation of one TPC run (sec.3.9) during that data with the calibration sources were acquired, and finally the found results are discussed in the next section 3.10 (page 127).

The analysis framework The analysis requires an own analysis framework that was designed specially for the data of the Bern test platform. It is used to read the files from the data processor (see sec.3.7, page 92), to analyse the data and to visualize them. The framework is written in Python 3.4 [91], using the Python packages NumPy [80] for numerical and mathematical calculations and Matplotlib for the 2D graphing [123]. Both are used as they are distributed with the SciPy package [81]. The framework itself is kept under version control using git [79].

Each analysis starts at the output of the processor data (sec.3.7, page 92) that are stored in a pickel file [90]. The data is stored as serialized class objects and the analysis framework imports their properties from the processor. Reading the data files requires de-serialization, which is done in blocks, to achieve a high input performance. Since reading de-serialized, nested objects into memory is memory intensive, the data gets filtered during input. To save memory the informations are abstracted from the object format, in which they are stored. So only the relevant numbers are kept in memory. This offers a fast analysis and plotting procedure with the drawback that the object structure is lost and adding informations, which were not read, requires a complete re-reading of the data file. If the data file is small, or enough memory is available, the complete data file, with the full object structure, can be de-serialized to memory. The data are fitted with SciPy or with Minuit [127] via iMinuit [177] or ROOTPy [197] in case of the LED gain analyses. The framework runs in a Jupyter notebook in a web browser. In principle it can also run in an interactive ipython shell or via dedicated Python programs.

3.8.1 Gain determination

The most important parameter for the PMT characterisation is its gain g [110, 50]. It quantifies the photoelectron amplification of a PMT: one initial released photoelectron

generates finally g times electrons, which are read out. The probability of releasing an initial photoelectron out of the cathode is called quantum efficiency.

The gain can be measured with a light source, illuminating the PMTs with single photons, such that a quantized distribution of the photoelectrons is measured for one, two, n photons. The standard procedure, of using a LED for illumination, was established here as well. For a detailed description of the hardware see sec.3.5.2 (page 87). The LED was tuned manually towards single photon signals observing the PMT response on an oscilloscope. The same method was applied for all small and for the large 3" PMT, but the LED voltage was varied for each PMT type and different PMT high voltage setting. This is necessary due to the changing PMT response. It turned out that the gains of the small PMTs varied widely over large ranges such that also the LED was driven with different settings with the same high voltage for the different small PMTs. This procedure made the gain calibration time intensive. Nevertheless, a standardized procedure could be established, being robust against changing experimental conditions.

The LED signal was generated with rectangular pulse signals. The best results were achieved with the following settings (the LED pulse heights vary depending on the PMT HV):

- pulse frequency: 200 Hz
- pulse width: 70 ns
- edge: 5 ns
- LED pulse height for 3" PMT in LXe: 3.35 to 3.39 V
- LED pulse height for 1" PMT in cold GXe: 3.590 to 3.700 V
- LED pulse height for 3" PMT in warm: 2.48 to 2.53 V
- LED pulse height for 1" PMT in warm: 2.59 to 2.63 V

The data acquisition for the LED-driven single photoelectron (SPE) was done by triggering the ADC externally with the LED pulse generator and acquiring 10 μs long waveforms without any pre-trigger window. The electronic noise conditions of the PMT signal readout were not ideal for acquiring small signals. The noise ranged from high frequency bipolar (HF) noise to lower frequency noise shifting the baseline or tilting the whole waveform. On top of that the time structure of the noise was highly irregular: amplitude, type, duration and frequency of the noise populations changed. Due to these conditions a none standard solution became necessary on top of the noise reducing methods described before (see sec.3.6, page 88 and sec.3.7.1, page 93).

Since the, by the LED pulse generated, peaks appear within a few μs, the waveform was cropped to this window. A peak finder was applied within that window selecting the highest point of this part of the waveform, assuming that this would be the SPE peak. This becomes necessary because the peak does not appear precisely always at the same position in the waveform. Furthermore, a bipolar noise filter and a filter on shifting baselines (RMS filter) were applied to reduce the influence of noisy waveforms further. Afterwards, the baseline around the peak was recalculated (normal procedure described in sec.3.7, page 92) correcting the impact from shifting baselines due to low frequency noise.

These waveforms feature then a almost flat baseline (inspecting around more than 1000 waveforms over various LED gain runs) and the peak finder identifies possible SPE pulses good as well. Because this procedure could not filter HF noise around the peak, the peak was integrated within various symmetric widths around the maximum position. This can be done because a waveform with low enough and regular noise would generate bipolar noise around zero where the integral over the whole waveform should be distributed around zero, plus the separated distribution from the SPE peak. It is equivalent to integrating the peak within a smaller integration range but yields to a minimized impact of the noise. Therefore, a signal-to-noise ratio is not given here. This method additionally reduces the influence of other SPE peaks or a few PE peaks appearing within the waveform because they do not get integrated. The integration window around the peak determines the acceptance for surrounding HF noise and the acceptance for the peak tales. Therefore the spectra were always done for various integration widths: {5, 4, 3, 2} bins (ADC bins of 10 ns) around the peak. Other integration widths were tested and are either too wide or too small.

The release of photoelectrons in a PMT at the photocathode bases on the photoelectric effect. The response of a PMT to a single photon by the integrated peak area can be described by a Gaussian [110]. That means the resulting spectrum can be fitted with a Gaussian for each peak in the spectrum, where the peak position results in the gain for SPE, 2PE, etc. The electronic noise can be described as Gaussian centred around 0 or as exponential tale, depending on its nature. Here most spectra were fit with an exponential noise tale plus Gaussians for the photoelectron peaks. Sometimes the intensity of the photoelectron peak in the spectrum had to be increased, by increasing the light emitted by the LED, to make the peak visible compared to the noise (changing the signal-to-noise ratio). At low signal-to-noise ratios the fit of the noise with an exponential tale failed. In these cases, only a Gaussian for the SPE peak was fit. The gains were finally derived from the mean of the results of the various integration widths and the error was given as their variance. The variance of the mean area includes the impact of the HF noise on the LED peak, the resolution for the peak itself and the acceptance for the peak tales,

which are differently affected by the integration widths. It is assumed that the mean averages these factors out.

The gains were determined for the thermodynamical conditions the detector is used in: warm (room temperature) under vacuum, warm gaseous Xenon and cold liquid Xenon. The results were always crosschecked for plausibility with the help of the peak height distribution, which is much more sensitive on the appearance of the SPE peak. The gains of most 1" PMTs were determined before in warm and air [237]. The gains measured by [237] agree with the values given by Hamamatsu. However, significantly lower values were measured here (for all but one 1" PMT). The analysis, shown here, has a more minimum bias approach while the study presented in [237] aimed for measuring gains in the range given by Hamamatsu. The here shown gains of the small PMTs were also verified with a dark noise based SPE gain method[7] and they agree with the light observed during the TPC runs by the small PMTs in comparison to the large PMT. Furthermore, the same gain measurement method was used for the small and the large PMTs while resulting in the expected gain for one small PMT, as well as for the large PMT. This makes the findings presented here more plausible as well.

Gains in warm and vacuum The gain was measured in vacuum at pressures $\leq 10^{-5}$ mbar (avoiding tripping PMT HV due to the long attenuation length of free electrons and ions generated by the high electric fields). For the 3" PMT, gains were measured for voltages of $-1200, -1300, -1400, -1500$ V. No gain could be measured for -1100 V. For the 1" PMTs HVs of $-750, -800, -850, -900$ V were applied. In fig.3.31 are the resulting spectra for the 3" PMT at -1300 V given. The fit was done for all 3" PMT spectra with an exponential for the noise plus Gaussian for the SPE peak or two Gaussians (SPE + 2PE peak). The gains show a slightly non linear behaviour over the applied HVs, as expected according to [110, 47]. The measured gain at -1500 V is above the nominal value (given at -1500 V). The gain of the large PMT in warm is slightly higher than in cold (see next paragraph). Fig.3.32 shows the SPE spectra for PMT 2 at -900 V. It shows at this voltage a nice SPE spectrum with a well from the background separated SPE peak. The from the fit result measured gain is $(7.2 \pm 0.1) \cdot 10^5$.

In fig.3.34 are the gains for the 1" PMTs shown. PMT 7 and 2 (serial no. LV1413, LV1418) were not operational during the gain determination run shown here. The gains of all small PMTs are slightly lower than in cold (see next paragraph). For -750 V and -800 V only PMT 6 showed a measurable gain. At -850 V the gains could be measured for PMT 5 and 6. The signal to noise ratio for PMT 1 was not good enough to allow

[7] One would expect that in randomly taken external triggered waveforms, without further illumination, a spectrum with SPE, 2PE, etc. distributions is generated as well by photons due to thermal noise.

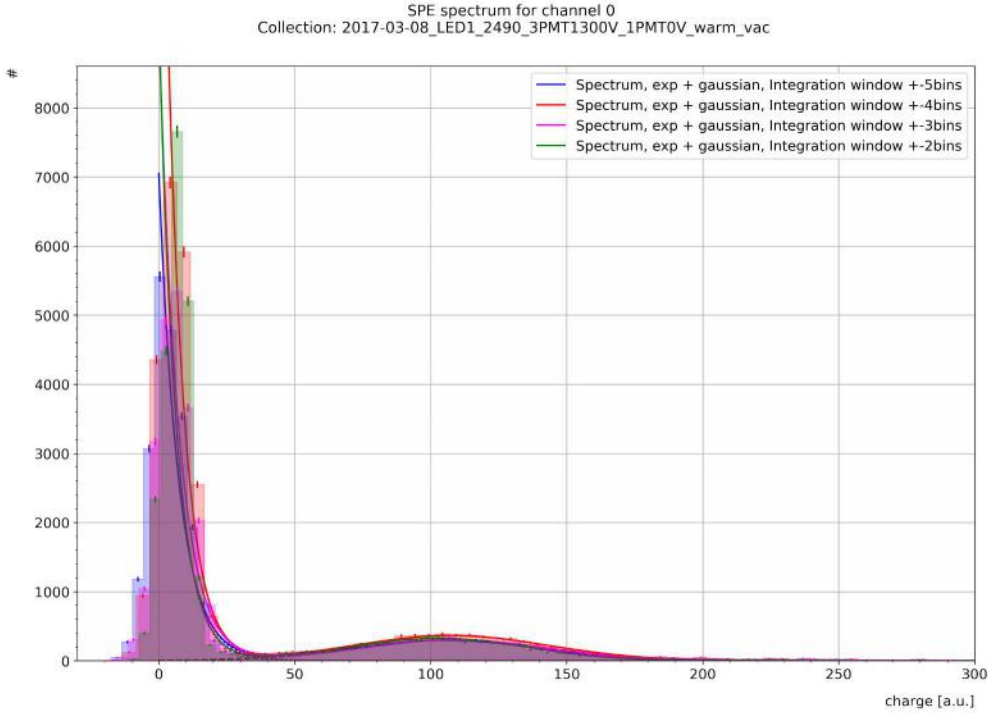

FIGURE 3.31: Spectra from the 3" PMT measured at −1300 V measured in warm and vacuum. The fit results of the various bin widths agree within their uncertainties of ±1 bin. The SPE peak is well separated from the noise, as expected due to the high gain of this PMT type.

for a reasonable measurement. Finally, at −900 V all operational small PMTs showed a measurable gain.

Fig.3.34 summarizes the results for the large and the small PMTs, also indicating the nominal gains given by Hamamatsu. While the large PMT showed a slightly higher gain than specified, the small PMTs showed a much lower gain than expected from the specification. These low gains agree with the gains determined in cold and in warm GXe, as well as they agree with the light seen during other measurements in comparison with the large PMT. They were also cross checked with measurements basing on dark noise.

Gains in warm GXe The gains in warm gaseous Xenon (GXe) were determined at 1 bar Xenon pressure. The pressure was stable within the uncertainty of the gauge. PMT 4 (1") was not operational stably, so it was exchanged: LV1452 was replaced by LV1421 in 2017. The gain was only for PMTs 1 and 6 determinable at all voltages. The gain of PMT 1 is slightly non-linear against the applied HV. For #2 and #4, the gain could be determined starting at −850 V while for PMTs 3, 5 and 7 the gain could already be determined starting at −800 V. For −750 V most given gains have to be understood as upper limits. The large PMT shows again a slightly non linear behaviour and the gain at the design voltage of −1500 V is significantly higher than the nominal gain of $5 \cdot 10^6$. The

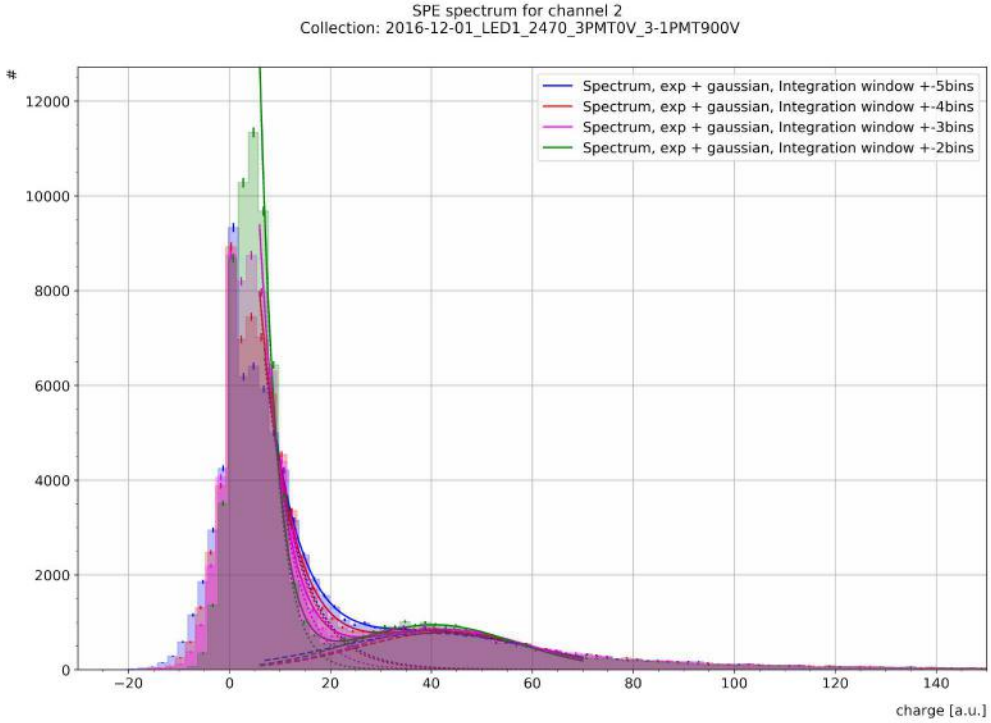

FIGURE 3.32: Spectra from PMT 2 at $-900\,\mathrm{V}$ measured in warm and vacuum. The fit results of the various bin widths agree within their uncertainties of ± 1 bin.

gains of the small PMTs are, as before, significantly lower than the nominal gains of 10^6. The integration results were again checked with the peak height distributions. The gains measured in warm Xenon gas are between 5% and 15% higher than in warm and vacuum while it was expected that the medium should make no difference. This indicates a high uncertainty in the gain measurements, that might be caused by the temperatures of the PMTs and electronics.

Gains in LXe The gain of a PMT depends on its operation temperature. The operation temperature of the PMTs during normal TPC operation is far below the temperatures of the previously mentioned two gain measurements. Therefore, the gain was measured as well in cold, having the 3" PMT immersed in liquid Xenon while the top PMTs were operated in the cold Xe gas phase. The temperature in the cryostat was stable at $(174 \pm 2)\,\mathrm{K}$ at 1.5 bar pressure. The LED voltage was increased due to the low temperatures. PMT 2 was switched off because it could not be operated stable at higher voltages than 750 V. PMT 7 showed no signal anymore after opening the cryostat for some service shortly before the run. Therefore it was switched off as well and their gains were not measured. Fig.3.35 summarizes the results for all PMTs, which were measured in cold GXe or even immersed in LXe.

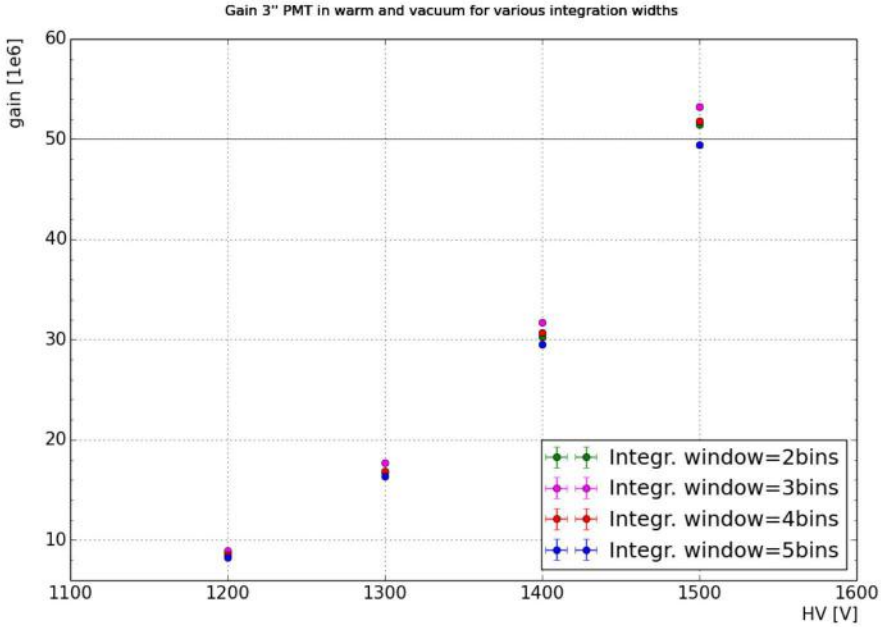

FIGURE 3.33: Gains derived for the 3" PMT in warm and vacuum. The gains were determined with an amplification of 10× gain, for which the plot was not corrected. The PMT shows an higher gain than specified at −1500 V.

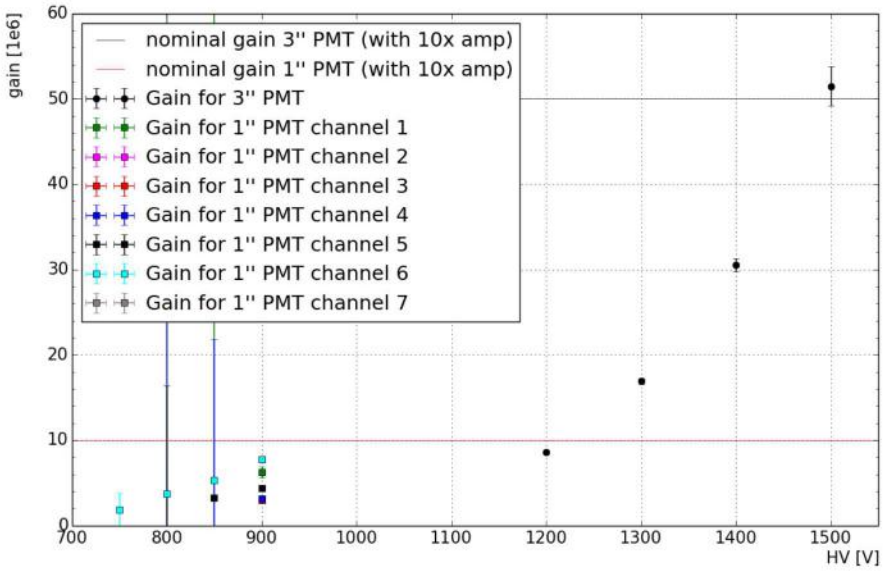

FIGURE 3.34: Gains as derived for all 1" and the 3" PMT in warm and vacuum, as well as the nominal gains (shown 10× from the amplifier) at −800 V for the 1" PMTs and −1500 V for the 3" PMT. The gains were determined with a 10× amplification, which is included in the values in the plot.

The small PMTs show still a very low gain, expect PMT 6. The non linear behaviour is due to variations in the results from the low gains at low signal to noise ratios. They would anyhow be operated at higher voltages (850 − 900 V) to compensate for the low gains. Only PMT 6 shows a nice linear rise in gain over applied high voltage, as expected for this PMT type. It also shows gain values slightly above the nominal value. This is by

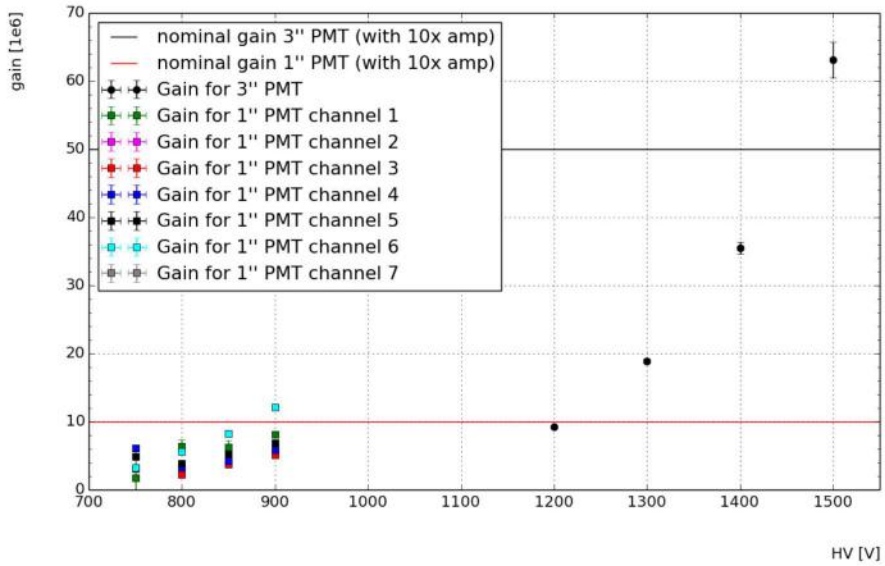

FIGURE 3.35: Gains as derived for all 1" and the 3" PMT in cold GXe or immersed in LXe as well as the nominal gains (shown 10× from the amplifier). The gains were determined with a 10× amplification, which is included in the values in the plot. The 3" PMT and the 1" PMT 6 show similar or higher gains than expected while the other small PMTs show lower gains than specified.

the way another indicator that the true reason for the strange, means low and unstable, gains of some of the small PMTs is really a problem of the PMTs and not an artefact of the electronics, DAQ or software.

The large PMT shows again a higher gain than specified at −1500 V [108]. Due to the lower thermal noise it was possible to fit even at −1300 V two Gaussians, so the SPE peak and the 2 PE peak (which was just used to check the SPE peak result). One can see again the slightly non linear behaviour of the gain vs. applied HV that was mentioned before and which is a feature of this PMT type. No gain could be determined below −1200 V because the SPE peak moved into the noise tail.

The gain measurements yield to the chosen PMT HV settings, as shown in table 3.3 on page 89. These settings aim for an homogeneous gain on the top array to achieve an as homogeneous as possible sensitivity for the event position. These settings take furthermore into account that some PMTs could not be operated stable above some HV. The HV setting of the large PMT is balanced between a high gain and a gain, at which the saturation of the readout electronics is below 5%.

3.9 Co57, Cs137 and background data at lower gain

One goal was to characterize the performance of the TPC in terms of light yield and charge yield (see sec.1.2.2, page 13), thus the measurement of the scintillation and ionization response of the TPC to a monoenergetic calibration source. These measurements are presented here and the measurement run is called *low gain run*.

A Co57 calibration source (Spectrum Techniques with 37 kBq [221]) and a 185 MBq Cs137 source were used during the measurements. The $\times 10$ amplifier was skipped, which led to a lower gain, to a lower saturation level and thus optimized DAQ lifetime. A dead time monitoring was set up as well, basing on the busy output of the ADC, employing a V1495 module as in XENON1T [62]. For more details about the applied external trigger logic see sec. 3.6.2 (page 91). The processing chain employed the software-trigger for the external trigger mode, as described in sec. 3.7.1 (page 93).

Since the small PMTs showed very low gains before (see 3.8.1, page 103) and two were not operational, only the large bottom PMT was operated. This also simplified the event structure. Nevertheless, the disabled top PMT array causes a lower light and charge yield and the x-y position cannot be reconstructed, thus the TPC could only be fiducialized in z direction. Nevertheless, the goal of measuring a charge and light yield is achievable because the large PMT on the bottom contributes the major sensitivity to them. The 3" PMT was operated at -1300 V for the data presented here.

The most important cryogenic detector parameters, representing the detector stability, are shown in fig.3.16 (page 78). The spikes on May 22nd and during May 23rd are caused by changing the recirculation conditions, i.e. switching the purification between on, off and bypass mode (see sec.3.3, page 70). The reason for the fluctuations on the evening May 25th is unknown but the detector conditions returned to be stable afterwards. The TPC was levelled at the start of the run within ≤ 0.4 mm (see fig.3.17, page 79).

Table 3.6 summarizes the data taking conditions for the relevant data sets during this run. The Cs137 source was collimated with lead blocks (in X and Y directions in detector coordinates) and placed in an height of about 10 cm above the top flange of the inner cryostat. There was no further collimation in z direction. It was placed about 3 m away from the setup, so about 3.5 m from the centre of the inner cryostat, to reduce the source activity seen by the detector.

The purification was operated during data taking, and before for about 2 days, at bypassing mode (partly bypassing the cryostat to allow the KNF pump to run at higher flow). The anode high voltage was supplied from an old CAEN N471A NIM module [66] and the cathode high voltage was operated with the CAEN main frame and the CAEN

name	source	$\bar{f}_{trigger}$ [Hz]	runtime [min]	r [%]
background(bg)	background	117.0	181	99.997
Co57	Co57	391.0	180	99.995
Cs137	Cs137	683.1	30	99.673

TABLE 3.6: Data sets as used for the analysis in this section. $\bar{f}_{trigger}$ is the average trigger rate. The lifetime ratio r is defined as: lifetime/runtime.

A1535 module that powered the PMTs as well [67]. Thus the anode was supplied with 1400 V and the cathode had to be set to −3500 V. These settings result in an extraction field of (1.94 ± 0.31) kV/cm and a drift field of (273.8 ± 2) V/cm (with $\epsilon_{LXe} = 1.88$ and $\epsilon_{GXe} = 1.0$ [104], taking into account the uncertainties of the applied potential, the mechanical uncertainties of the drift legnth and the uncertainties from the liquid level from the tilt adjustments).

Gain measurement To ensure gain stability, the gains were measured again for the 3" PMT. The gains were measured for −1200 and −1300 V in LXe. −1100 V was tried as well but the signal was not separable from the background, so no gain is specified for high voltages below −1200 V. The gains were determined with the same method as before (see sec. 3.8.1, page 103). Fig.3.36 shows the resulting gains for the tested HVs in comparison with the gains measured in February 2017 in LXe. The values do not agree within their fit errors (difference: $0.3 \cdot 10^5$; 13%), nevertheless the difference is small in fact and the given uncertainty is only the statistical error: the values would even agree within the scattering of the integration results for the various integration widths. The HV of the 3" PMT was set to −1300 V, so a gain of $(2.19 \pm 0.02) \cdot 10^6$.

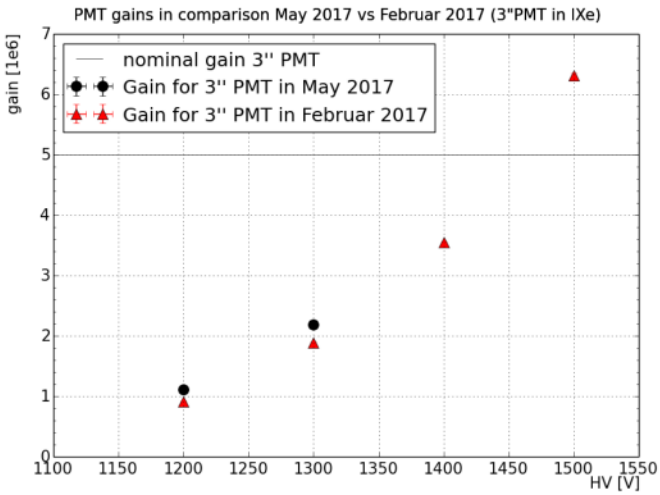

FIGURE 3.36: Gains of the 3" PMT as measured during the low gain run in comparison with previous measured gains. The measurements agree within 13%, which might be caused by changing readout conditions (e.g. different room temperature).

Detector response All plots shown in the following paragraphs are corrected with the DAQ lifetime. The discrimination between the peak types depends only on the area and width (see section 3.7.3, page 97). So the distributions of these properties are of interest.

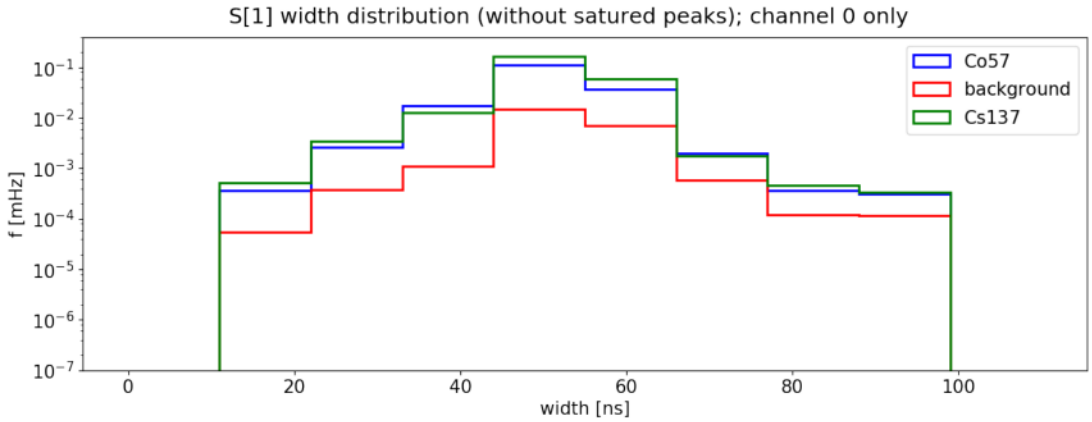

FIGURE 3.37: Distribution of the measured S1 FWHM widths (see Tab.3.4, page 100 and 3.5, page 101) observed in complete events (at least one S1 and one S2). The distributions behave as expected from the peak classification.

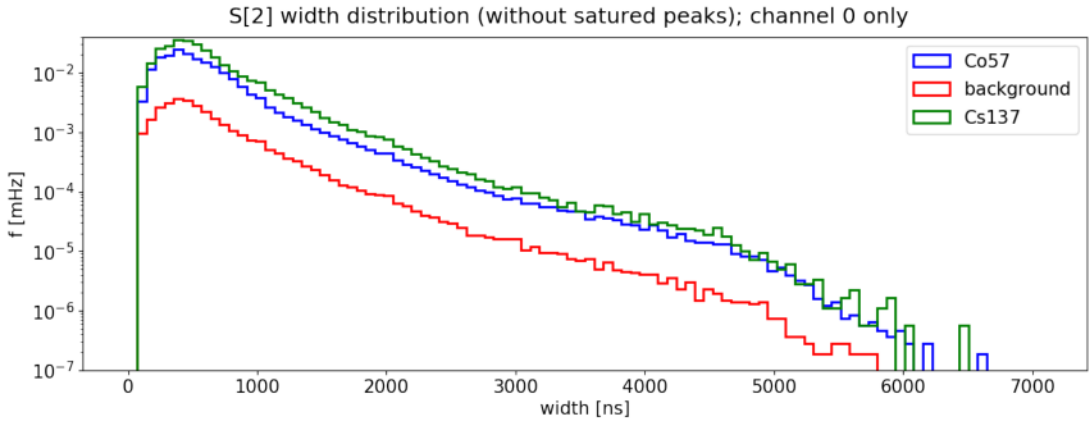

FIGURE 3.38: Distribution of the measured S2 FWHM widths (see Tab.3.4, page 100 and 3.5, page 101) observed in complete events (at least one S1 and one S2). The S2 widths start at the S2 definition threshold of 100 ns (see sec.3.7.3 on page 97).

The S1 width (fig.3.37) shows the expected behaviour, a normal distribution around a maximum, with a minimal width defined by the digitizer of 10 ns (see sec. 3.6, page 88) and a maximum width, which is defined by the peak classifier *Bern3* with 100 ns (sec. 3.7.3, page 97). The distribution of the S2 widths, as shown in fig.3.38, shows no significant differences in the shape between the Co57 S2s and the background or Cs137 S2 distributions. The distribution show steps at the different peak classification levels, as described in sec. 3.7.3 (page 97).

Fig.3.39 shows the S1 height, including saturated peaks, for the three datasets. One can see that the full dynamic range was used, avoiding a significant contribution of saturated

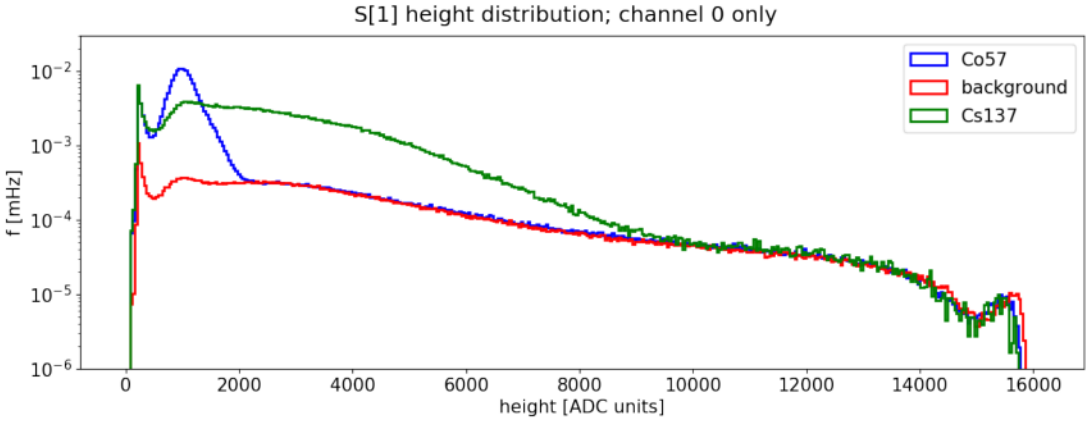

FIGURE 3.39: Distribution of the measured S1 heights (see Tab.3.4, page 100 and 3.5, page 101). The shown peaks appeared within events showing at least one S1 and one S2, including saturated events. Note the usage of the full dynamic range avoiding saturation.

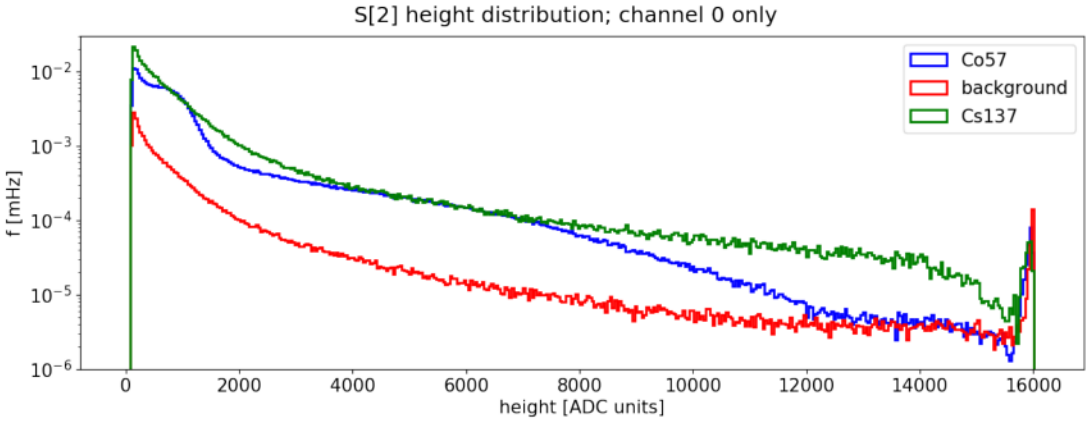

FIGURE 3.40: Distribution of the measured S2 heights (see Tab.3.4, page 100 and 3.5, page 101). The shown peaks appeared within events showing at least one S1 and one S2, including saturated events. Peak saturation happens when using the full dynamic range, what is true for the last bin at 16000 ADC units.

S1s. Nevertheless, a larger amount of saturated peaks would have been better to achieve a higher sensitivity at low energies. This would also increase the S2 heights, what would not be a problem, as visible in fig.3.40: the interesting region for the ionization response measurement is the first excess of the Co57 curve (blue) at about 1000 ADC units. Due to the low gain, the 122 keV Co57 peak probably is influenced by the trigger threshold. A more detailed discussion can be found in sec. 3.9.4. Comparing this with the S2 heights distribution as visible in fig.3.40 one can see that already there the amount of saturated peaks was increased significantly. This yields to a better separation of the 122 keV Co57 line from noise and the trigger threshold in the acquired S2 spectrum.

Most interesting is the energy response of the detector, which is measured with the area of the peaks. These are shown in fig.3.41 and 3.43, as they were measured for the two peak types. One would expect a peak structure in the S1 and S2 area distributions from

the Co57 122 keV line and for Cs137 a broad band like structure due to the Compton band. Both features can be identified in the distributions. The tail in the Cs137 S1 area distributions at around 1800 PE could be the Compton edge. Meanwhile a clear signature like that is missing for the S2 areas. Also the Cs137 full absorption peak is missing (mean free path of 662 keV photons in lXe: ≈ 5 cm [179]). Fig.3.42 shows the S1 spectrum of Co57 with subtracted background, showing clearly the Co57 gamma line at 122 keV.

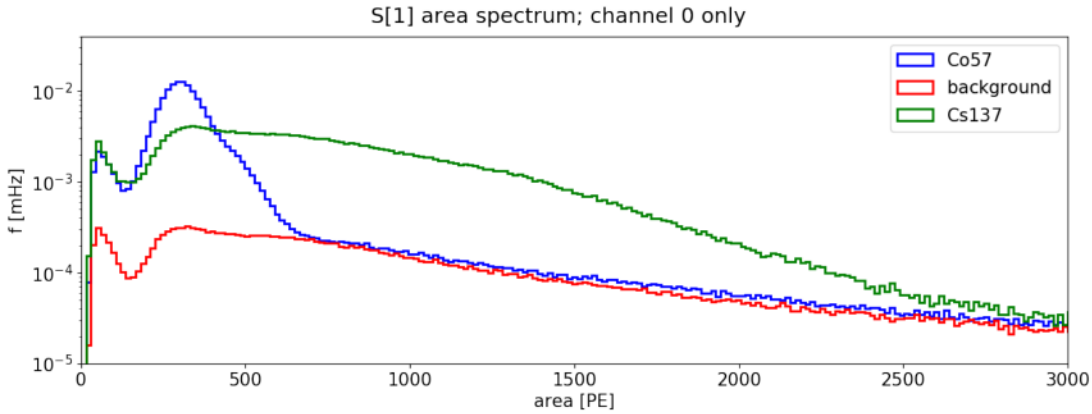

FIGURE 3.41: Area of the S1 peaks and the maximum of the areas. Shown are only not saturated peaks from events with at least one S1 and one S2 peak. Zoomed between 0 PE and 3000 PE. One sees that the minima at around 180 PE and maxima at around 300 PE are all at the same position. This is an indication that the high discriminator threshold effected the trigger efficiencies at low energies. In fig.3.54 are the unfolded spectra shown with the expected energy distributions.

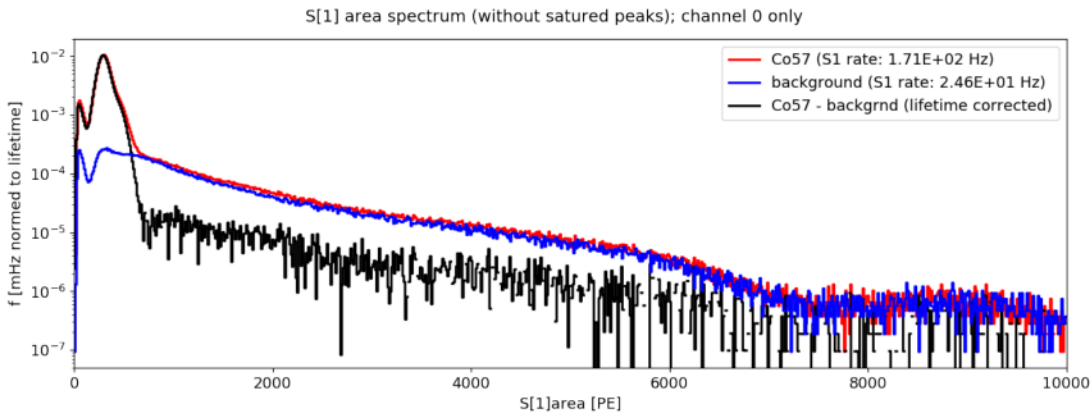

FIGURE 3.42: Co57 S1 area spectrum with subtracted background (using the bg dataset). The subtraction was done with the lifetime weighted histograms. The 122 keV line from Co57 becomes more prominent. It shows an unexpected, not normal distributed shape, what indicates a non-linear energy response.

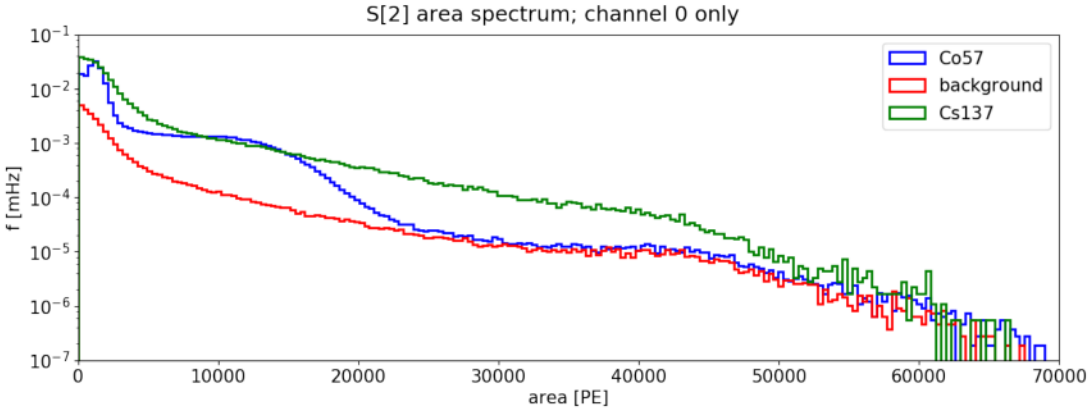

FIGURE 3.43: Area of S2 classified peaks. Shown are only not saturated peaks from events with at least one S1 and one S2 peak. The bins are weighted with the lifetime of the dataset. The full absorption peak from the 122 keV Co57 line is the first peak in the Co57 spectrum.

3.9.1 Drift time

The drift time is defined as the time between an S1 and its S2. It is determined by the first S1 before the first S2 in an event. Its distribution is shown in fig.3.44 and shows as expected a distribution between $0\,\mu$s and about $40\,\mu$s. The drift time depends on the drift velocity and thus the drift field. According to [86] at $\sim 250\,$V/cm the drift velocity is $\mathcal{O}(1.8 \cdot 10^5)\,$cm/s, which would correspond to a maximum drift time of $34\,\mu$s (here: 273.8 V/cm, see sec.3.9, page 111). Nevertheless, we can also go the other way around and assume that the cut off in the drift time distribution at $\sim 38\,\mu$s (or even slightly below that value) is the maximum electron drift time, which would result in a drift velocity of $1.8 \cdot 10^5\,$cm/s. This cut off appears for all two sources and the background measurement at similar values, as expected because the drift velocity is independent from the source. Interestingly, the first part of the Co57 drift times shows a steeper decay than the background and Cs137 data. This is likely caused by the position of the source close to the anode, what yields to a higher event rate of events (with short drift times) close to the anode: the mean free path of 122 keV gammas in LXe is less than 3 mm [179], so most gammas generate events close to the anode. From the differences in the cut off, an uncertainty of $\approx 0.2\,\mu$s is estimated. Thus the drift velocity of $(1.8 \pm 0.2)10^5\,$cm/s agrees as well with the drift velocity measured by [86, 20, 12]. The drift time was furthermore measured for the drift field at other cathode voltages as shown in fig.3.45. The acquired data have a shorter lifetime and show thus larger fluctuations.

Since the drift time translates into the z-coordinate of the TPC, one can use it for a vertical fiducialization of the detector. Fig.3.46 shows how the S1 area depends on the drift time and also illustrates the effect of fiducial volume cuts. There are some artefacts at low drift times, i.e. line structures below about $3\,\mu$s in fig.3.46 and 3.47, which appear

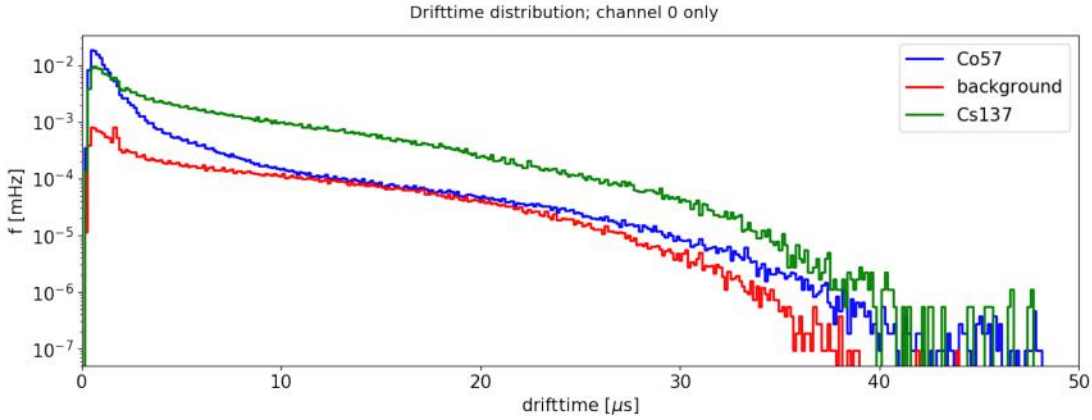

FIGURE 3.44: Distribution of the drift times during the low gain run with a drift field of (273.8 ± 2) V/cm (cathode HV: 3.5 kV). The observed cut-offs around 40 μs result in drift velocities of about $\mathcal{O}(1.8 \cdot 10^5)$ cm/s.

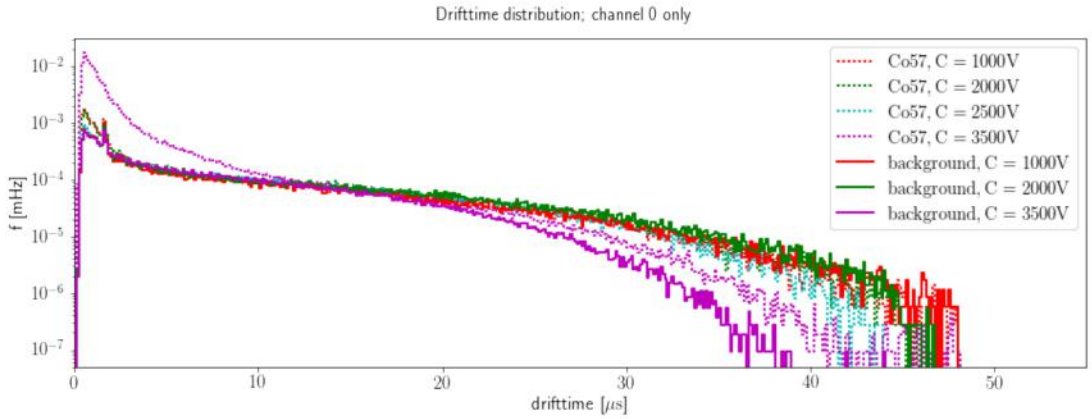

FIGURE 3.45: Distribution of the drift times during the low gain run for Co57 and background at different applied drift fields of: (273.8 ± 2) V/cm with a cathode HV of 3.5 kV, (195.6 ± 1.4) V/cm with a cathode HV of 2.5 kV, (156.4 ± 1.1) V/cm with a cathode HV of 2 kV and (78.2 ± 0.6) V/cm with a cathode HV of 1 kV. The lifetimes of the acquired data were shorter than in the data sets shown in fig.3.44. The Co57 data set at a cathode voltage of 3.5 kV is the same as shown before in fig.3.44. The drift time distributions show the expected cut-off behaviour of reaching higher maximum drift times with decreasing drift fields due to the lower electron drift velocities.

for all three sources over the entire S1 range. Similar artefacts are observed for S2s at the same drift times. Thus they might be caused by the gate or even anode since they appear below (0.5 ± 0.1) cm in the TPC. Without a x-y event position reconstruction no final conclusion can be derived. A fiducial volume can be used to improve the S1 area histogram quality and thus light yield determination (see sec.3.9.4). Fig.3.47 shows basically the same but for the Co57 and Cs137 dataset (just one drift time cut for each data set).

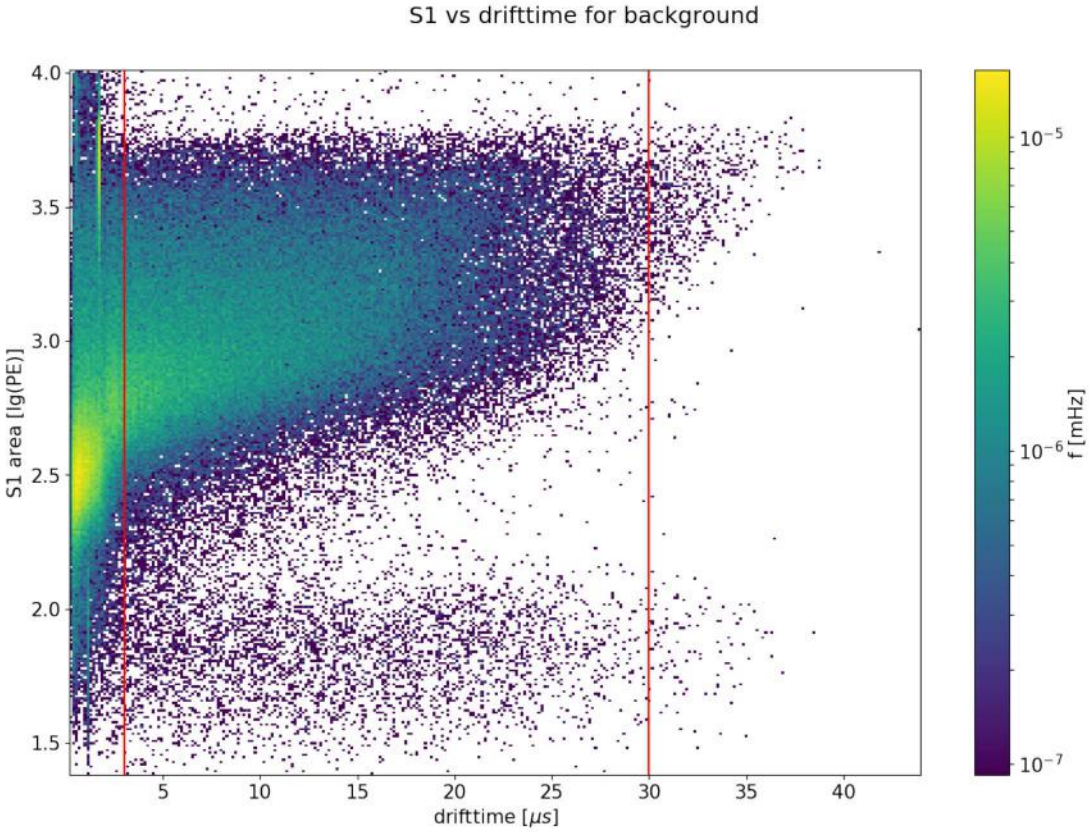

FIGURE 3.46: S1 area vs. drift time for the bg data set. In red is one drift time cut (at $3\,\mu s$ and $30\,\mu s$) shown that select a fiducial volume in the TPC restricted in z-direction. The S1 areas show artefacts for events close to the anode (low drift times $\approx 3\,\mu s$), which would be cut with the shown fiducial volume cut.

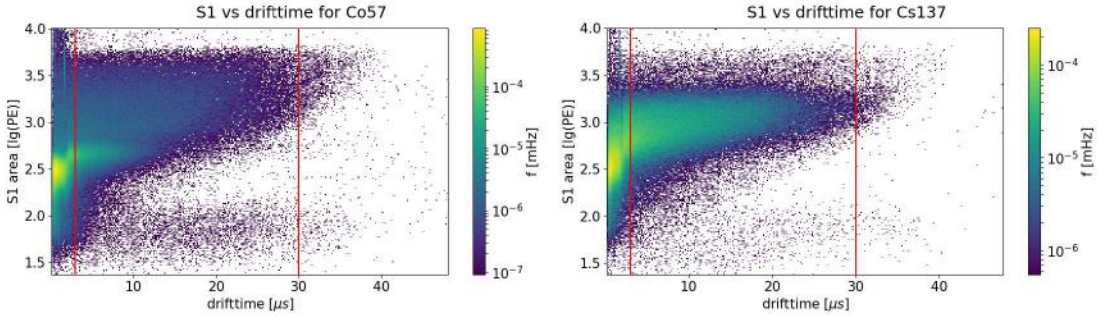

(A) Co57. (B) Cs137.

FIGURE 3.47: S1 area vs. drift time for the Co57 and Cs137 data set. In red are the drift time cuts shown that select a fiducial volume in the TPC restricted in z-direction. Shown are the drift time cuts at $3\,\mu s$ and $30\,\mu s$. Only one cut example is shown for each data set. The S1 areas show artefacts for events close to the anode (low drift times $\approx 3\,\mu s$). The Co57 line at 122 keV becomes again well visible at $lg(\mathrm{S1}) \approx 2.6$, comparing the Co57 plot (fig.3.47a) with background data (fig.3.46).

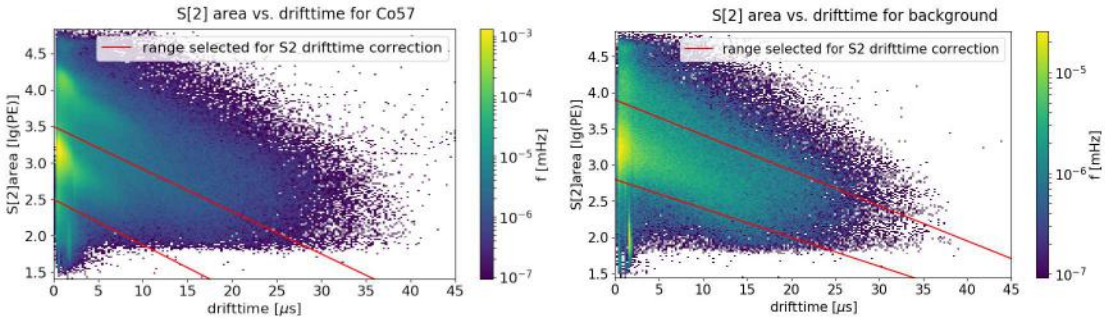

(A) Co57 with the cut region for the electron lifetime and S2 correction analysis.

(B) Background with the cut region for the electron lifetime and S2 correction analysis.

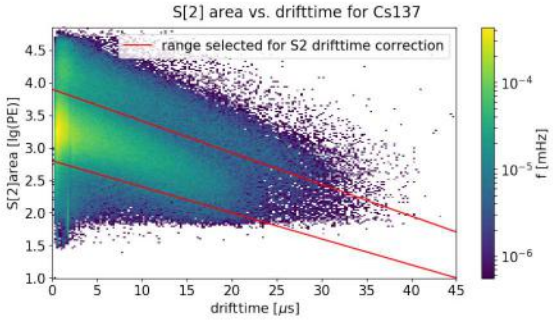

(C) Cs137.

FIGURE 3.48: S2 area vs. drift time for the Co57 (3.48a), background (3.48b) and Cs137 (3.48c) data sets. The strong correlation of the area with the drift time is well visible for all three data sets. The cut regions as used for the electron lifetime fits or for the S2 corrections. Similar artefact as observed for the S1 areas (fig.3.46 and 3.47) appear again at low drift times below $\approx 3\,\mu s$.

3.9.2 Electron lifetime

Looking now on the S2 area vs drift time dependence (see fig.3.48) one can see a strong correlation between the area and the drift time. This is due to a loss of drifted electrons, which get captured on impurities in the Xenon and due to charge diffusion. Therefore, the Xenon is continuously purified with a hot getter (see sec.3.3 on page 70). Since the recirculation system was not fully operational, the system was operated with a gas line partly bypassing the inner cryostat. Thus a lower purification performance is expected and thus a lower electron lifetime.

The electron lifetime characterizes with a $\frac{1}{e}$ decay how far a free charge can be drifted in the detector. Therefore, it is a measure for the purity of the Xenon. The longer the electron lifetime is, the less electrons get lost during the drift process and the more light is observable. Also the number of complete events containing both S1 and S2 improves and the energy resolution will improve due to a better charge yield. The electron lifetime can be determined from the information shown in fig.3.48. Since the impurities reduce

the electron lifetime τ_e, one can fit the distribution with an exponential [20]:

$$\langle S2 \rangle = \langle S2 \rangle_0 \cdot \exp(-\frac{t_{drift}}{\tau_e}) \tag{3.4}$$

with the drift time t_{drift}. The mean S2 area $\langle S2 \rangle$ per drift time is a proxy for the number of electrons.

Since all datasets show for the S2 areas various lines, always the first one, starting at around 10^3 PE, was selected for the fit and the fit was restricted to the region around the line. The cut regions are shown in fig.3.48b for the bg dataset, in fig.3.48c for the Cs137 dataset and in fig.3.48a for the Co57 dataset (no fiducialization applied).

It would be expected that the measurements for all three source yield to the same electron lifetime. The resulting fit for the background dataset is shown in fig.3.49 giving $\tau_e = (9.2 \pm 0.1)\mu$s, $\tau_e = (9.8 \pm 0.1)\mu$s for the Co57 dataset (fig.3.50) and $\tau_e = (9.5 \pm 0.5)\mu$s for Cs137 (fig.3.51). Only the value found for Cs137 agrees within its error with the values found from the other two sources. Nevertheless, all values agree within about 7%, which is within the fluctuations seen by varying the lifetime fit ranges. Assuming that the discrepancy is caused by the statistical fluctuation of the measured lifetimes, one can calculate the mean of these electron lifetimes as $\langle \tau_e \rangle = (9.5 \pm 0.3)\mu$s, which agrees within its uncertainty with all three single values.

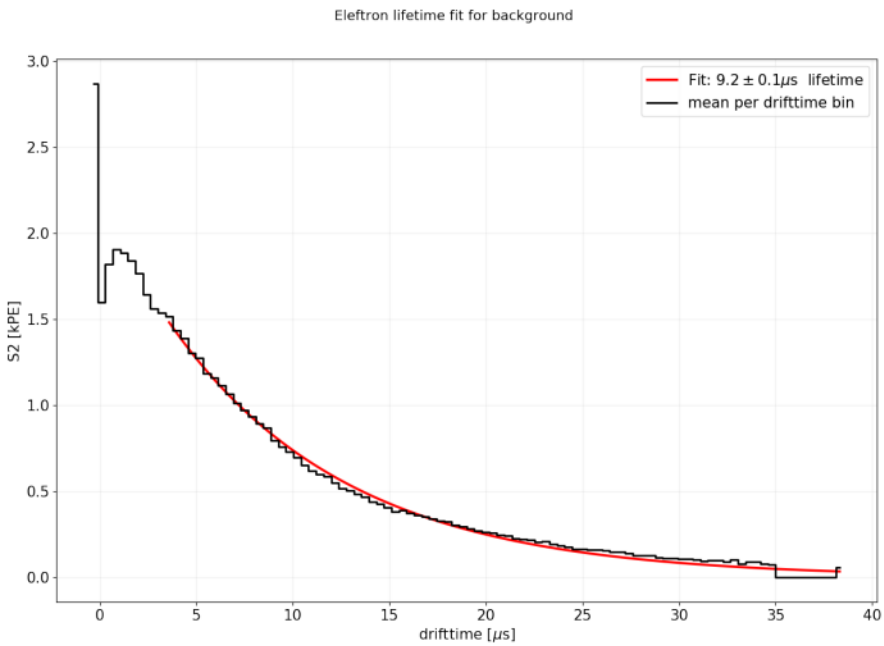

FIGURE 3.49: Mean S2 area of the bg dataset with the resulting electron lifetime fit based on eq.(3.4). The first line in the S2 spectrum at $lg10(S2) = 3.25$ PE was selected for the electron lifetime fit with a cut starting from $lg10(S2) = 2.8$ PE to $lg10(S2) = 3.8$ PE. The fit result is shown within the fit range. The artefacts at drift times below $3\,\mu$s disturb the expected exponential behaviour of the means S2 area.

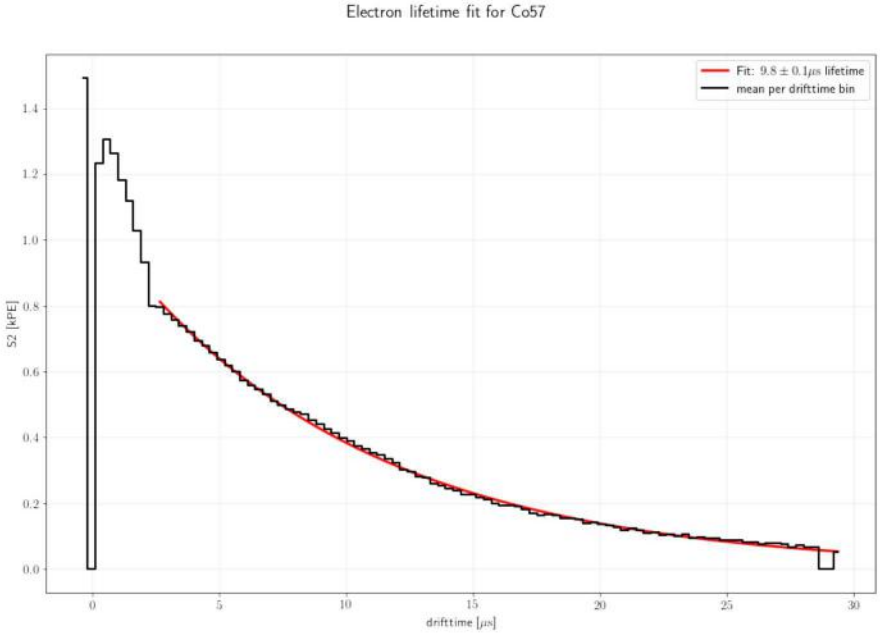

FIGURE 3.50: Mean S2 area of the bg dataset with the resulting electron lifetime fit based on eq.(3.4). The first line in the S2 spectrum at about $lg10(S2) = 3.2\,\mathrm{PE}$ was selected for the electron lifetime fit with a cut starting from $lg10(S2) = 2.5\,\mathrm{PE}$ to $lg10(S2) = 3.5\,\mathrm{PE}$. The fit results are shown within the fit range. The artefacts at drift times below $3\,\mu s$ disturb the expected exponential behaviour of the means S2 area.

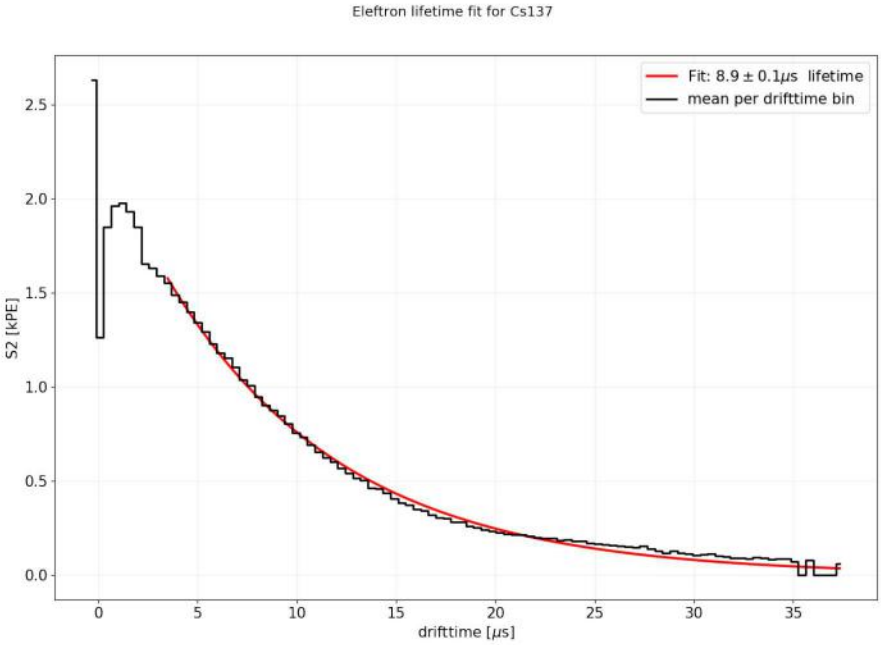

FIGURE 3.51: Mean S2 area of the Cs137 dataset with the resulting electron lifetime fit based on eq.(3.4). The first line in the S2 spectrum at about $lg10(S2) = 3.3\,\mathrm{PE}$ was selected for the electron lifetime fit with a cut starting from $lg10(S2) = 2.8\,\mathrm{PE}$ to $lg10(S2) = 3.8\,\mathrm{PE}$. The fit results are shown for one fit range. The artefacts at drift times below $3\,\mu s$ disturb the expected exponential behaviour of the means S2 area. The mean of all tested fit range results is $\tau_e = (9.5 \pm 0.6)\mu s$.

Following [20] one can calculate the attenuation length of the electrons λ from the electron lifetime as:

$$\lambda = \mu E \tau_e \tag{3.5}$$

with a drift field E and an electron mobility of pure Xenon of $\mu = (2000 \pm 200)\,\mathrm{cm}^2/\mathrm{Vs}$. For the found electron lifetime this results to $\lambda = (5.3 \pm 0.7)\,\mathrm{cm}$. It contributes to the start of the cut off in the drift time distribution (fig.3.44) at around $25\,\mu$s, which is a convolution of the spatial event distribution and τ_e.

3.9.3 S2 correction

The S2 area depends strongly on the distance between the interaction and the liquid surface because electrons will be lost due to capture on impurities [20]. Since this effect is well measurable, the expected S2 area, without any loss, can be calculated depending on the interaction depth in the TPC, i.e. drift time. This effect can be measured by fitting the S2 area vs. drift time with an exponential given as in eq.(3.4).

Based on the fit results one can compute the corrected S2 area. The background lifetime fit was chosen arbitrary for the correction. Fig. 3.52 shows the three resulting corrected S2 area vs drift time plots. Also shown is a linear fit, with which the correction quality was checked: one would expect a constant flat function in corrected S2 space, what is fulfilled for background and Cs137, as shown in fig.3.52a and 3.52c. Nevertheless, the result for the Co57 S2 spectrum (fig.3.52b) shows an artefact in corrected S2 space at low drift times. The bands become flat for drift times larger than $3\,\mu$s as well, so only the S2 reconstruction for small drift times suffered from this. The reason for the disturbance might be the source setting: the source was placed in the hight of the anode, generating a high and strongly localized rate close the anode, which might yield to the seen artefacts: it could be a photo peak from the anode or gate.

3.9.4 Light yield

One of the parameters characterizing the performance of a dual-phase TPC is the light yield (see sec.1.2.2, page 13). The light yield ly can be determined from the S1 area at a given energy. Here the 122 keV line of the Co57 source was used. By fitting this line appearing at ~ 300 PE in the S1 area space (fig.3.53) with a Gaussian, one gets the position and thus the light yield and from the width σ of the line, one gets the energy resolution using S1s only.

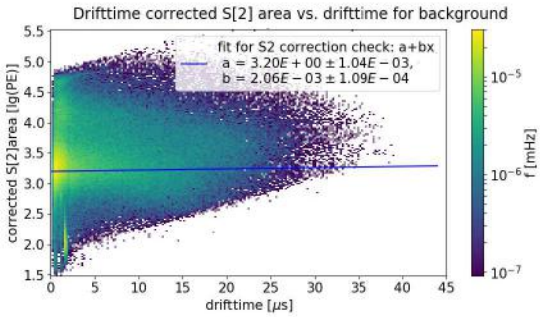

(A) Background with linear fit on the corrected S2 band as quality check. The fitted quality check approves the desired flatness of the S2 band.

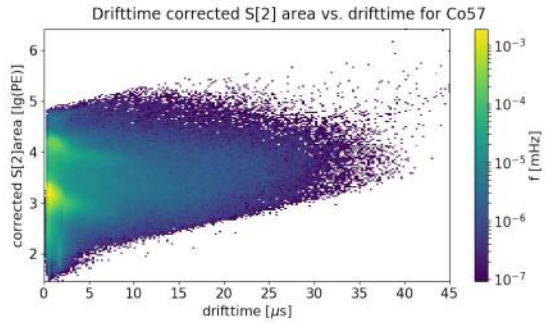

(B) Co57 spectrum. Due to the artefacts at low drift time no linear quality check fit was achieved. Nevertheless, the band flattens above $3\,\mu$s.

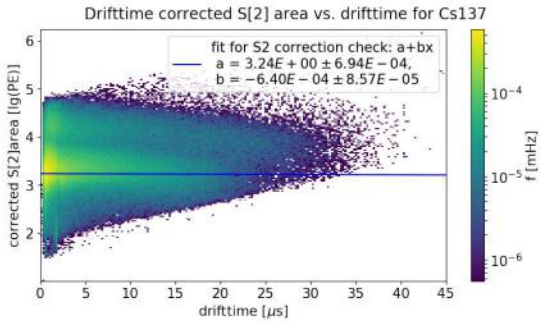

(C) Cs137 with linear fit on the corrected S2 band as quality check. The fitted quality check approves the desired flatness of the S2 band.

FIGURE 3.52: Corrected S2 area vs drift time plots. The figures show that the corrections work well. The fitted quality check approves the desired flatness of the S2 band.

For a Gaussian given as:

$$g(x) = A \cdot \exp\left(-\left(\frac{x-\mu}{2\sigma}\right)^2\right) \tag{3.6}$$

the fit of the raw S1 areas of the Co57 line (fig.3.53, 122 keV [221]) yields to $ly = (2.5 \pm 0.005)$ PE/keV (given is only the fit error as uncertainty). The ly yields to an energy resolution of (24.50 ± 0.03) keV FWHM for S1s only. Since a part of the S3 peaks might be misidentified S1 peaks, the variation of the result including the S3s was checked: finding an agreeing light yield of (2.5 ± 0.008) PE/keV (given is only the fit error as uncertainty). The values are an average over the entire TPC volume. It is discussed in sec.3.10 (page 129).

The S1 spectrum might be affected by a cut off from the discriminator threshold, as mentioned before (sec.3.9, paragraph *Detector response*). A strong indication is the position of the cut off towards lower energies, which happens for all three datasets at the same S1 area. Thus the before measured light yield might be too high because

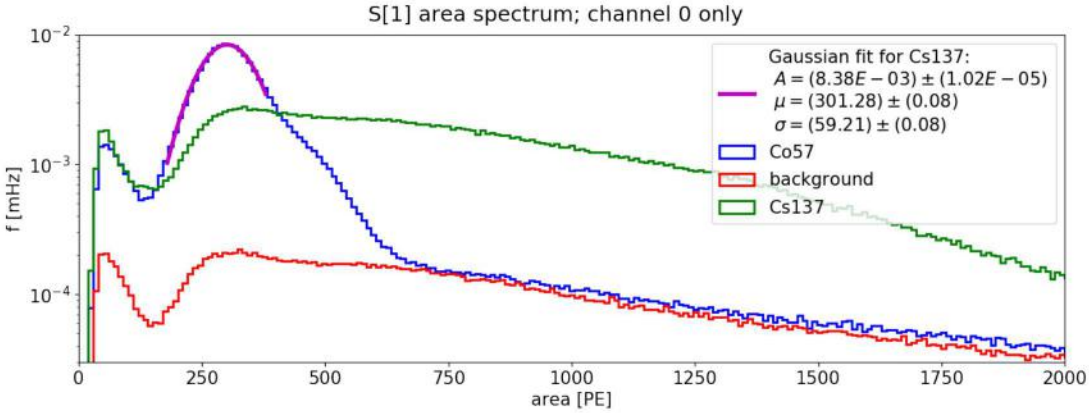

FIGURE 3.53: Fit of the S1 area of the 122 keV line of Co57 with a Gaussian resulting into: $A = (8.4 \cdot 10^{-3} \pm 1 \cdot 10^{-5})$ mHz, $\mu = (301.3 \pm 0.1)$ PE and $\sigma = (59.2 \pm 0.1)$ PE.

the fit gets shifted towards a higher S1 area. The original spectrum can be unfolded by calculating a correction function for the histogram $f_{\text{source}}(area)$ by fitting the part before the cutoff with an exponential function $e(area, f_{\text{source}}(area))$ in the region of the Compton scattering, where it shows an exponential behaviour. Assuming that these function would describe the area as well for lower areas, one can compute a correction function as:

$$c(area) = \frac{f_{\text{source}}(area)}{e(area, f_{\text{source}}(area))} \tag{3.7}$$

The S1 area spectrum can now be unfolded with this function and a constant, depending on the unfolding range (see fig.3.54 for the Cs137 based unfolding). The influence of the unfolding range was studied by varying the fit ranges and binning while aiming for extrema in the fit results. One found that the resulting peak position in the unfolded spectra is robust against the choice of the fit range and binning.

Light yields were calculated again for the unfolded Co57 spectra basing on the Cs137 and background data. The mean of the ly for the various unfolded spectra, with the uncertainty given by the variance, is: $\bar{ly} = (2.301 \pm 0.004)$ PE/keV. It is lower than the value found from the original spectra but both agree within 10%. The resulting mean energy resolution is (32.48 ± 0.26) keV FWHM, which is significantly worse than the resolution without unfolding. Nevertheless, these values are only valid under the assumption that the cut off is caused by the discriminator threshold and that the spectra could be unfolded as shown.

It is expected that the light yield depends on the interaction position in the TPC and that it decreases with an increasing distance to the PMT. This can be shown by using the fiducialization of the S1s. It allows to determine a depth depending light yield. One

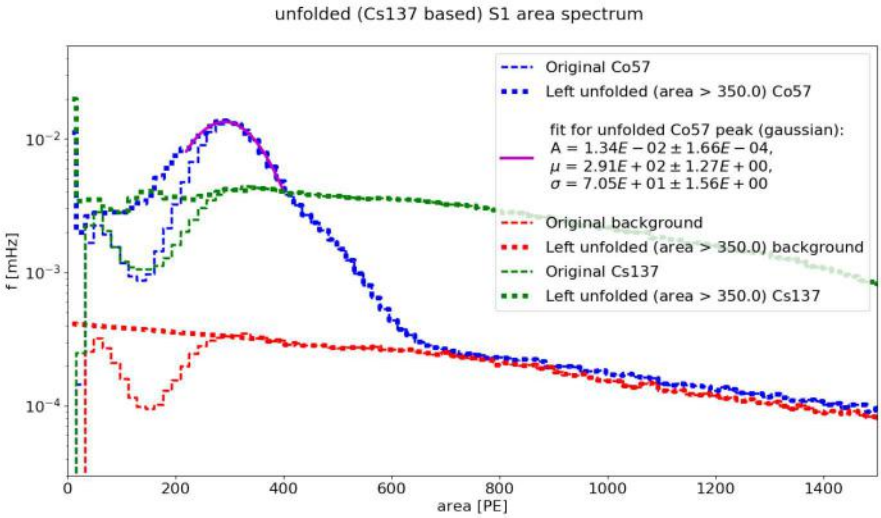

FIGURE 3.54: Unfolded and original S1 area spectra in comparison. The shown unfolding is based on the Cs137 dataset. The "left unfolded spectra" show the unfolded spectra where the unfolding is only applied left of a threshold. Shown is as well the resulting fit for the Co57 122 keV line (Gaussian, as eq.(3.6)) in the unfolded spectrum. The peak position in the Co57 moved slightly towards a lower area and thus lower light yield, compared to the original data.

sees quite some artefacts in fig.3.47 at low drift times, so events happening at the top of the active TPC volume. As before, the fiducialised S1 area distributions were fitted with a Gaussian yielding to the light yields. Fig.3.55 shows the fit results for various fiducial volume settings. Table 3.7 summarizes the fit results for the chosen fiducial volume settings. The found values disagree with the previously determined light yields, but the value for a fiducial volume between $t_d = 1\,\mu$s and $t_d = 30\,\mu$s shows a lower discrepancy, compared to the previously measured values. This yields to the conclusion that the light yield is strongly depth dependent and the previous results were averaged over the entire active TPC volume, what yields to a much lower light yield.

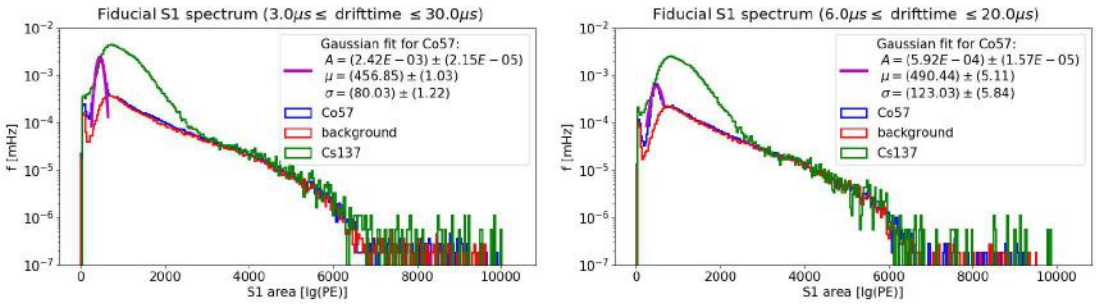

(A) Fiducial volume setting $z = 3$–$30\,\mu$s. (B) Fiducial volume setting $z = 6$–$20\,\mu$s.

FIGURE 3.55: S1 area and Co57 122 keV line fit for two example fiducial volume settings. The full absorption peak shrinks with decreasing fiducial volume. Table3.7 summarizes the result for all tested fiducial volumes.

z [μs]	μ [PE]	σ	ly [PE/keV]	$\sigma_{\text{energy}}^{\text{FWHM}}$ [keV]
1, 30	317.50 ± 1.53	85.99 ± 1.80	2.60 ± 0.01	33.06 ± 0.71
2, 30	432.72 ± 1.04	94.70 ± 1.22	3.54 ± 0.01	26.71 ± 0.35
3, 30	456.93 ± 1.29	81.33 ± 1.52	3.74 ± 0.01	21.72 ± 0.41
5, 15	474.11 ± 2.34	90.46 ± 2.74	3.88 ± 0.02	23.29 ± 0.71
6, 20	491.67 ± 6.59	128.97 ± 7.52	4.03 ± 0.05	32.02 ± 1.92
8, 30	477.07 ± 12.5	-	3.91 ± 0.10	-

TABLE 3.7: Results from the Gaussian fits determining ly for various fiducial volumes z. The fit failed for $z = [8, 30]\,\mu$s, thus the maximum at the Co57 122 keV line was given with the bin width as error. The values are, as expected, larger than the averaged value over the entire TPC volume and show a trend towards higher light yields with smaller fiducial volumes.

3.9.5 Charge yield

The light yield characterises the sensitivity of a TPC for the prompt scintillation light. The sensitivity for the ionization signal is another important performance parameter for a TPC. It is quantified by the so called charge yield cy, whereas the sum of charge and light yield should be constant against varying the electric drift field. It can be measured with a similar method as the light yield: by fitting the peak of a mono energetic line.

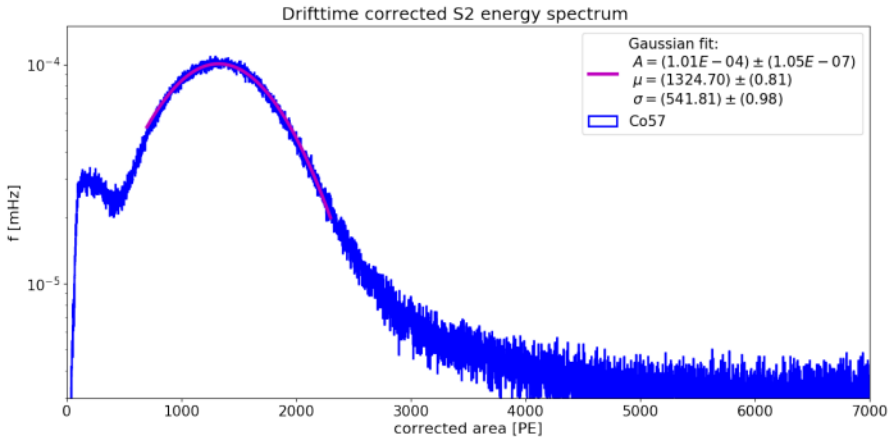

FIGURE 3.56: Drift time corrected S2 area histogram of Co57 (see sec.3.9.3). Gaussian fit of the 122 keV line, which gets shifted with the drift time correction towards higher areas.

It is expected that the S2 area is depending on the depths of the event in the TPC because of the electron loss due to impurities. Therefore the fit was performed with the corrected S2s (see sec.3.9.3). The resulting fit is shown in fig.3.56. One finds a charge yield of (10.85 ± 0.02) PE/keV at a FWHM resolution of (4.43 ± 0.03) PE/keV.

3.10 Summary and evaluation

The Bern LXe test platform was successfully designed, set up and tested. Furthermore a TPC was installed and a first characterization of the TPC in dual-phase mode was performed.

The cryogenic infrastructure consisting of a double wall cryostat with an changeable inner cryostat has been deployed. It allows for fast service intervals: it is ready for a cool down after ≈ 30 min. The cooling system consists of a cold LN2 bath and a Copper cold finger in the inner cryostat. The currently installed cooling power is about 45 W at $-100°$C, which is sufficient to cool down and liquefy 5 kg of Xenon and the inner cryostat with the TPC within about 8 h. Thus, the TPC can be operated after about 1 day. Since the space in the inner cryostat is very limited, especially around the top PMT array, an upgrade is planned with an enlarged gas volume above the inner cryostat. Also the top PMT array of the TPC will be upgraded with new PMTs.

The gas system was tested and demonstrated to be operational. However, it was found that the recirculation flow tends to oscillate. Thus a bypass mode for the inner cryostat turned out to be an important feature because it minimizes or completely suppresses the oscillations when the TPC was filled with LXe. The original gas system was extended by an gas analysis system. A better pipette system (more precise known volume and more dilution stages) would increase the usability a lot. Also a calibration of the dilution proportions, allowing for complete quantitative statements about residual gas contents, is missing yet.

A slow control system, Doberman [237, 238] that was developed for this platform, was deployed and plugins were implemented, allowing for monitoring and control of the parameters that are needed for the detector operation. The system was operated stably. The control of Doberman is done locally via the computer's terminal, to avoid external misconfiguration. Nevertheless, embedding the control of Doberman in its web display (used for the monitoring and visualization) would be convenient. The LXe levelmeters (1 long for filling, recuperation and liquid level monitoring and 3 short for levelling the TPC) were operated successfully and served very well [55]. The installed leveling mechanism allows for tilt adjustments down to the sub degree level. A reasonable upgrade of the tilt adjustment system would be an exchange of the currently used normal metric screws by some specially machined lifting rods with finer threads.

The high voltage system was deployed as well but showed some problems. The cathode high voltage was limited by the HV supply to 3.5 kV. A maximum anode high voltage of 1.4 kV was achieved. The anode field trips are suspected to be caused by an insufficient

insulation of anode and the screening mesh. It will be improved with an additional PTFE insulator.

A properly working top PMT array will allow for a x–y event position reconstruction and thus allow for a real 3D position reconstruction, which will improve the analyses results. The bottom PMT showed a slightly higher gain than specified. The current HV setting for the PMTs employs two redundant ground return channels for all PMTs together. Nevertheless, it is suspected to cause some noise amplification. Thus it might be worth splitting the return channels for the two voltage divider types of the 1" and 3" PMTs.

The DAQ system is based on the XENON1T DAQ system with CAEN V1724 ADCs [32]. Two trigger schemes were implemented: self-triggered as in XENON1T and externally triggered to acquire waveforms with the full possible event length (e.g. by a discriminator). The self-trigger mode is more flexible and thus is preferable to the here used external trigger mode that requires a more complicated cabling scheme. Furthermore, a dead time monitoring was implemented, allowing to determine the life time of a measurement. Further improvements to the current runs database, which is used for the measurement run condition monitoring, would be an easier correlation with the slow control variables and a more user-friendly interface, showing for example pre-defined source runs, run settings etc. The DAQ control could be improved by featuring automated run start and end dates and being controllable by a web interface.

A modular and scalable data processor was developed and deployed successfully. It showed a good performance. Nevertheless, it turned out that its development is very time consuming and it is not very efficient developing an own data processor, instead of modifying an existing one (like *pax*, which is used for XENON1T). Regardless of this decision, it would help if the processor would be more automated. Basing on the currently deployed processor, it would be fast to implement these features but the implementation of a widely used data processor would be more profitable.

Analysis Within the analysis of the first taken TPC data, an analysis environment was developed. The first data suffered greatly from dead time due to very high rates and a missing ADC busy monitoring. Also the dynamic range of the DAQ was exceeded, which led to problems with the peak identification, peak integration and thus event reconstruction. This was improved for the *low gain run* by running without the amplifier and having installed a dead time monitoring. Furthermore, the DAQ was operated in the external trigger scenario, which yields to a simplified event structure.

Future analyses can be improved with a better peak classification by exploiting the differences in the peak width differences (e.g. fig.3.38, page 113). This might yield to a better characterization of light and charge yield. A 10–12% higher gain than in the *low gain run* would increase the sensitivity at lower energies while not loosing important features on the high energetic tails of the S1 energies and thus might make a S1 unfolding, as shown in sec.3.9.4 in fig.3.54 (page 125), for the light yield determination unnecessary. A PMT HV of $-1350\,\mathrm{V}$ for the bottom PMT (see fig. 3.36, page 112) seems to be a better choice than the applied $-1300\,\mathrm{V}$. Furthermore, it was found that the full absorption peak in the Cs137 spectrum is missing (fig.3.41, page 115). A Monte Carlo simulation needs to be deployed to further analyse this and to understand the detector response to a Cs137 source.

The TPC was already fully operational right after its first filling with LXe. This means that events with S1 and S2 peaks were immediately observed at the applied drift and extraction fields. The electron lifetime was measured 3 days after the start of the TPC operation, i.e., the purification system was not operated for a long time before the measurement, resulting in a rather low LXe purity. An electron lifetime of $\langle\tau_e\rangle = (9.5 \pm 0.3)\,\mu\mathrm{s}$ was measured (see sec.3.9.2 on page 119). This is much lower than measured in comparable TPCs: e.g. with the XAMS TPC in Nikhef $(429 \pm 26)\,\mu\mathrm{s}$ were achieved (recirculation flow 5 SLM) [117]. Nevertheless, it should be taken into account that the purification system was not fully operational and thus was only operated in a mode where a bypass valve was partly opened, which yields to a lower Xenon flow through the inner cryostat and lowered purification. Therefore it is expected that the electron lifetime will rapidly increase, when operating the TPC with the full design recirculation flow of 3 SLM.

The drift velocity at a given drift field can be measured from the drift time distribution, as shown in fig.3.44 on page 117. With a maximum drift distance of 68 mm a drift velocity of $(1.8 \pm 0.2) \cdot 10^5$ cm/s was derived at 273.8 V/cm. Fig.3.57 illustrates the found drift velocities in comparison with other experiments. The found values agree well with the other measurements. The uncertainties in the measured velocities can be improved by acquiring more events to improve the statistics.

Light and charge yield The light yields from various detectors are hard to compare, since they depend on the drift field. The field quenching inhibits the recombination of liberated electrons with an ion [20]. These electrons are measured, after being extracted into the gas phase, by the emission of scintillation light from their collisions with Xenon atoms, which such get excited and de-excite. Electric field quenching depends on the field strength. Therefore, a light yield at zero field is used to compare the performance of different detectors.

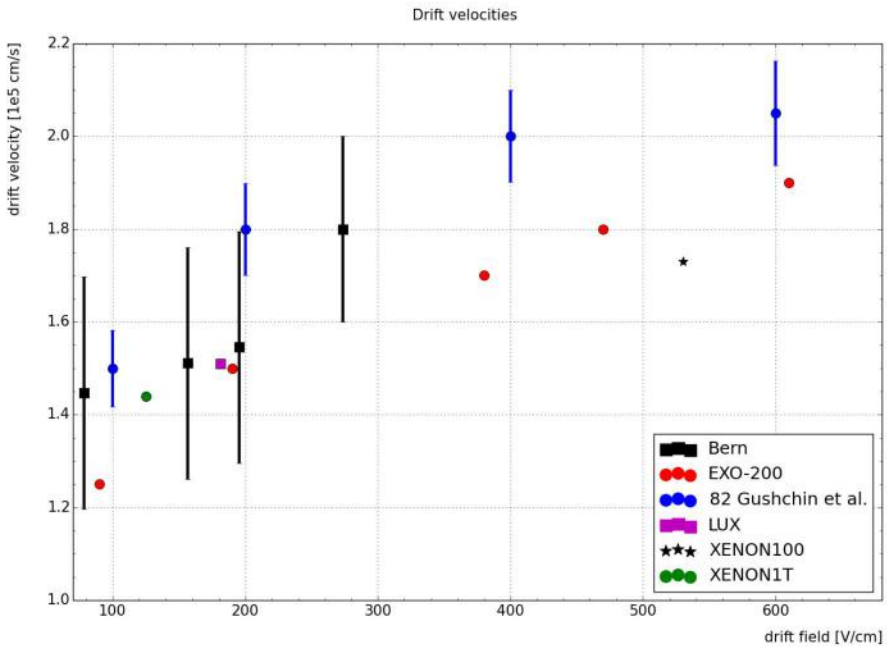

FIGURE 3.57: Drift velocities in LXe of various experiments. The velocities measured within this work are shown as black squares. The experimental uncertainties for the other experiments are shown if they are known. The results from EXO-200 are shown as red circles [12], from Gushchin et al. as blue circles [86], from the LUX dark matter search as magenta square [7], from XENON100 as black star [224] and from XENON1T as green circle [233]. The here found drift velocities agree within their uncertainties with the drift velocities found by the other experiments.

There are various conversion factors in common publications, e.g. (conversion factors k given at the applied drift field of 273.8 V/cm and for Co57 122 keV line):

1. Baudis et al. [161]: $k_1 = 0.67$
2. NEST model [218]: $k_2 = 0.68$
3. Aprile et al. [24]: $k_3 = 0.65$.

Here a value of $k_{\mathrm{NEST}} = 0.68$ will be used in the following, which yields to a conservative assumption.

At the electric field of 273.8 V/cm, applied during the low gain run (see sec.3.9, page 111), one can calculate the light yield at zero field $ly_{0\mathrm{f}}$ with the previously mentioned conversion factor and for the found light yields (sec.3.9.4, page 122). The light yield, determined from the unfolded S1 spectrum, depends highly on the assumption that the observed cut off is caused by the trigger threshold. Thus, the light yield measured from the original S1 spectrum is used here. The difference between both values will be used as systematic uncertainty on the light yield. This results in (2.5 ± 0.2) PE/keV at 273.8 V/cm for the 122 keV line. At zero field this yields to (3.7 ± 0.3) PE/keV. The

XENON100 collaboration quoted a light yield at zero field of: 4.3 PE/keV [235], for the LUX experiment a light yield of 8.8 PE/keV at zero field was given for 122 keV gammas [6], for XENON1T a light yield of (8.02 ± 0.06) PE/keV was found at a drift field of 125 V/cm with Kr83m source at 41.5 keV [233] and for the small XAMS TPC in Nikhef (5.6 ± 0.3) PE/keV was found [117]. The here used TPC shows a lower light yield, which is caused by the low gain of $(2.19 \pm 0.02)10^6$ due to skipping the 10× amplifier and low applied PMT HV of −1300 V. Furthermore, the transparency of the TPC electrodes was not optimized, which yields to a lower light yield as well. Although, the top PMT array will observe naturally much less light, its contribution to the light yield is missing because it was not operational. Nevertheless, the impact of the missing upper PMT array is expected to be rather small. The light yield is positively influenced by the high geometrical coverage of the bottom PMT and the full coverage of the walls with the PTFE reflector. A higher light yield would be achievable by diamond machining the PTFE surface, as for example done for XENON1T and demonstrated in chapter 2 (page 19).

The charge yield, that was found during the "low gain run" was also affected by the lower gain due to the lowered PMT HV and skipped 10× amplifier. A charge yield *cy* of (10.85 ± 0.02) PE/keV at a FWHM resolution of (4.43 ± 0.03) PE/keV was determined (sec.3.9.5, page 126). It was determined with the 122 keV line of the Co57 source at an applied drift field of 273.8 V/cm and with an extraction field of 1.94 kV/cm. The used dataset covered the entire TPC volume. The low extraction field might be the major reason that the charge yield is lower than in other experiments. For the Xürich II TPC, a charge yield of 783.24 PE/keV at 32.1 keV was measured (drift field of 2 kV/cm and extraction field of 10.32 kV/cm) [140]. Furthermore, the low purity affected the measured charge yield negatively because electrons get captured by the impurities.

For a uniform extraction field E, the photon yield per distance dN/dx of a single extracted electron can be described by [51]:

$$\frac{dN}{dx} = 70\left(\frac{E}{p} - 1\right)p, \tag{3.8}$$

depending on the pressure p. Thus, for the extraction field of 1.94 kV/cm and a pressure of $p = 1.42$ bar, one finds that a single electron would generate 9 photons. This agrees within 17% with the found charge yield *cy*. It means that the found charge yield originates from about 1.1 ± 0.2 electrons. Since the process has a conversion efficiency of 8% [18], this yields to about 14.2 ± 2.5 original electrons. Which is equivalent to an ionization yield of 14.2 e^-/keV for 122 keV gammas. Other experiments measured the ionization yield as well: for the neriX TPC about 34 e^-/keV was measured at about 20 keV and a drift field of 210 V/cm [17], for a ZEPLIN III prototype 55.6 e^-/keV at

3.75 kV/cm with a 80.2 keV ^{131}Xe source were measured [10]. The values depend on the extraction efficiency, so the extraction field, energy of the calibration source and loss of electrons during the drift process, i.e. the Xenon purity. The process was modelled as well by [218], resulting in about 50 e^-/keV at 130 keV. The here found value is significantly lower. It is caused by the lower applied fields, low purity, the lower sensitivity of the bottom PMT for the S2 light due to the 3 meshes and liquid surface, that are in the line of sight and the low gain.

Corrected S2 vs. S1 Using the S2 corrections, presented in sec.3.9.3 (page 122), one can compute the corrected S2 area vs. S1 area histograms for the various sources. One example is shown in fig.3.58 for Co57. Combining these informations now with the drift time property, one achieve a fiducial volume as used already in sec.3.9 (page 111) for the light yield analysis. Fig.3.59 shows the corrected S2 vs S1 area histogram for one fiducial volume. The Co57 line at 122 keV is the bright prominent feature at around $S2 = 10^3$ PE, $S1 = 10^2$ PE to $S1 = 10^3$ PE. The chosen fiducial volume excludes the artefacts at low drift times below 3 μs. The upper fiducial volume cut had barely an influence because the electron lifetime was low and thus acted as kind of a natural selection criteria.

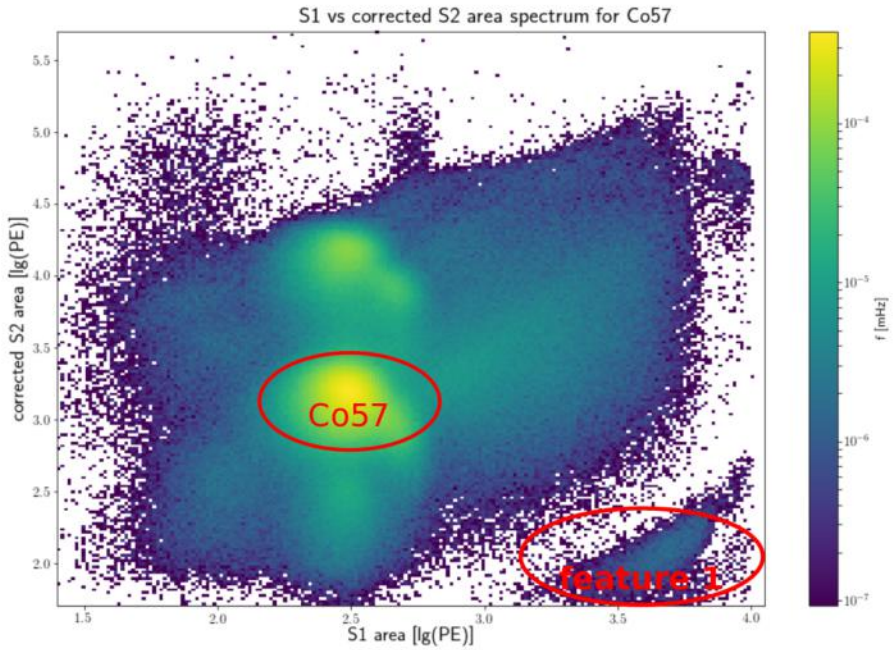

FIGURE 3.58: S1 vs. corrected S2 area for Co57. The location of the Co57 122 keV line and of the feature ("feature 1", might be caused by alphas: see text) are illustrated.

The double band structure for a given S1 is an interesting feature and it might be that always the two bands above each other for a given S1 belong to each other, even being the same peak originally. One feature at around $S2 = 10^2$ PE and $S1 = 10^3$ PE to $S1 = 10^4$ PE appears in all three datasets (feature 1, fig.3.58) and disappears when

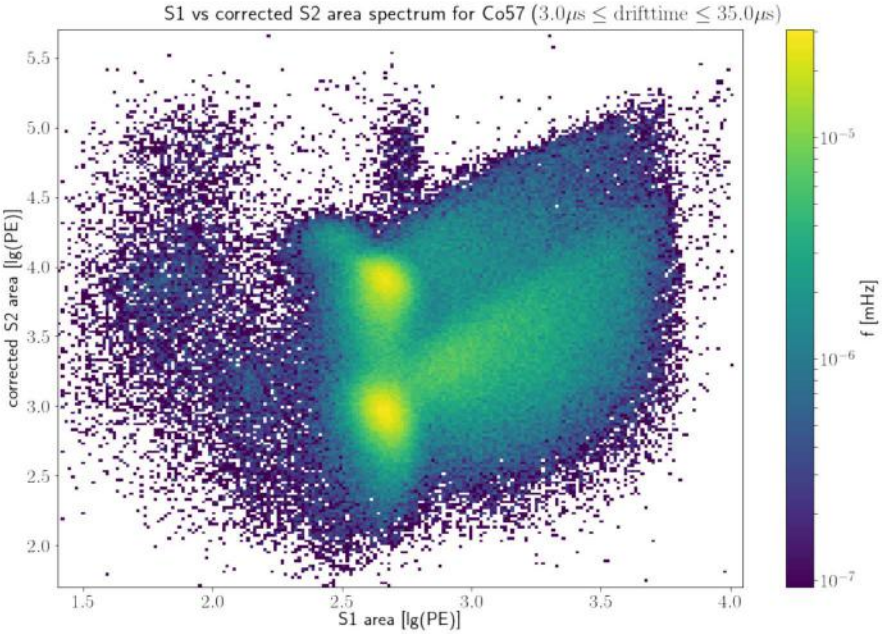

FIGURE 3.59: S1 vs. corrected S2 area for Co57 and a fiducial volume of:$[3.0, 35.0]\,\mu$s. The in fig.3.58 shown "feature 1" disappeared, what indicates that it happened close to the anode.

fiducializing the TPC (e.g. fig.3.59). The signal might be from alphas (low $S2/S1$ ratio) emitted from the TPC walls, that are only observable when happening close to the anode. The Co57 full absorption peak at 122 keV is shown in fig.3.60 in more detail. The anti-correlation between S1 and S2s becomes visible.

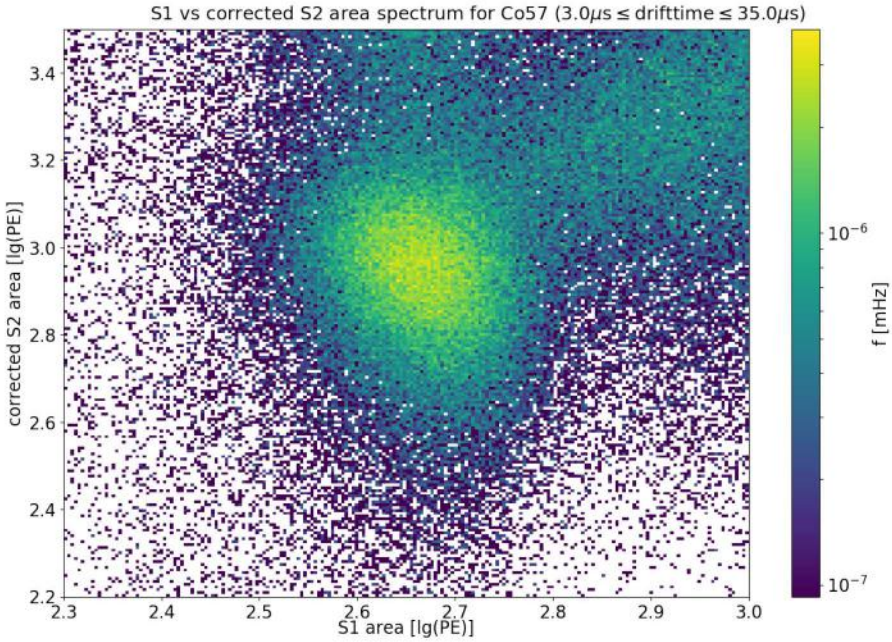

FIGURE 3.60: S1 vs. corrected S2 area for Co57 and a fiducial volume of:$[3.0, 35.0]\,\mu$s focusing on the full absorption peak around $S1 = 10^{2.6}$ PE and $S2 = 10^{3}$ PE. The full absorption peak shows already the expected anti-correlation of S2 and S1.

Chapter 4

Outlook

Liquid Xenon dual-phase time projection chambers (TPC) are currently used for the most sensitive WIMP searches [202, 201]. They deploy ton-scale target masses and exploit low background techniques to increase the sensitivity. They aim to detect a WIMP by its interaction with the Xenon atoms, which then emit VUV scintillation light. Their sensitivity depends on the used light detectors (normally PMTs) and the absorption probability of the photons on their way from the interaction to the light detector in the detector medium and on the absorption probability on the detector walls (i.e. the reflectivity of the detector walls). Within this work, the optimization of the reflectivity of the TPC walls of XENON1T was presented (chapter 2).

Beyond currently operated detectors, there is the project of constructing the ultimate dark matter detector, DARWIN [1]. It aims to explore the potential WIMP-nucleus cross section until reaching an irreducible background, limiting the further search. This background is defined by the coherent scattering of neutrinos off the target nuclei [57, 202]. This work introduced a cryogenic test platform (chapter 3) for the development of techniques that are suitable to attack the challenges during the development of future dark matter searches like DARWIN.

4.1 Reflectivity measurements and reflector design

The 178 nm scintillation light, that is emitted by an interaction with the Xenon atoms (sec.1.2.1, page 11), needs to be guided as efficiently as possible to the light detectors (sec.1.2.2, page 13). This efficiency is limited by the reflectivity of the detector walls. The XENON1T TPC walls are covered with PTFE reflectors, because PTFE as bulk material offers already a high reflectivity while showing a reasonably low outgassing

and sufficiently good radio pureness. The goal of this work was the optimization of the reflectivity of the PTFE reflectors by a surface machining. On the other side, PTFE, as reflector material, is responsible for (α,n) reactions, which yield to an important neutron background [1]. Thus, the search for alternative reflector materials and the characterization of their reflectivities will be important for future detectors like DARWIN. This and the design of PTFE reflectors demand for measuring the reflectivity of the reflectors in liquid Xenon at 178 nm.

4.1.1 Reflectivity measurements

The instrument that was used for the reflectivity measurements is the Münster reflectivity setup (sec.2.2, page 24). The measurements yield to a reflectivity profile depending on the incident angle and covering some reflection angle range with the PMT rotation (sec.2.2.2, page 29). This measurement principle has the advantage of achieving a high angular resolution and the ability to measure the reflectivity directly. Nevertheless, some draw backs of the setup were discovered (sec.2.3, page 40).

The total reflectivity can be measured alternatively, as impact on the light collection efficiency of a well characterized small TPC with changeable walls. The light collection efficiency would than only depend on the averaged wall reflectivity, assuming a homogeneous illumination of the TPC with an internal light source (e.g. Kr83m). This would result in a reflectivity relative to the initial wall reflectivity. It would be sufficient to improve the TPC reflectors and also allow to test new reflector materials.

A precise measurement of the reflection profile in liquid Xenon is challenging and affected by large uncertainties that are difficult to handle. It can be solved by using extrapolations from optical measurements to model the reflection profiles. The sample should be cooled to LXe temperatures to mimic surface structure changes at cryogenic temperatures. A measurement in vacuum would allow an extension of the results towards short wavelengths below 400 nm. The found reflection profiles can then be used to simulate the light propagation in the previous mentioned TPC. Thus, the assumptions of the extrapolation can be approved. Nevertheless, this requires a precise knowledge of the optical properties of the liquefied Xenon and assumes that the only difference is made by the total reflection in liquid Xenon on the reflector. This hypothesis can either be tested, as the simulation results depend on it, or by setting up a dedicated experiment, which aims to measure the light reflection on the reflector at large reflection angles.

The approach of measuring the reflectivity with a small TPC can be tested for example with the here presented cryogenic test platform. The use of a small TPC has the advantage that other systematics, like a limited attenuation length of the scintillation

light, have a minor influence, compared to the size of the TPC. The concept of extending the results from measurements in the optical range towards VUV wavelengths and the assumption that the major difference in LXe is due to the total refraction on the surface could be tested in first order with a simulation of the reflection processes in the Münster setup using the results of the PHIRE-2 measurements.

4.1.2 Reflector design

The reflectors for the XENON1T experiment were diamond machined, as suggested within this work (sec.2.3.4, page 49). This machining yields to a strongly increased specular reflection and optimal surface roughness. The decision is based on the increased specular peak, as observed in the measurements with the reflectivity setup. Thus it might be affected by a possible alignment issue that was found.

A quantisation of the impact of the increased specular reflectivity is hard to derive, because the achieved surface is highly inhomogeneous. Nevertheless, an estimation of the impact of the reflectivity on the light yield is of great interest because the specular reflection appears only at large incidence angles. Thus it might introduce a directional bias for events close to the detector walls. The answer on this question will help to decide whether a diamond machining for future detectors is the right way, or whether the diffuse reflection should be increased again.

If the diamond machining will be in future still the desired machining technique, some improvements are possible, regarding the XENON1T reflector machining. The machining should be done with a custom made diamond tool, that has a longer cutting edge than the used tool, to achieve a more homogeneous and less orientation dependent reflectivity. Furthermore, the stability of the surface should be tested, regarding mechanical stress due to dirt and installation work, because it might affect the reflectivity significantly.

4.2 Future development of the Bern LXe test platform

The design of future liquid Xenon TPCs will require new technologies, which will be developed and tested within small experiments. A test platform for this purpose was successfully developed and tested within this work. First data were acquired with a dual-phase TPC that was deployed in the LXe test platform.

One of the challenges designing bigger LXe TPCs is, how to achieve a homogeneous extraction field (sec.1.2.2, page 13). It demands a perfect alignment of the anode electrode, the gate electrode and the liquid level: the field becomes inhomogeneous if they are not

parallel to each other. It gets worse with the increasing size of the electrodes. Since they have to be as transparent as possible, their mechanical stability becomes an issue: they show significant deformations. One solution for this challenge might be the conversion towards single-phase TPCs. They use proportional scintillation in the presence of strong electric fields in LXe, to convert the ionization signal into scintillation light. This would have the further advantage that the top PMT array can be directly immersed in LXe, which will improve the light yield because the total reflection on the liquid surface does not reduce the amount of photons that are observable by the top array. The here introduced TPC aims for a direct comparison between the dual-phase mode, as presented here, and the single-phase mode. It allows for a straight forward conversion, as presented in [237].

The first measurements with the test platform indicated possible improvements (see sec.3.10, page 127). They are important to be implemented because they will yield to a stable performance of the TPC, which is crucial for a comparison between the performance in dual-phase mode and single-phase mode. One important issues is the low Xenon purity, which prevents the results from being reproducible. A second issue that needs to be solved, is the low extraction and drift field, because a high anode field is required to achieve proportional scintillation [31]. The hardware modification are straight forward to implement. The software changes are more challenging and the time requirement depends largely on the invested man power.

As mentioned before, the test platform with its TPC can also be used for future reflectivity measurements. It requires a second inner reflector tube and to test the reproducability of the measured light yield after opening and closing the TPC and exchange of the reflector tube. This concept would also allow to test different materials than PTFE as reflector for Xenon scintillation light.

Bibliography

[1] Aalbers, J., Agostini, F., Alfonsi, M., et al. 2016, Journal of Cosmology and Astroparticle Physics, 11, 017

[2] Aalseth, C. E., Barbeau, P. S., Colaresi, J., et al. 2011, Physical Review Letters, 107, doi:10.1103/physrevlett.107.141301. https://doi.org/10.1103/physrevlett.107.141301

[3] Aartsen, M. G., Abbasi, R., Abdou, Y., et al. 2013, Physical Review Letters, 110, 131302

[4] Abramowski, A., Aharonian, F., Ait Benkhali, F., et al. 2014, Phys. Rev. D, 90, 112012

[5] Accu-Glass. 2017, Accu Glass cables. https://accuglassproducts.com

[6] Akerib, D. S., Araújo, H. M., Bai, X., et al. 2014, Phys. Rev. Lett., 112, 091303. https://link.aps.org/doi/10.1103/PhysRevLett.112.091303

[7] Akerib, D. S., Araújo, H. M., Bai, X., et al. 2014, Physical Review Letters, 112, 091303

[8] Akerib, D. S., Alsum, S., Araújo, H. M., et al. 2017, Physical Review Letters, 118, 021303

[9] Akimov, D., Bewick, A., Davidge, D., et al. 2002, Physics Letters B, 524, 245–251. http://www.sciencedirect.com/science/article/pii/S0370269301014113

[10] Akimov, D., Afanasyev, V., Alexandrov, I., et al. 2014, Journal of Instrumentation, 9, P11014. http://stacks.iop.org/1748-0221/9/i=11/a=P11014

[11] Albers, J. 2017, XENON1T peak classification. http://xenon1t.github.io/pax/_modules/pax/plugins/peak_processing/ClassifyPeaks.html#AdHocClassification1T

[12] Albert, J. B., Barbeau, P. S., Beck, D., et al. 2017, Phys. Rev. C, 95, 025502. https://link.aps.org/doi/10.1103/PhysRevC.95.025502

[13] Alner, G., Araujo, H., Arnison, G., et al. 2005, Astroparticle Physics, 23, 444. https://doi.org/10.1016/j.astropartphys.2005.02.004

[14] Alpher, R. A., Bethe, H., & Gamow, G. 1948, Physical Review, 73, 803

[15] Amare, J., Cebrian, S., Cuesta, C., et al. 2015, ArXiv e-prints, arXiv:1508.07213

[16] Angloher, G., Bauer, M., Bavykina, I., et al. 2012, European Physical Journal C, 72, 1971

[17] Anthony, M. 2015, in Invisibles 2015 Workshop. https://indico.cern.ch/event/351600/contributions/1753915/attachments/695349/954819/matt_anthony_neriX_presentation_invisibles_mda_v4.pdf

[18] Aprile, E., Bolotnikov, A. E., Bolozdynya, A. I., & Doke, T. 2006, Noble Gas Detectors (Wiley-VCH)

[19] Aprile, E., & Doke, T. 2010, Reviews of Modern Physics, 82, 2053

[20] Aprile, E., & Doke, T. 2010, Rev. Mod. Phys., 82, 2053. `https://link.aps.org/doi/10.1103/RevModPhys.82.2053`

[21] Aprile, E., Giboni, K. L., Majewski, P., et al. 2005, Physical Review D, 72, 072006

[22] Aprile, E., Mukherjee, R., & Suzuki, M. 1991, in Conference Record of the 1991 IEEE Nuclear Science Symposium and Medical Imaging Conference, 486–489 vol.1

[23] Aprile, E., & XENON1T collaboration. 2012, ArXiv e-prints, arXiv:1206.6288

[24] Aprile, E., Dahl, C. E., de Viveiros, L., et al. 2006, Physical Review Letters, 97, 081302

[25] Aprile, E., Arisaka, K., Arneodo, F., et al. 2011, Physical Review Letters, 107, 131302

[26] Aprile, E., et al. 2012, Phys. Rev. Lett., 109, 181301

[27] Aprile, E., Budnik, R., Choi, B., et al. 2012, Physical Review D, 86, 112004

[28] Aprile, E., Beck, M., Bokeloh, K., et al. 2012, Journal of Instrumentation, 7, P10005

[29] Aprile, E., Agostini, F., Alfonsi, M., et al. 2014, Journal of Instrumentation, 9, P11006

[30] Aprile, E., Alfonsi, M., Arisaka, K., et al. 2014, Journal of Physics G Nuclear Physics, 41, 035201

[31] Aprile, E., Contreras, H., Goetzke, L. W., et al. 2014, ArXiv e-prints, arXiv:1408.6206

[32] Aprile, E., Aalbers, J., Agostini, F., et al. 2016, JCAP, 4, 027

[33] Aprile, E., Aalbers, J., Agostini, F., et al. 2017, ArXiv e-prints, arXiv:1705.06655

[34] Aprile, E., et al. 2017, Eur. Phys. J., C77, 275

[35] Archambault, S., Aubin, F., Auger, M., et al. 2009, Physics Letters B, 682, 185

[36] ArDM Collaboration, Badertscher, A., Bay, F., et al. 2013, ArXiv e-prints, arXiv:1307.0117

[37] Association, C. G. 2017, American National Standards. `http://www.cganet.com/american-national-standards.php`

[38] B. Zitzer for the VERITAS Collaboration. 2015, ArXiv e-prints, arXiv:1503.00743

[39] Baldini, A., Bemporad, C., Cei, F., et al. 2004, ArXiv Physics e-prints, physics/0401072

[40] Baldini, A., Bemporad, C., Cei, F., et al. 2005, Nuclear Instruments and Methods in Physics Research A, 545, 753

[41] Baldini, A., et al. 2005, Nucl. Instrum. Meth., A545, 753

[42] Barabanov, I. R., Gavrin, V. N., & Pshukov, A. M. 1987, Nucl. Instrum. Meth., A254, 355

[43] Barkov, L., Grebenuk, A., Ryskulov, N., Stepanov, P., & Zverev, S. 1996, Nuclear Instruments and Methods in Physics Research Section A: Accelerators, Spectrometers, Detectors and Associated Equipment, 379, 482–483, proceedings of the

Sixth International Conference on Instrumentation for Experiments at e+ e- Colliders. http://www.sciencedirect.com/science/article/pii/0168900299005185

[44] Barrow, P., Baudis, L., Cichon, D., et al. 2017, Journal of Instrumentation, 12, P01024

[45] Baudis, L. 2012, Physics of the Dark Universe, 1, 94. https://doi.org/10.1016/j.dark.2012.10.006

[46] Baudis, L. 2014, Physics of the Dark Universe, 4, 50

[47] Baudis, L., Behrens, A., Ferella, A., et al. 2013, Journal of Instrumentation, 8, P04026

[48] Baudis, L., Ferella, A., Kish, A., et al. 2014, Journal of Cosmology and Astroparticle Physics, 1, 044

[49] Behnke, E., Collar, J. I., Cooper, P. S., et al. 2008, Science, 319, 933. https://doi.org/10.1126/science.1149999

[50] Behrens, A. 2014, PhD thesis, Uni Zürich. http://www.physik.uzh.ch/groups/groupbaudis/darkmatter/theses/xenon/thesis_behrens.pdf

[51] Belogurov, S., Bolozdynya, A., Churakov, D., et al. 1995, in 1995 IEEE Nuclear Science Symposium and Medical Imaging Conference Record, Vol. 1, 519–523 vol.1

[52] Bernabei, R., Belli, P., Bussolotti, A., et al. 2008, Nuclear Instruments and Methods in Physics Research A, 592, 297

[53] Bernabei, R., Belli, P., Cappella, F., et al. 2008, European Physical Journal C, 56, 333

[54] Bernabei, R., Belli, P., Cappella, F., et al. 2010, European Physical Journal C, 67, 39

[55] Berner, R. 2016, Master's thesis, Uni Bern. http://old.lhep.unibe.ch/darkmatter/darkwiki/lib/exe/fetch.php?media=local:labtpc:levelmeter:bachelorthesis_romanberner_levelmeters.pdf

[56] Bertone, G., Hooper, D., & Silk, J. 2005, Physics Reports, 405, 279

[57] Billard, J., Figueroa-Feliciano, E., & Strigari, L. 2014, Physical Review D, 89, 023524

[58] Birkedal, A., Matchev, K., & Perelstein, M. 2004, Phys. Rev. D, 70, 077701. https://link.aps.org/doi/10.1103/PhysRevD.70.077701

[59] Bokeloh, K. 2013, PhD thesis, U. Münster. https://miami.uni-muenster.de/Record/741a8147-268c-4c0c-bc9d-dac89e67d601

[60] Braun, J., Hubert, D., & for the IceCube Collaboration. 2009, ArXiv e-prints, arXiv:0906.1615

[61] Bricola, S., Menegolli, A., Prata, M., et al. 2007, Nuclear Physics B - Proceedings Supplements, 172, 260–262, proceedings of the 10th Topical Seminar on Innovative Particle and Radiation Detectors. http://www.sciencedirect.com/science/article/pii/S0920563207006093

[62] Bütikofer, L. 2017, PhD thesis, Uni Bern. https://baselbern.swissbib.ch/Record/441386180

[63] CAEN. 2017, N840 8 Channel Leading Edge Discriminator. http://www.caen.it/csite/CaenProd.jsp?parent=12&idmod=272

[64] CAEN. 2017, NIM N1470 HV. http://www.caen.it/csite/CaenProd.jsp?parent=21&idmod=599

[65] CAEN. 2017, V1724. http://www.caen.it/csite/CaenProd.jsp?parent=11&idmod=483

[66] CAEN. 2017, NIM N471A HV. http://www.caen.it/csite/CaenProd.jsp?parent=21&idmod=240

[67] CAEN. 2017, A1535 HV board. http://www.caen.it/csite/CaenProd.jsp?parent=20&idmod=533

[68] Cannon, J. R. 1984, The one-dimensional heat equation, Vol. 23 (Addison-Wesley Pub. Co.)

[69] Cao, X., Chen, X., Chen, Y., et al. 2014, Science China Physics, Mechanics, and Astronomy, 57, 1476

[70] CDMS Collaboration, Agnese, R., Ahmed, Z., et al. 2013, ArXiv e-prints, arXiv:1304.4279

[71] CDMS II Collaboration, Ahmed, Z., Akerib, D. S., et al. 2010, Science, 327, 1619

[72] Coderre, D. 2017, kodiaq. https://github.com/XENON1T/kodiaq

[73] Conrad, J., Cohen-Tanugi, J., & Strigari, L. E. 2015, Soviet Journal of Experimental and Theoretical Physics, 121, 1104

[74] Contreras Palacios, H. A. 2015, PhD thesis, Columbia University, doi:10.7916/d8wh2p43. https://academiccommons.columbia.edu/catalog/ac:207892

[75] Corbelli, E., & Salucci, P. 2000, Monthly Notices of the RAS, 311, 441

[76] CryoCon. 2017, Model 22C Cryogenic Temperature Controller. http://www.cryocon.com/M22CProdFolder.php

[77] Dar, A. 1995, Astrophysical Journal, 449, 550

[78] DEAP-3600 Collaboration, :, Amaudruz, P.-A., et al. 2017, ArXiv e-prints, arXiv:1707.08042

[79] developers, G. 2017, Git. https://git-scm.com/

[80] developers, N. 2017, NumPy. http://www.numpy.org

[81] developers, S. 2017, SciPy. http://www.numpy.org

[82] Durell, C., Scharpf, D., McKee, G., et al. 2015, in Sensors, Systems, and Next-Generation Satellites XIX, ed. R. Meynart, S. P. Neeck, & H. Shimoda (SPIE). https://doi.org/10.1117/12.2195503

[83] Edwards, B., Araújo, H. M., Chepel, V., et al. 2008, Astroparticle Physics, 30, 54

[84] Eidelman, S., Hayes, K., Olive, K., et al. 2004, Physics Letters B, 592, 1+. http://pdg.lbl.gov

[85] Elsässer, D., & Mannheim, K. 2005, New Astronomy Review, 49, 297

[86] E.M. Gushchin, A. K., & Obodovskii, I. 1982, Sov. Phys. JETP, 55. http://jetp.ac.ru/cgi-bin/dn/e_055_04_0650.pdf

[87] Engineering, G. L. 2017, Custom made etched meshes. https://www.greatlakeseng.com/

[88] et al., E. A. 2013, Facility and method for supplying liquid xenon

[89] Fields, B. D., Freese, K., & Graff, D. S. 2000, Astrophysical Journal, 534, 265

[90] Foundation, P. S. 2017, pickle — Python object serialization. https://docs.python.org/3/library/pickle.html

[91] Foundation, P. S. 2017, Python 3.6. https://www.python.org/downloads/release/python-360/

[92] Fox, P. J., Harnik, R., Kopp, J., & Tsai, Y. 2011, Physical Review D, 84, doi:10.1103/physrevd.84.014028. https://doi.org/10.1103/physrevd.84.014028

[93] Frandsen, M. T., Kahlhoefer, F., March-Russell, J., et al. 2011, Physical Review D, 84, 041301

[94] Frankiewicz, K. 2015, ArXiv e-prints, arXiv:1510.07999

[95] Freeman, K. C. 1970, Astrophysical Journal, 160, 811

[96] Freese, K., Fields, B., & Graff, D. 2000, Nuclear Physics B Proceedings Supplements, 80, 03

[97] Freese, K., Lisanti, M., & Savage, C. 2013, Reviews of Modern Physics, 85, 1561

[98] French, R. H., Rodríguez-Parada, J. M., Yang, M. K., et al. 2009, in 2009 34th IEEE Photovoltaic Specialists Conference (PVSC), 000394–000399

[99] Gas, S. P. 2017, Rare Gas/Nitrogen Purification - PS3-MT3. http://www.saespuregas.com/Products/Gas-Purifier/PS3-MT3.html

[100] GmbH, P. G. . O. 2017, PGO praezisions glas and optik. Quartz glass transmission. https://www.pgo-online.com/de/katalog/quarzglas.html

[101] Grace, E., & Nikkel, J. A. 2017, Nucl. Instrum. Meth., A867, 204

[102] Griest, K. 2002, Encyclopedia of Astronomy and Astrophysics, doi:10.1888/0333750888/2634

[103] Griest, K., Alcock, C., Allsman, R. A., et al. 1995, ArXiv Astrophysics e-prints, astro-ph/9506016

[104] Guillory, J. K. 2009, Journal of Medicinal Chemistry, 52, 5560, pMID: 19586035. http://dx.doi.org/10.1021/jm9009026

[105] Gunderson, K., Thomas, N., & Whitby, J. A. 2006, PLANSS, 54, 1046

[106] Haffke, M., Baudis, L., Bruch, T., et al. 2011, Nuclear Instruments and Methods in Physics Research A, 643, 36

[107] Hamamatsu. 2017, R8520-406 PMT. R8520-406

[108] Hamamatsu. 2017, R11410-10 PMT. https://www.hamamatsu.com/sp/hpe/HamamatsuNews/HamaNews_0211.pdf

[109] Hamamatsu. 2017, R8520-406 PMT. http://www.hamamatsu.com/us/en/product/category/3100/3001/R8520-406/index.html

[110] Hamamatsu. 2017, PHOTOMULTIPLIER TUBES. https://www.hamamatsu.com/resources/pdf/etd/PMT_handbook_v3aE.pdf

[111] Hastings, T. 2017, HFM-300 / HFC-302. http://www.teledyne-hi.com/products-services/thermal-mass-flow/hfm-300-hfc-302

[112] Hayashi, E., & White, S. D. M. 2008, Monthly Notices of the RAS, 388, 2

[113] Heath, D. F., & Sacher, P. A. 1966, Applied Optics, 5, 937. https://doi.org/10.1364/ao.5.000937

[114] Heusser, G. 1995, Annual Review of Nuclear and Particle Science, 45, 543. https://doi.org/10.1146/annurev.ns.45.120195.002551

[115] Hinshaw, G., Weiland, J. L., Hill, R. S., et al. 2009, Astrophysical Journal, Supplement, 180, 225

[116] Hitachi, A., Takahashi, T., Funayama, N., et al. 1983, Phys. Rev. B, 27, 5279. https://link.aps.org/doi/10.1103/PhysRevB.27.5279

[117] Hogenbirk, E., Aalbers, J., Bader, M., et al. 2016, Nuclear Instruments and Methods in Physics Research A, 840, 87

[118] Hoh, S. Y., Komaragiri, J. R., & Wan Abdullah, W. A. T. 2016, in American Institute of Physics Conference Series, Vol. 1704, American Institute of Physics Conference Series, 020005

[119] Horn, B. K. P., & Sjoberg, R. W. 1979, Appl. Opt., 18, 1770–1779. http://ao.osa.org/abstract.cfm?URI=ao-18-11-1770

[120] Horn, M., Belov, V., Akimov, D., et al. 2011, Physics Letters B, 705, 471–476. http://www.sciencedirect.com/science/article/pii/S0370269311012822

[121] Huang, S. S.-S., & Freeman, G. R. 1978, The Journal of Chemical Physics, 68, 1355. https://doi.org/10.1063/1.435954

[122] HUBER+SUHNER. 2017, RF cables and cable assemblies. http://www.hubersuhner.com/en/Products/Radio-Frequency/Cables

[123] Hunter, J. D. 2007, Computing In Science & Engineering, 9, 90

[124] Inc., E. 2017, Residual Gas Analyzer Models XTx00(M). http://www.extorr.com/products/specifications

[125] Instruments, N. 2017, USB-6008. http://sine.ni.com/nips/cds/view/p/lang/it/nid/201986

[126] Instruments, O. 2017, Oxford Instruments cryostat. https://www.oxford-instruments.com/

[127] James, F., & Roos, M. 1975, Comput. Phys. Commun., 10, 343

[128] Janecek, M. 2012, IEEE Transactions on Nuclear Science, 59, 490

[129] Janecek, M. 2012, IEEE Transactions on Nuclear Science, 59, 490

[130] Janecek, M., & Moses, W. W. 2008, IEEE Transactions on Nuclear Science, 55, 2432

[131] Jost, B., Gundlach, B., Pommerol, A., et al. 2013, Icarus, 225, 352

[132] Jungman, G., Kamionkowski, M., & Griest, K. 1996, Physics Reports, 267, 195

[133] Kadkhoda, P., Ristau, D., & von Alvensleben, F. 1999, in Laser-Induced Damage in Optical Materials: 1998, ed. G. J. Exarhos, A. H. Guenther, M. R. Kozlowski, K. L. Lewis, & M. J. Soileau (SPIE). https://doi.org/10.1117/12.344390

[134] Kadkhoda, P., Ristau, D., & von Alvensleben, F. 1999, in Laser-Induced Damage in Optical Materials: 1998, ed. G. J. Exarhos, A. H. Guenther, M. R. Kozlowski, K. L. Lewis, & M. J. Soileau (SPIE). https://doi.org/10.1117/12.344390

[135] Kaminsky, B. 2017, A rough test of the reflectivity at optical wavelengths. http://old.lhep.unibe.ch/darkmatter/darkwiki/doku.php?id=xenon:tpc:optical_tests:1st_green_test

[136] Kaminsky, B. 2017, Systematic measurements and X calibration 2nd. http://old.lhep.unibe.ch/darkmatter/darkwiki/doku.php?id=xenon:tpc:systematics_x_calib

[137] Kapteyn, J. C. 1922, Astrophysical Journal, 55, 302

[138] Kastens, L. W., Cahn, S. B., Manzur, A., & McKinsey, D. N. 2009, Physical Review C, 80, 045809

[139] Kiko, J. 2001, Nuclear Instruments and Methods in Physics Research A, 460, 272

[140] Kish, A. 2017, in Swiss Physical Society Annual Meeting. https://indico.cern.ch/event/611331/contributions/2645659/attachments/1512783/2359702/Kish_XurichII_SPS-CHIPP_2017.pdf

[141] Kourkchi, E., Khosroshahi, H. G., Carter, D., et al. 2012, Monthly Notices of the RAS, 420, 2819

[142] Kowalski, M., Rubin, D., Aldering, G., et al. 2008, Astrophysical Journal, 686, 749

[143] Kubota, S., Suzuki, M., & Ruan(Gen), J.-z. 1980, Phys. Rev. B, 21, 2632. https://link.aps.org/doi/10.1103/PhysRevB.21.2632

[144] Kuijken, K., & Gilmore, G. 1989, Monthly Notices of the RAS, 239, 651

[145] Lakeshore. 2017, Model 336 Cryogenic Temperature Controller. http://www.lakeshore.com/products/Cryogenic-Temperature-Controllers/Model-336/Pages/Overview.aspx

[146] Lambert, J. H. 1760, Photometria, sive De mensura et gradibus luminus, colorum et umbrae (Leipzig : W. Engelmann)

[147] Lansiart, A., Seigneur, A., Moretti, J.-L., & Morucci, J.-P. 1976, Nuclear Instruments and Methods, 135, 47. https://doi.org/10.1016/0029-554x(76)90824-7

[148] Lesker, K. J. 2017, Multi-Pin Bayonet Feedthrough - CF Flange, Single-Ended. http://www.lesker.com/newweb/feedthroughs/instrument_feedthroughs_mpc_singleend.cfm?pgid=cf

[149] Lesker, K. J. 2017, Power Feedthroughs - CF Flanged 5,000 Volts. http://www.lesker.com/newweb/feedthroughs/power_feedthroughs.cfm?pgid=5kv_cf

[150] Levy, C. 2014, PhD thesis, WWU Münster. http://repositorium.uni-muenster.de/document/miami/42495273-2cc7-4632-99af-accf074921e7/diss_levy.pdf

[151] Leybold. 2017, TRIVAC. https://www.leybold.com/en/products/oil-sealed-vacuum-pumps/trivac/

[152] Leybold. 2017, TRIVAC. https://www.leyboldproducts.de/en/products/high-vacuum-pumps/turbovac-turbovac-mag/turbovac-i-ix-hybrid-bearings/pumps/680/turbovac-450-i/ix?c=7171

[153] Liddle, A. 2015, An Introduction to Modern Cosmology (Wiley)

[154] Lin, Q., Wei, Y., Bao, J., et al. 2014, Journal of Instrumentation, 9, P04014

[155] Lisanti, M. 2017, in New Frontiers in Fields and Strings (TASI 2015) - Proceedings of the 2015 Theoretical Advanced Study Institute in Elementary Particle Physics. Edited by POLCHINSKI JOSEPH ET AL. Published by World Scientific Publishing Co. Pte. Ltd., 2017. ISBN #9789813149441, pp. 399-446, ed. J. Polchinski & et al., 399–446

[156] Low, L. F. 2016, Modern Physics Letters A, 31, 1675002. http://www.worldscientific.com/doi/abs/10.1142/S021773231675002X

[157] Lung, K., Arisaka, K., Bargetzi, A., et al. 2012, Nuclear Instruments and Methods in Physics Research A, 696, 32

[158] LUX Collaboration, Akerib, D. S., Araújo, H. M., et al. 2015, ArXiv e-prints, arXiv:1512.03133

[159] LUX Collaboration, Akerib, D. S., Alsum, S., et al. 2016, ArXiv e-prints, arXiv:1608.05381

[160] Madrid, C. 2017, HAMAMATSU R8520 PMTs PRESSURE TEST. http://wwwae.ciemat.es/~puerta/doublechoozpubs/P_test_v4.pdf

[161] Manalaysay, A., Undagoitia, T. M., Askin, A., et al. 2010, Review of Scientific Instruments, 81, 073303

[162] Masaki Yamashita for the XMASS collaboration. 2015, ArXiv e-prints, arXiv:1511.07597

[163] Massey, R., Rhodes, J., Ellis, R., et al. 2007, Nature, 445, 286

[164] McPherson. 2017, 632 Deuterium lamp. http://www.mcphersoninc.com/pdf/632.pdf

[165] Mei, D.-M., & Hime, A. 2006, Physical Review D, 73, 053004

[166] Meirose, B. 2016, Overview of Dark Matter searches at the ATLAS experiment, Tech. Rep. ATL-PHYS-PROC-2016-023, CERN, Geneva. https://cds.cern.ch/record/2128978

[167] Merle, A. 2017, ArXiv e-prints, arXiv:1702.08430

[168] Merritt, D., Graham, A. W., Moore, B., Diemand, J., & Terzić, B. 2006, Astronomical Journal, 132, 2685

[169] MongoDB, I. 2017, MongoDB. https://www.mongodb.com/

[170] Monteiro, C. M. B., Fernandes, L. M. P., Lopes, J. A. M., et al. 2007, Journal of Instrumentation, 2, P05001. http://stacks.iop.org/1748-0221/2/i=05/a=P05001

[171] More, S., Diemer, B., & Kravtsov, A. V. 2015, The Astrophysical Journal, 810, 36. http://stacks.iop.org/0004-637X/810/i=1/a=36

[172] Navarro, J. F., Frenk, C. S., & White, S. D. M. 1996, Astrophysical Journal, 462, 563

[173] Neumeier, A., Dandl, T., Heindl, T., et al. 2015, EPL (Europhysics Letters), 109, 12001

[174] Neves, F., Lindote, A., Morozov, A., et al. 2017, Journal of Instrumentation, 12, P01017. http://stacks.iop.org/1748-0221/12/i=01/a=P01017

[175] Neves, F., Lindote, A., Morozov, A., et al. 2017, Journal of Instrumentation, 12, P01017

[176] Nicodemus, F. E., Richmond, J. C., Hsia, J. J., Ginsberg, I. W., & Limperis, T. 1977, National Bureau of Standards

[177] Ongmongkolkul, P. 2017, Interactive Minimization Tools based on MINUIT. https://github.com/iminuit/iminuit

[178] Oort, J. H. 1932, Bulletin Astronomical Institute of the Netherlands, 6, 249

[179] Ozone, K. 2005, PhD thesis, University of Tokyo. http://meg.icepp.s.u-tokyo.ac.jp/docs/theses/ozoned.pdf

[180] Palacios, H. A. C. 2015, PhD thesis, Columbia University. https://doi.org/10.7916/D8WH2P43

[181] PandaX-II Collaboration, :, Tan, A., et al. 2016, ArXiv e-prints, arXiv:1607.07400

[182] PandaX-II Collaboration, :, Cui, X., et al. 2017, ArXiv e-prints, arXiv:1708.06917

[183] Peacock, J. A., Cole, S., Norberg, P., et al. 2001, Nature, 410, 169

[184] Peccei, R. D., & Quinn, H. R. 1977, Physical Review Letters, 38, 1440

[185] Percival, W. J., Cole, S., Eisenstein, D. J., et al. 2007, Monthly Notices of the RAS, 381, 1053

[186] Planck Collaboration, Adam, R., Ade, P. A. R., et al. 2016, Astronomy and Astrophysics, 594, A1

[187] Plante, G. 2012, PhD thesis, Columbia University

[188] Plante, G., Aprile, E., Budnik, R., et al. 2011, Phys. Rev. C, 84, 045805. https://link.aps.org/doi/10.1103/PhysRevC.84.045805

[189] PONT, D. 2017, Teflon PTFE. http://www.rjchase.com/ptfe_handbook.pdf

[190] Products, M. V. 2017, Angle Valve. https://www.mdcvacuum.com/DisplayPart.aspx?d=MDC&wr=&p=312029

[191] Queiroz, F. S. 2016, ArXiv e-prints, arXiv:1605.08788

[192] Raine, D., & Thomas, E. 2001, An Introduction to the Science of Cosmology (Series in Astronomy and Astrophysics) (CRC Press)

[193] Rau, W., & Heusser, G. 2000, Applied Radiation and Isotopes, 53, 371–375. http://www.sciencedirect.com/science/article/pii/S096980430000155X

[194] Read, J. I. 2014, Journal of Physics G Nuclear Physics, 41, 063101

[195] Refregier, A. 2003, Annual Review of Astron and Astrophys, 41, 645

[196] Regenfus, C. 2008, ArXiv e-prints, arXiv:0812.1497

[197] rootpy developers. 2017, rootpy: Pythonic ROOT. http://www.rootpy.org/

[198] Rosendahl, S. 2015, PhD thesis, WWU Münster. https://www.uni-muenster.de/Physik.KP/AGWeinheimer/en/arbeitsgruppe/arbeiten.html

[199] Schneider, S. 2012, Master's thesis, WWU Münster. http://www.uni-muenster.de/Physik.KP/AGWeinheimer/Files/theses/Bachelor_Sergej_Schneider.pdf

[200] Schumann, M. 2012, ArXiv e-prints, arXiv:1206.2169

[201] Schumann, M. 2015, in European Physical Journal Web of Conferences, Vol. 96, European Physical Journal Web of Conferences, 01027

[202] Schumann, M., Baudis, L., Bütikofer, L., Kish, A., & Selvi, M. 2015, JCAP, 10, 016

[203] Scientific, P. 2017, 776 Sixteen Channel Photomultiplier Preamplifier. http://www.phillipsscientific.com/preview/776pre.htm

[204] Silva, C., Pinto da Cunha, J., Pereira, A., et al. 2010, Journal of Applied Physics, 107, 064902

[205] Silva, C., Pinto da Cunha, J., Pereira, A., et al. 2010, Nuclear Instruments and Methods in Physics Research A, 619, 59

[206] Silva, C. P., Pinto da Cunha, J., Chepel, V., et al. 2007, Nuclear Instruments and Methods in Physics Research A, 580, 322

[207] Smartec. 2017, Smartec UTI. http://smartec-sensors.com/cms/pages/products/uti-interface.php

[208] Solovov, V. N., Chepel, V., Lopes, M. I., & Hitachi, A. 2004, Nucl. Instrum. Meth., A516, 462

[209] Solovov, V. N., Chepel, V., Lopes, M. I., et al. 2004, Nuclear Instruments and Methods in Physics Research A, 516, 462

[210] Sorensen, P., & Dahl, C. E. 2011, Physical Review D, 83, 063501

[211] Sprenger, A. 2007, PhD thesis, WWU Münster. https://www.uni-muenster.de/Physik.KP/AGWeinheimer/en/arbeitsgruppe/arbeiten.html

[212] Steigman, G. 2015, Physical Review D, 91, 083538

[213] Steinberger, I. T., & Asaf, U. 1973, Phys. Rev. B, 8, 914. https://link.aps.org/doi/10.1103/PhysRevB.8.914

[214] Swagelok. 2017, 316L VIM-VAR UHP Diaphragm Sealed Valve. https://www.swagelok.com/en/catalog/Product/Detail?part=6LVV-DPFR4-P

[215] Swagelok. 2017, 316L VIM-VAR UHP High Pressure Diaphragm Sealed Valve. https://www.swagelok.com/en/catalog/Product/Detail?part=6LVV-DPHFR4-P

[216] Swagelok. 2017, Stainless Steel Bellows Sealed Valve. https://www.swagelok.com/en/catalog/Product/Detail?part=SS-4BW-V51

[217] Swagelok. 2017, Pressure Regulators K Series. https://www.swagelok.com/downloads/webcatalogs/EN/MS-01-24.PDF

[218] Szydagis, M., Barry, N., Kazkaz, K., et al. 2011, ArXiv e-prints, arXiv:1106.1613

[219] Takahashi, T., Konno, S., Hamada, T., et al. 1975, Phys. Rev. A, 12, 1771. https://link.aps.org/doi/10.1103/PhysRevA.12.1771

[220] Taylor, A. N., Dye, S., Broadhurst, T. J., Benítez, N., & van Kampen, E. 1998, Astrophysical Journal, 501, 539

[221] Techniques, S. 2017, Co57 spectrum. http://www.spectrumtechniques.com/products/sources/cobalt-57/

[222] Teragon. 2017, LC2 Liquid Nitrogen Level Controller. http://www.trgn.com/LC2/LC2.html

[223] The LZ Collaboration, Akerib, D. S., Akerlof, C. W., et al. 2015, ArXiv e-prints, arXiv:1509.02910

[224] The XENON100 Collaboration, Aprile, E., Alfonsi, M., et al. 2012, ArXiv e-prints, arXiv:1207.3458

[225] Toolbox, E. 2017, Thermal Conductivity of common Materials and Gases. http://www.engineeringtoolbox.com/thermal-conductivity-d_429.html

[226] Tsai, B. K., Allen, D. W., Hanssen, L. M., Wilthan, B., & Zeng, J. 2008, in Reflection, Scattering, and Diffraction from Surfaces, ed. Z.-H. Gu & L. M. Hanssen (SPIE). https://doi.org/10.1117/12.798138

[227] Vacuum, P. 2017, TPR 280. https://www.pfeiffer-vacuum.com/en/products/measurement/activeline/activeline-gauges/?detailPdoId=3937

[228] Vacuum, P. 2017, PKR 251, FPM sealed, DN 40 CF-F. https://www.pfeiffer-vacuum.com/en/products/measurement/activeline/activeline-gauges/?detailPdoId=3918

[229] Vacuum, P. 2017, HiCube 80 Eco, DN 63 CF-F, MVP 015-2, 100-240. https://www.pfeiffer-vacuum.com/en/products/pumping-stations/turbo-pumping-stations/hicube-eco/?detailPdoId=20022

[230] Weinberg, S. 2008, Cosmology (Oxford University Press)

[231] Wikipedia, t. f. e. 2017, Lambert's cosine law. https://en.wikipedia.org/wiki/Lambert%27s_cosine_law

[232] Wikipedia, t. f. e. 2017, PID controller. https://en.wikipedia.org/wiki/PID_controller

[233] XENON Collaboration, Aprile, E., Aalbers, J., et al. 2017, ArXiv e-prints, arXiv:1708.07051

[234] XENON Collaboration, Aprile, E., Aalbers, J., et al. 2017, ArXiv e-prints, arXiv:1705.01828

[235] Xenon100 Collaboration, Aprile, E., Arisaka, K., et al. 2012, Astroparticle Physics, 35, 573

[236] Yamashita, M., Doke, T., Kawasaki, K., Kikuchi, J., & Suzuki, S. 2004, Nuclear Instruments and Methods in Physics Research A, 535, 692

[237] Zappa, P. 2016, Master's thesis, Uni Bern

[238] Zappa, P., Bütikofer, L., Coderre, D., et al. 2016, Journal of Instrumentation, 11, T09003

[239] Zboril, M. 2011, PhD thesis, WWU Münster. http://nbn-resolving.de/urn:nbn:de:hbz:6-91469497689

[240] ZELDOVICH, Y. 1965, in Advances in Astronomy and Astrophysics (Elsevier), 241–379. https://doi.org/10.1016/b978-1-4831-9921-4.50011-9

[241] Zwicky, F. 1933, Helvetica Physica Acta, 6, 110

Erklärung

gemäss Art. 28 Abs. 2 RSL 05

Name/Vorname:	Basho Kaminsky
Matrikelnummer:	13-139-753
Studiengang:	PhD in Physics
Titel der Arbeit:	Optimizing liquid Xenon TPCs
Leiter der Arbeit:	Prof. Dr. Marc Schumann

Ich erkläre hiermit, dass ich diese Arbeit selbständig verfasst und keine anderen als die angegebenen Quellen benutzt habe.
Alle Stellen, die wörtlich oder sinngemäss aus Quellen entnommen wurden, habe ich als solche gekennzeichnet. Mir ist bekannt, dass andernfalls der Senat gemäss Artikel 36 Absatz 1 Buchstabe r des Gesetzes vom 5. September 1996 über die Universität zum Entzug des auf Grund dieser Arbeit verliehenen Titels berechtigt ist. Ich gewähre hiermit Einsicht in diese Arbeit.

Bern/Datum

Unterschrift

Basho Kaminsky

Personal data

Basho Kaminsky
Gerberngasse 7
3011 Bern
Switzerland

Date of Birth: 23.09.1988

Education

11/2017	**PhD in Physics**
06/2015	**ISAPP 2015 School on Cosmology** (Paris, France)
2013–11/2017	**PhD studies in Physics at the University of Bern**
2013	**Master of Science in Physics**
07–09/2011	**DESY Summer School** (Berlin, Germany)
2010	**Bachelor of Science in Physics**
2008-2010	**Studies in Physics at the University of Leipzig**
2007	**Abitur**